Mass Spectrometric and NMR Studies of Some β-ketoenolate and Monothio-β-ketoenolate Complexes of Rhodium(III) and Iridium(III).

by

Gary A. Stern, B.Sc., M.Sc.

A Thesis submitted to
the Faculty of Graduate Studies
in partial fulfillment of the requirements
for the degree of
DOCTOR OF PHILOSOPHY

Chemistry Department
University of Manitoba
Winnipeg, Manitoba
December, 1990

ISBN 0-315-71906-0

MASS SPECTROMETRIC AND NMR STUDIES OF SOME B-KETOENOLATE AND MONOTHIO-B-KETOENOLATE COMPLEXES OF RHODIUM(III) AND IRIDIUM(III)

BY

GARY A. STERN

A thesis submitted to the Faculty of Graduate Studies of the University of Manitoba in partial fulfillment of the requirements of the degree of

DOCTOR OF PHILOSOPHY

TABLE OF CONTENTS

ACKNOWLEDGEMENTS

I wish to thank Professor John B. Westmore, my research supervisor for his advice, helpful suggestions and enlightening discussions throughout this project. I would also like to thank the other members of my advisory committee, Professors A.F. Janzen, K.S. Sharma and G.R.B. Webster.

I would like to express my appreciation to Dr. Mark Reimer for his helpful advice, Mr. Wayne Buchannon for the sharing of his expertise in the running of the mass spectrometer, Mr. Terry Wolowiec for obtaining the NMR spectra discussed in this study and to Mr. Rudy Subastian and Mr. Christian Beaulieu for their help regarding the use of the program Numarit.

Finally, I wish to express love and appreciation to my wife Elzbieta and daughter Cora for their support and understanding throughout these years.

TO ELZBIETA AND CORA

ABSTRACT

Electron ionization (70 eV) positive ion mass and ^{19}F and/or ^{1}H NMR spectra of rhodium(III) chelates of the β-ketoenols $R^1C(OH)=CHCOR^2$ ($R^1= C_6H_5$, $R^2 = C_2F_5$, C_3F_7) and monothio-β-ketoenols $R^1C(SH)=CHCOR^2$ ($R^1= C_6H_5$, $R^2 = C_2F_5$, C_3F_7 ; $R^1= CH_3$, $R^2 = CH_3$, CF_3) and of the iridium(III) chelates of the β-ketoenols $R^1C(OH)=CHCOR^2$ ($R^1= CH_3$, $R^2 = CH_3$, CF_3 ; $R^1= R^2 = CF_3$) are reported. Also presented is a crystal structure determination of $Rh(CH_3CSCHCOCF_3)_3$.

Mass spectral behaviour of these compounds are interpreted in terms of the principle of Hard and Soft Acids and Bases (HSAB), the influence (inductive and mesomeric) of the R^1 and R^2 groups, the metal's ability to undergo a change in oxidation state and to form single and multiple bonds with carbon. Mechanisms of ion decomposition, supported by results from linked scanning, accurate mass and deuterium labelling, are proposed.

The ^{19}F and ^{1}H NMR studies show that the β-ketoenolates are formed as a nearly statistical mixture of *fac* and *mer* isomers when the ligands are asymmetric, while the thio complexes adopt a facial octahedral structure. The splitting patterns observed in the ^{19}F NMR spectra of the rhodium perfluoroalkyl complexes $Rh(C_6H_5CSCHCOC_3F_7)_3$, $Rh(C_6H_5COCHCOC_2F_5)_3$ and $Rh(C_6H_5COCHCOC_3F_7)_3$ are consistent with an ABX_3 type spin system. Vicinal F-F couplings were found to be < 2 Hz, while geminal F-F couplings were in the order of 270 Hz. Long range F-F couplings in the two perfluoropropyl complexes were in the order of 9 Hz.

Geminal F-F coupling was not observed for the thio complex $Rh(C_6H_5CSCHCOC_2F_5)_3$ and for one of the isomers in the analogous dioxo complex (in toluene solution) indicating, that both fluorines of their CF_2 groups are chemically equivalent.

LIST OF TABLES

Table

LIST OF FIGURES

Figure Page

Figure Page

Figure

Page

LIST OF SCHEMES

Scheme Page

Scheme Page

ABBREVIATIONS AND SYMBOLS

(i) Abbreviations

Sacac-H	4-mercaptopent-3-en-2-one
Stfa-H	1,1,1-trifluoro-4-mercaptopent-3-en-2-one
bzC_2F_5-H	1,1,1,2,2-pentafluoro-5-phenyl-3,5-pentanedione
bzC_3F_7-H	1,1,1,2,2,3,3-heptafluoro-6-phenyl-4,6-hexanedione
$SbzC_2F_5$-H	1,1,1,2,2-pentafluoro-5-phenyl-5-mercaptopent-4-en-3-one
$SbzC_3F_7$-H	1,1,1,2,2,3,3-heptafluoro-6-phenyl-6-mercaptohex-5-en-4-one
acac-H	2,4-pentanedione
tfa-H	1,1,1-trifluoro-2,4-pentanedione
hfa-H	1,1,1,5,5,5-hexafluoro-2,4-pentanedione
$Rh(Sacac)_3$	Tris[4-mercaptopent-3-en-2-onato]rhodium(III)
$Rh(Stfa)_3$	Tris[1,1,1-trifluoro-4-mercaptopent-3-en-2-onato]rhodium(III)
$Rh(bzC_2F_5)_3$	Tris[1,1,1,2,2-pentafluoro-5-phenyl-3,5-pentanedionato]rhodium(III)
$Rh(bzC_3F_7)_3$	Tris[1,1,1,2,2,3,3-heptafluoro-6-phenyl-4,6-hexanedionato]rhodium(III)
$Rh(SbzC_2F_5)_3$	Tris[1,1,1,2,2-pentafluoro-5-phenyl-5-mercaptopent-4-en-3-onato]rhodium(III)
$Rh(SbzC_3F_7)_3$	Tris[1,1,1,2,2,3,3-heptafluoro-6-phenyl-6-mercaptohex-5-en-4-onato]rhodium(III)
$Ir(acac)_3$	Tris[2,4-pentanedionato]iridium(III)
$Ir(tfa)_3$	Tris[1,1,1-trifluoro-2,4-pentanedionato]iridium(III)
$Ir(hfa)_3$	Tris[1,1,1,5,5,5-hexafluoro-2,4-pentanedionato] iridium(III)

FFR	Field free region.
IKES	Ion kinetic energy spectroscopy.
NMR	Nuclear magnetic resonance.
mer	Meridional.
fac	Facial.
u	Dalton or mass unit (^{12}C = 12 daltons).
e	Electronic charge.
m	The mass of an ion.
z	The charge number of an ion.
m/z	The mass-to-charge ratio of an ion.
m*	The peak resulting from ion decomposition in a field free region of the mass spectrometer.
M^+	Parent ion.
A^+	Fragment or daughter ion.
N	Neutral fragment.
IE	Ionization energy.
V	Accelerating voltage.
B	Magnetic field.
E	Electric field.
%RA	The relative abundance of an ion as a percentage of the abundance of the base peak.

(ii) Symbols

Each structure in a given scheme is represented by a capital letter followed by a number. These correspond to the complex and the mass of the ion or neutral it represents, respectively (e.g. In Scheme 3.3 the A in A946 represents the complex $Rh(SbzC2F5)_3$, while 946 corresponds to the m/z value of the ion RhL_3^+). Different structures

for an ion or neutral having the same mass are indicated by the addition of a small letter following the number (i.e. C848a and C848b, Scheme 3.4).

$\xrightarrow{*}$ Process confirmed by metastable ion decomposition evidence

$\longrightarrow$ Indication of a two electron shift

$\rightarrowtail$ Indication of a one electron shift

1 Introduction

1.1 Mass Spectrometric studies of Metal-β-ketoenolates and monothio-β-ketoenolates.

In 1966, Macdonald and Shannon, with their studies of metal acetylacetonates[1], opened a whole new dimension in the mass spectrometry of metal-β-ketoenolates and monothio-β-ketoenolates. Since then, over four hundred different complexes of alkaline earth, lanthanide and transition metals, with ligands having various donor atoms (typically oxygen, nitrogen and sulfur) and a wide range of aryl and alkyl substituents have been studied by mass spectrometry, involving nearly all of the modern ionization techniques available. Several excellent reviews are available[2-5].

When discussing the mass spectra of metal-β-ketoenolates and monothio-β-ketoenolates, the ability of the metal to undergo a change in valence state has been shown to be of fundamental importance[6,7]. The idea of changing the valence state of the metal is essentially an offshoot of the "even-electron rule", an often quoted generalization important for the understanding and prediction of the

mass spectral behavior of organic compounds[8,9]. It states that odd-electron ions (such as molecular ions, or fragment ions formed by rearrangements) may eliminate either odd-electron or even-electron neutrals, but decompositions of even-electron ions (such as fragments formed by a single bond cleavage) are strongly influenced by the preference for the formation of an even-electron ion and, consequently an even-electron neutral. Production of an odd-electron ion must be accompanied by formation of a neutral radical, which involves the energetically unfavorable separation of an electron pair. In the case of metal-β-ketoenolates and monothio-β-ketoenolates, to avoid violation of the "even-electron rule", consecutive losses of neutral radicals have been interpreted in terms of a change in oxidation state of the metal atom of an ion, with consequent reversal of the even-to-odd electron character.

In an attempt to rationalize much of what has been observed in the mass spectra of metal-β-ketoenolates and monothio-β-ketoenolates, Westmore[4] made the following three generalizations concerning the relationship between metal oxidation and molecular ion stabilities. First, the molecular ion will be stabilized if metal-to-ligand π-electron donation is favored, i.e. if facile increase in metal oxidation state can occur. The molecular ion will be relatively abundant and the loss of even-electron neutral species from the molecular ion will be enhanced. Secondly, if the metal ion does not undergo facile increase of oxidation state the molecular ion is not appreciably stabilized and hence may be of low abundance. Fragmentation usually proceeds through loss of a neutral radical, followed by loss of even-electron neutrals when decrease of

oxidation does not readily occur. Finally, if the metal ion is amenable to a decrease in oxidation state, then the molecular ion may be of low abundance. Fragmentation usually occurs by two successive losses of neutral radicals. Succeeding losses will occur through the elimination of odd- or even- electron neutrals, depending upon the ease of a further decrease of metal oxidation state.

1.2 Hard and soft acids and bases.

Although monothio-β-ketoenolates are stronger Brønsted-Lowry acids than are their analogous β-ketoenolates, stability constant data indicate that some metals form more stable complexes with the former than with the latter.[10] Thus, while β-ketoenolate chelates of Ti(IV), Al(III) and Co(III) are more stable than their monothio analogues the situation is reversed for chelates of Ag(I), Hg(II) and Pt(II).

1.2.1 Classification of acids and bases as hard or soft.

Metal ions and ligands have been classified as belonging to either type (a) or type (b) according to their preferential bonding with each other[10]. Class (a) metal ions include those of alkali metals, alkaline earth metals, lighter transition metals in higher oxidation states (such as Ti(IV), Cr(III), Fe(III), Co(III)), and also the hydrogen ion, H^+. Class (b) metal ions include those of heavier transition metals, and lighter transition metals in lower oxidation states (such as Cu(I), Ag(I), Hg(I), Pd(II) and Pt(II)). Ligands also may be classified as either type (a) or (b), indicating preferences toward

either class (a) or class (b) metal ions, respectively. Relative stabilities of metal-ligand complexes, summarized in Table 1.1[10], enable us to predict that β-ketoenolates will have a greater tendency than monothio-β-ketonenolates to coordinate with class (a) metal ions, and that these tendencies will be reversed for class (b) metal ions.

Table 1.1 Relative stability of metal-ligand complexes having the indicated donor atoms.

Tendency to complex with class (a) metal ions	Tendency to complex with class (b) metal ions
N >> P > As > Sb	N << P > As > Sb
O >> **S** > Se > Te	**O** << **S** < Se = Te
F > Cl > Br > I	F < Cl < Br < I

Pearson[11] suggested that the members of classes (a) and (b) be described by the terms "hard" and "soft", respectively. Therefore, a type (a) metal is a hard acid and a ligand such as ammonia or the fluoride ion is a hard base. Conversely, a type (b) metal ion is a soft acid and a ligand such as phosphine or the iodide ion is a soft base. In hard and soft interactions the hard species, both acids and bases, tend to be small and slightly polarizable, and the soft acids and bases tend to be large and more polarizable. A simple rule of thumb, sometimes referred to as Pearson's principle, or the hard and soft acid base (HSAB) rule, helps us to predict qualitatively the relative stabilities of complexes between acids and bases. This rule states that: hard acids prefer to bind to hard bases and soft acids prefer to bind to soft bases.

Tables 1.2 and 1.3 list some hard and soft acids and bases[10]. The terms hard and soft are relative ones and there is no sharp dividing line between them, so that some acids and bases fall on the borderline between hard and soft. Even within a hard or soft group, not all species will have equivalent hardness or softness. For example, even though all alkali metal ions are hard acids, a cesium ion, which is larger and more polarizable than a lithium or scandium ion, is less hard.

The hardness or softness of any metal ion is also a function of the other groups bonded to it. Thus, the presence of soft polarizable substituents can soften an otherwise hard acid, and of electron-withdrawing groups can harden the acid, to facilitate the addition of further soft or hard donors, respectively. Jorgensen[12] was the first to comment on this important effect, and used the term "symbiosis" to describe it. For example, boron(III) falls on the borderline between hard and soft acids. In BF_3, three hard electronegative fluorines harden boron and make it a hard acid. Conversly, in BH_3, the three soft electropositive hydrogens soften boron and make it a soft acid. In BH_3 the easily polarized hydride species lose a portion of their negative charge to boron, which thus has an effective charge much less than +III, but in BF_3 the only slightly polarizable fluoride ions hold on to their electrons and the effective charge on boron is closer to +III. Thus, BH_3 forms a stable compound, BH_3CO, with CO (a typical soft base) while BF_3CO is not known. On the other hand, BF_3 forms stable compounds such as BF_3NR_3 or BF_3OR_2 with amines and ethers, respectively[13].

Table 1.2 Classification of hard and soft acids

Hard acids

H^+, Li^+, Na^+, K^+ (Rb^+, Cs^+)
Be^{2+}, $Be(CH_3)_2$, Mn^{2+}, Ca^{2+}, Sr^{2+} (Ba^{2+})
Sc^{3+}, La^{3+}, Ce^{4+}, Gd^{3+}, Lu^{3+}, Th^{4+}, U^{4+}, UO_2^{2+}, Pu^{4+}
Ti^{4+}, Zr^{4+}, Hf^{4+}, VO^{2+}, Cr^{3+}, Cr^{6+}, MoO^{3+}, WO^{4+}, Mn^{2+},
Mn^{7+}, Fe^{3+}, Co^{3+}
BF_3, BCl_3, $B(OR)_3$, Al^{3+}, $Al(CH_3)_3$, $AlCl_3$, AlH_3, Ga^{3+}, In^{3+}
CO_2, RCO^+, NC^+, Si^{4+}, Sn^{4+}, CH_3Sn^{3+}, $(CH_3)_2Sn^{2+}$
N^{3+}, RPO_2^+, $ROPO_2^+$, As^{3+}
SO_3, RSO_2^+, $ROSO_2^+$
Cl^{3+}, Cl^{7+}, I^{5+}, I^{7+}
HX (hydrogen-bonding molecules)

Borderline acids

Fe^{2+}, Co^{2+}, Ni^{2+}, Cu^{2+}, Zn^{2+}
Rh^{3+}, Ir^{3+}, Ru^{3+}, Os^{2+}
$B(CH_3)_3$, GaH_3
R_3C^+, $C_6H_5^+$, Sn^{2+}, Pb^{2+}
NO^+, Sb^{3+}, Bi^{3+}
SO_2

Soft acids

$Co(CN)_5^{3-}$, Pd^{2+}, Pt^{2+}, Pt^{4+}
Cu^+, Ag^+, Au^+, Cd^{2+}, Hg^+, Hg^{2+}, CH_3Hg^+
BH_3, $Ga(CH_3)_3$, $GaCl_3$, $GaBr_3$, GaI_3, Tl^+, $Tl(CH_3)_3$
CH_2, carbenes
π-acceptors: trinitrobenzene, chloroanil, quinones, tetracyanoethylene, *etc.*
HO^+, RO^+, RS^+, RSe^+, Te^{4+}, RTe^+
Br_2, Br^+, I_2, I^+, ICN, *etc.*
O, Cl, Br, I, N, $RO\cdot$, $RO_2\cdot$
M^0(metal atoms) and bulk metals

Table 1.3 Classification of hard and soft bases

Hard bases
NH_3, RNH_2, N_2H_4
H_2O, OH^-, O^{2-}, ROH, RO^-, R_2O
CH_3COO^-, CO_3^{2-}, NO_3^-, PO_4^{3-}, SO_4^{2-}, ClO_4^-
F^-
Borderline bases
$C_6H_5NH_2$, C_5H_5N, N_3^-, N_2
NO_2^-, SO_3^{2-}
Br^-, Cl^-
Soft bases
H^-
R^-, C_2H_4, C_6H_6, CN^-, RNC, CO
SCN^-, R_3P, $(RO)_3P$, R_3As
R_2S, RSH, RS^-, $S_2O_3^{2-}$
I^-

Hardness and softness refer to the special stability of hard-hard and soft-soft interactions and should be carefully distinquished from acid and base strength[14,15]. For example, both OH^- and F^- ions are *hard* bases but the former is a much *stronger* base than is the latter (see Table 1.4). Furthermore, a strong acid or base displaces a weaker one from an acid-base adduct (by definition), even when this appears to contradict the HSAB principle. Thus, from data in Table 1.4, we see that sulfite ion, a strong, soft base, displaces fluoride ion, a weak, hard base, from its adduct with a hard acid, the proton, H^+ (Equation 1.1). Similarly, the hydroxide ion, a very strong, hard base displaces this strong, soft base from its adduct with the soft acid, the methylmercury cation (Equation 1.2).

$$\underset{\text{(H-H)}}{SO_3^{2-} + HF} \text{ -------> } \underset{\text{(H-S)}}{HSO_3^- + F^-} \qquad K_{eq} = 10^4 \qquad [1.1]$$

$$\underset{\text{(S-S)}}{OH^- + CH_3HgSO_3^-} \text{ -------> } \underset{\text{(S-H)}}{CH_3HgOH + SO_3^{2-}} \qquad K_{eq} = 10 \qquad [1.2]$$

Therefore, because of the relative strengths of these bases ($OH^- > SO_3^{2-} > F^-$) reactions 1.1 and 1.2 are forced to the right in spite of the HSAB principle. However, if a competitive situation exists, in which both strength and hardness-softness are considered, the hard-soft principle works (Equations 1.3 and 1.4).

$$\underset{\text{(S-H)}}{CH_3HgF} + \underset{\text{(H-S)}}{HSO_3^-} \text{ -------> } \underset{\text{(S-S)}}{CH_3HgSO_3^-} + \underset{\text{(H-H)}}{HF} \qquad K_{eq} \sim 10^3 \qquad [1.3]$$

Table 1.4 Basicity[a] toward the proton and methylmercury cation.

Base	Linking atom	pK_s[b](CH_3Hg^+)	pK_h[c](H^+)
F^-	F	1.50	2.85
Cl^-	Cl	5.25	-7.0
Br^-	Br	6.62	-9.0
I^-	I	8.60	-9.5
OH^-	O	9.37	15.7
HPO_4^-	O	5.03	6.79
S^{2-}	S	21.20	14.2
$HOC_2H_4S^-$	S	16.12	9.52
SCN^-	S	6.05	~4
SO_3^{2-}	S	8.11	6.75
$S_2O_3^{2-}$	S	10.90	negative
NH_3	N	7.60	9.42
$NH_2C_6H_4SO_3^-$	N	2.60	3.06
$(C_6H_5)_2PC_6H_4SO_3^-$	P	9.15	~0
$Et_2PC_2H_4OH$	P	14.6	8.1
Et_3P	P	15.0	8.8
CN^-	C	14.1	9.14

[a] Basicity is defined here as: a negative character of a chemical species that is decreased by reaction with an acid.[10]

[b] $pK_s = \log[CH_3HgB]/[CH_3Hg^+][B]$ [c] $pK_h = \log[HB]/[H^+][B]$

$$CH_3HgOH + HSO_3^- \text{ -------> } CH_3HgSO_3^- + H_2O \qquad K_{eq} > 10^7 \quad [1.4]$$

(S-H) (H-S) (S-S) (H-H)

Thus, in interpreting acid-base interactions one must consider both strength and hardness-softness. Table 1.4 lists $pK_{(h,s)}$ values for the reaction of various bases with the proton and the methylmercury cation[10]. Bases such as the sulfide ion (S^{2-}) and triethylphosphine (Et_3P) are very strong toward both the methylmercury ion and the proton but about a million times better toward the methylmercury ion, and therefore they are considered to be soft. The hydroxide ion (OH^-) is a strong base toward both acids but, in this case, about a million times better toward the proton, and therefore it is considered to be hard. The fluoride ion (F^-) is not a particularly good base toward either acid, but slightly better toward the proton as would be expected since it is a hard base.

1.2.2 Theoretical basis of hardness and softness.

Pearson[16] pointed out an interesting difference between the HSAB rule and Pauling's original method of defining electronegativity. According to the latter, the greatest ionic resonance energies occur for bonds formed between elements furthest apart in electronegativity, i.e. between cesium and fluorine[10]. Thus, one would predict the following reaction:

$$CsI + LiF \text{ -------> } LiI + CsF \qquad [1.5]$$

Experimentally it is found that, in accord with the HSAB rule, the reaction actually proceeds in the reverse direction (Equation 1.6).

$$LiI + CsF \text{ -------> } LiF + CsI \qquad \Delta H = \sim -63 \text{ kJmol}^{-1} \qquad [1.6]$$

The atomization enthalpies of the four compounds are: LiF = +573, CsF = +502, LiI = +347 and CsI = +335 ($kJmole^{-1}$) from which we see that the hard-hard interaction (LiF) is greatest and the soft-soft interaction (CsI) is smallest and that the hard-hard interaction drives reaction 1.6 to the right despite the weak soft-soft interaction.

A similar explanation can be qiven for reaction 1.7 for which the atomization enthalpies of the participating species are: BeF_2 = +1264, HgF_2 = +536, BeI_2 = +577 and HgI_2 = +293 ($kJmol^{-1}$).

$$HgF_2 + BeI_2 \text{ -------> } BeF_2 + HgI_2 \qquad \Delta H = \sim -397 \text{kJmol}^{-1} \qquad [1.7]$$

(S-H) (H-S) (H-H) (S-S)

The driving force for this reaction is provided mainly by the very high energy term for BeF_2. The extremely high hard-hard interaction could arise from formation of strong covalent bonds, as well as to strong electrostatic attractions between Be and F. This is reasonable because, as pointed out earlier, hard species (both acid and base) tend to be small and slightly polarizable, while soft acids and bases tend to be larger and more polarizable. Covalent bonds between small atoms are relatively strong because the atomic orbitals have a large overlap while those between large atoms are relatively weak due to a small amount of atomic orbital overlap. In

addition, since the electrostatic energy of an ion pair is inversely proportional to the interatomic distance then, the smaller are the ions involved, the greater is the attraction between them.

Calculations of the relative importance of covalent and ionic bonding are only approximate, but they indicate that each contributes to an appreciable extent in LiF. Of the total atomization energy of LiF (573 $kJmol^{-1}$) approximately one fourth comes from covalent bonding, one half from electrostatic attraction between the partial charges on the lithium and fluorine atoms (approximately two thirds of an electronic charge) and about one fourth from the transfer of partial charge from the more electropositive lithium atom to the more electronegative fluorine atom (Pauling's ionic resonance energy)[17,18].

In general, there may be several contributions to soft-soft interactions.[19] For soft character, a metal ion should possess a large number of electrons in its outer d-shell. Many typical soft acids have the d^{10} configuration, while the d^6 to d^9 configurations typically result in soft character (fewer than five d-electrons result in hard properties in all but a very few cases)[19]. For elements with partially completed outer d-shells (i.e. transition metals) it follows that their softness will be more marked in lower oxidation states, e.g. Rh(I) (d^8) is softer than Rh(III) (d^6). A d^5 transition element can have soft character only in its zero oxidation state. However, the presence of many outer d-shell electrons does not necessarily guarantee that an element will behave as a soft acid because electrons outside the d-shell cause a considerable decrease in softness by shielding the d-shell. Thus, Tl(III), (d^{10}), is a softer acid than Tl(I), ($d^{10}s^2$).[20]

In many cases, an unshielded d^6 to d^{10} configuration is not the only prerequisite for soft acid behavior. For metal d-electrons to be available for bonding their energies must approximate those of other bonding electrons, in which case the metal ion will be highly polarizable. For metal ions of a given net charge and outer electronic configuration the polarizability increases as the number of electronic shells increases. The softness therefore increases as the period number of the element increases. This is especially noticeable in going from first row to second row transition metals.

Oxidation state is another factor that greatly influences the hard-soft character of a metal ion. First, a change of oxidation state means a change of electronic configuration, which by itself will cause a very significant change of the bonding properties, as discussed above. Furthermore, polarizability varies as the charge varies; the higher is the oxidation state the lower is the polarizability. Therefore, an increase in oxidation state should decrease the softness of the acid.

The effect of changes of the metal ion oxidation state on the strength of metal-ligand bonding is less clear. An increase of oxidation state will increase the polarization of coordinated ligands and increase the availability of their electrons for covalent bond formation. This effect should be greater the stronger the polarizing influence of the metal. Therefore, an increase in metal ion oxidation state makes its own electrons less available, but those of the ligand more available, for bonding. Whether the net result is a strengthening or a weakening of the bond will depend on the relative magnitudes of these influences. Finally, an increase in oxidation state enhances the electrostatic interaction between metal ion and

ligand, which increases the ionic relative to the covalent contribution to bonding.

Whether a metal-ligand bond is mainly covalent or ionic depends on the ligand as well as on the metal ion. As a general rule, the more polarizable is the ligand the greater is the softness of the metal ion. The polarizability of a ligand is determined by the electronegativity of its donor atom and the properties of the adjoining atom(s). If the ligand is an elementary ion its electronegativity is therefore the only factor of importance. A low electronegativity implies high polarizability and, consequently, a strong tendency to form covalent bonds. However, besides high polarizability, a ligand should have further properties to be a soft donor, e.g. empty orbitals of suitable energy and symmetry to accommodate d-electrons (which are seemingly of decisive importance for formation of an essentially covalent bond) from the metal ion. In many instances the ligand may use vacant d-orbitals to accommodate the metal electrons, because a great jump in affinity for soft acids is observed on going from ligands that have first row donor atoms (O, N) that have no d-orbitals of the same principal quantum number as the metal d-electrons, to ligands that have second (S, P) and third row donor atoms where such vacant d-orbitals do exist. Certain neutral ligands, such as carbonyl and nitrosyl groups, form with a metal a bond of order approximately equal to two. This bond is described as a σ-bond made up mainly by electrons donated by the ligand, and a π-bond formed with d-electrons contributed by the metal. For the latter bond, empty

π^*-orbitals on the ligand are utilized. This is simply referred to as back bonding[21].

If a soft metal ion is offered various soft ligands at the same time it will, as a rule, coordinate them into a mixed complex, of composition determined by the relative affinities of the ligands for the metal ion. This is the well known phenomenon that soft ligands tend to come together in mixed complexes formed with soft acids (as do, of course, hard ligands in mixed complexes with hard acids)[19]. If, however, an extremely soft ligand is coordinated to a transition metal ion it may take care of all available d-electrons and leave none for further soft ligands, with the result that the residual coordination capacity of the metal ion can be used only by hard ligands that use mainly electrostatic forces for bonding. In other words, the coordination of very soft ligands to a soft acid will decrease its softness, or even turn it into a hard acid[19]. A good example of this is provided by Burmeister and Basolo[22] who found that the very soft ligand triphenylphosphine causes Pt(II) and Pd(II) to coordinate thiocyanate ion by its hard nitrogen end, while the less soft triphenylstibine causes thiocyanate ion to attach by its soft sulfur end. This result is contrary to the symbiotic tendency mentioned previously.

In review, one can say that strong hard-hard interactions occur between two atoms when the bond has both covalent and ionic contributions, while weak soft-soft interactions arise mainly from π-bonding and to a lesser extent from electrostatic interactions. Thus, when referring to a hard and soft acid-base reaction (equations

1.6 and 1.7) one could say that: soft acids prefer to bond to soft bases only because hard acids are preferentially bonded to hard bases.

1.2.3 HSAB theory applied to halogen transfer in mass spectrometry.

Miller *et al*[23], were the first to apply hard and soft acid base (HSAB) theory to the phenomenon of halogen transfer observed in electron ionization (70 eV) positive ion mass spectra of organometallic compounds. Their study of a series of group IV and V perfluoro phenyl complexes of the type $(C_6F_5)_nMet^+$ (Met = Si(IV), Sn(IV), Ge(IV), Pb(IV), P(III), As(III), and Sb(III)), revealed mass spectral evidence for Met-F bond formation, especially in the Sn(IV), Si(IV) and Sb(IV) complexes. They also studied a set of Hg(II) complexes $(C_6X_5)_2Met$ (X = F, Cl, Br) and reported observing several Hg-Br bonded ions, but no Hg-F or Hg-Cl containing species. If the halide is treated as the base, and the central atom as the acid, these results make sense in terms of HSAB theory. Mercury, being particularly soft favours the softer bromide ligand in preference to the harder fluoride or chloride ligand. The elements of groups IV and V, all being reasonably hard acids, favour the harder fluoride ligand. Similarly a series of C_6F_5Pt derivatives was studied, and for none of these was any Pt-F containing species observed.

Morris and Koob[24] extended the HSAB principle to the mass spectra of the fluorinated β-ketoenolates of Co(II), Fe(II), Fe(III), Cr(III), Al(III), Zn(II), Ni(II), Mn(II) and Cu(I). In the spectra of hexafluoroacetylacetonate derivatives many ions corresponding to rearrangements of a fluorine to the metal were observed and several demonstrated the loss of neutral metal fluorides *via* metastable

transitions (except in the case of Cu(I)). With the exception of Cu(I) all of the above mentioned metals can be considered as either hard or borderline hard acids. Fluorine migration to these centers is therefore in keeping with HSAB theory (the two electron-withdrawing CF_3 substituents on the ligand would be expected to 'harden' the borderline metals, making them more receptive to fluorine transfer). The absence of fluorine rearrangement in the case of Cu(I) is understandable since Cu(I) is recognized as a soft acid and so should not be expected to bond with fluorine.

In the gas phase, since no solvent is present, the acidity of the metal is influenced only by its ligands. Among the fluorinated or partially-fluorinated β-ketoenolates the hardest acid ligands occur in the hfa chelates. If a CF_3 group is replaced with a more electron rich species, such as a methyl, ethyl, isopropyl, phenyl or a thienyl group, resulting in the softening of the acidity of the metal, it is to be expected that fluorine rearrangement to the metal would be less prevalent. Relevent data for complexes of $Met(CF_3COCHCOR)_3$ are given in Table 1.5[24]. As expected, it seems that fluorine rearrangement ions become less important (lower relative abundance) as the softness of the metal environment increases.

1.3 General principles of a conventional double focussing magnetic sector mass spectrometer.

After a substance is ionized, ions are accelerated through a potential difference of 2 to 10 keV away from the ion source and into the analyser region of the mass spectrometer. Provided that the

Table 1.5 Abundances, relative to $MetL_2^+$ = 100, of fluorine rearrangement ions for $Met(CF_3COCHCOR)_3$[24]

	R = CF_3	CH_3	C_2H_5	i-C_3H_7	t-C_4H_9	C_6H_5	C_4H_3S
$[Fe^{III}F_2(L\text{-}CF_3)]^+$	5	1.5	0.3	0	0	1.5	2
$[Fe^{II}F(L\text{-}CF_3)]^+$	80	46	33	30	29	27	25
$[Cr^{III}F_2(L\text{-}CF_3)]^+$	20	12	7	4	0	9	-
$[Cr^{II}F(L\text{-}CF_3)]^+$	21	20	16	17	14	13	0

energy increment is large compared with the initial energy, ~1 eV, of the ions entering the accelerating region of the ion source all ions carrying the same charge are accelerated to approximately the same kinetic energy. In a conventional double focussing magnetic sector instrument (Figure 1.1) the analyser region consists of an electric sector followed by a magnetic sector, along with three field regions (FFR's). This type of instrument is said to have Nier-Johnson geometry because the deflections of the ion beam, in the electric and magnetic fields, are both in the same direction[25-27].

First, let us consider the situation when no electric sector is present so that the ions after acceleration enter the magnetic sector with a kinetic energy given by

$$zeV=mv^2/2 \qquad [1.8]$$

where V is the accelerating voltage, and v is the velocity of an ion of mass m and charge ze (e is the electronic charge and z is a small integer, usually 1). On passing through the magnetic field, B, these ions experience a deflecting force, Bze, which causes the ion to follow a path of radius, R, such that

$$Bze = mv/R \qquad [1.9]$$

For the ion to reach the detector, R must be equal to the radius of curvature of the magnetic sector. We now combine equations 1.8 and 1.9 to obtain the relation governing the path of an ion through the magnetic sector:

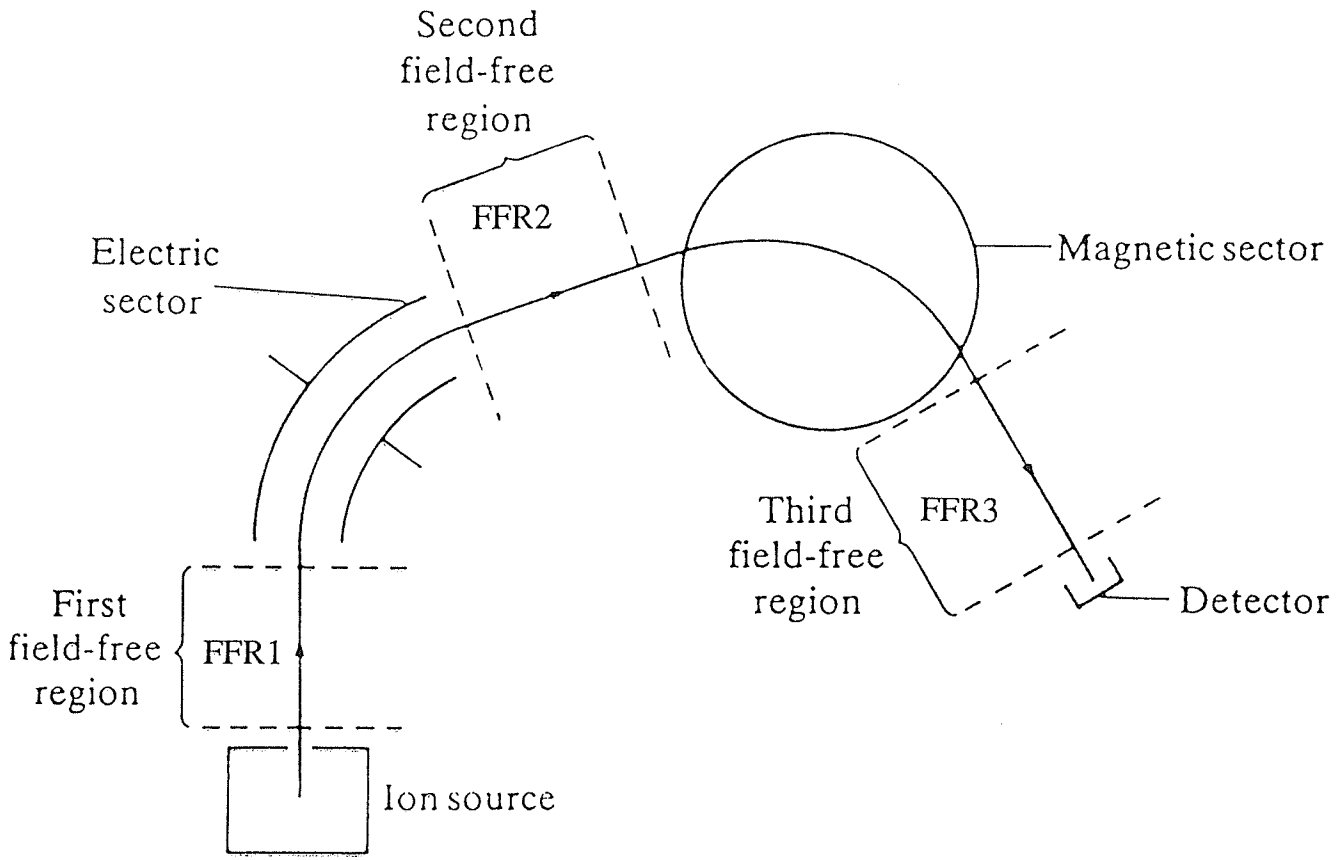

Figure 1.1 Path of main ion beam through a mass spectrometer of Nier-Johnson geometry, showing the first, second and third field-free regions[25].

$$m/z = B^2R^2e/2V \qquad [1.10]$$

By varying either the magnetic field at a constant accelerating voltage, or *visa versa*, one can bring each m/z species to a focus, thereby aquiring a mass spectrum.

Because the accelerated ions are not exactly mono-energetic they will be deflected by slightly different amounts at constant magnetic field. This causes broadening of the mass spectral peaks and usually limits the instrument resolution[25]. To reduce the image spread in the focussed beam reaching the detector, an electric sector of radius R_e, which produces a radial electric field, E, is employed. If the outer plate of the electric sector is made positive with respect to the inner plate and a beam of positive ions, varying slightly in kinetic energy, enters the radial electric field, only those ions with a kinetic energy such that the electrostatic force, Eze, on the ions causes them to follow the correct path of radius, R_e, will pass through the electric sector:

$$Eze = mv^2/R_e \qquad [1.11]$$

By combining equations 1.8 and 1.11 we obtain the relation for the path of an ion through the electic sector:

$$R_e=2V/E \qquad [1.12]$$

The electric sector, when its voltage is kept constant (E is proportional to the electric sector voltage), focusses ions according to

their kinetic energy only (independent of m/z) and is therefore referred to as an energy focussing device. The combined use of the electric and magnetic sectors in this manner gives a double-focussing mass spectrometer because the ion beam is focussed first for kinetic energy and then for mass-to-charge ratio.

1.4 Metastable ions

To understand the origin of metastable ions, consider a decomposition in which a parent ion of mass m_1 yields a fragment ion A^+, of mass m_2, and a neutral fragment N (equation 1.13).

$$\begin{array}{ccccc} P^+ & \text{--------}> & A^+ & + & N \\ m_1 & & m_2 & & (m_1 - m_2) \end{array} \qquad [1.13]$$

When molecules are ionized, ions with a range of energies are produced, and decomposition may occur. The rate of decomposition depends upon the internal energy of the ion, the greater it is the faster is the rate of decomposition. P^+ ions with sufficient internal energy fragment whilst still in the ion source, whereas ions with small internal energies may reach the detector before they have time to fragment and are detected as P^+ ions. Ions with intermediate internal energies may fragment during flight through the instrument (i.e. after leaving the ion source and before reaching the detector) and give rise to A^+ ions. The apparent m/z value at which they are detected depends upon where they decompose. Such ions, with decomposition rate constants in the range of 10^5-10^6 s^{-1} in a

conventional double focussing mass spectrometer, are said to be metastable[25,28].

When P^+ decomposes after acceleration, and one assumes that no internal energy is released as translational energy during fragmentation, the translational energy of P^+, namely zeV, must be shared between A^+ and N in proportion to their masses (law of conservation of momentum) (equation 1.14):

$$zeV = \underset{A^+}{(m_2/m_1)zeV} + \underset{N}{((m_1-m_2)/m_1)zeV} \qquad [1.14]$$

Thus, 'metastable' ions give rise to product ions, which reach the detector with less than the full translational energy originally imparted to ions by the ion source.

The actual place in the mass spectrometer where fragmentation occurs (reaction 1.13) determines how the metastable ions may be detected. As mentioned above, with a normal geometry double focussing mass spectrometer, there are three distinct regions where metastable ions may be formed and these are referred to as the first, second and third field free regions (Figure 1.1). Fragmentations occurring in the second field free region (FFR2) (the region between the electric and magnetic sectors) give rise to diffuse peaks at an apparent mass m* given by m_2^2/m_1[25-28] in the normal mass spectrum. The broadness and relatively low abundance usually associated with these peaks, as well as the fact that there may be no unique solution for m* (two unknown variables m_1 and m_2), make it difficult in some cases, to assign unambiguous values to m_1 and m_2.

Techniques for detecting metastable ion decompositions in the first field-free region, however, can give one a direct indication of parent-daughter relationships between ions in a mass spectrum. Any product ions formed in this region will have the wrong energy to pass through the electric sector because, as shown earlier, it is an energy focussing device. In order to study metastable ion decompositions occurring in this region, either the accelerating voltage or the the electric sector voltage must be altered to allow passage of the product ions.

Several different scanning methods for identifying all daughter ions from the same parent ion, or all parent ions of the same daughter ion, are possible with a double focussing mass spectrometer. Defocussing techniques[25,28], which involve scanning the accelerating voltage at fixed electric sector voltage, or scanning the electric sector voltage at fixed accelerating voltage, allow daughter ions with the correct translational energy to pass through the electric sector and at the same time prevent passage of normal (full-energy) ions (thus the term defocussing). The electric sector scan method has been termed ion kinetic energy spectroscopy (IKES). Other methods, referred to as linked scanning[25,29,30], involve varying the electric sector voltage simultaneously with either the accelerating voltage or the magnetic field so as to maintain a specified relationship between them throughout the scan. Three of the more usual linked scans are performed (a) at constant E^2/V or (b) at constant B/E, for recording daughter ions of a common parent ion, or (c) at constant B^2/E for recording parent ions of a common daughter ion. Methods (b) and (c) are usually preferred over method (a) (and

also the defocussing technique involving variation of V) because their use does not restrict the mass range over which metastable ions may be studied and does not alter the efficiency of the ion source during scanning[29,31]. The following discussion will therefore be restricted to B-E scans.

As mentioned above, the B/E linked scan is a daughter ion scan; in other words, this method enables the daughter ions, A^+, formed from a particular parent ion, P^+, to be identified. This statement can be justified as follows: The kinetic energies of P^+ ions and A^+ ions formed in FFR1 are $zeV=m_1v_1^2/2$ and $zeV(m_2/m_1)=m_2v_2^2/2$, respectively. Thus A^+ ions formed in FFR1 will have velocity $v_2=v_1=v=(2zeV/m_1)^{1/2}$. If B and B_o are the respective magnetic fields required to transmit P^+ ions and A^+ ions formed in FFR1, through the magnetic sector, then from equation 1.9 we obtain:

$$B = m_1v/zeR$$

$$B_o = m_2v/zeR$$

and therefore:

$$B_o/B = m_2/m_1, \quad \text{or} \quad B_o = (m_2/m_1)B \qquad [1.15]$$

The magnetic field, initially set to focus only P^+ ions, must therefore be decreased by a factor of m_2/m_1 so as to allow A^+ ions to pass through the magnetic sector.

If E and E_o are the respective electric sector fields needed to transmit P^+ ions and A^+ ions formed in FFR1 through the electric sector then, from equation 1.11, we have

$$E = m_1 v^2 / R_e z e$$

$$E_o = m_2 v^2 / R_e z e$$

and therefore:

$$E_o/E = m_2/m_1, \quad \text{or} \quad E_o = (m_2/m_1)E \qquad [1.16]$$

The electric sector voltage, initially set to focus those ions with the full kinetic energy imparted to them in the ion source must, like B, be decreased by a factor of m_2/m_1 so as to allow A^+ ions formed in FFR1 to pass through the electric sector. On combining equations 1.15 and 1.16 we have:

$$B_o/B = E_o/E = m_2/m_1$$

$$B_o/E_o = B/E = \text{constant} \qquad [1.17]$$

Since B and E are changed by the same factor, m_2/m_1, then scanning the magnetic and electric fields simultaneously such that B/E remains constant will discover all the product ions resulting from dissociation of selected FFR1 metastable parent ions.

In the B^2/E linked scanning method the electric sector voltage and the magnetic field are initially set to transmit A^+ ions

formed in the ion source. After acceleration, their velocity is $v = (2zeV/m_2)^{1/2}$. The velocity of A^+ ions formed in FFR1 from metastable P^+ ions, however, is $v_o = (2zeV/m_1)^{1/2}$. Therefore, if B and B_o are the respective magnetic fields needed to transmit normal A^+ ions and A^+ ions formed in FFR1 through the magnetic field then from equation 1.9, we have:

$$B_o = m_2(2zeV/m_1)^{1/2}/Rze$$

$$B = m_2(2zeV/m_2)^{1/2}/Rze$$

and therefore:

$$B_o = (m_2/m_1)^{1/2}B \qquad [1.18]$$

As in the B/E linked scan, the electric sector voltage in this linked scan must be decreased by a factor of m_2/m_1 so as to allow the transmission of daughter ions through the electric sector (i.e. $E_o = (m_2/m_1)E$). On combining equations 1.16 and 1.18 we obtain:

$$B^2_o/ B^2 = E_o/E = m_2/m_1$$

$$B^2_o/E_o = B^2/E = \text{constant} \qquad [1.19]$$

Thus, observation of parent ions of a chosen daughter ion, A^+, requires scanning such that B^2/E remains constant.

The idea behind linked B-E scanning is illustrated by a simple mass spectrum consisting of a parent ion (m/z 226) and its fragment ion (m/z 99) (Figure 1.2)[30]. At constant accelerating voltage and

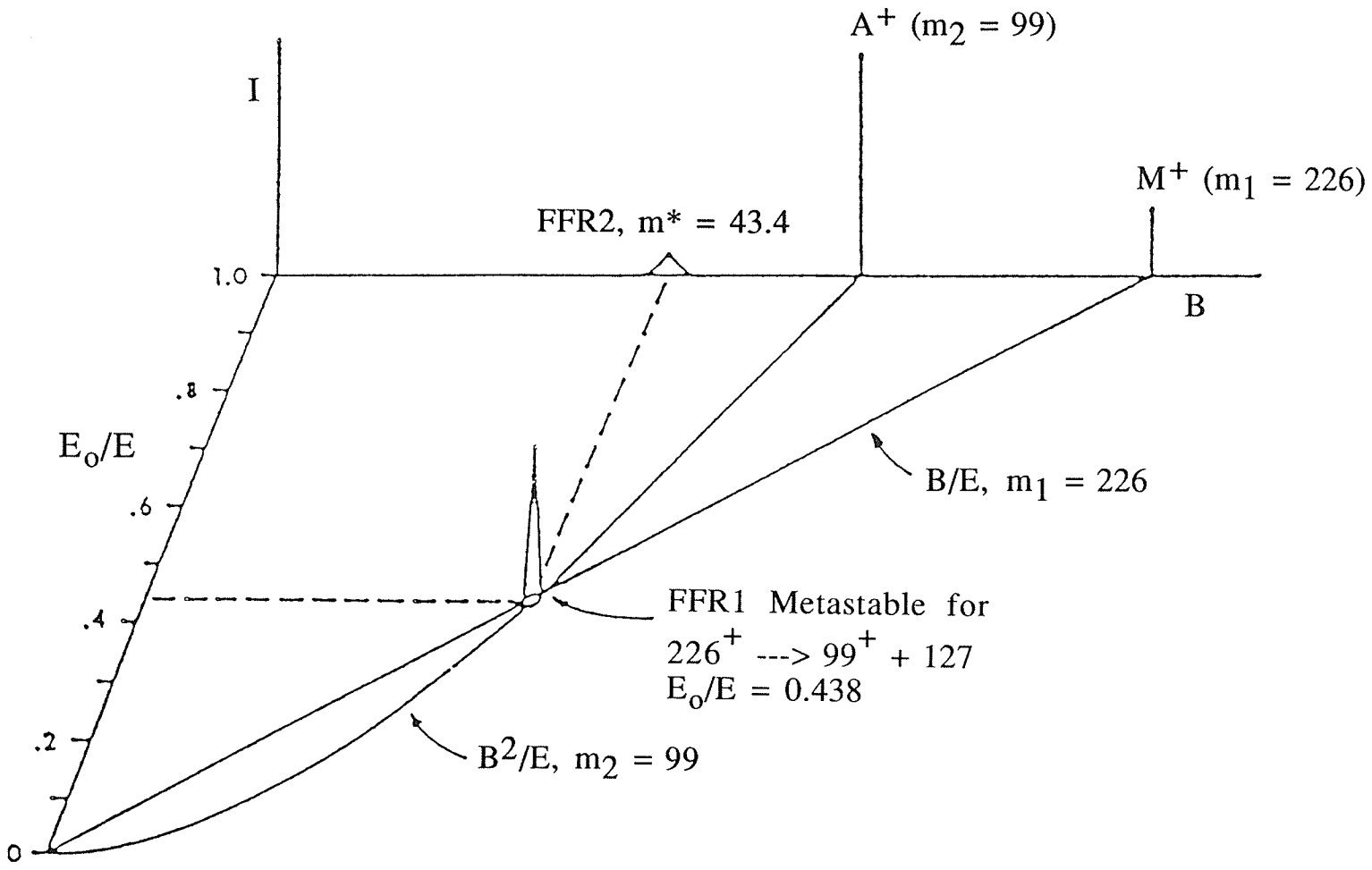

Figure 1.2 Schematic diagram of linked scans in the B-E plane[30].

electric sector voltage the normal mass spectrum (B scan) consists of two focused peaks (m/z 226 and 99), and a broad peak (m*/z = 43.4) due to metastable decomposition of m/z 226 in FFR2. In B/E linked scanning, all daughter ions of m/z 226 formed in FFR1 will lie on the B/E line shown, while in B^2/E linked scanning parent ions of m/z 99 will lie on the B^2/E curve shown. Scans along these curves are therefore referred to as daughter and parent ion scans, respectively. The B/E line for parent m/z 226 and the B^2/E curve for daughter m/z 99 intersect when $E_o/E = 99/226 = 0.438$, and $m^*/z = 43.4$

The E_o/E versus mass (time) curves with which the B/E and B^2/E scans must proceed (i.e., the values corresponding to the constants given in equations 1.17 and 1.19) are calculated by using the linked scanning equations below (1.23 and 1.24) derived as follows: By recalling equation 1.10 for detection of stable ions in a normal mass spectrum (B scan) the apparent mass, m*, at which the product of FFR2 metastable decompositions appear is given by:

$$m^* = B_o^2 R^2 ze/2V \qquad [1.20]$$

Furthermore, as shown above, daughter ions from FFR1 decompositions are transmitted through the electric sector (for both B/E and B^2/E scans) when the electric field is given by equation 1.16 (i.e. $E_o = (m_2/m_1)E$). For a daughter ion scan (m_1 constant) the relationship between the electric field and m*, found by substituting $m^* = m_2^2/m_1$ into equation 1.16, is given by:

$$m^* = m_1(E_o/E)^2 \qquad [1.21]$$

Similarly, for a parent ion scan (m_2 constant) we have:

$$m^* = m_2(E_o/E) \qquad [1.22]$$

Combining equation 1.20 with equations 1.21 and 1.22 gives us the linked scan equations 1.23 and 1.24, respectively:

$$B_o/E_o = (2Vm_1/ez)^{1/2}(1/ER) \qquad [1.23]$$

$$B_o^2/E_o = 2Vm_2/ER^2ze \qquad [1.24]$$

A rapid computer-controlled repetitive scanning procedure[25,30] (as used in the current study) is feasible because of the existence of an accurate correlation between magnetic field and time elapsed from initiation of the magnetic scan. The procedure is initiated by scanning from high values of B (time) along the $E_o/E = 1$ axis (i.e. normal B scan). A prior mass calibration of the instrument (the same calibration that is used for mass assignment of low resolution spectra) allows a departure from the $E_o/E = 1$ axis to occur when the magnetic field reaches the value corresponding to that for the chosen parent or daughter ion linked scan of interest. The scan at this point then proceeds along the E_o/E versus B (time) line that was precalculated from the appropriate linked scanning equation. Scans on subsequent cycles of the magnet may follow different precalculated B-E curves, or the mass spectrometer may return to recording the normal spectrum (B scan).

In the discussion thus far it has been assumed that, on decomposition, the internal energy of P^+ is partitioned between the daughter ion, A^+, and the neutral species, N, in proportion to their masses. However, some internal energy may be released as kinetic energy during the decomposition[25,28,29]. Fragment ions may therefore have a range of kinetic energies, which would necessitate a range of values of electric sector voltage and magnetic field strength for them to be focussed on the collector. Consequently broad peaks may result for these ions. Values of E and B corresponding to the mean value of the energy of these product ions and thus to the center of the observed peak, might be exactly correct, but whether the extreme range of energies of these ions will be transmitted depends on the way in which B varies with E. The kinetic energy range depends upon the difference between the square of the maximum and minimum ion velocities, while the momentum range depends upon the first power of this difference. Therefore, to avoid any discrimination in recording the width of the observed peak, the magnetic field strength only needs to vary from B to $B(1 + \Delta v/v)$ to accommodate a velocity range Δv, whilst the electric sector voltage needs to vary from E to $E(1 + \Delta v/v)^2$. This will only occur for a linked scan in which B^2/E is constant (i.e. $B^2(1 + \Delta v/v)^2/E(1 + \Delta v/v)^2$ = constant). Useful kinetic energy release data can be found by analyzing the resultant peak shapes[25,28], but in many situations these data are not required and the width of the peaks prevents accurate determination of their positions[25]. In particular, when the peaks are so broad that they overlap, the masses of the ions are difficult to estimate. However, discrimination against extremes in

kinetic energy during, for example, a B/E linked scan results in peaks that are uniformly narrow, irrespective of the amount of internal energy converted to kinetic energy during fragmentation[25,29,30]. Daughter ion masses can therefore be readily assigned.

B/E linked scans may be complicated by the presence of additional peaks arising from isotope-containing precursor ions or from any precursor ion which is one or two amu different from the precursor ion under investigation and which also undergoes fragmentation in FFR1[30]. The presence of such peaks is primarily due to low resolution with respect to precursor mass selection. Resolution can be enhanced but will result in decreased daughter ion sensitivity[25]. B^2/E linked scans can provide valuable complementary data which can, in many cases, help resolve the ambiguous precursor mass assignments.

1.5 Collisional Activation

If ions possessing high kinetic energies (keV) collide with neutral atoms or molecules, a small fraction of their kinetic energy is converted into internal energy. This ensuing increase in internal energy of the ion can cause decomposition. In practice, a gas (usually helium or argon) is introduced into one of the field-free regions. The gas is leaked into a small collision cell, which can be maintained at a relatively high pressure, while the regions around it are still at very low pressures. The large amount of energy transferred on collision (as much as 10 eV) makes the subsequent fragmentation virtually independent of the original internal energy of the precursor ion[25,28].

Thus, ion abundances observed in collisional activation mass spectra are reproducible and largely independent of the mode of ionization.

Fragment (daughter) ions increase in abundance if a high background pressure is created in the appropriate FFR. Also, the number of different types of fragments ions will increase because some fragmentation pathways are only observed when collisional activation is used. Thus, collisional activation can provide additional information concerning the pathways leading to formation of normal ions present in the conventional mass spectrum. If the pressure in the collision cell becomes too high ions will be scattered out of the ion beam and few will reach the detector; therefore, careful control and measurement of pressure in the collision cell is necessary to obtain the best results. The optimum pressure for highest sensitivity is usually between 1.33×10^{-4} and 1.33×10^{-2} Pa[25,28].

1.6 ^{19}F-^{19}F NMR coupling constants

Unlike the mechanisms of H-H coupling, those involving coupling between ^{19}F nuclei are not well understood. Various explanations have been put forward over the years for such experimental facts as: signs of the coupling constants, substituent effects, dihedral angle dependence, and near zero coupling between vicinal fluorines compared to larger long range coupling constants over four and five-bonds[32-38].

Petrakis and Sederholm[32] investigated the NMR spectra of several fluorinated organic compounds and introduced the concept of "through-space" coupling to explain the unusually large couplings

observed between fluorines four and five bonds apart. They postulated a mechanism involving overlap of electronic clouds of fluorine atoms when their internuclear separation is less than twice their van der Waals' radii (i.e. less than 2.72 Å). As the F-F distance decreases (i.e. orbital overlap increases) the coupling constants increase monotonically. The small (near zero) vicinal coupling observed in perfluoroethyl groups was thought to reflect the large spacial separation of the vicinal fluorine nuclei (2.72 Å in a staggered configuration, which was assumed to be favored). This mechanism was criticized[39-42], since it failed to include a "through-bond" as well as a "through-space" contribution, but this was rectified later by Ng and Sederholm[33] who showed that only the "through-bond" mechanism is normally important for vicinal fluorines and that the magnitude of the coupling is governed by the electronegativity of the other substituents. When the sum of these electronegativities is sufficiently high, as with perfluorinated groups, they predicted a near zero coupling. They also provided further experimental evidence to support the "through-space" mechanism for long range F-F coupling.

1.6.1 Vicinal couplings

Cavalli and Abraham[34,35], investigating substituent effects on vicinal F-F couplings in substituted fluoroethanes, showed that rotationally averaged coupling constants, $J_{av} = [(J_t + 2J_g)/3]$, are negative in all types of >CF-CF< fragments (except in CF_3CF_3). (J_t and J_g are the coupling constants for *trans* ($\theta = 180°$) and *gauche* ($\theta = \pm 60°$) conformations, respectively, where θ is the dihedral angle

between the C-F bonds.) There is a roughly linear dependence on the sum of the Huggins electronegativities[43], ΣE, of the substituents given by: J_{av} (Hz) = -91.4 + 6.15ΣE (Figure 1.3).

Subsequently, Cavalli[36] observed that J_{av} has a good linear dependence on ΣE for each of the three series of halofluoroethanes, CF_3CF_2X, CF_3CFXY and XCF_2CF_2Y where X = Y and X ≠ Y (X, Y = F, Cl, Br, I) (Figure 1.3) and that, for compounds containing a $-CF_2CF_2-$ fragment, J_t varies enormously and becomes more positive as the electronegativites of other substituents increase, while J_g is almost unaffected. Any observable changes in J_g seemed to be opposite to those of J_t. He concluded that J_{av} is here related to the substituent electronegativities only and that possible dihedral angle changes must have a negligible effect. If this were not so a nonlinear dependence of J_{av} on ΣE would have been expected. Furthermore, if the effect of the dihedral angle is important J_g would vary more than J_t (because the curve of J versus θ has a turning point at θ = 180° J_t is insensitive to small changes in θ)[44].

In contrast to the above results, vicinal couplings for the hydrofluoroethanes CF_3CF_2H, CF_3CFH_2 and CF_2HCF_2H did not correlate with those for the corresponding halofluoroethanes[36]. It was suggested that such couplings were influenced by other factors, such as an angularly dependent electronegativity effect and/or dihedral angle changes.

For light nuclei (e.g. ^1H, ^{13}C, ^{19}F) the indirect nuclear spin-spin coupling constant originates from three electron-nucleus interaction hamiltonians, i.e. the orbital, spin dipolar and Fermi contact terms[45-50]. The orbital term represents the interaction

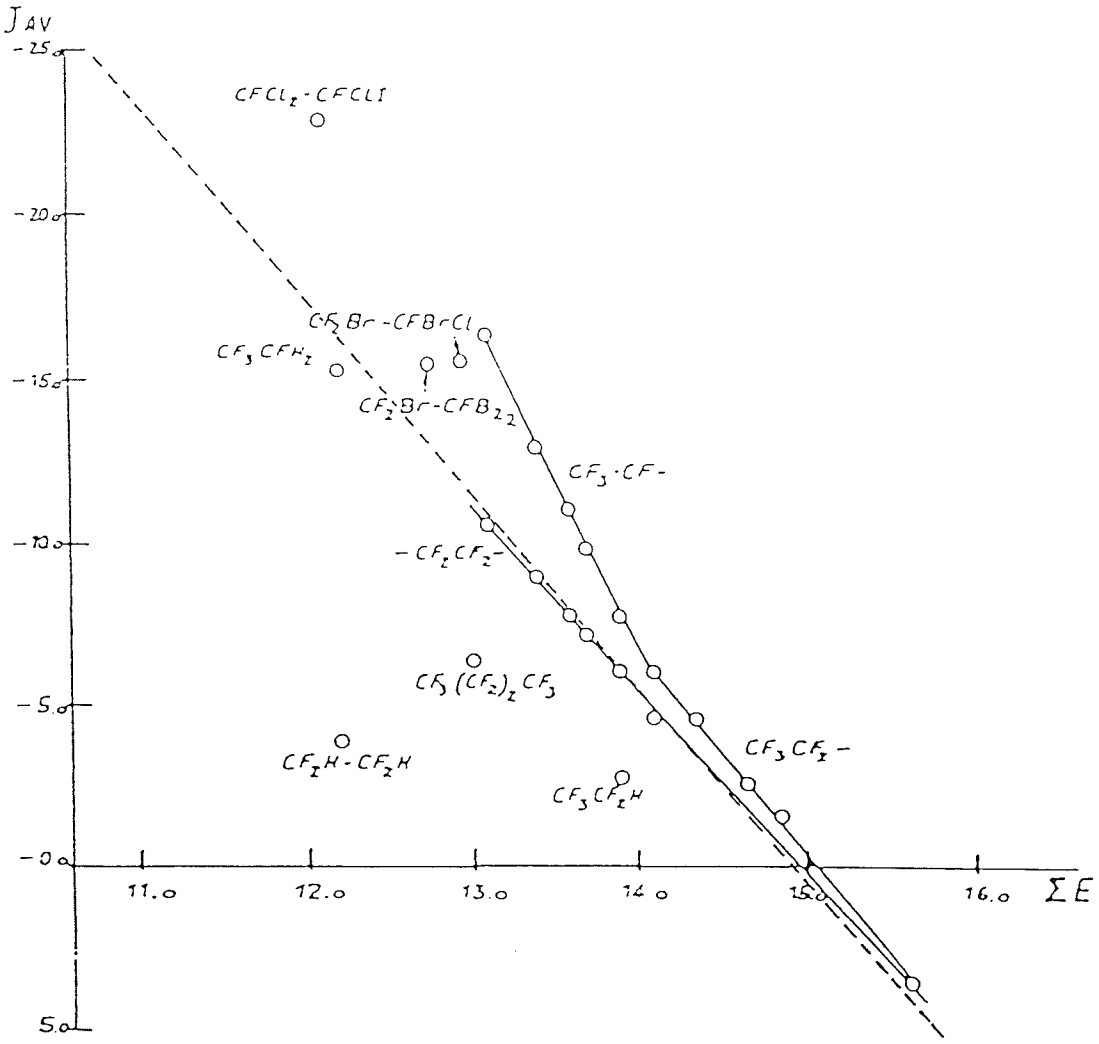

Figure 1.3 Rotationally averaged couplings, $J_{av} = [(J_t + 2J_g)/3]$, plotted against the sum of the Huggins electronegativities, ΣE, of the four remaining substituent atoms on the >CF-CF< fragment[36].

between the nuclear spin and the induced dipole moment due to orbital motion of electrons. The spin dipolar and Fermi contact terms represent, respectively, the dipole-dipole and Fermi contact interactions between the nuclear and electron spins.

Based on the INDO-MO approximation and the sum-over-states perturbation method, Hirao *et al* calculated F-F coupling constants in various fluorine-containing compounds and found that the spin dipolar and orbital terms can be important sources of F-F couplings and sometimes rival the Fermi contact term[37,38]. This result is in marked contrast to those obtained for proton couplings, for which the latter term dominates[45,49,50]. They also showed that, in hydrofluoroethanes, all three terms are sensitive to dihedral angle changes[37,38]. For example, in CH_2F-CH_2F (Figure 1.4a), the spin dipolar contribution is nearly zero when $\theta < 105°$ and reaches an appreciably large positive value near $\theta = 180°$ (*s-trans* conformation). The orbital contribution is at a maximum at $\theta = 0°$ (*s-cis* conformation) and decreases to a minimum having an appreciably large negative value at $\theta \sim 100°$. At $\theta = 180°$, the orbital contribution is negligible. The Fermi contact contribution is positive for most angular values, with minima near the staggered conformations ($\theta = \pm 60°$ (*gauche*) and $\theta = 180°$ (*trans*)) and maxima near the eclipsed conformations ($\theta = 0°$ (*cis*) and $\theta = \pm 120°$).

Comparison of calculations for CH_2F-CH_2F (Figure 1.4a) with those for CH_2F-CF_3 (Figure 1.4b) shows that the dependencies of the spin dipolar and orbital terms on the dihedral angle are very similar, but the Fermi contact contributions differ. The latter term has smaller overall values for the second compound, with minima at

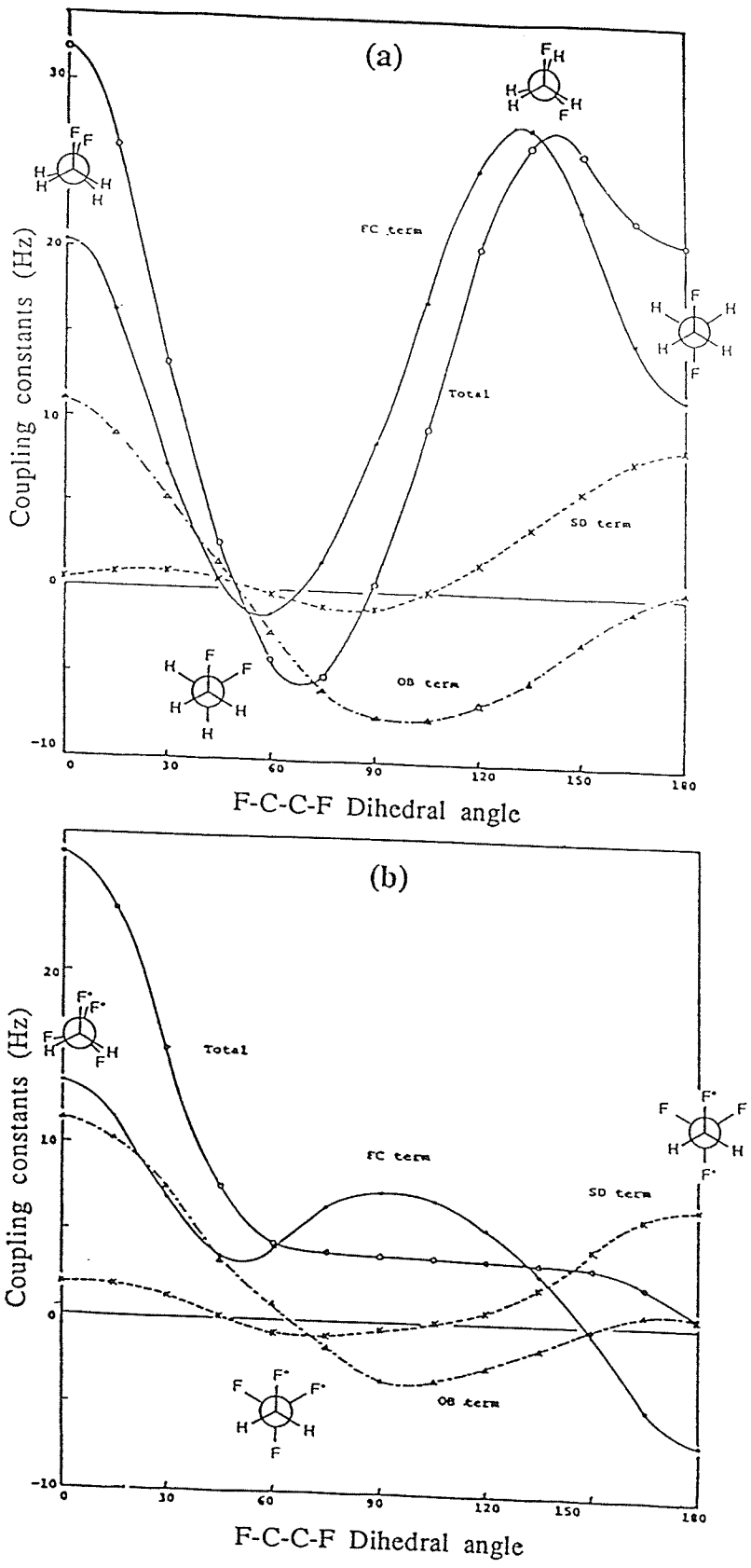

Figure 1.4 Plots of vicinal F-F coupling constants *vs.* the dihedral angle,θ, for (a) CH_2F-CH_2F and (b) CH_2F-CF_3[38].

$\theta \sim 50°$ and 180° and maxima at $\theta = 0°$ and $\sim 90°$. This change was earlier attributed to the presence of more highly electronegative substituents in the second compound[34-36].

Calculations of dihedral angular dependencies of vicinal F-F couplings in perfluoroacetaldehyde (CF_2F-COF) and perfluoropropene (CF_2=CF*-CF*F_2) show that, while the spin dipolar and orbital terms are similar to those for CH_2F-CH_2F and CH_2F-CF_3, the Fermi contact terms are again very different[37,38]. In particular, the Fermi contact term for CF_2F-COF has minima at $\theta = 0°$ and 180°, and only one maximum near $\theta = 105°$. Thus, substituents influence both the magnitude and the angular dependence of the Fermi contact term contribution to vicinal F-F couplings.

In summary, the anomalously low coupling between vicinal fluorines in perfluoroethyl groups (these couplings are smaller than the F-F couplings across *two* C-C single bonds) may be a consequence of the averaging effects of internal rotation about the C-C single bond and, in part, to cancellation of the orbital, spin dipolar and Fermi contact terms of nonuniform sign[37,38]. Note in Figure 1.4, that trends in the angular dependence of the total coupling accord approximately with that of the rotational potential curve of the compound. In other words, the total coupling has a minimum value in the energetically favored staggered conformations (θ = 60 and 180°)[37,38]. This seems to be a reason for near-zero coupling.

1.6.2 Geminal couplings

All three of the above terms make significant contributions to calculated geminal F-F couplings for a wide range of saturated,

unsaturated and ring-containing compounds[37,38]. The spin dipolar contribution is always positive within a small range of values (20.9-36.7 Hz for all compounds studied). However, both the orbital and Fermi contact terms vary considerably, from 12.2 to 84.4 Hz and from -2.1 to -103.9 Hz, respectively. The total couplings (sum of all three contributions) are positive in all cases, in agreement with experimental findings[39]. The n--->σ^* transition energies of the fluorine lone-pair electrons determine the spin-dipolar term and the primary features (i.e., sign and order of magnitude) of the orbital term. (The secondary features, such as substituent effects and structural changes, are determined mainly by the n(F)--->π^*(C-F) transition energies.) Because both the n and σ^* orbitals are localized approximately in the CF_2 fragment, the calculated spin dipolar term and the primary features of the orbital term are common to all geminal couplings regardless of the multiplicity of the adjacent C-C bond, substituent effects and F-C-F angles. On the other hand, the Fermi contact term is much more complicated since it is sensitive not only to substituent effects but also to the F-C-F angle. The dependencies of the calculated geminal F-F couplings on the F-C-F angles in CH_2F_2 and CH_2=CF_2 are shown in Figures 1.5a and 1.5b, respectively[37,38]. Unlike geminal H-H couplings, where coupling was found to increase monotonically with increasing H-C-H angle[51], geminal F-F couplings change markedly with the F-C-F angle and have a minimum near 110°.

The equilibrium state F-C-F bond angles of 108.5°[52] and 109.3°[53] for CH_2F_2 and CH_2=CF_2, respectively, closely correspond to those which minimize geminal F-F couplings. Any changes from these

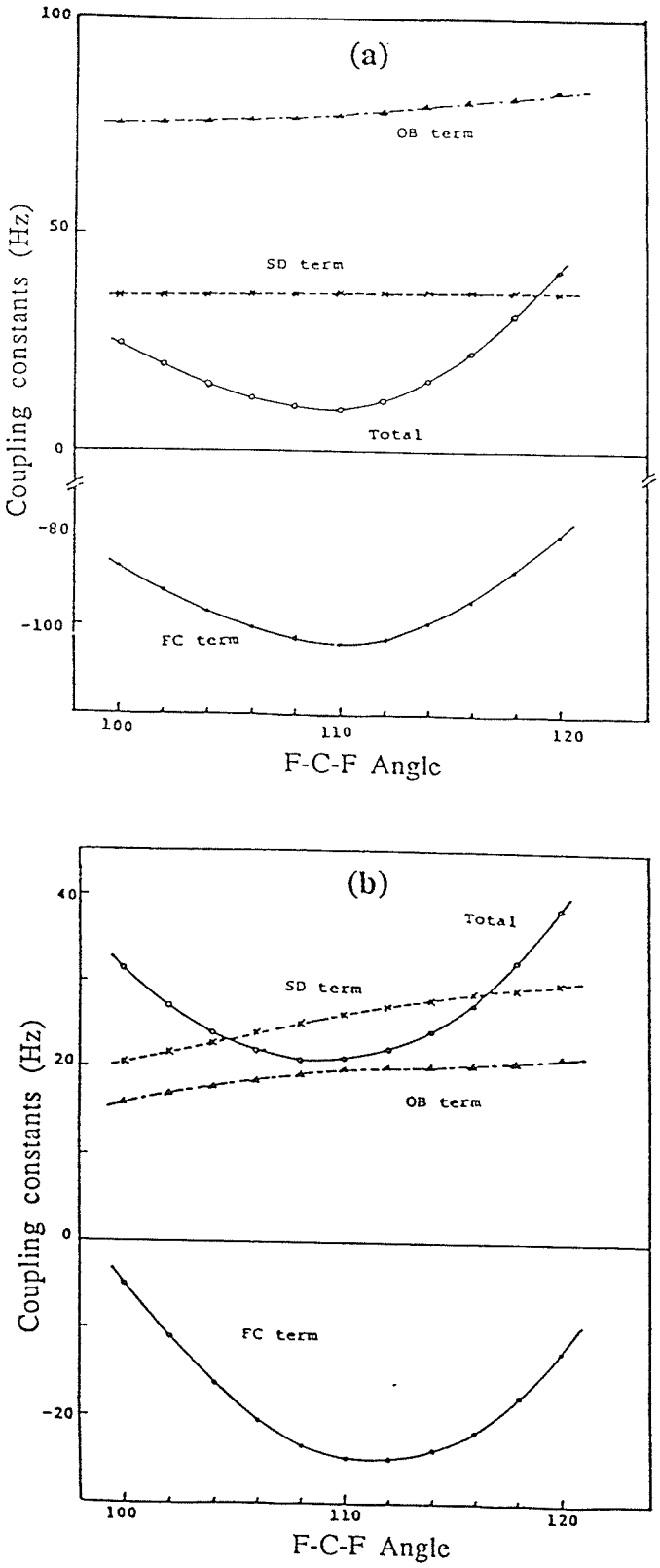

Figure 1.5 Plots of geminal F-F coupling constants *vs.* the F-C-F angle for (a) CH_2F_2 and (b) $CH_2{=}CF_2$[38].

angles produce large geminal couplings. Large variations (150-400 Hz) in experimental geminal F-F coupling constants were therefore ascribed partly to the sensitivity of the Fermi contact term to changes in F-C-F bond angle and also partly to the sensitivity of the orbital and Fermi contact terms to substituent effects.

1.6.3 Long range couplings

In the *s-cis* conformation of the fluorobutadienes (Figure 1.6), a positive, surprisingly large, five-bond coupling constant is observed[37,38]. Because orbital and spin dipolar contributions to long range four- and five- bond F-F coupling constants are small the Fermi contact term must therefore dominate[37,38]. The Fermi contact term can originate by the participation of bonding F·····F σ orbitals (Figure 1.7). In the valence-bond treatment, the wave function for *s-cis*-difluorobutadiene is given by a linear combination of wave functions for the canonical structures shown in Figure 1.7 ($^{S}\Psi_{O}$ for the singlet ground-state and $^{T}\Psi_{E}$ for the triplet excited-states). In this mechanism, referred to by the authors as "fragment" coupling, the direct orbital overlap in the F-F fragment, which is strongly antibonding in the ground-state, but bonding in the excited state, becomes important. The "fragment" couplings are extremely sensitive to the internuclear separation, and the Fermi contact term becomes large only for short F·····F distances. This is true for both four- and five- bond F-F couplings, although the latter are greater at the same internuclear separation. Calculations confirm the experimentally observed positive sign for five-bond couplings[23] but

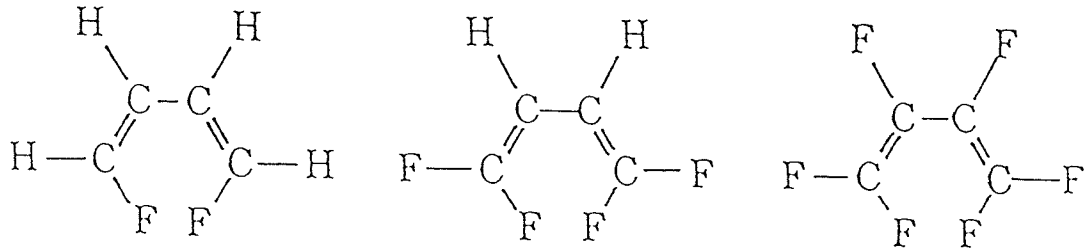

Figure 1.6 Long range F-F coupling constants for three fluorobutadienes in the *s-cis* conformation[38].

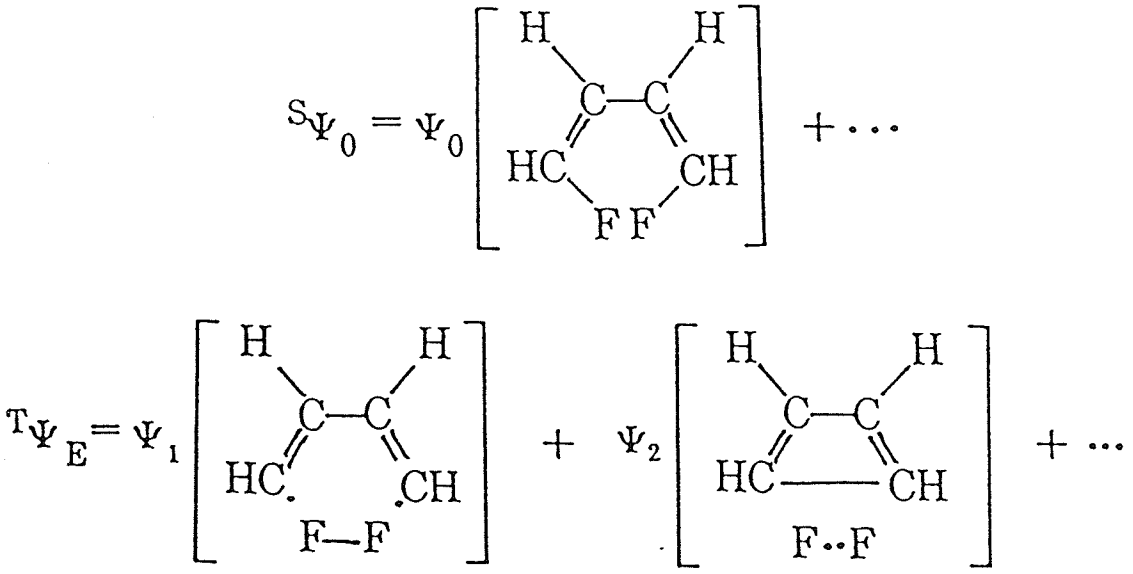

Figure 1.7 Wave function for *s-cis* fluorobutadiene[37,38].

predict a negative sign for four-bond couplings when the F-F internuclear separation is greater than 2.0 Å. This result became a topic of considerable debate and was subsequently shown experimentally to be incorrect[55-59]. No negative four- or five-bond F-F coupling constants have yet been discovered for two fluorine nuclei in close proximity, indicating that the calculations made by these authors[37,38] should be amended.

Five-bond F-F couplings are strongly dependent on the dihedral angle, θ, between the C-F bonds[37,38] and decrease rapidly with slight distortion (θ = 0-30°) from the *s-cis* planar configuration and thereafter decrease monotonically with increase of θ. Four-bond couplings also decrease monotonically as θ increases from 0 to 180°.

1.7 Structures of octahedral complexes with asymmetric, bidentate ligands.

If three bidentate ligands are added one at a time to a metal ion to form an octahedral complex the resulting structures can be represented as shown in Figure 1.8. One of these can be identified as facial (*fac*), while the three structures labelled meridional (*mer*) isomers are, in fact, superimposable, and therefore equivalent. This method of presentation emphasizes that the *mer* isomer is statistically three times more probable than the *fac* isomer. Both the *fac* and *mer* isomers can form enantiomeric pairs.

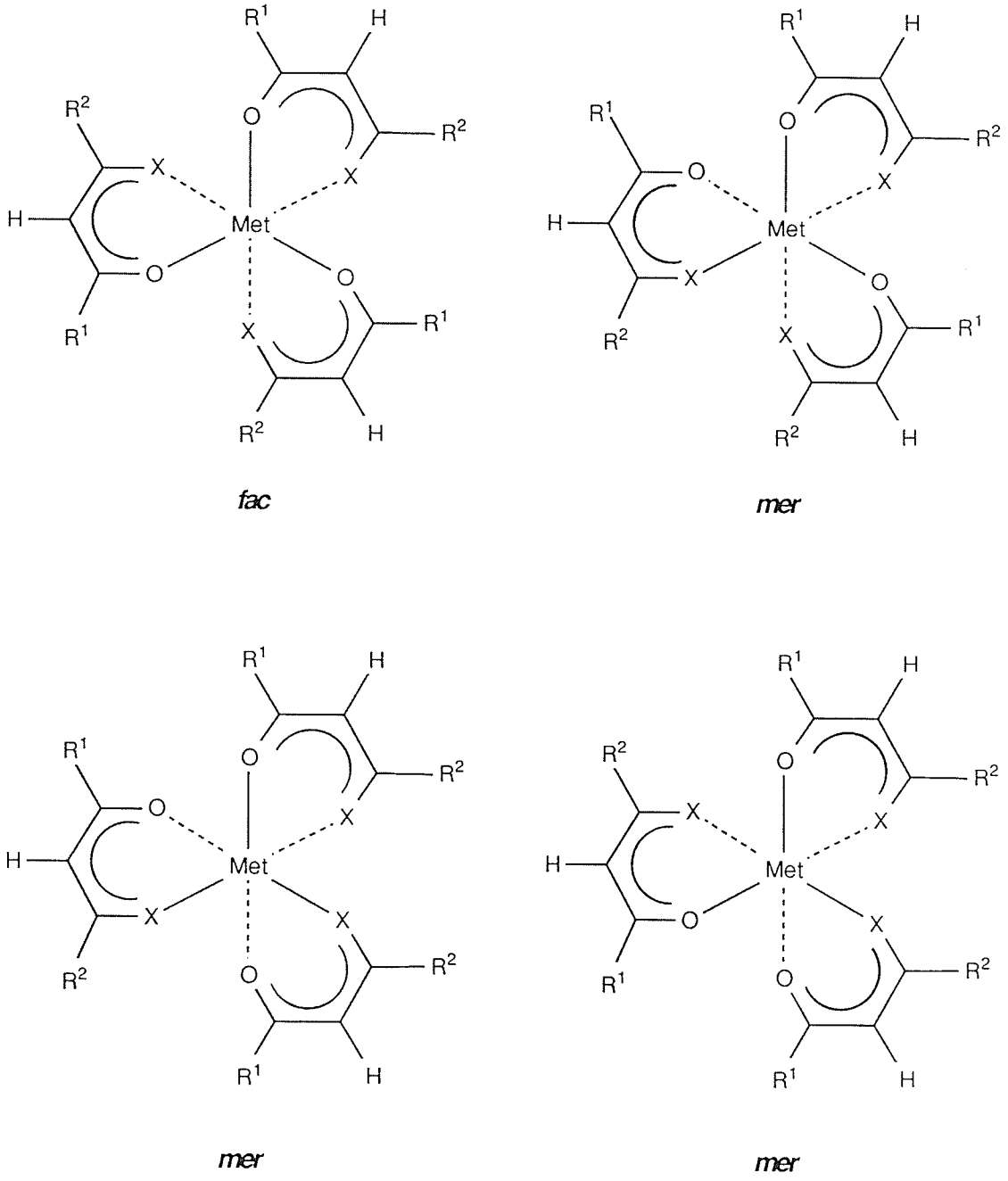

Figure 1.8 *fac* and (superimposable) *mer* isomers of an octahedral complex with asymmetric, bidentate ligands (X = O or S). (When X = O, $R_1 \neq R_2$)

2 *Experimental*

2.1 Mass spectrometry

Electron ionization mass spectra were recorded in the positive ion mode with a VG-7070E-HF double focussing mass spectrometer of EB geometry operating at an electron beam energy of 70 eV and current of 200 μA, a source temperature of *ca* 200°C, and an ion acceleration voltage of 6 keV. For complexes introduced by the direct insertion probe the mass range was scanned to > 2M but no ions were detected above M, where M is the molar mass of the monomeric complex. Exact masses of ions were measured at a spectrometer resolution of $M/\Delta M$ = 5000, using perfluorokerosene (M < 650 amu) or Ultramark 2500F (M > 650 amu) as a mass calibrant, and high resolution mass spectrometry was used to resolve isobaric ions. Ionic decompositions in the first field-free region (FFR1) were identified by a series of linked scans at constant B/E (daughter ion spectra). Collisional activation was implemented, when necessary, to enhance ion decomposition by introducing helium gas

into the collision cell in FFR1 at a pressure sufficient to give approximately 50% attenuation of the molecular ion beam.

2.2 Nuclear magnetic resonance spectroscopy

All NMR spectra were recorded with a Bruker AM300 spectrometer, at a frequency of 282.4 MHz for $\{^1H\}^{19}F$ (C_6F_6 internal reference, -162.90 ppm with respect to $CFCl_3$) and at 300 MHz for ^1H (tetramethylsilane internal reference).

2.3 X-ray crystallography

Reflection data were measured by a Nicolet R3*m* automated diffractometer and collected in the range $3°<2\theta<58°$ using an ω-2θ scan mode. Scan speeds were in the range of 0.49-29.30 $°min^{-1}$. A Patterson map[60,61] revealed the positions of the rhodium atom. Refinement of rhodium, followed by difference Fourier syntheses[60,61], yielded the positions of all remaining non-hydrogen atoms. Anisotropic thermal parameters and positions of all non-hydrogen atoms were refined by full-matrix least squares procedures[60,61].

2.4 Synthesis

2.4.1 Ligands

The ligands Sacac-H[62], Stfa-H[63], bzC_2F_5-H[64], bzC_3F_7-H[64], $SbzC_2F_5$-H[64] and $SbzC_3F_7$-H[64] were prepared by published methods, while acac-H, tfa-H and hfa-H were obtained from Fisher Scientific

Co., Aldrich Chemical Co. Inc., and PCR Research Chemicals Inc., respectively.

Deuteration of compounds bzC_2F_5-H, $SbzC_2F_5$-H and acac-H at the bridging carbon atom was achieved by mixing with CH_3OD containing DCl (35% sol'n in D_2O).

2.4.2 Rhodium chelates

A) *Rh(Sacac)$_3$*

This complex was prepared as described by Kawanishi *et al*[65]. Purification by fractional sublimation, *in vacuo*, yielded a yellow-orange crystalline product.

B) *Rh(Stfa)$_3$*

$RhCl_3 \cdot 3H_2O$ (0.37 mmole) in 15 ml of ethanol was added to a solution of ligand (1.22 mmole) in 15 ml of ethanol. The solution was refluxed for one hour, then cooled and a small amount of water was added. The product was then extracted with methylene chloride and the extract was dried over sodium sulfate. The resulting red-brown product was added to a silica gel column (60-200 mesh), through which methylene chloride was passed. A single red band separated while the rest of the sample remained at the top of the column. This band was found to contain the desired product. After removal of solvent purification of the residue by fractional sublimation, *in vacuo*, yielded large, well-defined, red monoclinic crystals[61].

C) *$Rh(bzC_2F_5)_3$ and $Rh(bzC_3F_7)_3$*

$RhCl_3 \cdot H_2O$ (0.32 mmole) in 10 ml of ethanol was added to a solution of either ligand (0.96 mmole) in 10 ml of ethanol. This solution was refluxed for one hour, then cooled and a small amount of water was added. The product was then extracted with methylene chloride and the extract was dried over sodium sulfate. After removal of the solvent, the resulting oily red product was added to a silica gel column (60-200 mesh), through which methylene chloride was passed. Two bands separated, while a portion of the sample still remained at the top of the column. The first band eluted quite readily and, on removal of the solvent, yielded a red liquid that did not contain the desired complex. The second (yellow) band, which contained the desired product, eluted slowly, so the silica containing the second fraction was removed from the column and the product was extracted from it with acetone. After removal of acetone the product was purified by fractional sublimation, *in vacuo*, to yield the pure, yellow rhodium chelate.

D) *$Rh(SbzC_2F_5)_3$ and $Rh(SbzC_5F_7)_3$*

Both monothio-β-ketoenolate complexes were prepared as above. The desired products were again found in the second band on the silica gel column and were purified by fractional sublimation, *in vacuo*, to yield the pure red complexes.

E) *Deuterated chelates*

Rhodium chelates of the deuterated ligands were prepared by the above methods, modified by using CH_3OD in place of ethanol and

by adding a small amount of anhydrous sodium acetate to the reaction mixture prior to refluxing.

2.4.3 Iridium chelates

A) *Ir(acac)$_3$, Ir(tfa)$_3$ and Ir(hfa)$_3$*

All three iridium chelates were prepared as described by Davignon *et al*[66,67]. Purification by fractional sublimation, *in vacuo*, yielded yellow [Ir(acac)$_3$ and Ir(tfa)$_3$] and orange [Ir(hfa)$_3$] crystalline products.

B) *Ir(acac)$_3$-d$_3$*

This complex was prepared by the above method for Ir(acac)$_3$, modified by using the deuterated ligand and DO_2CCO_2D, LiOD and DCl instead of oxalic acid, sodium hydroxide and acetic acid, respectively. The resulting product was a yellow powder.

3 Results and Discussion

3.1 $Rh(SbzC_2F_5)_3$, $Rh(SbzC_3F_7)_3$, $Rh(bzC_2F_5)_3$ and $Rh(bzC_3F_7)_3$

3.1.1 Mass spectral studies

A) *General features*

Before discussing details of the mass spectra attributable to specific features of the complexes we first compare and contrast some obvious trends. The electron ionization (70 eV) positive ion mass spectra of $Rh(SbzC_2F_5)_3$, $Rh(SbzC_3F_7)_3$, $Rh(bzC_2F_5)_3$, and $Rh(bzC_3F_7)_3$ are shown in Figures 3.1-3.4, respectively. Tables 3.1 and 3.2 give the abundances of characteristic ions as a percentage of that of the most abundant metal-containing ion (%RA). Figures 3.5-3.8 show the daughter ion spectra (B/E scans) of the RhL_2^+ ion for each complex and fragmentation pathways are summarized in Schemes 3.1 and 3.2.

In the mass spectra of all four complexes, RhL_3^+ is the most abundant rhodium-containing ion and, for both complexes with dioxo ligands, is the base peak ion. For comparison, of the three complexes

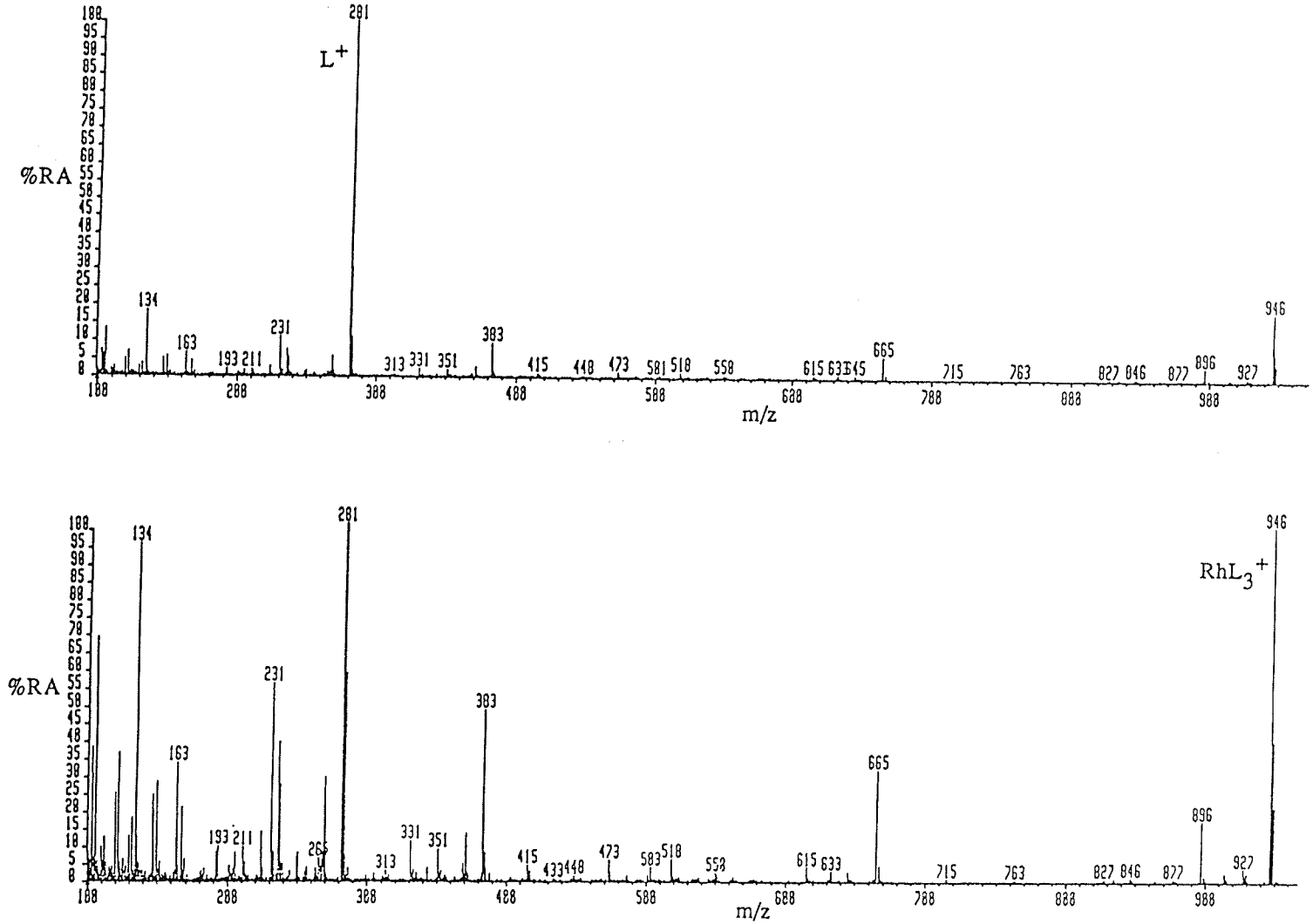

Figure 3.1 Mass spectrum of $Rh(SbzC_2F_5)_3$ normalized to the base peak, L^+, (upper) and to the most abundant metal-containing ion, RhL_3^+, (lower).

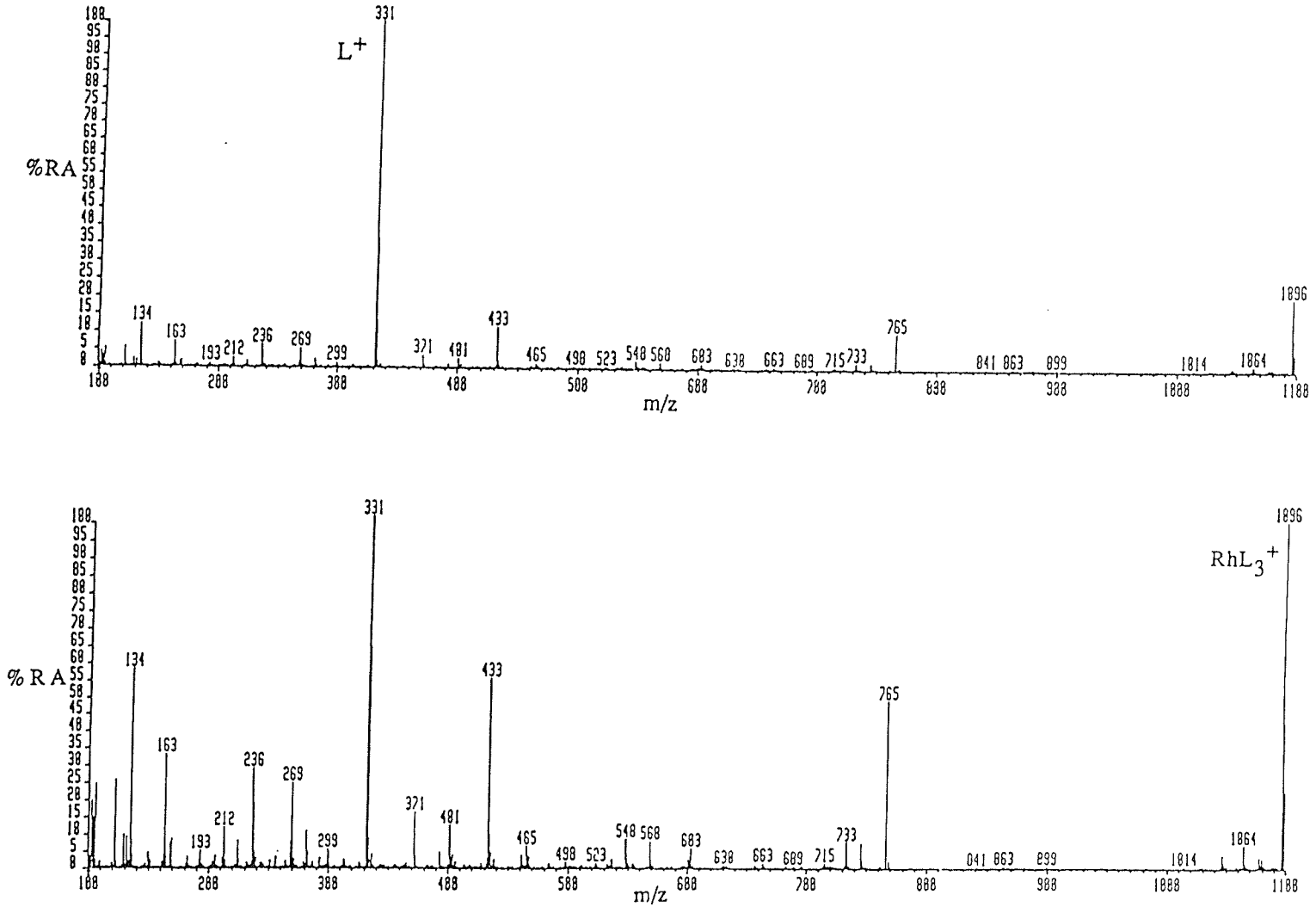

Figure 3.2 Mass spectrum of $Rh(SbzC_3F_7)_3$ normalized to the base peak, L^+, (upper) and to the most abundant metal-containing ion, RhL_3^+, (lower).

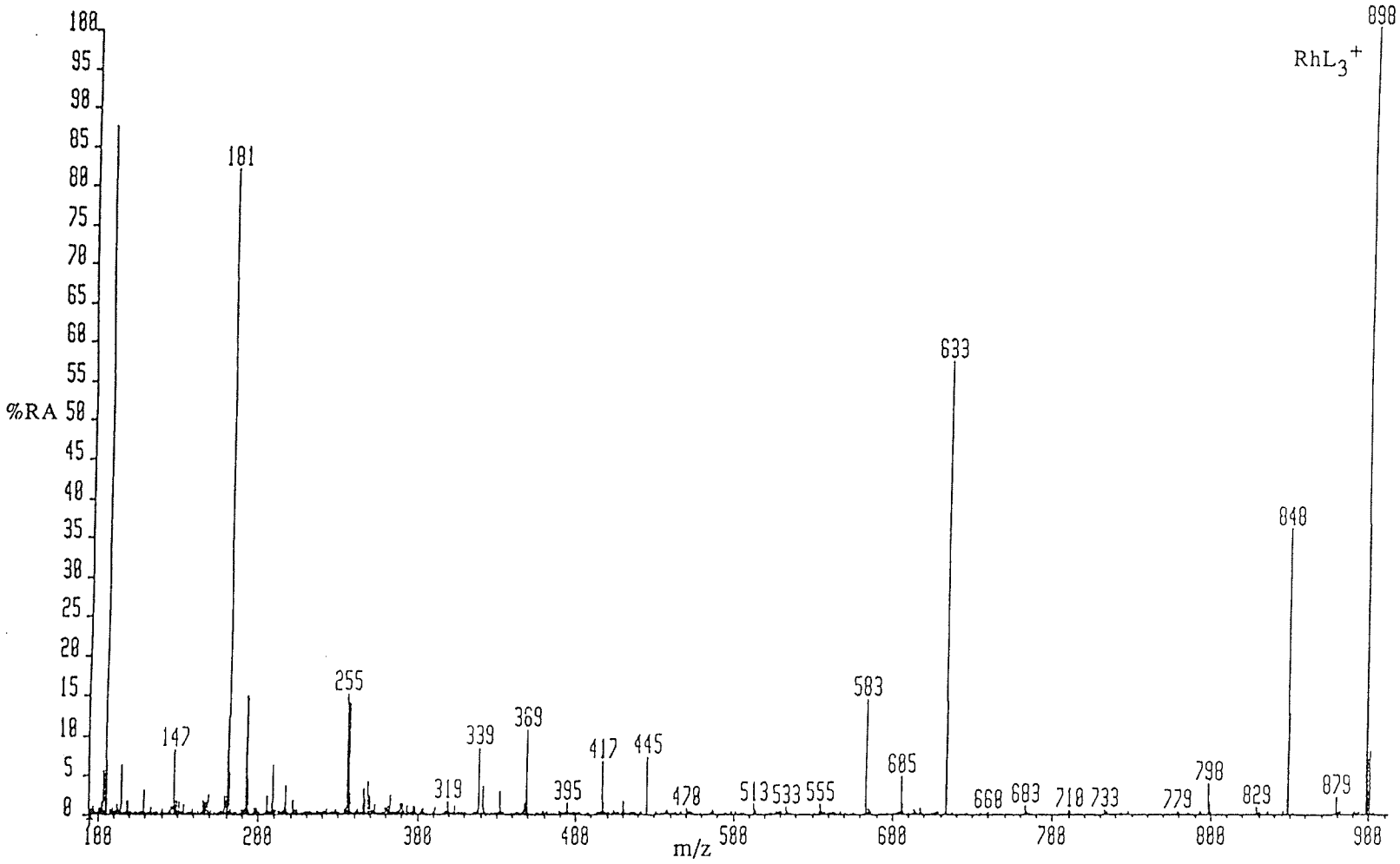

Figure 3.3 Mass spectrum of $Rh(bzC_2F_5)_3$ normalized to the base peak, RhL_3^+.

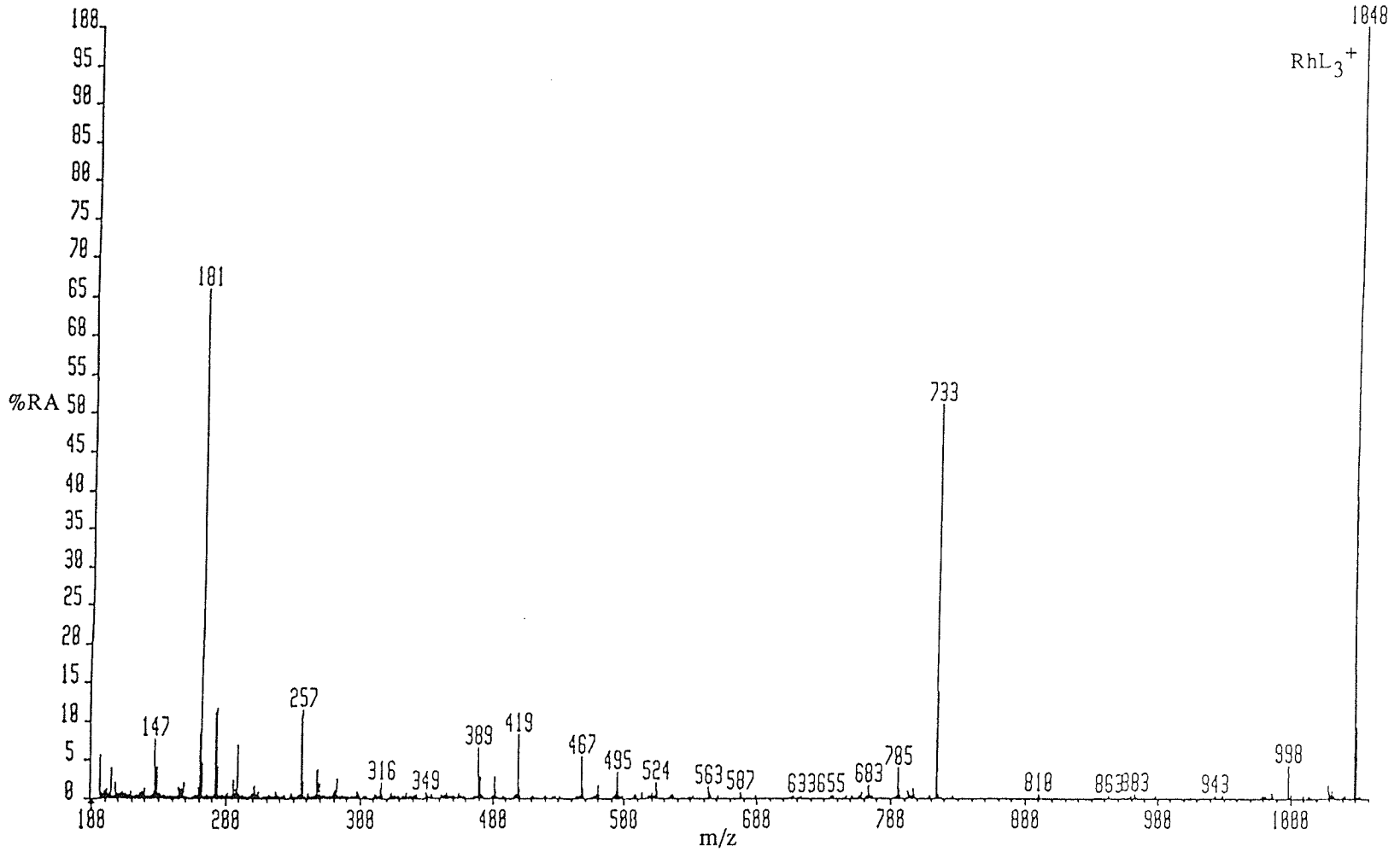

Figure 3.4 Mass spectrum of $Rh(bzC_3F_7)_3$ normalized to the base peak, RhL_3^+.

Table 3.1 70 eV-EI mass spectra of $Rh(SbzC_2F_5)_3$ and $Rh(SbzC_3F_7)_3$.

	$Rh(SbzC_2F_5)_3$			$Rh(SbzC_3F_7)_3$		
Ion	m/z	%RA	Structure (Scheme 3.n)	m/z	%RA	Structure (Scheme 3.n)
RhL_3^+	946	100.0	A946(3,4,16)	1096	100.0	B1096(3,4)
$[RhL_2(L\text{-}F)]^+$	927	3.5		1077	3.0	
$[RhL_2(L\text{-}S)]^+$	914	2.0	A914(16)	1064	6.5	B1064(16)
$[RhL_2(L\text{-}CF_2)]^+$	896	17.1	A896a(4) A896b(4)	1046	3.5	
RhL_2^+	665	31.6	A665(4,6-10, 12-14)	765	48.7	B765(3,7-9, 11-14)
$[RhL(L\text{-}HF)]^+$	645	2.4	A645(10)	745	7.1	B745(11)
$[RhL(L\text{-}S)]^+$	633	2.6	A633(16)	733	7.3	B733(16)
$[RhL(L\text{-}CF_2)]^+$	615	4.8	A615(4-6)	715	1.1	
$[RhL(L\text{-}C_6H_5CCH)]^+$	563	1.3		663	1.1	
$RRhL^+$	503	3.8		603	5.6	
$[SRhL(L\text{-}RCO)]^+$	550	2.4		600	2.5	
$[RhL(L\text{-}RCO)]^+$	518	6.2	A518(6-9,17)	568	7.7	B568(7-9,17)
$[RhL_2\text{-}S\text{-}RCO]^+$	486	1.5		536	2.4	
$[Rh(L\text{-}CF_2)(L\text{-}RCO)]^+$	468	< 1.0	A468(6)	518	-	
$[SRhL+H]^+$	417	1.8	A417a(13,14) A417b(13)	467	2.4	B467a(13,14) B467b(13)
$SRhL^+$	416	1.9	A416(7,8)	466	2.3	B466(7,8)
$[SRh(L\text{-}H)]^+$	415	4.5	A415(12)	465	6.3	B465(12)
$[2L\text{-}S\text{-}R]^+$	411	-		461	3.6	
$[SRh(L\text{-}CO)]^+$	388	2.1		438	2.3	
$HRhL^+$	385	1.0		435	1.5	
RhL^+	384	1.9	A384(7,9)	434	2.2	B434(7,9)
$[Rh(L\text{-}H)]^+$	383	48.6	A383(5,12,15)	433	55.2	B433(11,12,15)
$[Rh(L\text{-}H\text{-}HF)]^+$	363	1.0	A363(15)	413	1.0	B413(15)
$[Rh(L\text{-}CO)]^+$	356	1.8		406	1.8	
$[Rh(L\text{-}H\text{-}CO)]^+$	355	< 1.0	A355(15)	405	< 1.0	B405(15)
$[SRh(L\text{-}RCO)_2]^+$	403	1.0		403	3.7	
$[2L\text{-}2S\text{-}RCO]^+$	351	9.2	A351(17)	401	12.3	B401(17)

Table 3.1 Continued

	$Rh(SbzC_2F_5)_3$			$Rh(SbzC_3F_7)_3$		
Ion	m/z	%RA	Stucture (Scheme 3.n)	m/z	%RA	Stucture (Scheme 3.n)
$[Rh(L\text{-}COCH)]^+$	343	3.9		393	4.7	
$[Rh(L\text{-}H\text{-}HF\text{-}CO)]^+$	335	2.2	A335(15)	385	<1.0	B385(15)
$[Rh(L\text{-}H\text{-}CF_2)]^+$	333	2.1	A333(5)	383	<1.0	
$[Rh(L\text{-}RCO)_2]^+$	371	13.7	A371(7,8)	371	16.3	B371(7,8)
$RhSC_9H_5F_3^+$	305	2.1	A305(5)	354	< 1.0	
L^+	281	534.0	A281(3,4,16)	331	495.1	B331(3,16)
$[L\text{-}CF_2]^+$	231	55.9	A231(4)	281	10.8	
$[HSRh(L\text{-}RCO)]^+$	270	4.6		270	4.7	
$[SRh(L\text{-}RCO)]^+$	269	29.0	A269(7,8)	269	24.0	B269(7,8)
$[SRh(L\text{-}H\text{-}RCO)]^+$	268	8.5	A268(12)	268	7.5	B268(12)
$[Rh(L\text{-}H\text{-}R)]^+$	264	2.2	A264(15)	264	2.1	B264(15)
$RhSC_8H_6F^+$	256	3.9		256	3.1	
$RhSC_8H_5F^+$	255	2.6	A255(15)	255	1.7	B255(15)
$[Rh(L\text{-}RCO)]^+$	237	23.9	A237(7,9)	237	16.2	B237(7,9)
$[Rh(L\text{-}H\text{-}RCO)]^+$	236	39.7	A236(5)	236	28.8	
$SRhC_7H_5^+$	224	14.1		224	7.9	
$RhC_7H_6^+$	193	9.4	A193(7,9)	193	4.9	B193(7,9)
$RhC_7H_5^+$	192	8.7	A192(5)	192	2.2	
RhS_2^+	167	21.3	A167(7,8,12)	167	7.4	B167(7,8,12)
Rh^+	103	5.6	A103(9)	103	3.6	B103(9)

Table 3.2 70 eV-EI mass spectra of $Rh(bzC_2F_5)_3$ and $Rh(bzC_3F_7)_3$.

	$Rh(bzC_2F_5)_3$			$Rh(bzC_3F_7)_3$		
Ion	m/z	%RA	Structure (Scheme 3.n)	m/z	%RA	Structure (Scheme 3.n)
RhL_3^+	898	100.0	C898(4)	1048	100.0	
$[RhL_2(L\text{-}F)]^+$	879	2.2		1029	1.7	
$[RhL_2(L\text{-}CF_2)]^+$	848	36.1	C848a(4) C848b(4)	998	4.2	
$[RhL(L\text{-}CF_2)_2]^+$	798	3.7		948	-	
RhL_2^+	633	57.4	C633(4,18-22)	733	51.1	D733(18-22)
$[RhL(L\text{-}CO)]^+$	605	4.7	C605(19,21,23)	705	3.7	D705(19,21,23)
$[RhL(L\text{-}CF_2)]^+$	583	14.4	C583(4)	683	1.5	
$[Rh(L\text{-}CF_2)(L\text{-}CO)]^+$	555	1.1		655	-	
$[RhL(L\text{-}CF_2)_2]^+$	533	<1.0		633	-	
$[RhL(L\text{-}H\text{-}R)]^+$	513	1.1		563	-	
$LRhC_6H_5^+$	445	7.1	C445(18-20)	495	3.3	D495(18-20)
$[C_6H_5Rh(L\text{-}CO)]^+$	417	6.6	C417(19,20)	467	5.2	D467(19,20)
$[C_6H_5Rh(L\text{-}CF_2)]^+$	395	1.4		445	-	
$HRhL^+$	369	10.5	C369(22,23)	419	8.1	D419(22,23)
$[HRh(L\text{-}CO)]^+$	341	2.7		391	2.6	
$[Rh(L\text{-}COH)]^+$	339	8.3	C339a(20,21) C339b(20,21)	389	6.4	D389a(20,21) D389b(20,21)
$[HRh(L\text{-}CF_2)]^+$	319	1.5		369	-	
$[HRh(L\text{-}CF_2\text{-}CO)]^+$	291	1.3		341	-	
LH^+	266	3.2		316	1.2	
$Rh(C_6H_5)_2^+$	257	13.9	C257(18)	257	11.3	D257(18)
$RhC_{12}H_8^+$	255	15.0		255	10.6	
$[HRh(CO)(C_6H_5)]^+$	209	6.1		209	6.8	
$RhC_7H_6^+$	193	13.6		193	10.7	
$RhC_7H_5^+$	192	14.9		192	10.9	
$HRhC_6H_5^+$	181	81.2		181	65.1	
$RhC_6H_5^+$	180	12.2	C180(18)	180	8.3	D180(18)
RhC^+	115	6.2		115	3.8	
Rh^+	103	5.4		103	4.3	

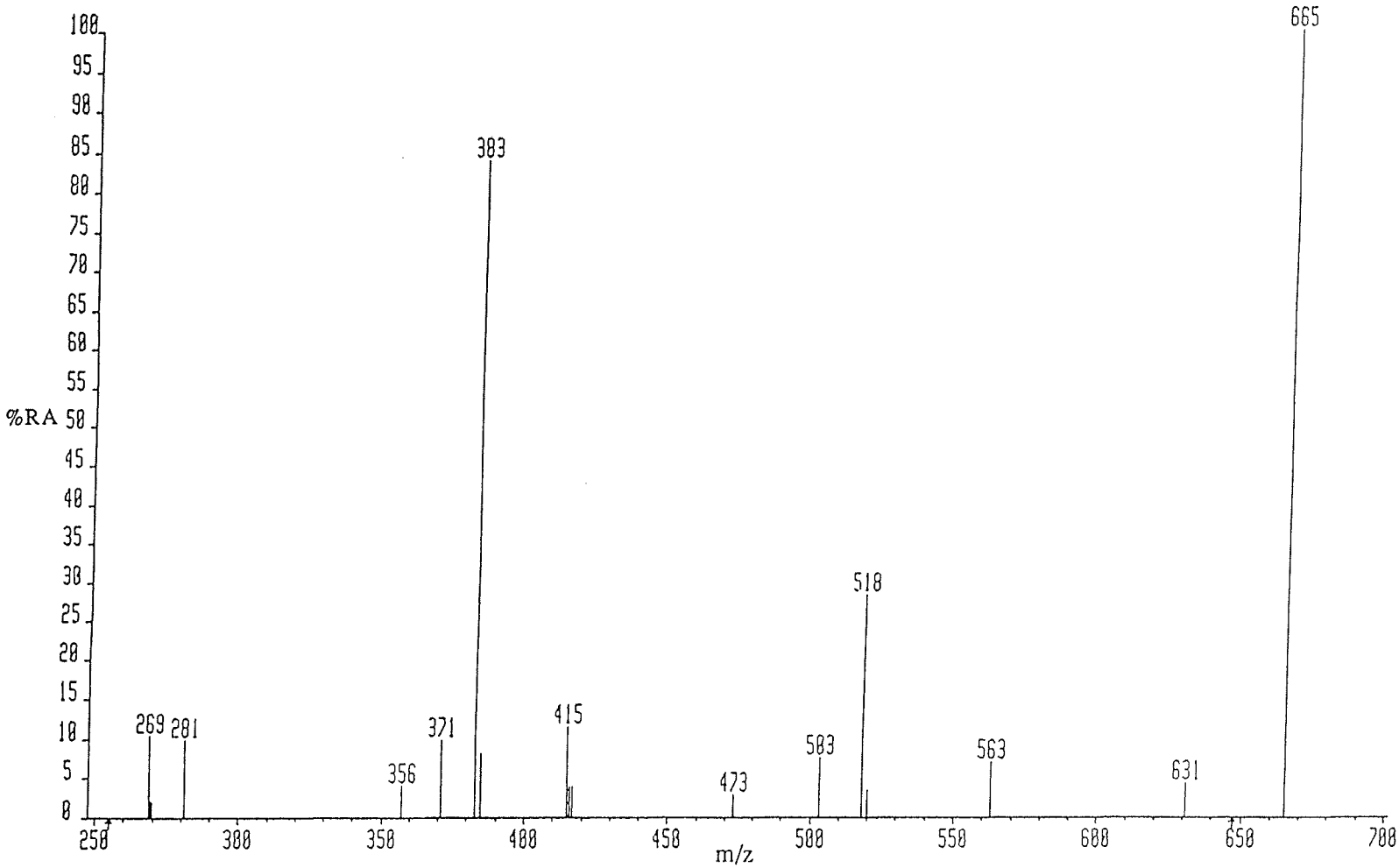

Figure 3.5 Daughter ion spectrum (B/E scan) of $Rh(SbzC_2F_5)_2^+$ (Ion intensity x10 between arrows).

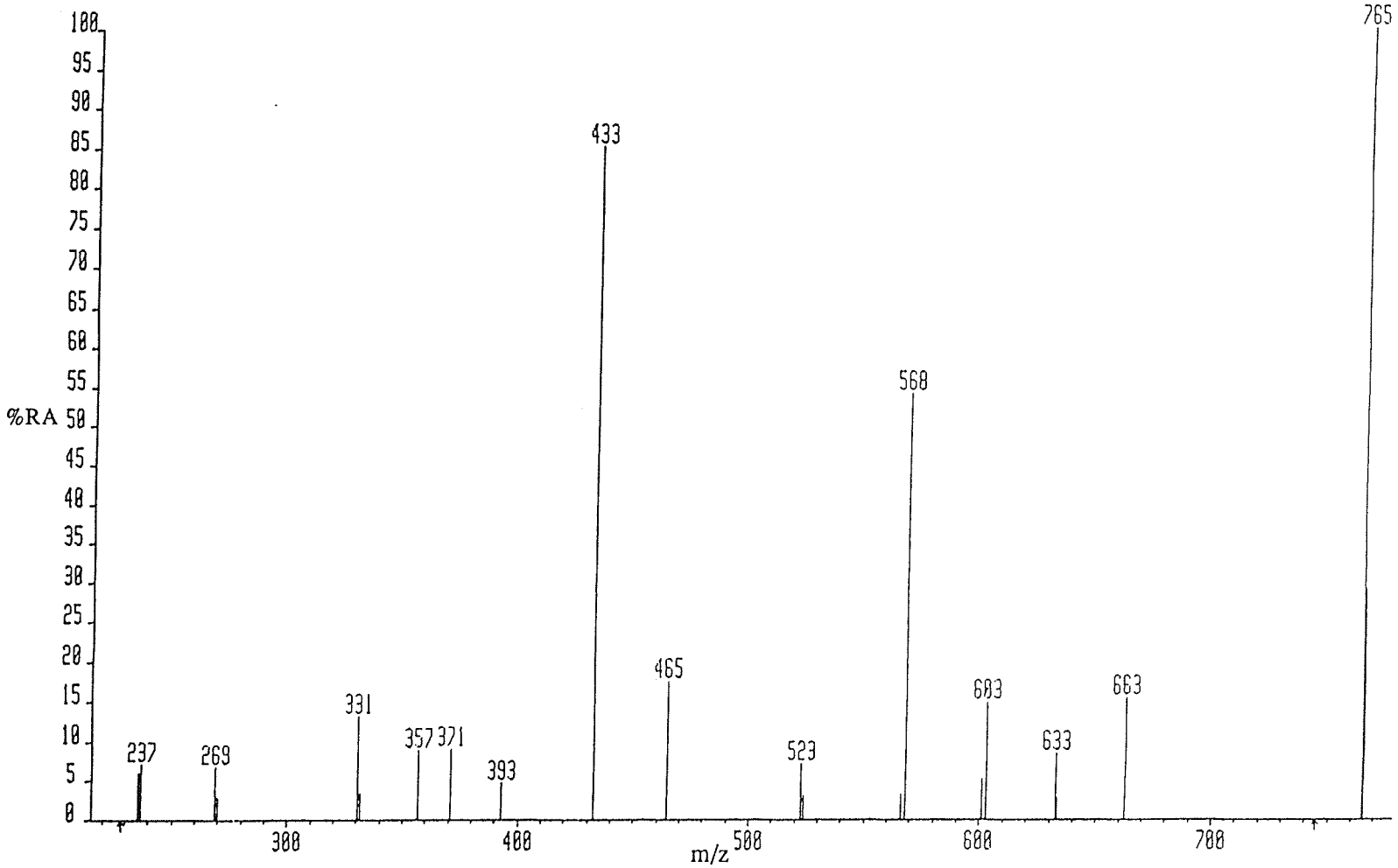

Figure 3.6 Daughter ion spectrum (B/E scan) of $Rh(SbzC_3F_7)_2^+$ (Ion intensity x5 between arrows).

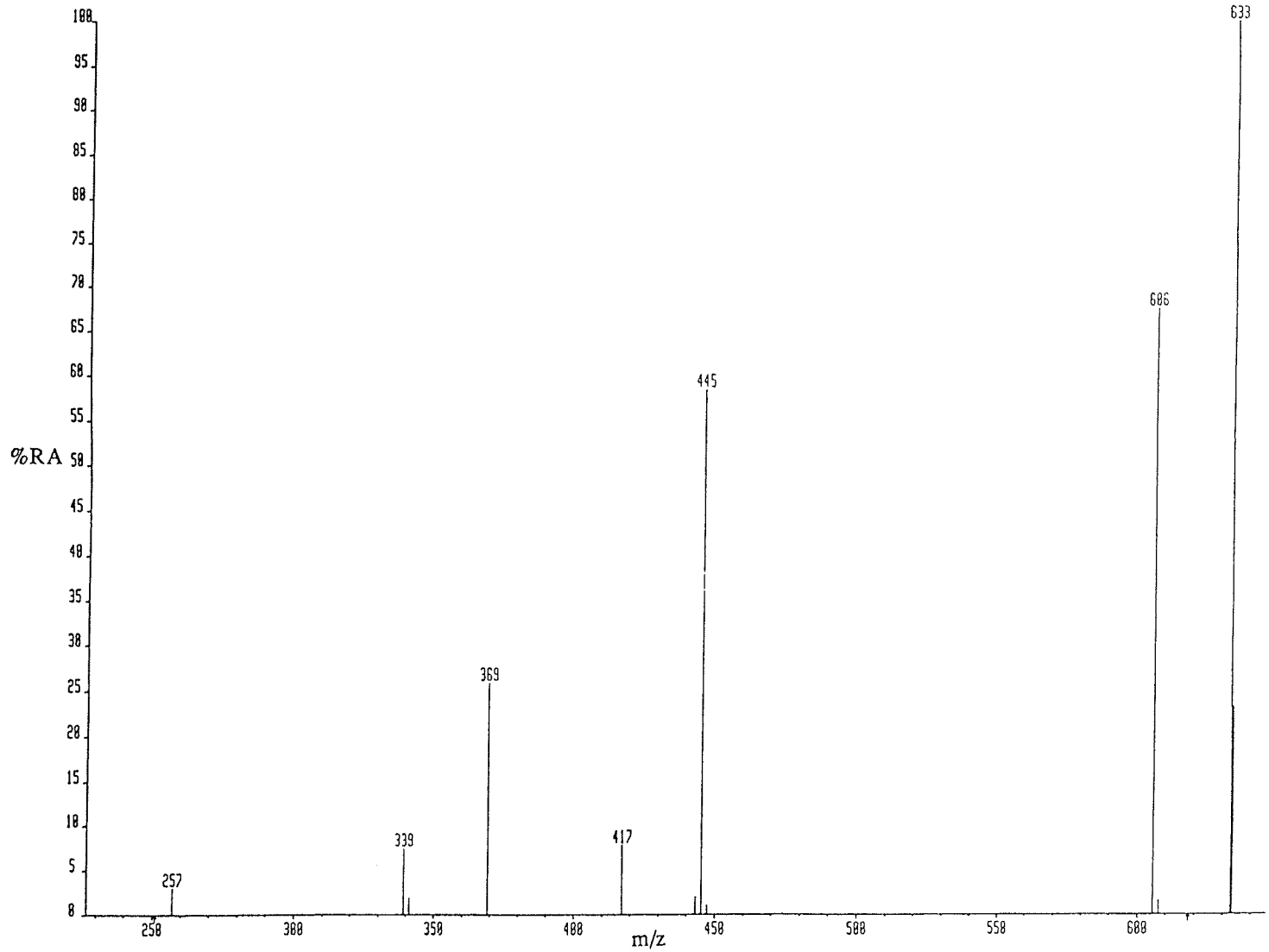

Figure 3.7 Daughter ion spectrum (B/E scan) of $Rh(bzC_2F_5)_2^+$ (Ion intensity x10 between arrows).

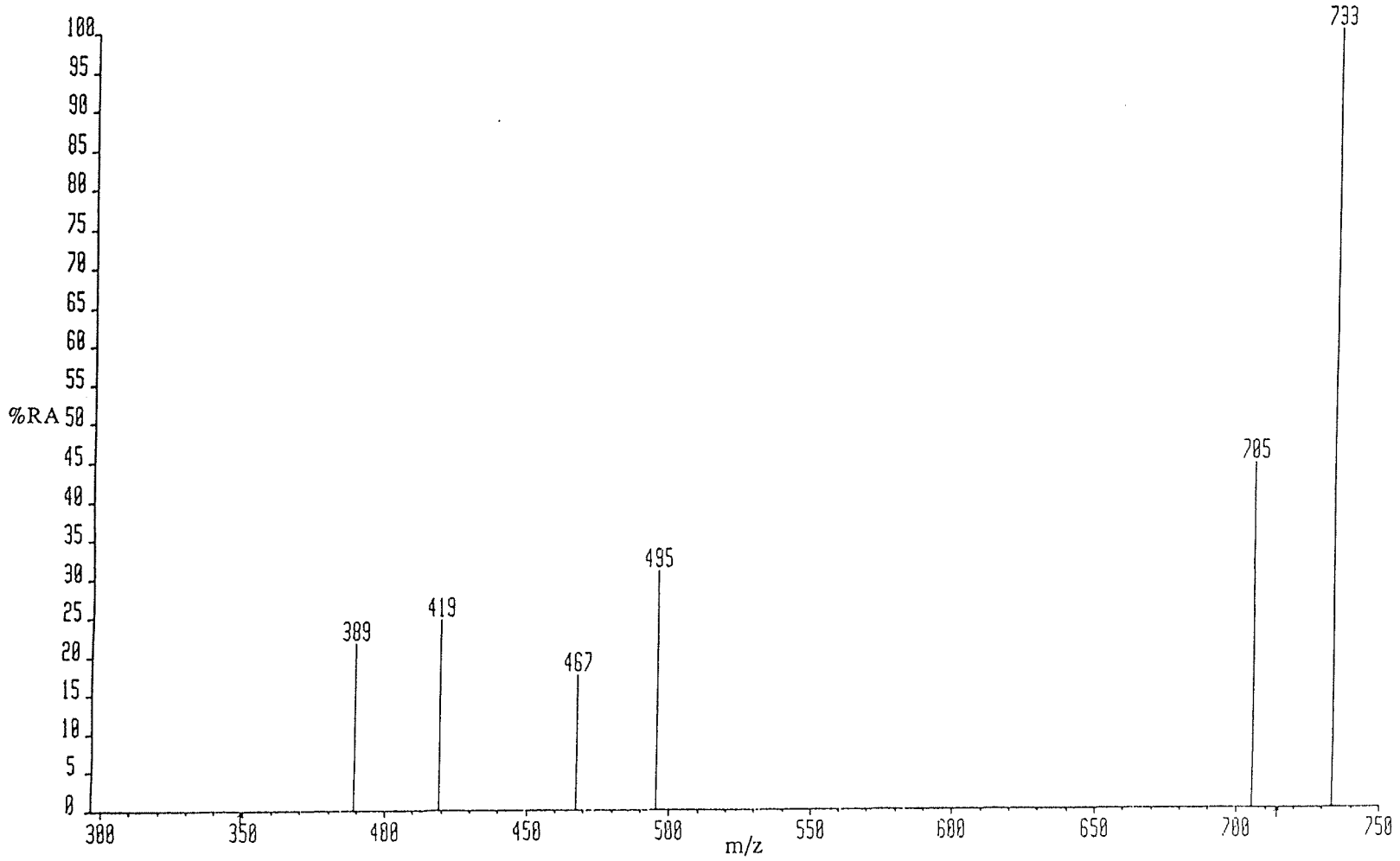

Figure 3.8 Daughter ion spectrum (B/E scan) of $Rh(bzC_3F_7)_2^+$ (Ion intensity x20 between arrows).

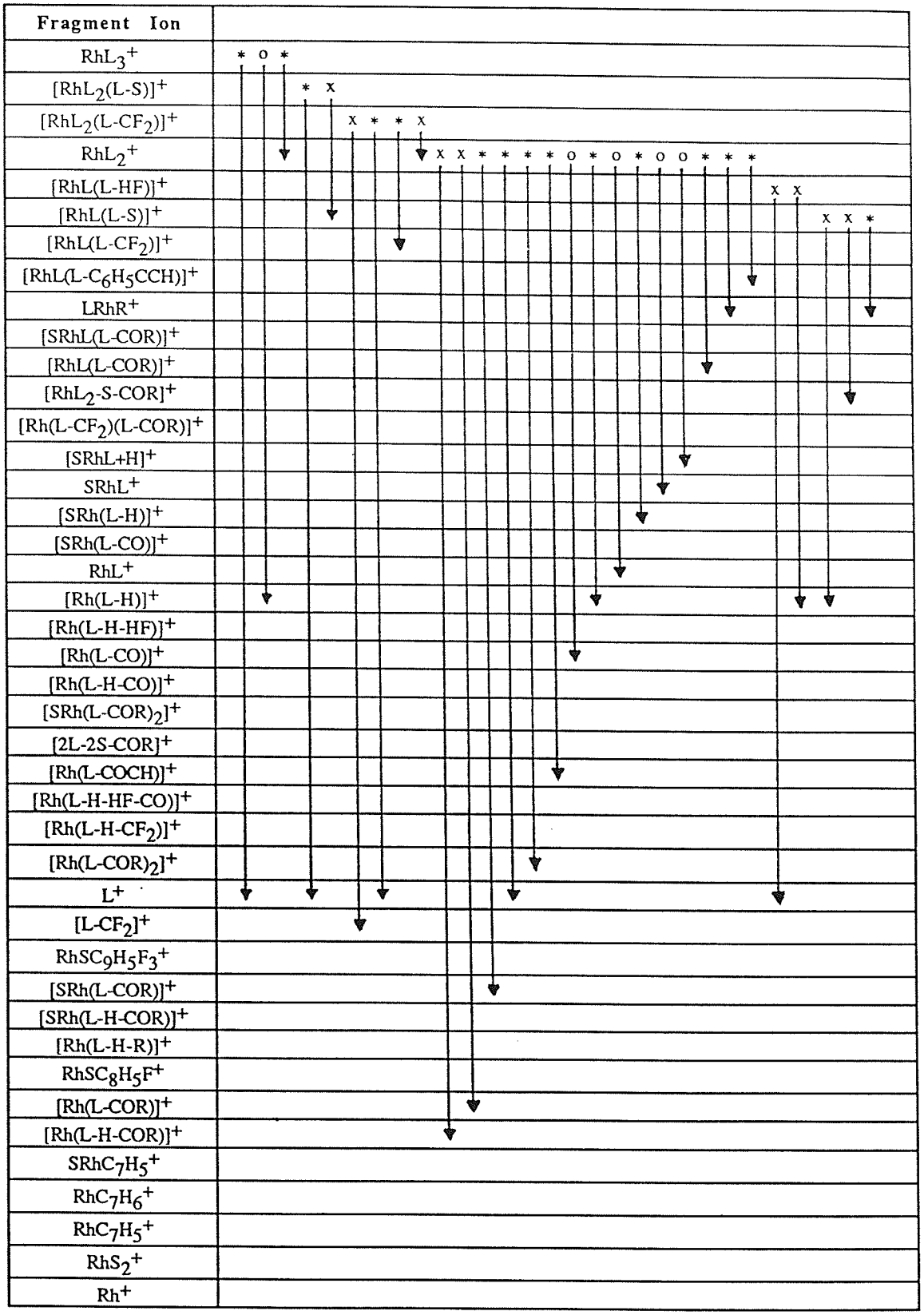

Scheme 3.1 Fragmentation pathways of $Rh(SbzC_2F_5)_3$ (o) and $Rh(SbzC_3F_7)_3$ (x). Pathways common to both complexes are indicated by the symbol *.

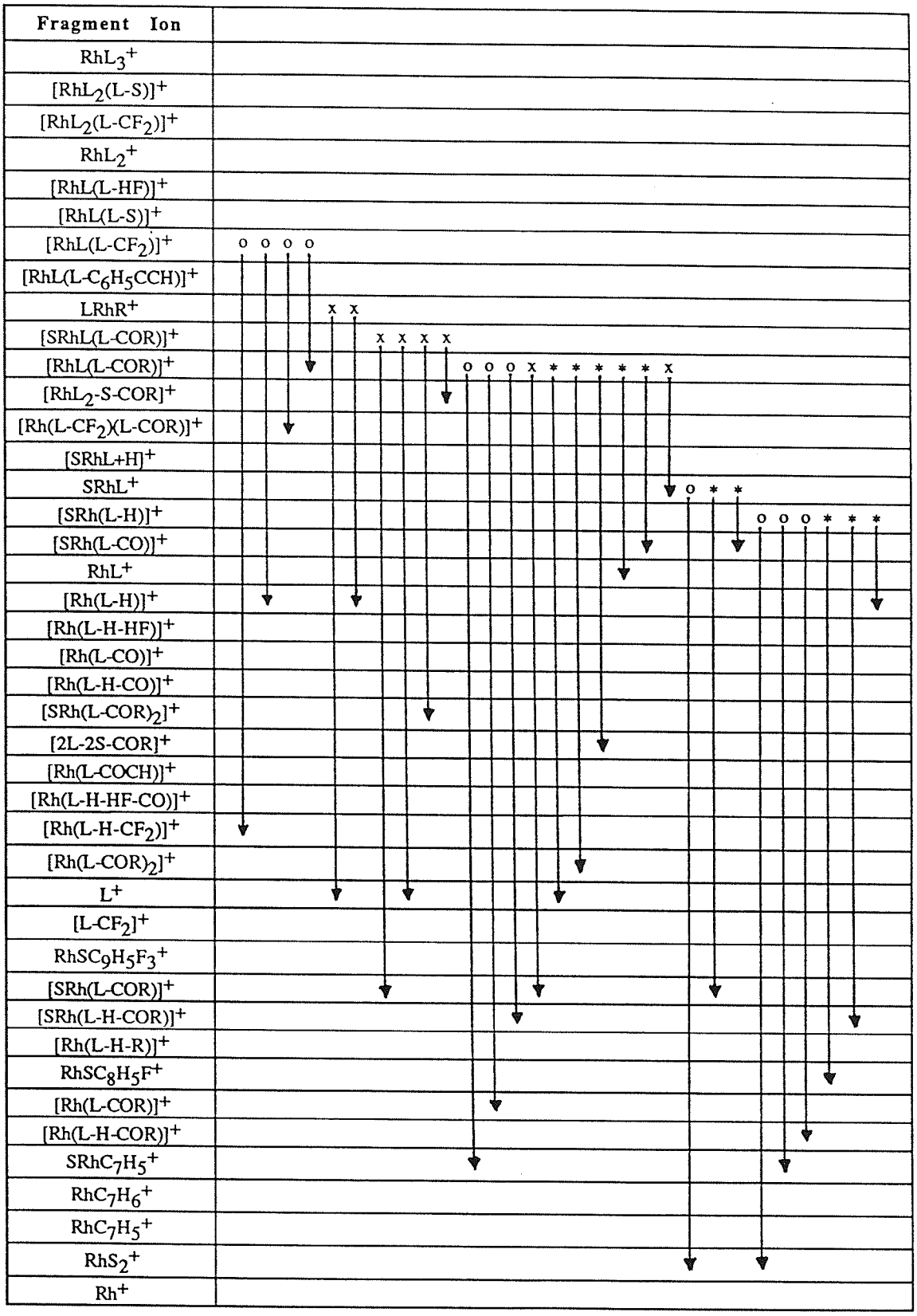

Scheme 3.1 (continued)

Fragment Ion	
RhL_3^+	
$[RhL_2(L\text{-}S)]^+$	
$[RhL_2(L\text{-}CF_2)]^+$	
RhL_2^+	
$[RhL(L\text{-}HF)]^+$	
$[RhL(L\text{-}S)]^+$	
$[RhL(L\text{-}CF_2)]^+$	
$[RhL(L\text{-}C_6H_5CCH)]^+$	
$LRhR^+$	
$[SRhL(L\text{-}COR)]^+$	
$[RhL(L\text{-}COR)]^+$	
$[RhL_2\text{-}S\text{-}COR]^+$	
$[Rh(L\text{-}CF_2)(L\text{-}COR)]^+$	
$[SRhL+H]^+$	
$SRhL^+$	
$[SRh(L\text{-}H)]^+$	
$[SRh(L\text{-}CO)]^+$	
RhL^+	
$[Rh(L\text{-}H)]^+$	
$[Rh(L\text{-}H\text{-}HF)]^+$	
$[Rh(L\text{-}CO)]^+$	
$[Rh(L\text{-}H\text{-}CO)]^+$	
$[SRh(L\text{-}COR)_2]^+$	
$[2L\text{-}2S\text{-}COR]^+$	
$[Rh(L\text{-}COCH)]^+$	
$[Rh(L\text{-}H\text{-}HF\text{-}CO)]^+$	
$[Rh(L\text{-}H\text{-}CF_2)]^+$	
$[Rh(L\text{-}COR)_2]^+$	
L^+	
$[L\text{-}CF_2]^+$	
$RhSC_9H_5F_3^+$	
$[SRh(L\text{-}COR)]^+$	
$[SRh(L\text{-}H\text{-}COR)]^+$	
$[Rh(L\text{-}H\text{-}R)]^+$	
$RhSC_8H_5F^+$	
$[Rh(L\text{-}COR)]^+$	
$[Rh(L\text{-}H\text{-}COR)]^+$	
$SRhC_7H_5^+$	
$RhC_7H_6^+$	
$RhC_7H_5^+$	
RhS_2^+	
Rh^+	

Scheme 3.1 (continued)

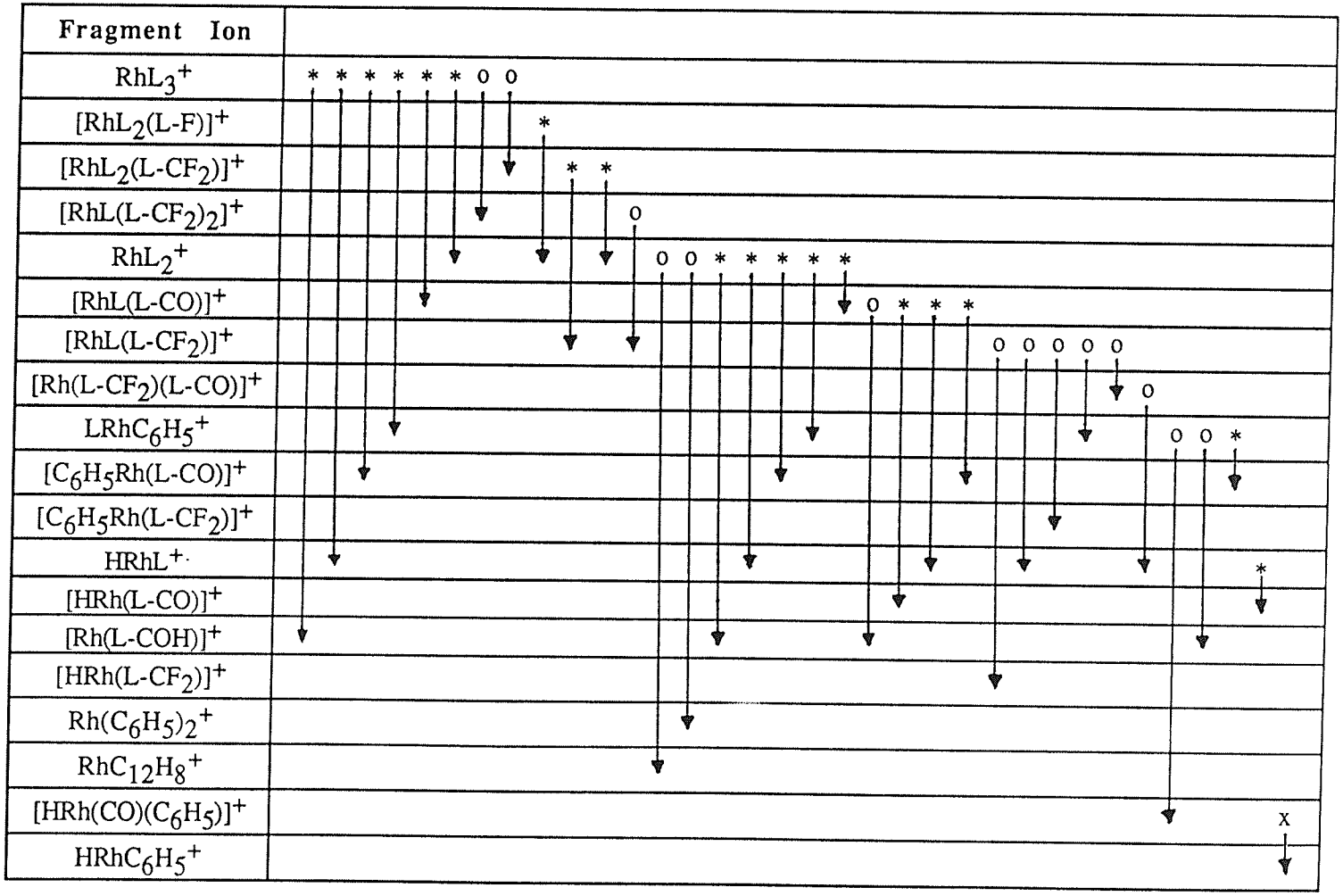

Scheme 3.2 Fragmentation pathways of $Rh(bzC_2F_5)_3$ (o) and $Rh(bzC_3F_7)_3$ (x). Pathways common to both complexes are indicated by the symbol *.

$Rh(acac)_3$, $Rh(tfa)_3$ and $Rh(hfa)_3$ formed from dioxo ligands, only for the latter is RhL_3^+ the base peak ion; otherwise RhL_2^+ is the most abundant ion[68]. In the spectra of the sulfur-containing complexes L^+ is the base peak ion but, in the complexes formed from dioxo ligands L^+ is of low abundance; this result is consistent with earlier reports on the mass spectra of other monothio-β-ketoenolate chelates of rhodium[69-71]. The daughter ion spectrum of RhL_3^+ indicates that L^+ is formed, at least in part, from RhL_3^+ by elimination of the neutral species $Rh^{II}L_2$; this reaction could be driven by formation of L^+ in a resonance-stabilized cyclic structure (**A281,B331**) (Scheme 3.3), and by the ability of rhodium to adopt the +II oxidation state with S-donor ligands. Furthermore, the presence of sulfur instead of oxygen enables the cyclic ion to better accommodate the positive charge.

In addition to the major differences between the mass spectra that can be attributed to the substitution of sulfur for oxygen there is a noteworthy effect of the substituent R; that is, the loss of $:CF_2$ from RhL_3^+ is much more prominent for the C_2F_5-substituted complexes $Rh(SbzC_2F_5)_3$ and $Rh(bzC_2F_5)_3$ than for the C_3F_7-substituted complexes $Rh(SbzC_3F_7)_3$ and $Rh(bzC_3F_7)_3$. The facile loss of this even-electron neutral fragment from RhL_3^+, verified for $Rh(bzC_2F_5)_3$ by daughter ion linked scanning, indicates that rhodium has undergone oxidation to Rh(IV). Under such circumstances loss of an even-electron neutral fragment from an even-electron ion can compete energetically with loss of a radical from an odd-electron ion (see Section 1.1). The mechanism proposed in Scheme 3.4 involves scission of the rhodium-oxygen bond, then rotation about the OC-CH

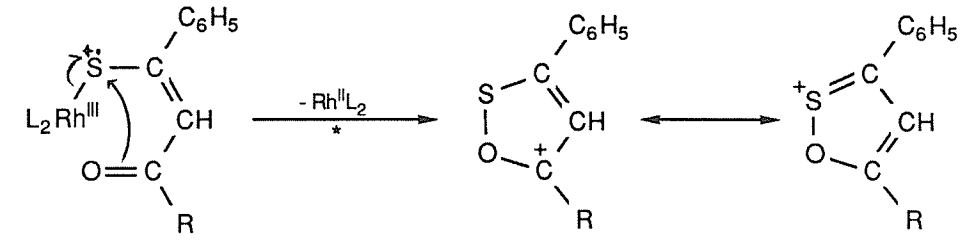

(A946,B1096); RhL_3^+

($R = C_2F_5, C_3F_7$)

(A281,B331); L^+

Scheme 3.3

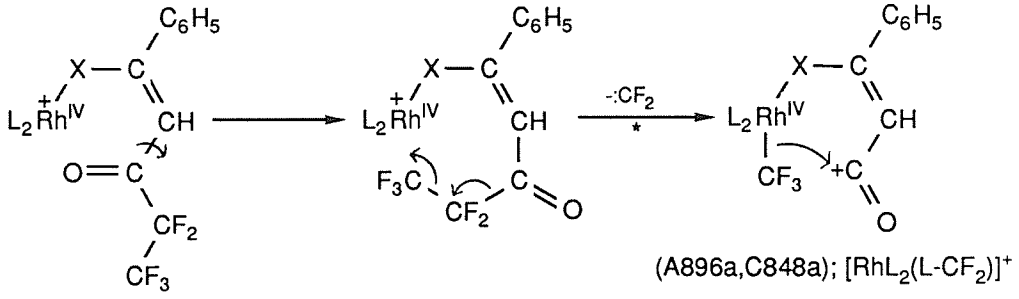

A946 (X = S), C898 (X = O); RhL_3^+

(A896a,C848a); $[RhL_2(L\text{-}CF_2)]^+$

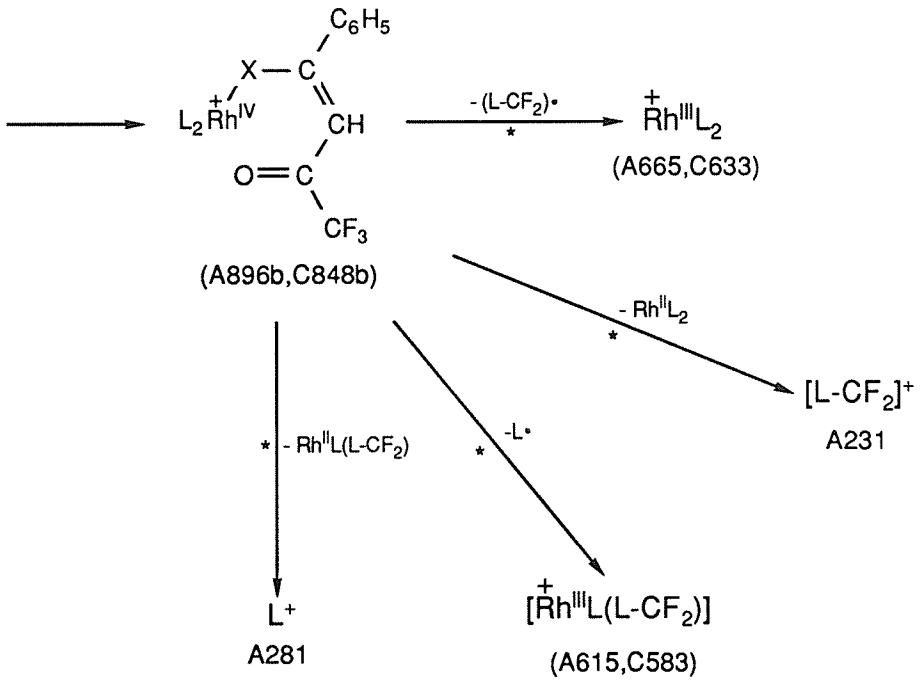

Scheme 3.4

bond to bring the CF_3 group of the perfluoroethyl substituent close to the rhodium atom, and then by formation of a Rh-CF_3 bond and subsequent loss of $:CF_2$ to give $RhL_2(L\text{-}CF_2)]^+$, **(A896a,C848a)**. However, migration of $\cdot CF_3$ back to the carbonyl carbon to give $[RhL_2(L\text{-}CF_2)]^+$, **(A896b,C848b)**, is required to explain first field-free region (FFR1) decompositions of $[RhL_2(L\text{-}CF_2)]^+$ to RhL_2^+, **(A665,C633)**, and to $[L\text{-}CF_2]^+$, **A231**. The existence of several compounds with a Rh-C_F bond[72-74] (C_F = fluoroalkyl), and the presence of $LRhR^+$ in the mass spectra of $Rh(SbzC_2F_5)_3$ and $Rh(SbzC_3F_7)_3$, give credence to the idea of a labile Rh-CF_3 bond. To account for the low abundance of $[RhL_2(L\text{-}CF_2)]^+$ in the mass spectra of the C_3F_7-substituted complexes we note that conformations in which the CF_3 moiety can migrate to the rhodium atom have lower probability than when R = C_2F_5. Instead, loss of $:CF_2$ from the C_3F_7 substituent would involve migration of the more bulky C_2F_5 moiety. To explain formation of the $[RhL_3\text{-}2CF_2]^+$ ion, observed for $Rh(bzC_2F_5)_3$ we assume that it is actually $[RhL(L\text{-}CF_2)_2]^+$ formed from RhL_3^+ by successive losses of $:CF_2$ fragments from each of two separate ligands, but this is not supported by evidence from metastable ion decompositions. Loss of C_2F_4, or two separate $:CF_2$ fragments from one ligand, is considered less likely since it would involve formation of a Rh-F bond. For $Rh(hfa)_3$, having two electron-withdrawing CF_3 substituents, no evidence of fluorine migration to the metal was observed[68]. It is therefore unlikely to be observed for a complex such as $Rh(bzC_2F_5)_3$ whose ligands contain an electron-donating phenyl group. The $[RhL_2(L\text{-}CF_2)]^+$ ion decomposes, by elimination of $\cdot L$, to give $[RhL(L\text{-}CF_2)]^+$, **(A615,C583)**. For

$Rh(bzC_2F_5)_3$, loss of the neutral radical ·(L-CF_2) from $[RhL(L\text{-}CF_2)_2]^+$, is also confirmed.

B) *$Rh(SbzC_2F_5)_3$ and $Rh(SbzC_3F_7)_3$*

Several fragment ions originate from $[RhL(L\text{-}CF_2)]^+$, **A615**, of $Rh(SbzC_2F_5)_3$ (Schemes 3.5 and 3.6). Initially, elimination of (LH-CF_2) and LH lead to $[Rh(L\text{-}H)]^+$ and $[Rh(L\text{-}H\text{-}CF_2)]^+$, respectively. Our deuterium-labelling studies show that the hydrogen lost to the neutral fragments comes mainly from the phenyl substituent (*ca* 96% in both cases). This result thus differs from earlier assumptions, made for various other metal chelates, that the departing hydrogen originates from the bridging position of the ligand[69,70]. In Scheme 3.5, the eliminations of (LH-CF_2) and LH lead to **A383** and **A333**, respectively, in which formation of a bond between rhodium and the aromatic ring is proposed. These ions decompose by losses of $C_2F_5\dot{C}O$ and $CF_3\dot{C}O$, respectively, to give $[Rh(L\text{-}H\text{-}COR)]^+$, **A236**, in both cases, which can then lose CS to give $RhC_7H_5^+$, **A192**. Alternatively, they can decompose by losses of CF_2CO and CO, respectively, to yield $RhSC_9H_5F_3^+$, **A305**, in both cases. Scheme 3.6 shows two other decompositions of **A615**. Losses of $CF_3\dot{C}O$ or $C_2F_5\dot{C}O$ yield $[RhL(L\text{-}COR)]^+$, **A518**, or $[RhL(L\text{-}CF_2)(L\text{-}COR)]^+$, **A468**, respectively. The high %RA of **A518** (6.2%) compared to **A468** (<1%), together with the assumption that losses of $CF_3\dot{C}O$ and $C_2F_5\dot{C}O$ from **A615** occur with equal probability, indicates that the confirmed loss of $C_2F_5\dot{C}O$ from RhL_2^+, **B665**, is the major pathway to $[RhL(L\text{-}C_2F_5CO)]^+$. In the mass spectrum of $Rh(SbzC_3F_7)_3$ the

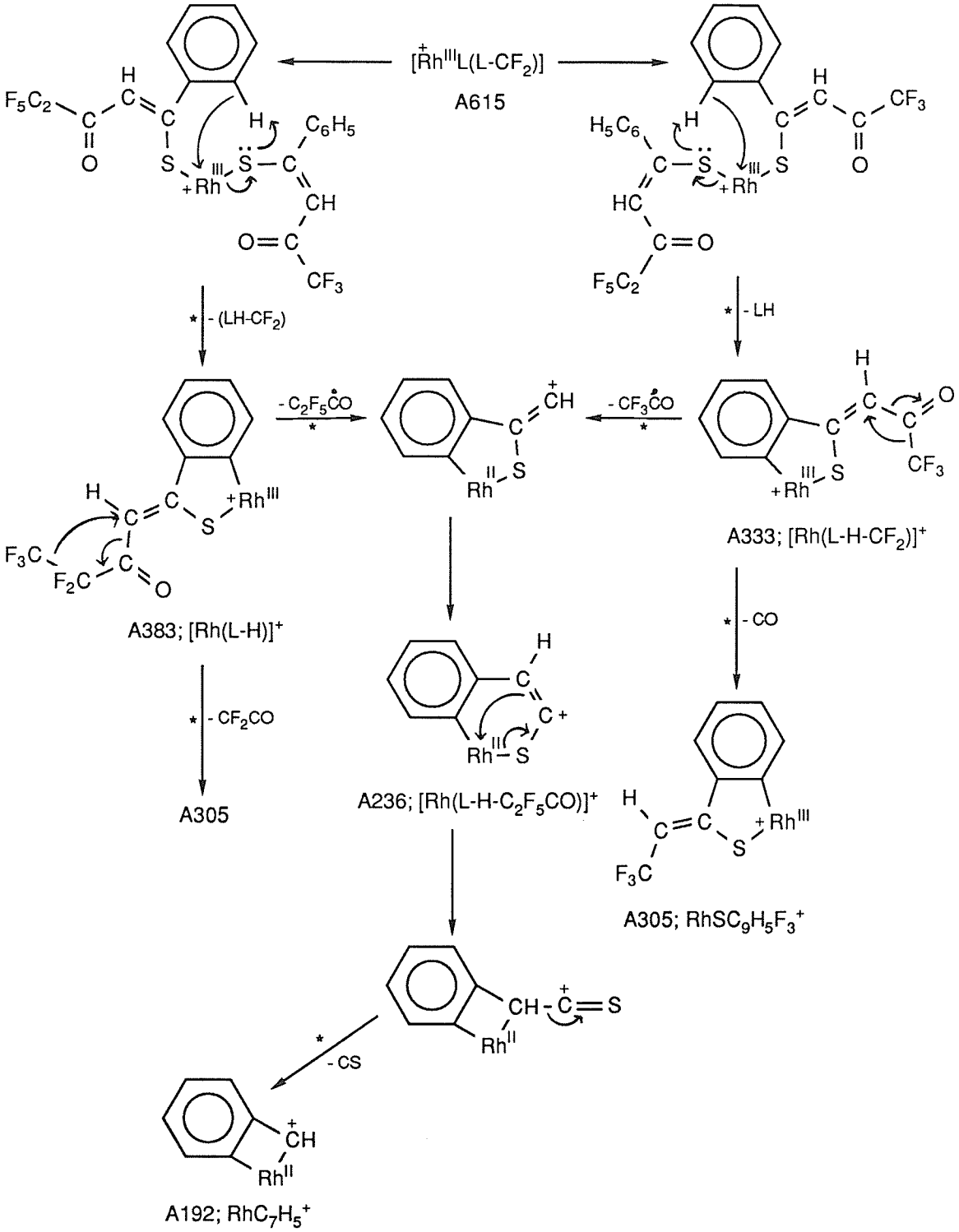
[Rh^III L(L-CF2)]+
A615
- (LH-CF2)
- LH
- C2F5CO
- CF3CO
A383; [Rh(L-H)]+
A333; [Rh(L-H-CF2)]+
- CF2CO
- CO
A305
A236; [Rh(L-H-C2F5CO)]+
A305; RhSC9H5F3+
- CS
A192; RhC7H5+

Scheme 3.5

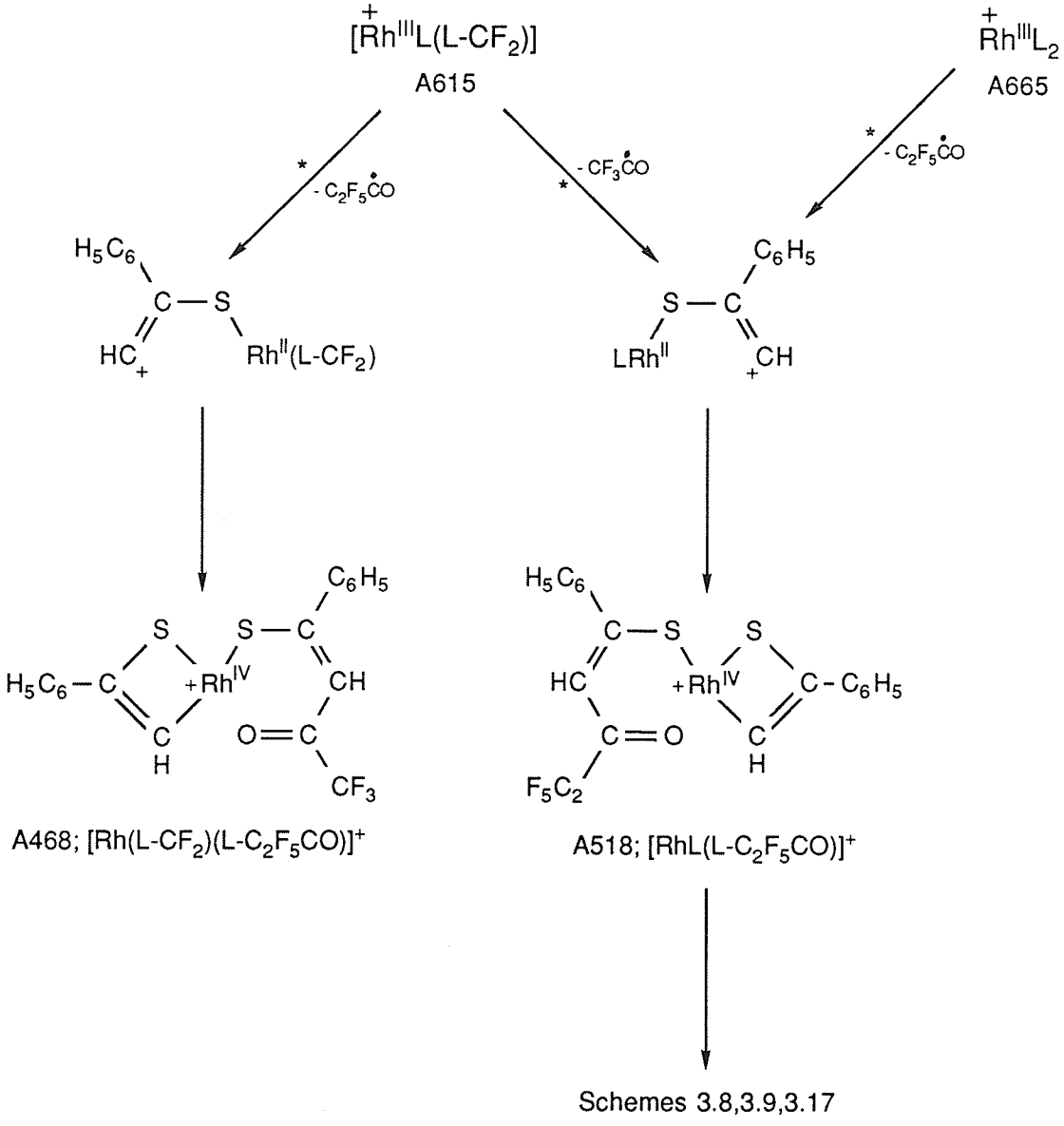
[Rh^III L(L-CF2)]+
A615
Rh^III L2+
A665
- C2F5CO•
- CF3CO•
- C2F5CO•
H5C6
C
S
HC+
Rh^II(L-CF2)
C6H5
S
C
LRh^II
CH+
S
S
C
H5C6
C
+Rh^IV
CH
C
H
O
C
CF3
C6H5
H5C6
C
S
S
HC
+Rh^IV
C - C6H5
C
O
C
H
F5C2
A468; [Rh(L-CF2)(L-C2F5CO)]+
A518; [RhL(L-C2F5CO)]+
Schemes 3.8,3.9,3.17

Scheme 3.6

corresponding ion $[RhL(L\text{-}C_3F_7CO)]^+$, **B568**, is also of significant abundance (7.7%).

Scheme 3.7 shows decomposition pathways of $[RhL(L\text{-}RCO)]^+$, (**A518,B568**), and its daughter ions, that terminate at RhS_2^+ and $RhC_7H_6^+$. These pathways are rationalized by the mechanisms proposed in Schemes 3.8 and 3.9, respectively. In Scheme 3.8, loss of RCO from $[RhL(L\text{-}COR)]^+$ gives $[Rh(L\text{-}COR)_2]^+$, (**A371,B371**), which can then lose $C_6H_5C{=}CH$ to give $[SRh(L\text{-}COR)]^+$, for which the cyclic ion, (**A269,B269**), should be a preferred structure. Alternatively, $[RhL(L\text{-}COR)]^+$ can lose $C_6H_5C{=}CH$ first to give $LRhS^+$, (**A416,B466**), which then loses RCO to give, once again, $[SRh(L\text{-}COR)]^+$. Further loss of $C_6H_5C{=}CH$ yields RhS_2^+, (**A167,B167**).

In Scheme 3.9, $[RhL(L\text{-}RCO)]^+$, loses ·L to yield $[Rh(L\text{-}RCO)]^+$, (**A237,B237**). In an alternative pathway, this ion is formed by losses of $C_6H_5C{=}CHS$ (to give the low abundance ion RhL^+, (**A384,B434**)), and then RCO. (Note that RhL^+ is also formed from RhL_2^+ by loss of ·L). $[Rh(L\text{-}COR)]^+$ can decompose by loss of CS to yield $Rh{=}CHC_6H_5^+$, (**A193,B193**), or by loss of $C_6H_5C{=}CHS$ to give the bare metal ion Rh^+, (**A103,B103**).

An interesting ion, $[RhL(L\text{-}HF)]^+$, occurs with a %RA ratio of approximately 1:3 in the mass spectra of $Rh(SbzC_2F_5)_3$ and $Rh(SbzC_3F_7)_3$, respectively. The mechanisms proposed (Schemes 3.10 and 3.11) for loss of HF from RhL_2^+, (**A665,B765**), involve the bridging hydrogen of the ligand and one of the terminal fluorines of the perfluoroalkyl substituent to form the four- and five- membered ringed structures **A645** and **B745**, respectively. The lower %RA of **A645** for $Rh(SbzC_2F_5)_3$ might therefore be attributed to strain

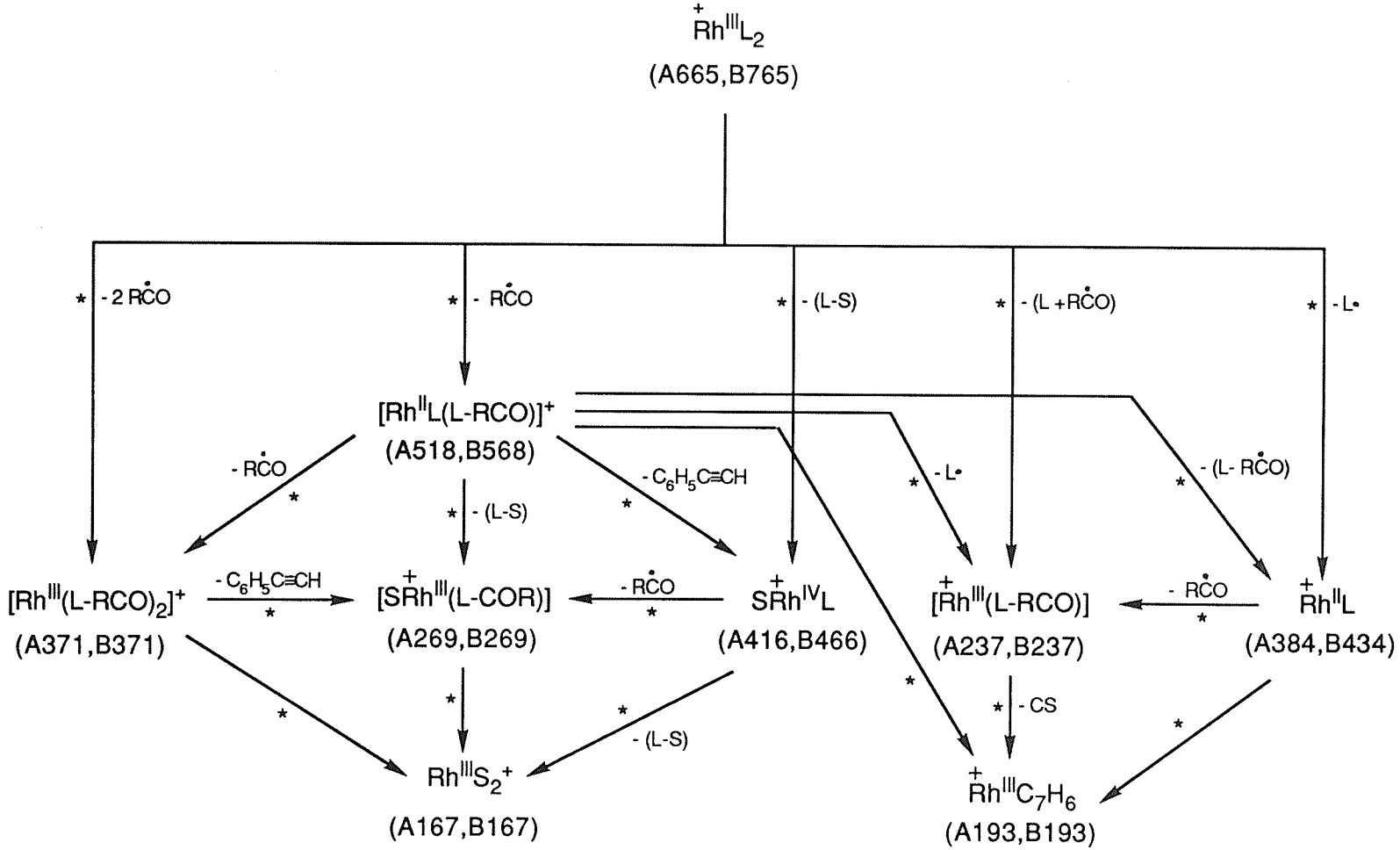
Rh^III L2
(A665,B765)
- 2 RCO
- RCO
- (L-S)
- (L +RCO)
- L
[Rh^II L(L-RCO)]+
(A518,B568)
- RCO
- C6H5C≡CH
- L
- (L- RCO)
- (L-S)
[Rh^III(L-RCO)2]+
(A371,B371)
- C6H5C≡CH
[SRh^III(L-COR)]
(A269,B269)
- RCO
SRh^IV L
(A416,B466)
[Rh^III(L-RCO)]
(A237,B237)
- RCO
Rh^II L
(A384,B434)
- CS
- (L-S)
Rh^III S2+
(A167,B167)
Rh^III C7H6
(A193,B193)

Scheme 3.7

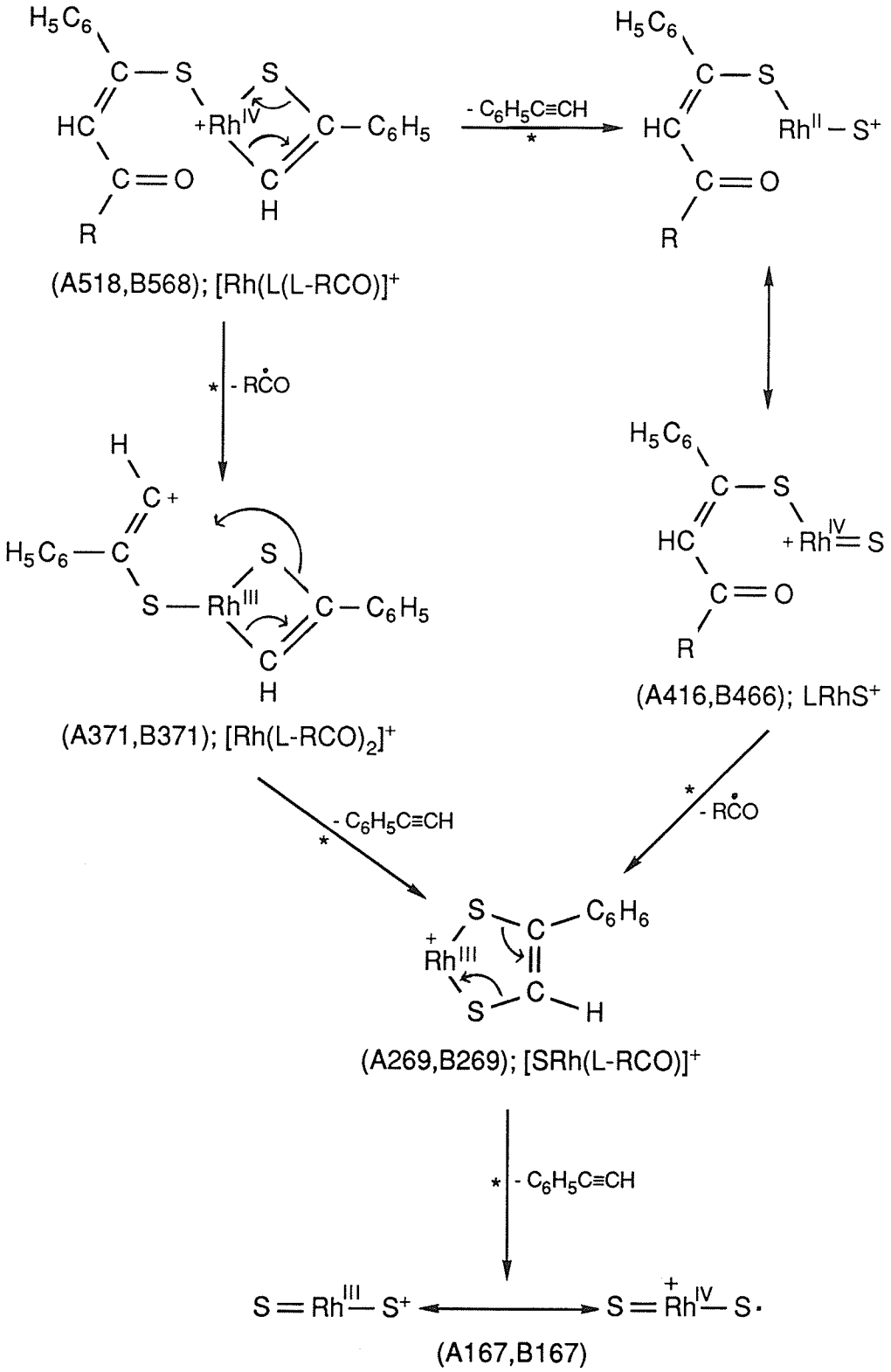
(A518,B568); [Rh(L(L-RCO)]+
(A371,B371); [Rh(L-RCO)2]+
(A416,B466); LRhS+
(A269,B269); [SRh(L-RCO)]+
(A167,B167)

Scheme 3.8

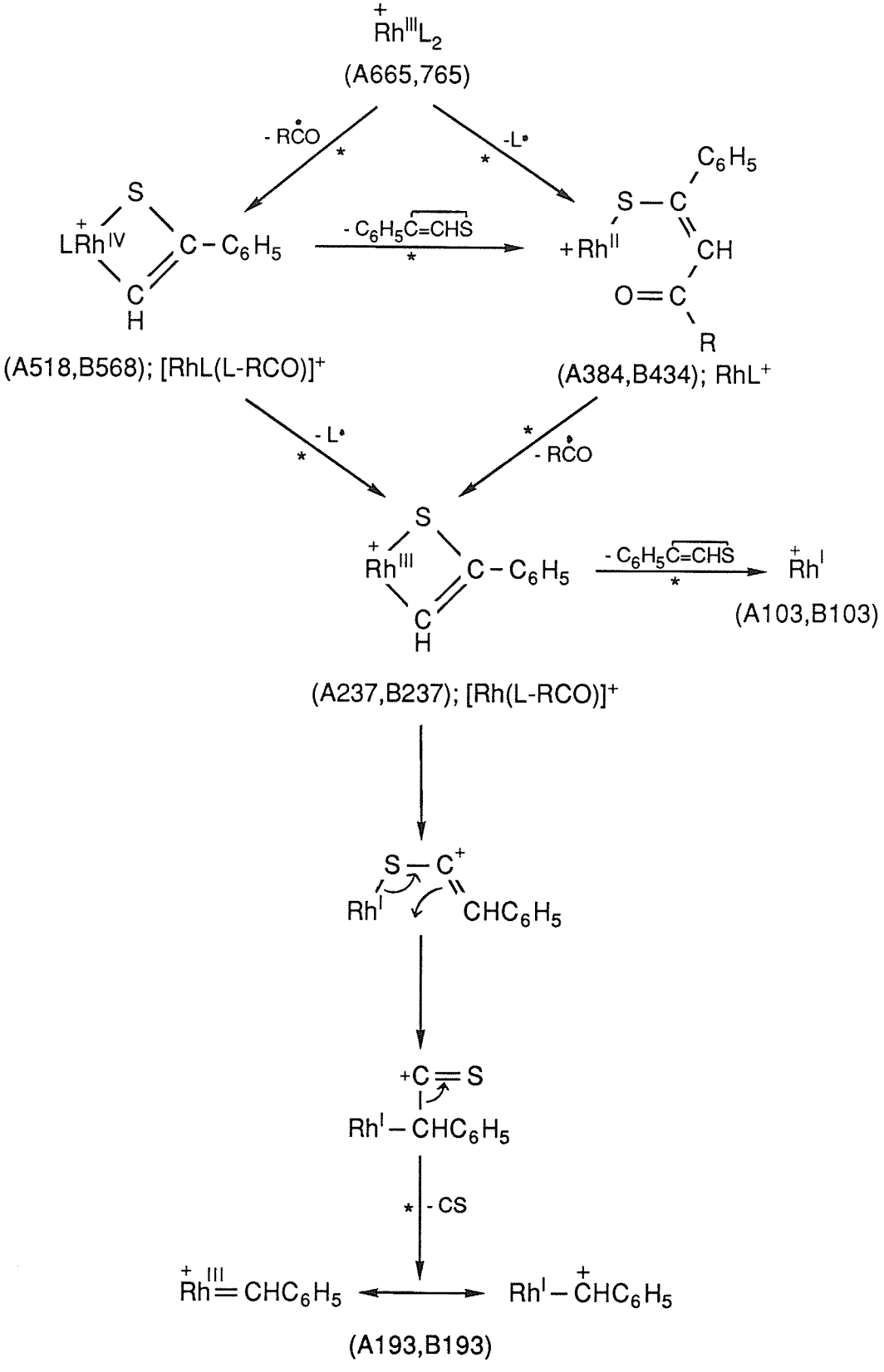
+
Rh^III L2
(A665,765)
- RCO
*
-L•
*
S
+
LRh^IV
C – C6H5
C
H
- C6H5C=CHS
*
C6H5
S – C
+Rh^II
CH
O = C
R
(A518,B568); [RhL(L-RCO)]+
(A384,B434); RhL+
- L•
*
*
- RCO
S
+
Rh^III
C – C6H5
C
H
- C6H5C=CHS
*
+
Rh^I
(A103,B103)
(A237,B237); [Rh(L-RCO)]+
S – C+
Rh^I
CHC6H5
+C = S
Rh^I – CHC6H5
*
- CS
+ III
Rh = CHC6H5
Rh^I – +CHC6H5
(A193,B193)

Scheme 3.9

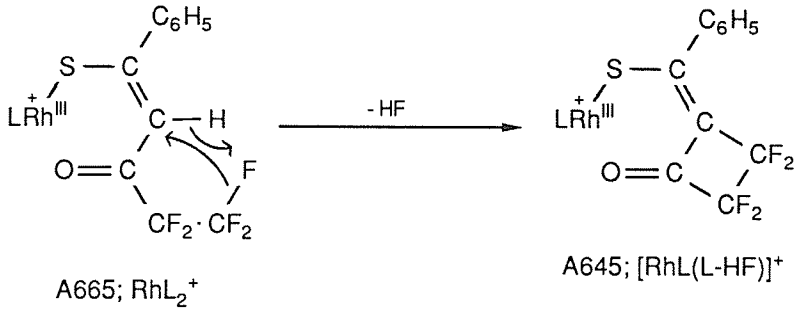

Scheme 3.10

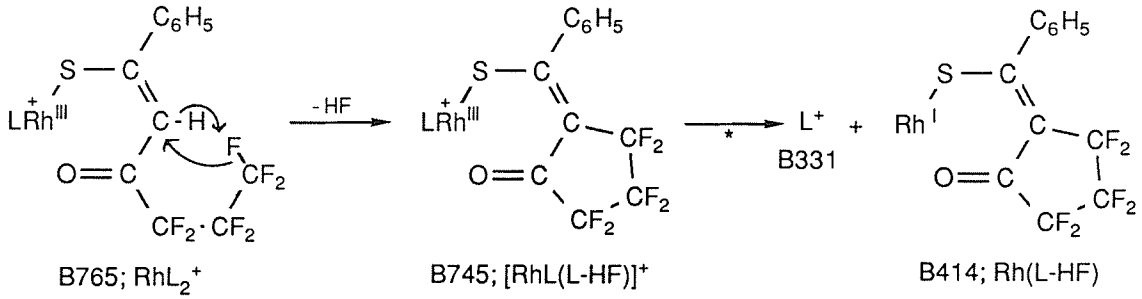

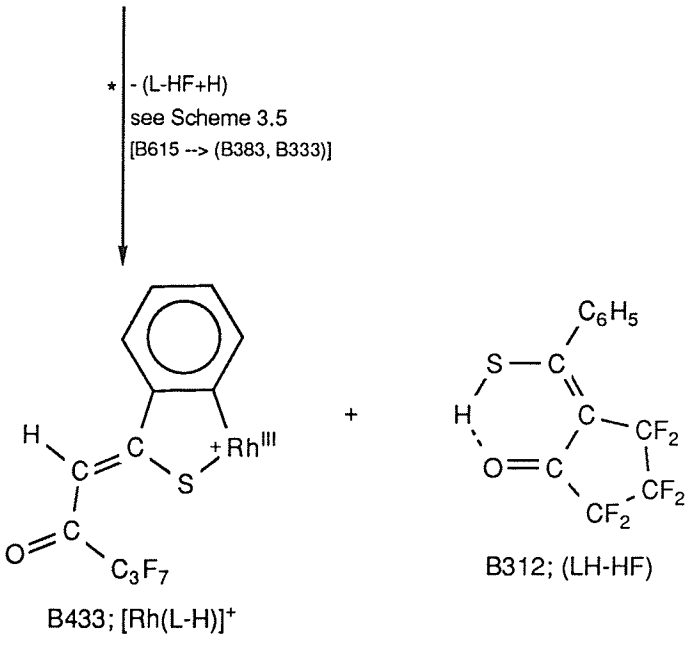

Scheme 3.11

associated with a four-membered ring. Ion **B745** undergoes further decomposition to L^+, **B331**, and $[Rh(L-H)]^+$, **B433**, by losses of the stable neutral fragments **B414** and **B312**, respectively.

The only observable parent of the ions $[SRh(L-H)]^+$ and $[SRhL+H]^+$ in the mass spectra of $Rh(SbzC_2F_5)_3$ and $Rh(SbzC_3F_7)_3$, is RhL_2^+, **(A665,B765)**. The deuterium labelling studies showed that, for the former ion, most (*ca* 84%) of the hydrogen transferred to the eliminated neutral species originates from the phenyl group of the retained ligand. In Scheme 3.12, the hydrogen atom is transferred to the thio carbon with concurrent formation of a bond between the aromatic ring and sulfur, **(A415,B465)**. Sequential losses of $R\dot{C}O$ and $HC{\equiv}C\dot{C}_6H_4$ then lead to formation of $[SRh(L-H-COR)]^+$, **(A268,B268)**, and RhS_2^+, **(A167,B167)**, respectively. An alternative decomposition of **(A415,B465)**, involves the loss of sulfur to give $[Rh(L-H)]^+$, **(A383,B433)**.

Pathways for the formation of $[SRhL+H]^+$, are shown in Schemes 3.13 and 3.14. It was found that ~69% of the hydrogen retained originates from the bridging carbon atom and ~31% from the phenyl substituent. In the former case, two mechanisms are postulated. The first (Scheme 3.13a) involves migration of the bridging hydrogen to rhodium and the second (Scheme 3.13b) to sulfur. In both instances the neutral fragment $C_6H_5C{\equiv}CCRO$ is lost simultaneously, giving rise to $[LRh(S)H]^+$, **(A417,B467)a**, and $LRhSH^+$, **(A417,B467)b**, respectively. In the latter case (Scheme 3.14) we propose migration of a phenyl hydrogen to rhodium, followed by rearrangement of the bridging hydrogen to the resulting phenyl

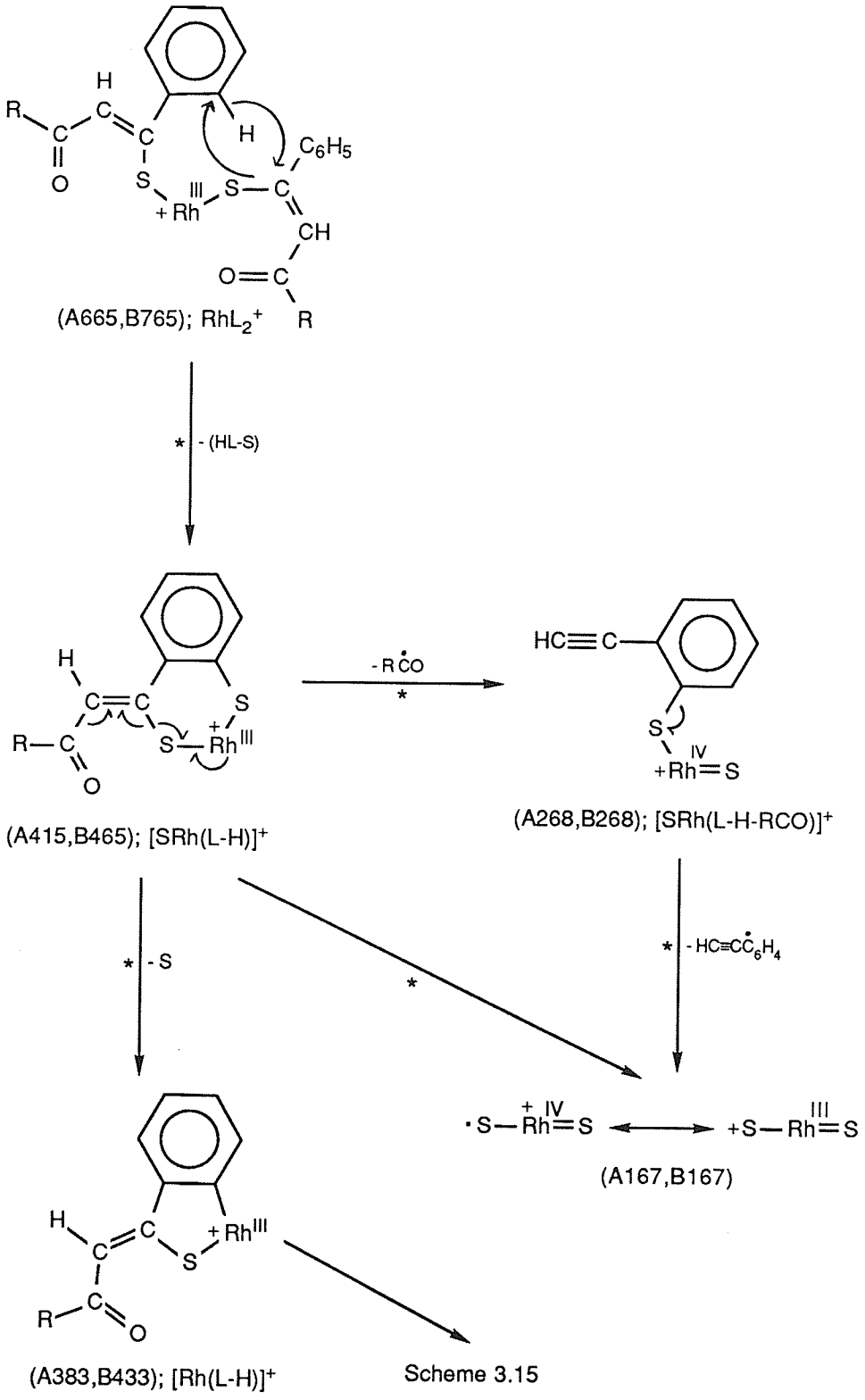

Scheme 3.15

Scheme 3.12

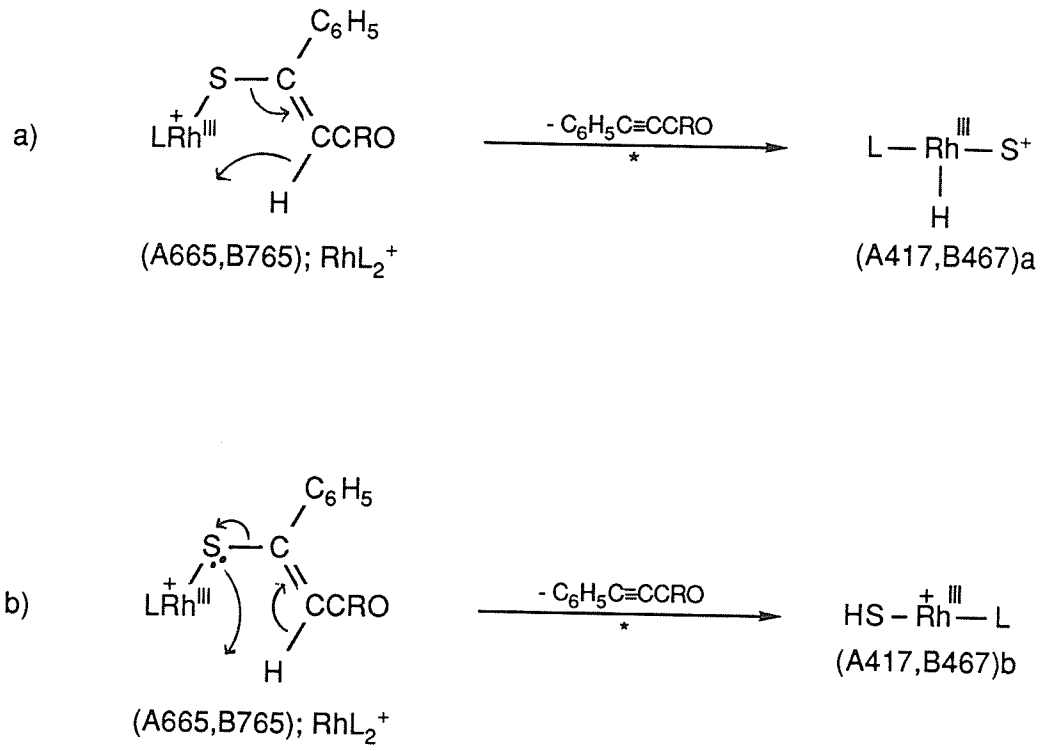

Scheme 3.13

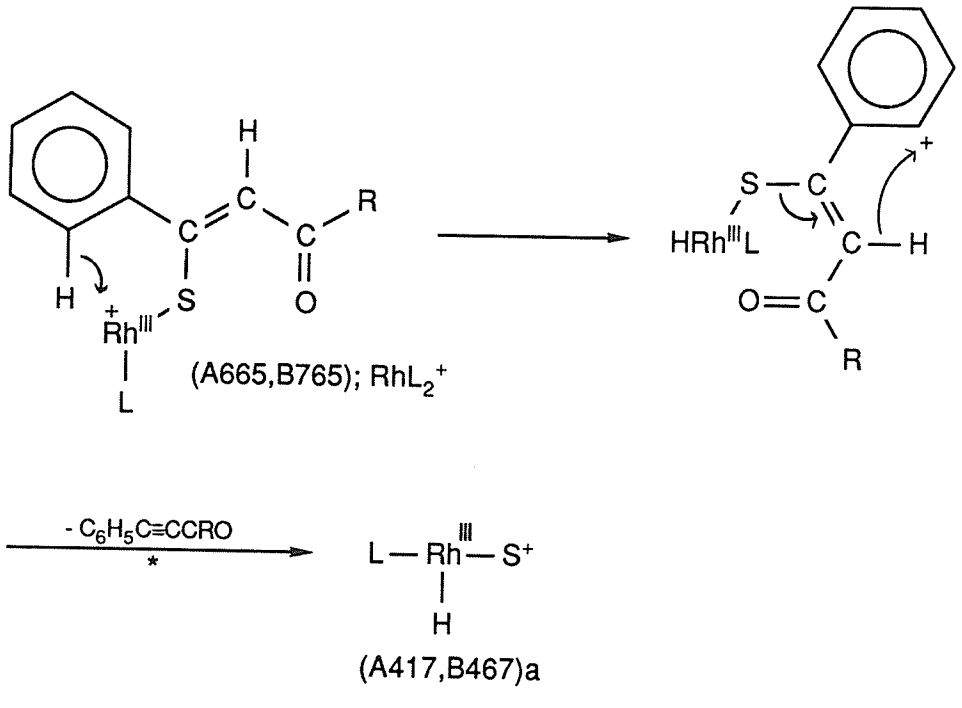

Scheme 3.14

cation. This ion, in turn, loses $C_6H_5C{\equiv}CCRO$ to give, once again, **(A417,B467)a**.

In all, five different precursors of RhS_2^+ have been identified by metastable ion decompositions in FFR1, namely, $[Rh(L\text{-}COR)_2]^+$, $LRhS^+$, $[SRh(L\text{-}COR)]^+$ (Scheme 3.8), $[SRh(L\text{-}H)]^+$ and $[SRh(L\text{-}H\text{-}COR)]^+$ (Scheme 3.12), though decompositions of $[Rh(L\text{-}COR)_2]^+$, $LRhS^+$ and $[SRh(L\text{-}H)]^+$ may involve two steps. All decompositions were observed for $Rh(SbzC_2F_5)_3$, and two for $Rh(SbzC_3F_7)_3$ ($[SRh(L\text{-}COR)]^+$ and $[SRh(L\text{-}H\text{-}COR)]^+$).

Thus far, we have seen that $[Rh(L\text{-}H)]^+$, the second most abundant rhodium-containing ion (after the molecular ion) in the mass spectra of both complexes, can be formed *via* the decomposition of $[RhL(L\text{-}CF_2)]^+$, **A615**, (Scheme 3.5), $[RhL(L\text{-}HF)]^+$, **B745**, (Scheme 3.11) and $[SRh(L\text{-}H)]^+$, **(A415,B465)**, (Scheme 3.12) and that it can itself decompose to $[Rh(L\text{-}H\text{-}COR)]^+$, **A236**, (and its descendent) and, $RhSC_9H_5F_3^+$, **A305**, (Scheme 3.5). In additional decompositions (Scheme 3.15), it sequentially loses ·R, CO and HF in a variety of permutations, and can also yield $RhSC_8H_5F^+$, **(A255,B255)**, by loss of the even-electron neutral fragment $CF_3CF{=}CO$ ($Rh(SbzC_2F_5)_3$) or $CF_3CF_2CF{=}CO$ ($Rh(SbzC_3F_7)_3$).

The accessibility of the rhodium +IV oxidation state imparts sufficient stabilization to RhL_3^+ that the losses of even-electron neutrals (in particular, $:CF_2$ and S) become competitive with losses of odd-electron neutrals. As previously noted, loss of $:CF_2$ from RhL_3^+ occurs less readily for $Rh(SbzC_3F_7)_3$ than for $Rh(SbzC_2F_5)_3$, perhaps enabling the competing loss of S from RhL_3^+ to be greater for the former complex ($[RhL_2(L\text{-}S)]^+$, %RA = 6.5) than for the latter one

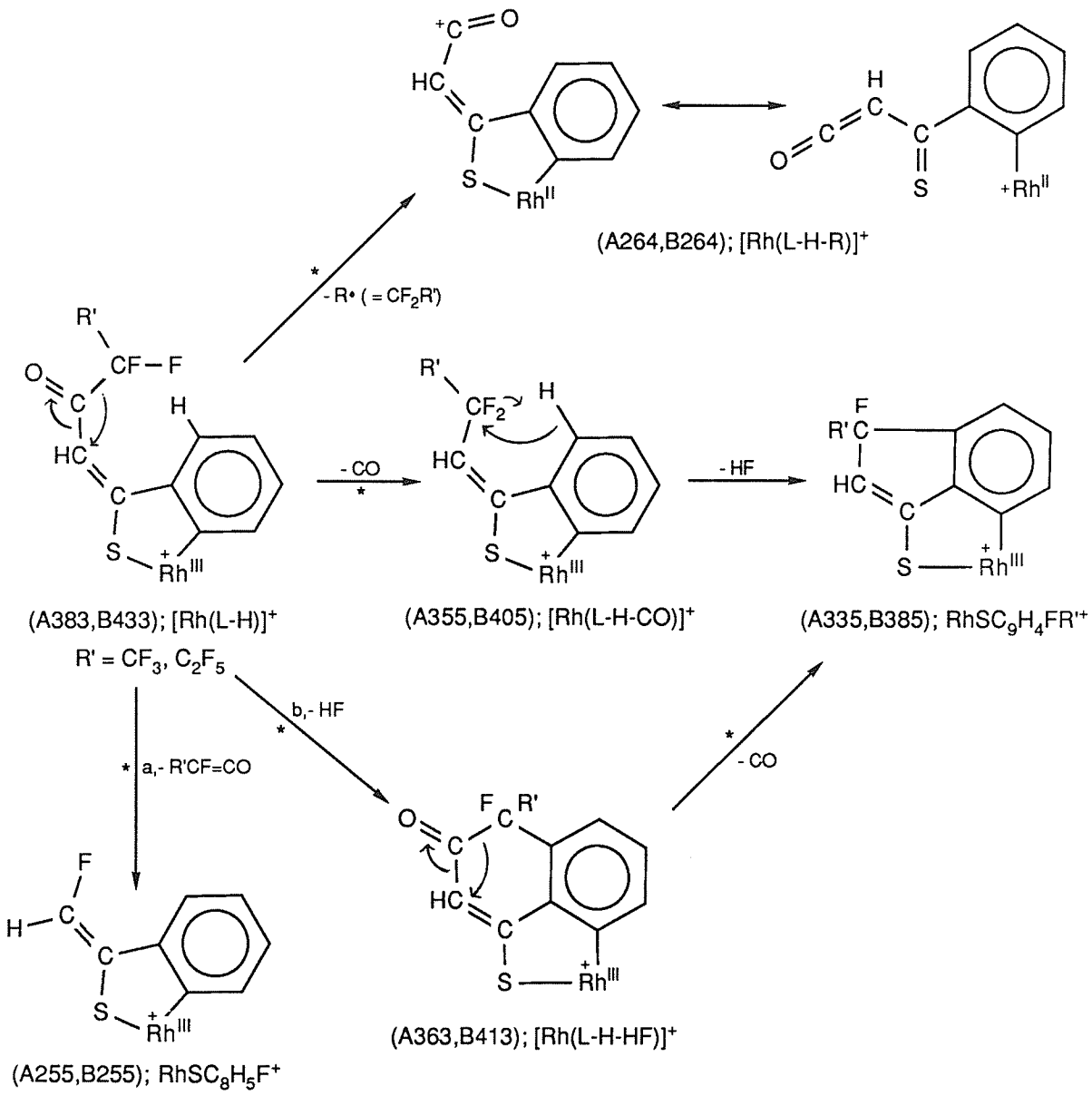
(A264,B264); [Rh(L-H-R)]+
- R• (= CF2R')
(A383,B433); [Rh(L-H)]+
- CO
(A355,B405); [Rh(L-H-CO)]+
- HF
(A335,B385); RhSC9H4FR'+
R' = CF3, C2F5
b,- HF
a,- R'CF=CO
- CO
(A363,B413); [Rh(L-H-HF)]+
(A255,B255); RhSC8H5F+

Scheme 3.15

(%RA = 2.0%). The loss of S from RhL_3^+ is noteworthy because the formation of abundant ionic species in which the Rh-S bond is retained implies strong Rh-S bonds. Sulfur is a soft base (class (b) ligand), which should preferably bond to soft acids (class (b) metals) such as rhodium (especially in a low oxidation state). However, the positive charge on RhL_3^+ formally raises the oxidation state of rhodium to +IV, while the three sulfur atoms compete for rhodium $d\pi$-electrons. Both factors contribute to a decrease in the b-character of rhodium (i.e. increase in acid hardness). The $[RhL(L\text{-}S)]^+$ ion, also present in these spectra, is not formed by loss of S from RhL_2^+ (in which Rh(III) is a softer acid) but by loss of ·L from $[RhL_2(L\text{-}S)]^+$ (Scheme 3.16). Loss of the neutral fragment $[Rh^{II}L(L\text{-}S)]$ from $[Rh(L_2(L\text{-}S)]^+$ giving rise to L^+, **(A281,B331)**, is also observed. Ions corresponding to $[NiL(L\text{-}S)]^+$ in the mass spectra of some trifluoromethyl-substituted monothio-β-ketonenolates of Ni(II) have been observed[75], but this can be ascribed to Ni(II) having less b-character than Rh(III).

The mass spectra of both complexes exibit a metal-free peak corresponding to $[2L\text{-}2S\text{-}COR]^+$, **(A351,B401)**, formed from $[RhL(L\text{-}COR)]^+$, **(A518,B568)**, by loss of RhS_2 (Scheme 3.17). Loss of MetS (Met = metal) has been previously documented in the mass spectra of the trifluoromethyl-substituted monothio-β-ketoenolates of Ni(II), Pd(II), Fe(III), Ru(III), Co(III) and Rh(III)[69,70,76].

C) *$Rh(bzC_2F_5)_3$ and $Rh(bzC_3F_7)_3$*

We have noted above that rhodium-containing ions are much more abundant in the mass spectra of the $Rh(bzC_2F_5)_3$ and

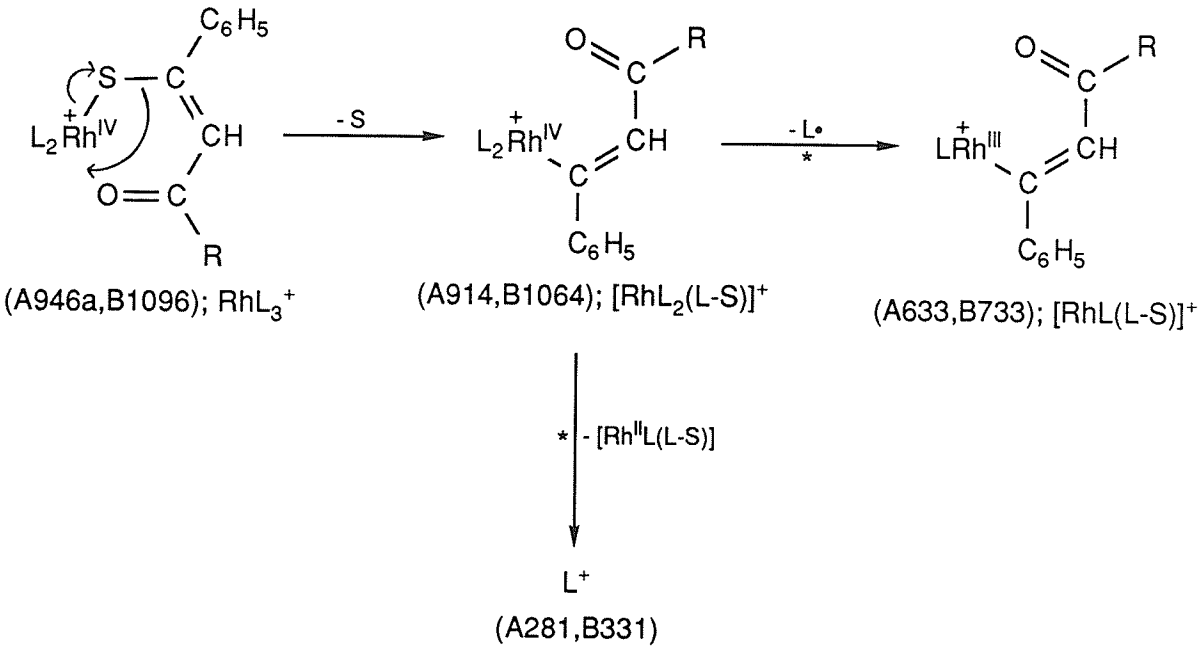

(A946a,B1096); RhL_3^+ (A914,B1064); $[RhL_2(L\text{-}S)]^+$ (A633,B733); $[RhL(L\text{-}S)]^+$

(A281,B331)

Scheme 3.16

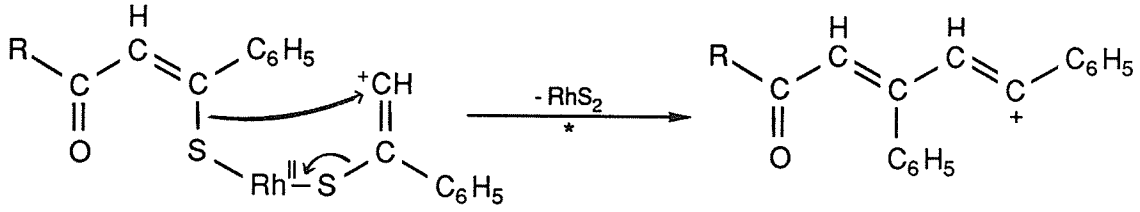

(A518,B568); $[RhL(L\text{-}RCO)]^+$ (A351,B401); $[2L\text{-}2S\text{-}RCO]^+$

Scheme 3.17

$Rh(bzC_3F_7)_3$ than in those of the sulfur-containing analogs $Rh(SbzC_2F_5)_3$ and $Rh(SbzC_3F_7)_3$. This is ascribed to the lower tendency for RhL_3^+ of the former complexes to decompose to L^+.

A major feature of the mass spectra of $Rh(bzC_2F_5)_3$ and $Rh(bzC_3F_7)_3$ is the presence of ion species that must contain a rhodium-phenyl bond. Several precursors have been identified. The proposed reaction mechanisms involve four-membered cyclic transition states (Scheme 3.18). For example, in the reaction RhL_2^+ **(C633,D733)** ---> $LRhC_6H_5^+$ **(C445,D495)**, migration of the phenyl substituent to rhodium involves simultaneous breaking of a rhodium-oxygen bond[77]. (The migration of the phenyl substituent in an analogous ion decomposition of $Rh(SbzC_2F_5)_3$ and $Rh(SbzC_3F_7)_3$ would require rhodium-sulfur bond scission, which would be less facile than rhodium-oxygen bond scission due to strengthening of the rhodium-sulfur bond by $d\pi$-$d\pi$ bonding). These results, involving the migration or non-migration of the phenyl substituent to the metal, are consistent with those found for the mass spectra of various fluorinated palladium(II) monothio-β-ketoenolate and β-ketoenolate chelates[77,79]. A second rhodium-phenyl bond is formed in the reaction $LRhC_6H_5^+$**(C445,D495)** ---> $Rh(C_6H_5)_2^+$ **(C257,D257)**. $LRhC_6H_5^+$ can also decompose by loss of ·L to give $RhC_6H_5^+$, **(C180,D180)** (Scheme 3.18), or by loss of CO to give $[C_6H_5Rh(L\text{-}CO)]^+$, **(C417,D467)**, (Scheme 3.19). In the latter decomposition, the extrusion of CO may be assisted by the formation of a labile Rh-C_F bond, as has been proposed earlier for elimination of CF_2 (Scheme 3.4). This formation of rhodium-phenyl bonds also applies to decomposition of $[RhL(L\text{-}CO)]^+$ **(C605,D705)** to **(C417,D467)**.

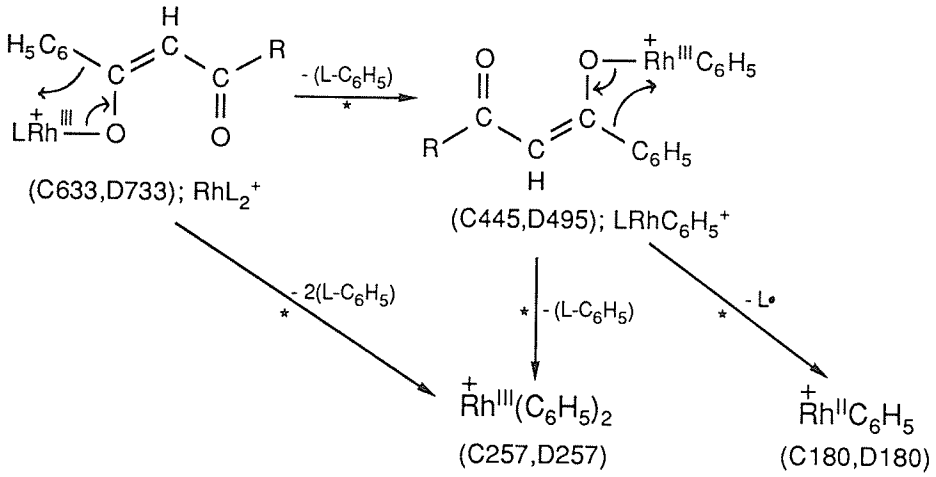

Scheme 3.18

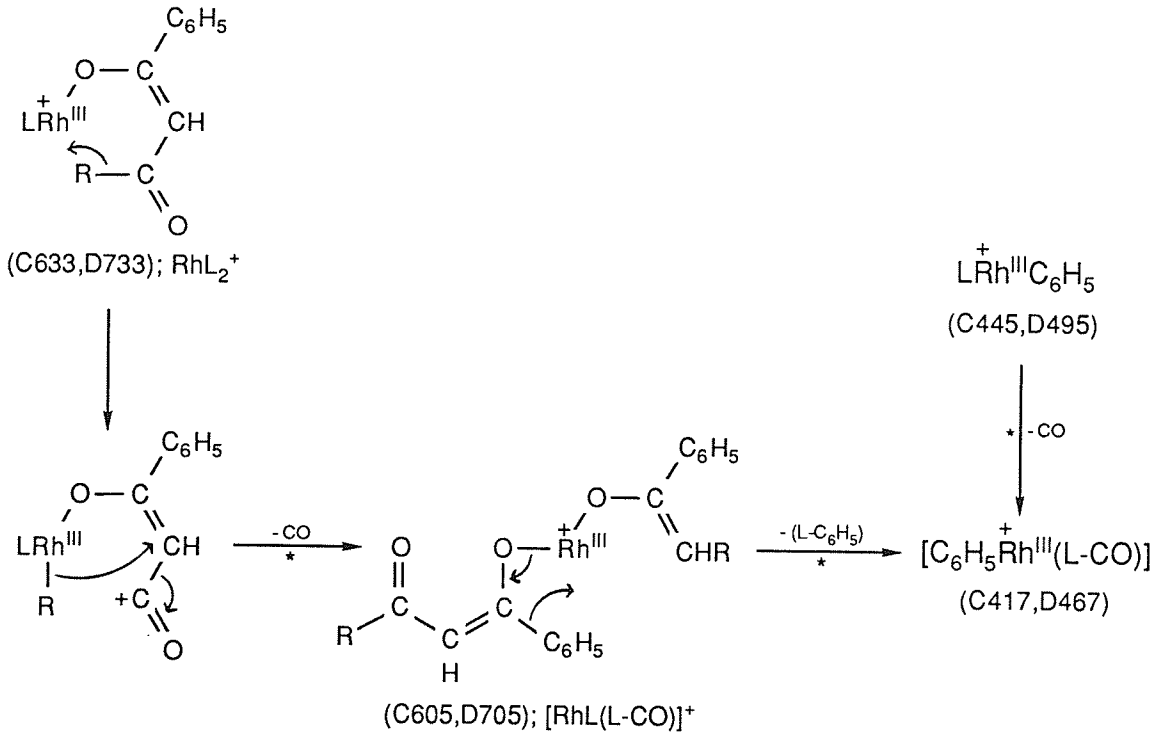

Scheme 3.19

Although not shown, analogous decompositions involving the losses of CO and (L-C_6H_5) from $[RhL(L\text{-}CF_2)]^+$ of $Rh(bzC_2F_5)_3$ are observed, yielding the ions $[Rh(L\text{-}CF_2)(L\text{-}CO)]^+$ and $[C_6H_5Rh(L\text{-}CF_2)]^+$, respectively.

Ion decompositions in FFR1 indicate that $[Rh(L\text{-}COH)]^+$, **(C339,D389)a,b**, has four potential precursors, namely $LRhC_6H_5^+$, **(C445,D495)**, RhL_2^+, **(C633,D733)**, $[C_6H_5Rh(L\text{-}CO)]^+$, **(C417,D467)**, and $[RhL(L\text{-}CO)]^+$, **(C605,D705)**. The latter two precursor ions indicate that formation of **(C339,D389)a,b** from **(C445,D495)** or **(C633,D733)** is a two-step process involving loss of CO followed by losses of C_6H_6 from **(C417,D467)** and LH from **(C605,D705)**, respectively. The origin of the hydrogen atom transferred in these reactions was established by deuteration of the central carbon atom of the ligand. This revealed that, for $Rh(bzC_2F_5)_3$, there are competing reactions in which the transferred hydrogen atom originates from both phenyl substituent (*ca* 67%) and from the bridging carbon (*ca* 33%). Mechanisms are proposed in Schemes 3.20 and 3.21.

Hydrogen transfer also occurs in the formation of $HRhL^+$, a major ion species observed for $Rh(bzC_2F_5)_3$ and $Rh(bzC_3F_7)_3$. For the deuterated analogue of $Rh(bzC_2F_5)_3$, incorporation of a phenyl hydrogen into $HRhL^+$, **(C369,D419)**, is the more prominent (*ca* 71%) reaction, for which the mechanism in Scheme 3.22, similar to that suggested for the formation of $HMetL^+$, where Met = Co(II), Ni(II) and Cu(II), from the molecular ion[77,80], has been proposed for its formation from RhL_2^+, **(C633,D733)**. It requires both carbonyl groups of the ligand to play a major role. Analogous mechanisms

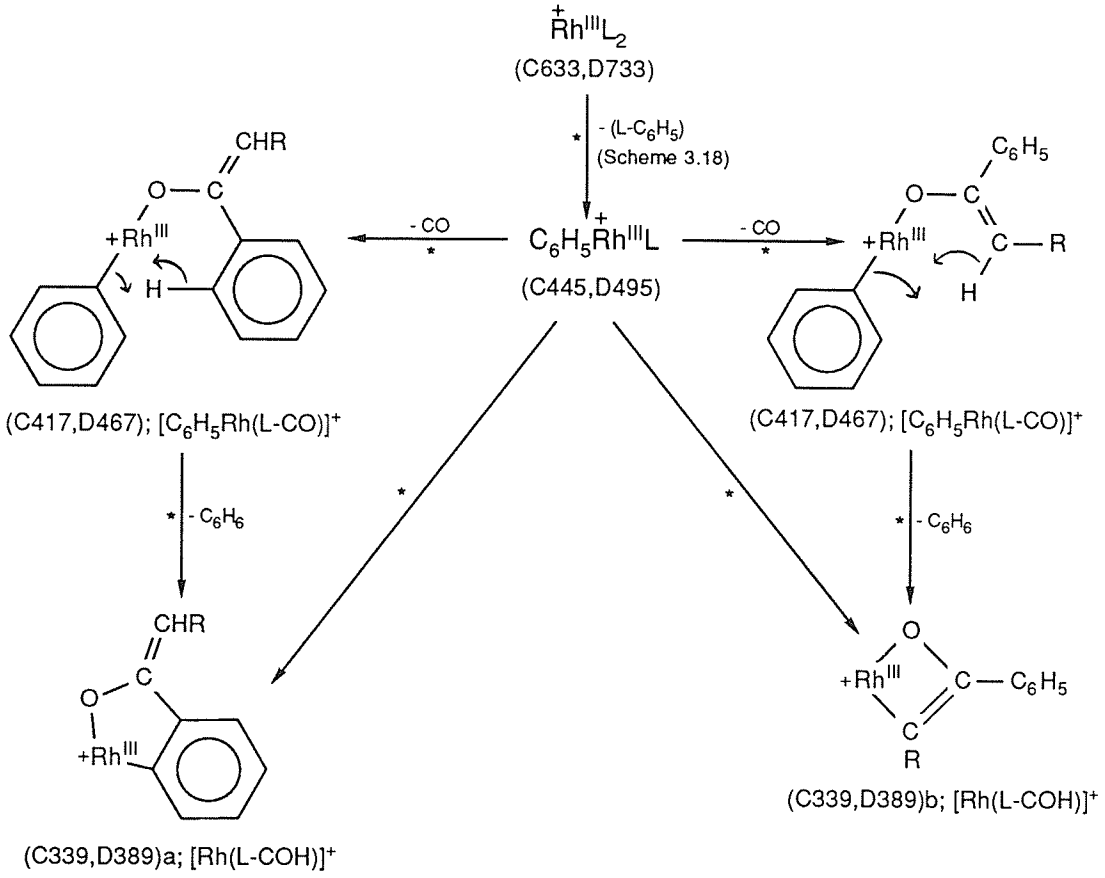

Scheme 3.20

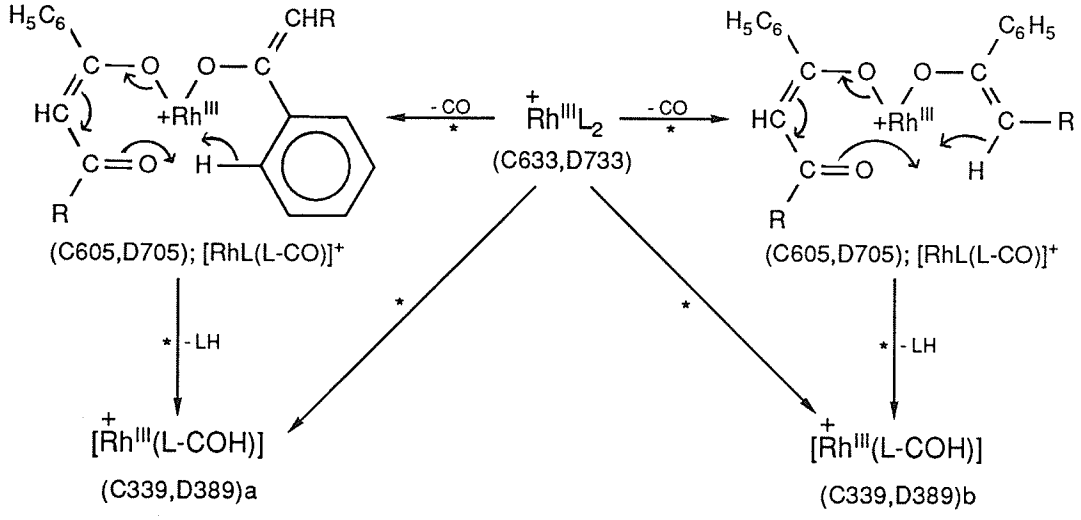

Scheme 3.21

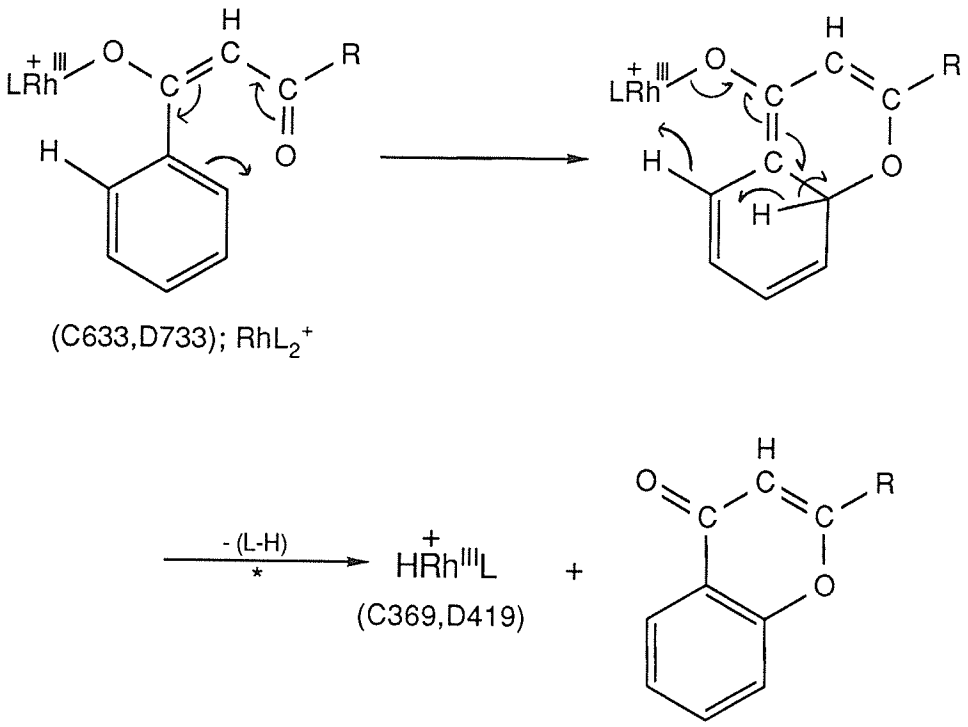

Scheme 3.22

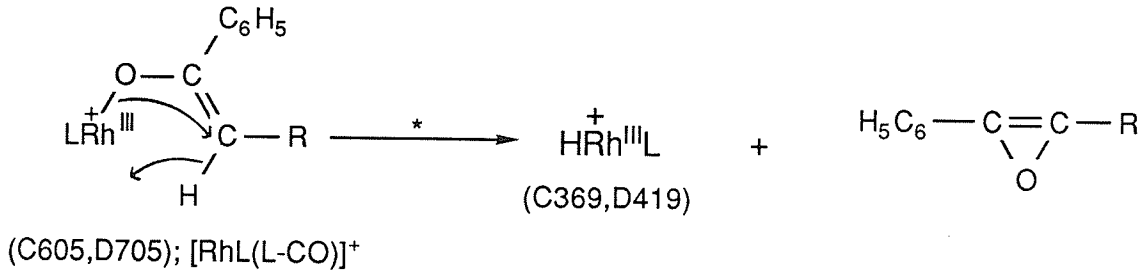

Scheme 3.23

(not shown) can be proposed for the formation of $HRhL^+$ and $[HRh(L\text{-}CF_2)]^+$ from $[RhL(L\text{-}CF_2)]^+$. Formation of $RhLH^+$ from RhL_2^+ *via* hydrogen transfer from the bridging carbon of one ligand to the oxygen atom of the other can be ruled out because $[Rh(L\text{-}H)]^+$, a major product ion associated with this reaction pathway[77,80], is not observed in the mass spectra of either complex. For the less prominent reaction (*ca* 29%) we therefore propose an alternative precursor, $[RhL(L\text{-}CO)]^+$, **(C605,D705)**, identified from ion decompositions in FFR1. The mechanism of Scheme 3.22 is based on the premise that if one of the carbonyl groups is missing then migration of a phenyl hydrogen to the rhodium atom, according to Scheme 3.22, can no longer occur. The only alternative is for the hydrogen to come from the bridging carbon atom (Scheme 3.23). This mechanism simply involves the migration of the bridging hydrogen to the rhodium atom with subsequent loss of the neutral fragment $C_6H_5\dot{C}=\overline{CR}\dot{O}$.

The second most abundant ion in the mass spectra of both $Rh(bzC_2F_5)_3$ and $Rh(bzC_3F_7)_3$ is $HRhC_6H_5^+$. Despite a lack of supporting evidence from metastable ion decompositions, the two main sources are probably $C_6H_5RhL^+$ and $HRhL^+$.

D) *Labelling Results*

The formation of many of the ions observed in the mass spectra of all four complexes discussed in this section involve hydrogen transfer. The origin of the hydrogen transferred in these reactions was determined by deuterium labelling at the chelate ring middle carbon of $Rh(SbzC_2F_5)_3$ and $Rh(bzC_3F_7)_3$. Results were interpreted

with the aid of the computer program, Isotope Cluster Examiner (ICE)[81], designed specifically to help in the analysis of mass spectral data. Using this program one can tabulate the theoretical isotope cluster pattern for any fragment ion and calculate its relative contribution to the group of overlapping clusters of interest in the experimental spectrum.

Complete deuteration of the complex under study usually does not occur and therefore various amounts of the complex with zero to three labelled ligands may be present (i.e. RhL_3-d_3 to RhL_3-d_0). The total labelling achieved can be determined from the mass spectrum of the mixture by simply subtracting the theoretical isotope cluster of each possible molecular ion, $[RhL_3\text{-}d_3]^+$ to $[RhL_3\text{-}d_0]^+$, from the experimental isotope cluster (see Tables 3.3 and 3.4).

The cluster of peaks occurring between m/z 383 and 387 in the mass spectrum of the labelled complex $Rh(SbzC_2F_5)_3$ is caused by overlap of the ions shown in Table 3.5. The program ICE revealed that the ion $[RhL_D\text{-}H]^+$ accounts for 63.66% and $[RhL_D\text{-}D]^+$ plus $[RhL_H\text{-}H]^+$ to the remainder of the experimental cluster (L_D = deuterated ligand, L_H = protiated ligand). Any remaining contribution can be attributed to the presence of small amounts of RhL_H^+, $HRhL_H^+$ and their deuterated analogues. From the observed molecular ion isotope cluster pattern, one can deduce that the total labelling achieved was 66.35%. Therefore, 66.35-63.66 = 2.69% of the total ion intensity of the cluster is due to the ion $[RhL_D\text{-}D]^+$. From this we can conclude that (63.66/66.35) x 100 = 95.95% of the hydrogen lost in the formation of the ion $[RhL\text{-}H]^+$ originates from the phenyl substituent and 4.05% from the bridging carbon atom.

Table 3.3 Relative contribution (%) of the ions $[RhL_3\text{-}d_0]^+$ to $[RhL_3\text{-}d_3]^+$, to the observed molecular ion isotope cluster pattern in the mass spectrum of $Rh(SbzC_2F_5)_3$ (labelled).

m/z	RhL_3^+ (Expt.)	$[RhL_3\text{-}d_0]^+$	$[RhL_3\text{-}d_1]^+$	$[RhL_3\text{-}d_2]^+$	$[RhL_3\text{-}d_3]^+$	Remaining Intensity
946	8.34	100.00	-	-	-	-
947	44.52	39.71	100.00	-	-	-
948	100.00	21.59	39.70	100.00	-	-
949	98.03	5.96	21.58	39.68	100.00	-
950	43.39	1.71	5.96	21.58	39.67	0.84
951	19.10	0.33	1.70	5.96	21.57	1.37
952	5.88	-	0.33	1.70	5.95	1.01
953	-	-	-	0.33	1.70	-1.23
954	-	-	-	-	0.33	-0.19
		4.44%	**21.97%**	**43.63%**	**29.94%**	

Total labelling achieved = 21.97/3 + (43.63)2/3 + 29.94 = **66.35%**

Table 3.4 Relative contribution (%) of the ions $[RhL_3\text{-}d_0]^+$ to $[RhL_3\text{-}d_3]^+$, to the observed molecular ion isotope cluster pattern in the mass spectrum $Rh(bzC_2F_5)_3$ (labelled).

m/z	RhL_3^+ (Expt.)	$[RhL_3\text{-}d_0]^+$	$[RhL_3\text{-}d_1]^+$	$[RhL_3\text{-}d_2]^+$	$[RhL_3\text{-}d_3]^+$	Remaining Intensity
898	30.51	100.00	-	-	-	-
899	75.72	37.44	100.00	-	-	-
900	100.00	8.02	37.43	100.00	-	-
901	69.86	0.91	8.02	37.41	100.00	-
902	29.81	-	0.90	8.01	37.40	9.53
903	9.17	-	-	0.90	8.01	5.55
904	-	-	-	-	0.90	0.34
		14.86%	**31.32%**	**35.80%**	**17.99%**	

Total labelling achieved = 31.32/3 + (35.80)2/3 + 17.99 = **52.30%**

Table 3.5 Relative contribution (%) of the ions $[RhL_H\text{-}H]^+$ and $[RhL_D\text{-}H]^+$ to the observed cluster pattern occurring between m/z 383 and m/z 387 in the mass spectrum of $Rh(SbzC_2F_5)_3$ (labelled).

m/z	%RA(Expt.) Normalized	$[RhL_H\text{-}H]^+$ $[RhL_D\text{-}D]^+$	$[RhL_D\text{-}H]^+$	Remaining Intensity
383	53.06	100.00	-	-
384	100.00	13.22	100.00	-
385	20.19	5.44	13.21	5.02
386	8.04	0.59	5.44	2.66
387	2.06	-	0.59	1.51
		36.34%	**63.66%**	

Table 3.6 Relative contribution (%) of the ions $RhC_6H_5^+$, $HRhC_6H_5^+$ and $DRhC_6H_5^+$ to the observed cluster pattern occurring between m/z 180 and m/z 184 in the mass spectrum of $Rh(bzC_2F_5)_3$ (labelled).

m/z	%RA(Expt.) Normalized	$RhC_6H_5^+$	†$HRhC_6H_5^+$	$DRhC_6H_5^+$	Remaining Intensity
180	23.59	100.00	-	-	-
181	100.00	6.79	100.00	-	-
182	24.14	0.19	6.79	100.00	-
183	2.75	-	0.19	6.79	1.38
184	-	-	-	0.19	-0.04
		16.92%	**75.59%** **(84.98)**	**12.48%** **(15.02)**	

† Hydrogen retained can be from a labelled or unlabelled parent ion.

The cluster of peaks occurring between m/z 180 and 184 in the mass spectrum of labelled $Rh(bzC_2F_5)_3$ arises from the overlap of the ions shown in Table 3.6. Once again, the ICE program reveals that the ions $RhC_6H_5^+$, $HRhC_6H_5^+$ and $DRhC_6H_5^+$, account for 16.92, 75.59 and 12.48%, respectively, of the experimental pattern. While the only possible source of the latter ion can be a labelled parent, the former ion can be formed from either labelled or unlabelled parents. The origin of the hydrogen transferred from the labelled parent must be the phenyl substituent. According to the observed molecular ion isotope cluster pattern the total labelling achieved was 52.30%. Therefore, 52.30-15.02 = 37.28% of the combined $HRhC_6H_5^+$ and $DRhC_6H_5^+$ ion abundance can be attributed to the former ion, where the origin of the hydrogen transferred in the reaction is the phenyl group. We can conclude therefore, that in the mass spectrum of $Rh(bzC_2F_5)_3$, [37.28/(37.28+15.02)] x 100 = 71.28% of the hydrogen retained in $HRhC_6H_5^+$ originates from the phenyl substituent and 28.72% from the bridging carbon atom of its precursor ion(s). The results of all labelling experiments are presented in Table 3.7.

3.1.2 ^{19}F NMR studies

A) *$Rh(SbzC_2F_5)_3$*

The ^{19}F NMR spectrum of $Rh(SbzC_2F_5)_3$, recorded in acetone (Figure 3.9), consists of only two absorptions, both appearing as singlets, with no evidence for vicinal or geminal couplings (i.e. J < 1.0 Hz). The absorptions at -81.38 ± 0.01 ppm (relative intensity = 3) and at -119.41 ± 0.01 ppm (relative intensity = 2) must be assigned to the fluorine atoms of the CF_3 and CF_2 groups, respectively.

Table 3.7 Source (%) of hydrogen transferred in the formation of the indicated ions for the complexes $Rh(SbzC_2F_5)_3$ and $Rh(bzC_2F_5)_3$.

	Ion species	Lost from ion		Retained in ion	
		phenyl	chelate ring	phenyl	chelate ring
$Rh(SbzC_2F_5)_3$	$[Rh(L-H)]^+$	~96	~4		
	$[Rh(L-H-CF_2)]^+$	~96	~4		
	$[SRh(L-H)]^+$	~84	~16		
	$[SRhL+H]^+$			~31	~69
$Rh(bzC_2F_5)_3$	$[Rh(L-HCO)]^+$	~67	~33		
	$HRhL^+$			~71	~29
	$HRhC_6H_5^+$			~71	~29
	$[HRh(CO)(C_6H_5)]^+$			~70	~30

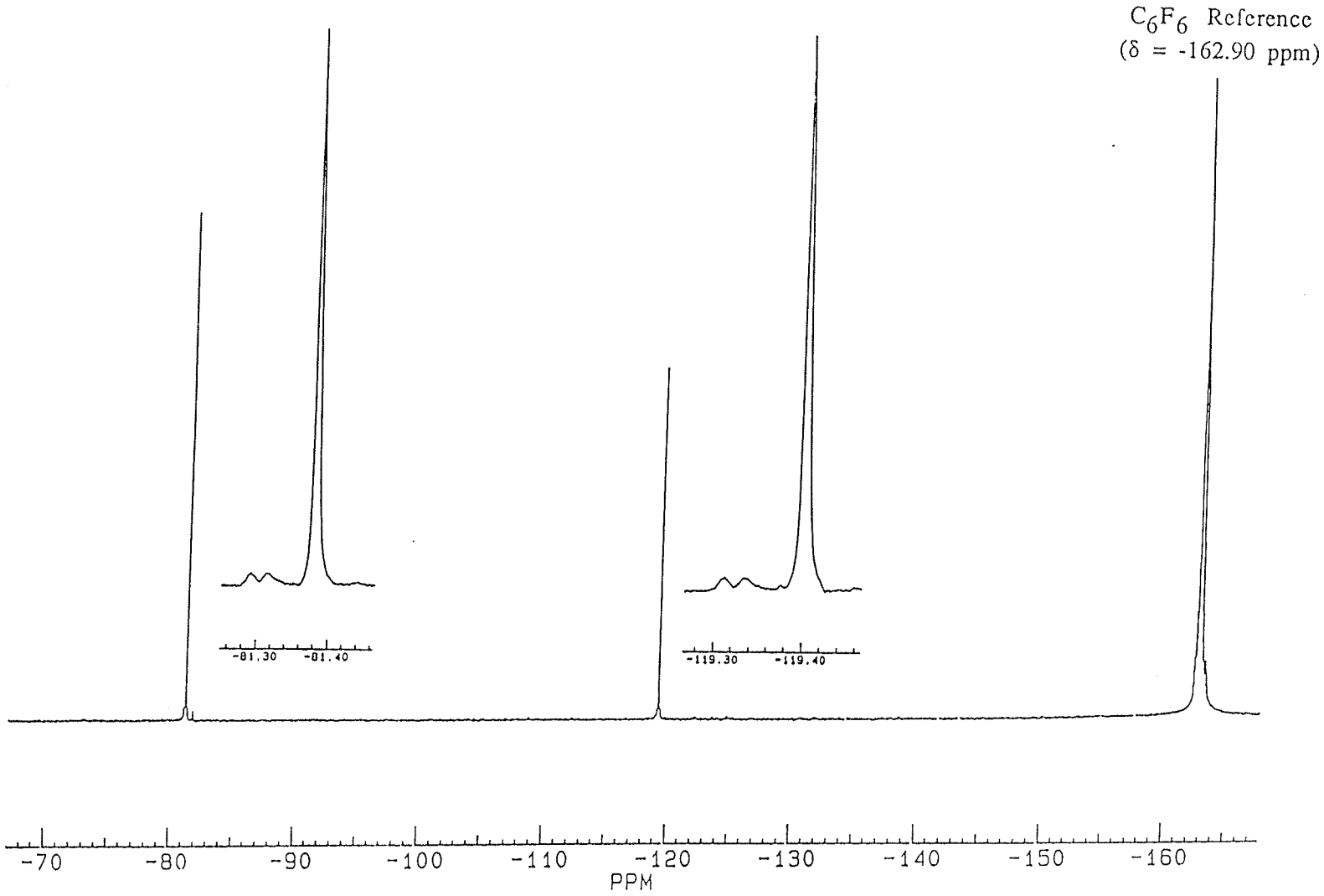

Figure 3.9 $\{^1H\}^{19}F$ NMR spectrum of $Rh(SbzC_2F_5)_3$ recorded at 282.38 MHz in acetone at room temperature.

B) *$Rh(SbzC_3F_7)_3$*

The ^{19}F NMR spectrum of $Rh(SbzC_3F_7)_3$ shows three major absorptions appearing as a triplet, a quintet and a singlet, with relative intensities of 3:2:2, respectively (Figure 3.10). The triplet must be assigned to the fluorine atoms of the CF_3 group and the singlet to those of the β-CF_2 group since vicinal couplings between the latter fluorines and those of the CF_3 and α-CF_2 groups are expected, on the basis of the earlier discussion (see Section 1.6), to be about zero. The quintet, with peak intensity ratios of 1.01:4.02:6.02:4.01:1.00, is associated with two outer sets of four low intensity peaks, and is assigned to the fluorines of the α-CF_2 group. The triplet plus quintet splitting pattern is consistent with a special case of an ABX_3 spin system that arises as follows. (In the general case for this spin system, the AB part of the spectrum consists of sixteen resolved peaks corresponding to four AB-type sub-spectra of relative intensities 1:3:3:1, each with the same value of J_{AB}, but with effective chemical shift differences given by $\delta^*_{AB} = \delta_{AB} + m_X(J_{AX} - J_{BX})$, where m_X ($= \pm 1/2, \pm 3/2$) is the resultant nuclear spin of the X_3 nuclei. The repeated spacings between the AB spectra are equal to $(J_{AX} + J_{BX})/2$. The X_3 part consists of fourteen resolved peaks, of which two, together containing half the total intensity of the X_3 region, are always separated by $J_{AX} + J_{BX}$[82].) When $J_{AX} = J_{BX}$ the X_3 part collapses to a symmetrical 1:2:1 triplet with spacings equal to J_{AX}. The repeated spacings between the AB sub-spectra now equal J_{AX} and the effective chemical shift differences all equal δ_{AB}. The eight strong central peaks of the four AB sub-spectra can only collapse to the observed 1:4:6:4:1 quintet if $\Delta = J_{AX}$, where Δ is the

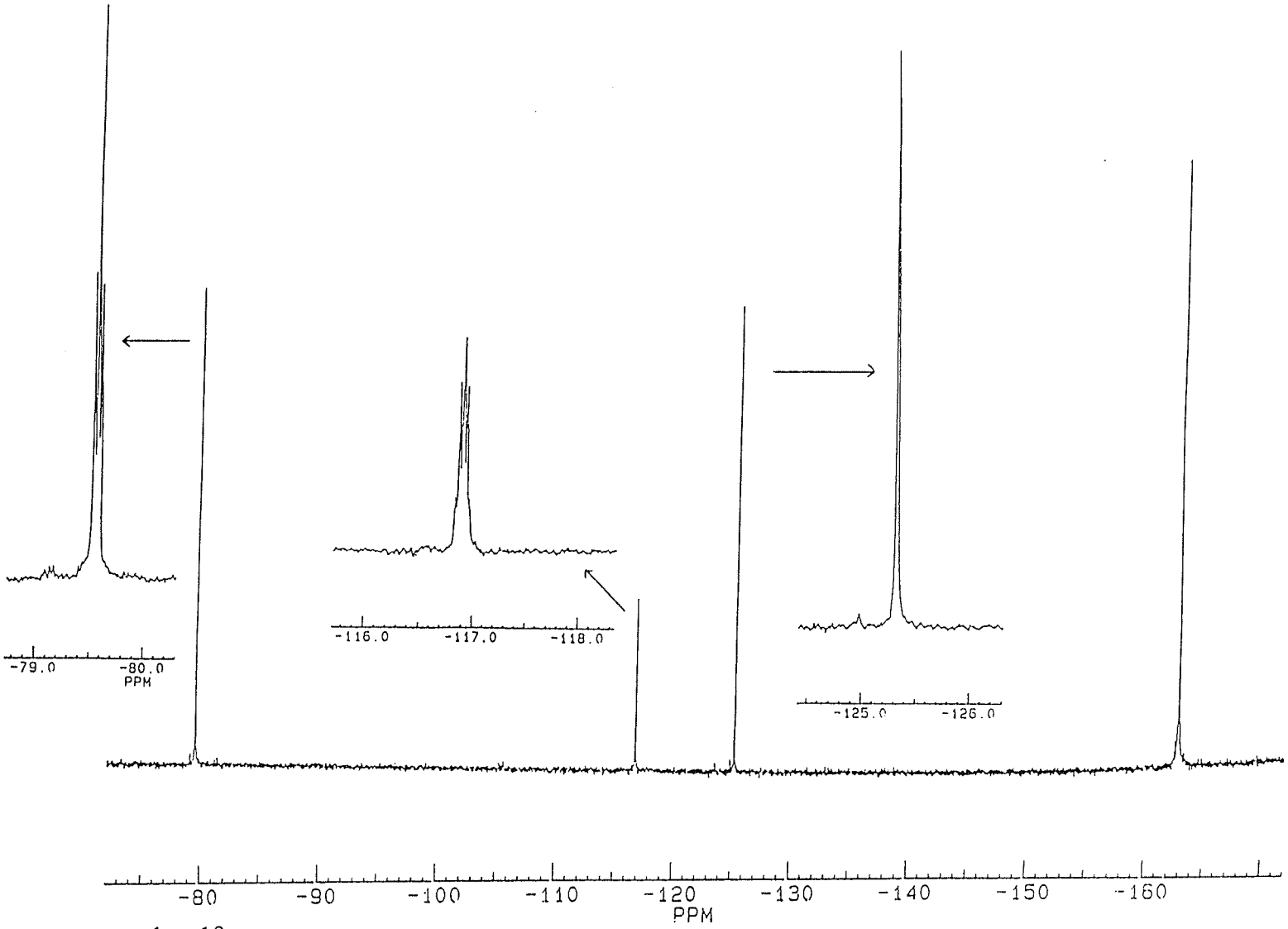

Figure 3.10 $\{^1H\}^{19}F$ NMR spectrum of $Rh(SbzC_3F_7)_3$ recorded at 282.35 MHz in acetone at room temperature.

common separation between the central peaks of the AB sub-spectra. The remaining eight peaks are assigned to the low intensity outer peaks, with spacings equal to J_{AX}. The AB portion of the experimental spectrum is compared with a computer simulated spectrum, generated with the program Numarit[83], in Figure 3.11. The input parameters δ_A, δ_B, δ_X, J_{AB}, J_{AX}, J_{BX} and linewidth were adjusted until the best match between the X_3 and AB regions of the experimental and simulated spectra was obtained. The resulting NMR parameters are presented in Table 3.8.

The NMR spectra of both sulfur-containing complexes support a *facial* octahedral geometry, for which the perfluoroalkyl groups are necessarily equivalent owing to the presence of a C_3 symmetry axis. In contrast, for a *meridional* configuration, which lacks the C_3 axis, there would be three sets of absorptions, one set for each type of perfluoroalkyl group (see Section 1.7). A *facial* octahedral geometry for these complexes agrees with our structure determination of $Rh(Stfa)_3$[61] (see Section 3.2.3) and is consistent with structures of various other *tris*(monothio-β-ketoenolate)rhodium(III) complexes[84,85]. Preference for the *facial* structure has been explained by better d_π-d_π bonding between the rhodium and sulfur atoms when the three rhodium-sulfur bonds are mutually perpendicular. Also, the relatively short S----S distances (less than twice the van der Waals radius of sulfur) in various monothio-β-ketoenolate metal complexes[61,86], suggest the presence of weak non-bonding interactions between these atoms.

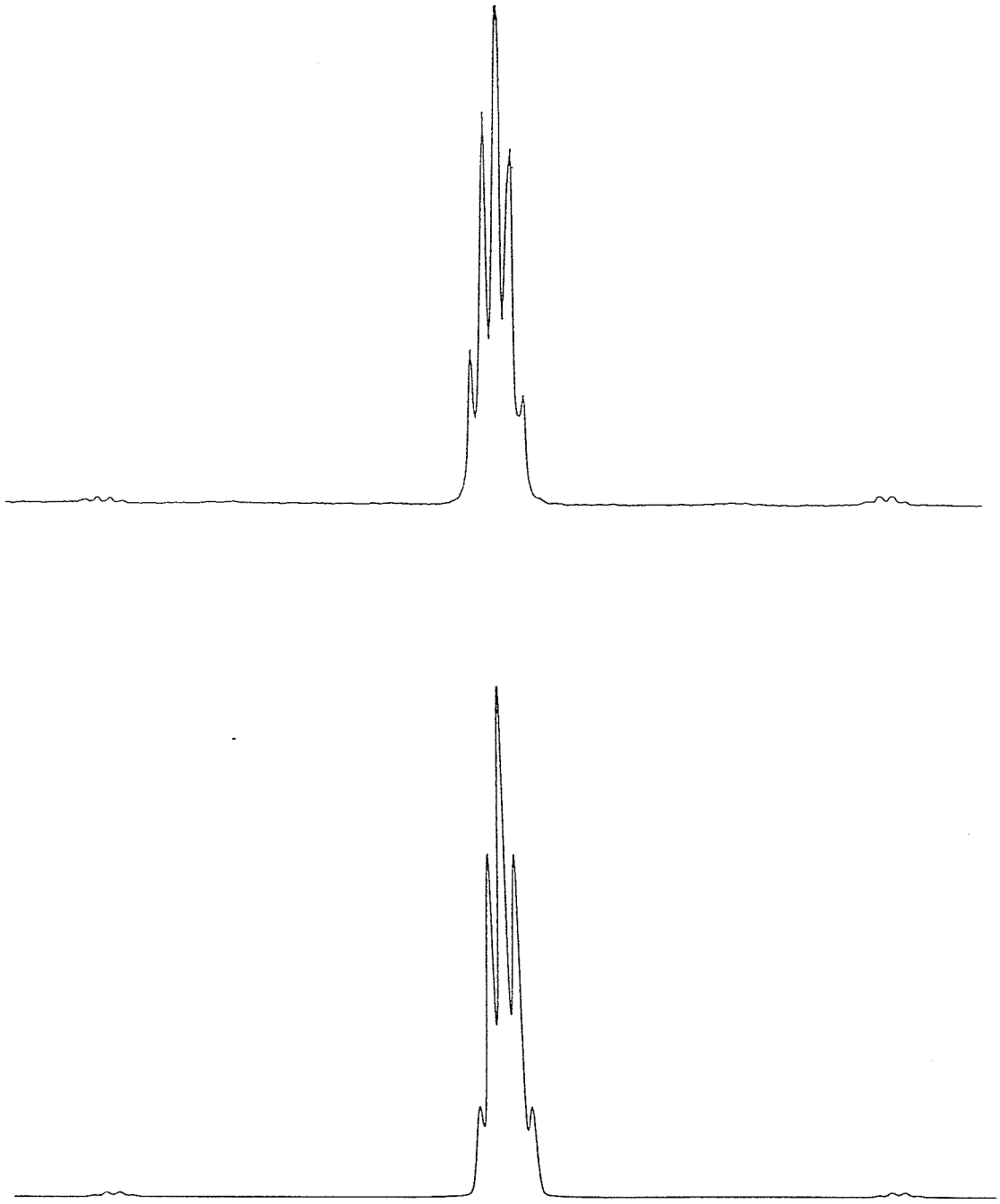

Figure 3.11 Comparison between experimental (upper) and computer simulated (lower) AB parts of the $\{^1H\}^{19}F$ NMR spectrum of $Rh(SbzC_3F_7)_3$.

Table 3.8 Peak positions and relative intensities in the simulated $\{^1H\}^{19}F$ NMR spectrum of $Rh(SbzC_3F_7)_3$ in acetone at room temperature.

Input parameters: δ_X = -79.55, δ_A = -116.781, δ_B = -117.041 ppm; $J_{AX} = J_{BX}$ = 8.9, J_{AB} = 270.0, LW = 6.0 Hz.

(a) CF_3 (X_3) and β-CF_2 spectral regions.

	ppm	Int.	ppm	Int.	ppm	Int.
CF_3	-79.52	11.980	-79.55	24.000	-79.59	12.020
β-CF_2	-125.34	32.000	-	-	-	-

(b) α-CF_2 (AB) spectral region.

	A				B			
	ppm	Int.	ppm	Int.	ppm	Int.	ppm	Int.
AB sub-spec 1	-115.890	0.035	-116.846	1.970	-116.881	1.970	-117.837	0.035
AB sub-spec 2	-115.922	0.105	-116.878	5.900	-116.913	5.900	-117.869	0.105
AB sub-spec 3	-115.953	0.105	-116.910	5.890	-116.944	5.890	-117.901	0.105
AB sub-spec 4	-115.985	0.035	-116.941	1.960	-116.976	1.960	-117.932	0.035

Note:
(i) The total signal intensity for one fluorine = 16

(ii) With the exception of δ_X, all optimized experimental parameters of this ABX_3 spin system are determined from the best simulation of the AB spectral region. The input parameter, δ_X, is simply its measured experimental value, determined from the central peak of the observed triplet. The positions of the outer peaks are calculated from the optimized values of J_{AX} and J_{BX} in the AB spectral region. The uncertainties involved in the peak positions of both the CF_3, and β-CF_2 group fluorines therefore correspond to their experimental uncertainties (0.01 ppm).

(iii) The uncertainties in the NMR parameters, estimated by noting how much variation in the input parameters is possible before a noticeable difference between simulated and experimental spectra in the AB region occurred, are 0.002 ppm for chemical shifts and 0.3 Hz for coupling constants. These uncertainties are less than the experimental uncertainties.

C) *Rh(bzC$_2$F$_5$)$_3$*

The ^{19}F NMR spectra of Rh(bzC$_2$F$_5$)$_3$, recorded in acetone (Figure 3.12) and toluene (Figure 3.13), show two sets of peaks, one set (relative intensity = 3) between -81.65 and -82.10 ppm (acetone) or between -82.20 and -82.60 ppm (toluene), and the other set (relative intensity = 2) between -117.20 and -119.80 ppm (acetone) or -118.20 and -120.60 ppm (toluene). These must be assigned to the fluorines of the CF_3 and CF_2 groups, respectively. In both solvents, the first set contains four major absorptions and a number of minor peaks, while the second set contains at least six major absorption peaks in acetone, seven in toluene, and a number of minor peaks. The minor peaks are assigned to impurities that could not be removed by using techniques such as column chromatography and fractional sublimation, despite several attempts. These observations can be understood by recalling that these complexes can exist as *fac* and *mer* isomers, with the *mer* isomer being statistically three times more probable than the *fac* isomer (see Section 1.7). However, for kinetic or thermodynamic reasons, the complexes may not be formed in these proportions and, in extreme cases, one may be formed exclusively (as, in fact, noted above for formation of the *fac* isomer of the monothio complexes). The perfluoroalkyl groups of the *fac* isomer are necessarily equivalent by symmetry but those of the *mer* isomer are non-equivalent, i.e. one of the three perfluoroacyl residues is *trans* to a benzoyl residue, while the other two are *trans* to each other but not equivalent by symmetry. The existence of four major peaks in the CF_3 (X_3) region indicates that both *fac* and *mer* isomers are present in solution.

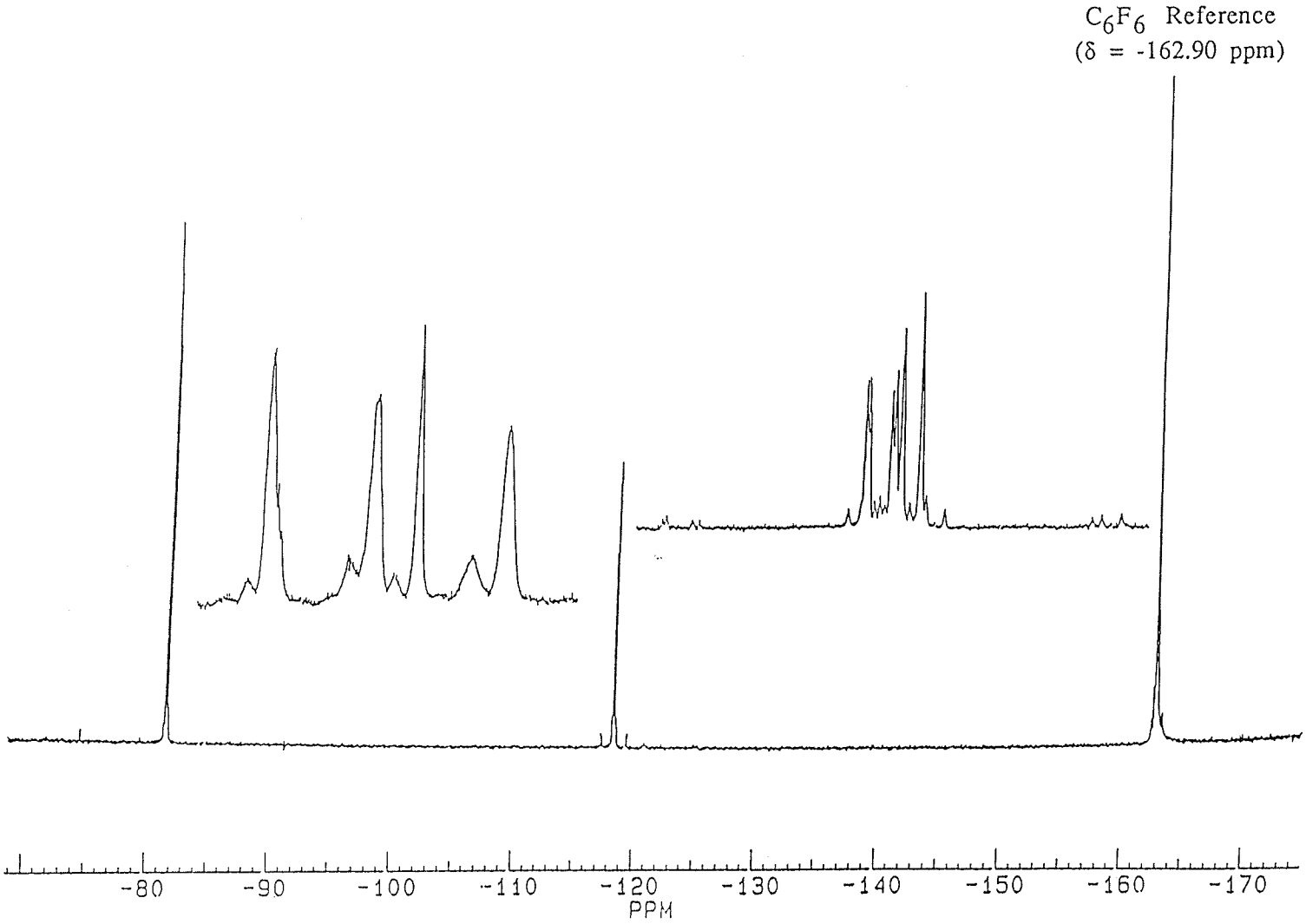

Figure 3.12 $\{^1H\}^{19}F$ NMR spectrum of $Rh(bzC_2F_5)_3$ recorded at 282.35 MHz in acetone at room temperature.

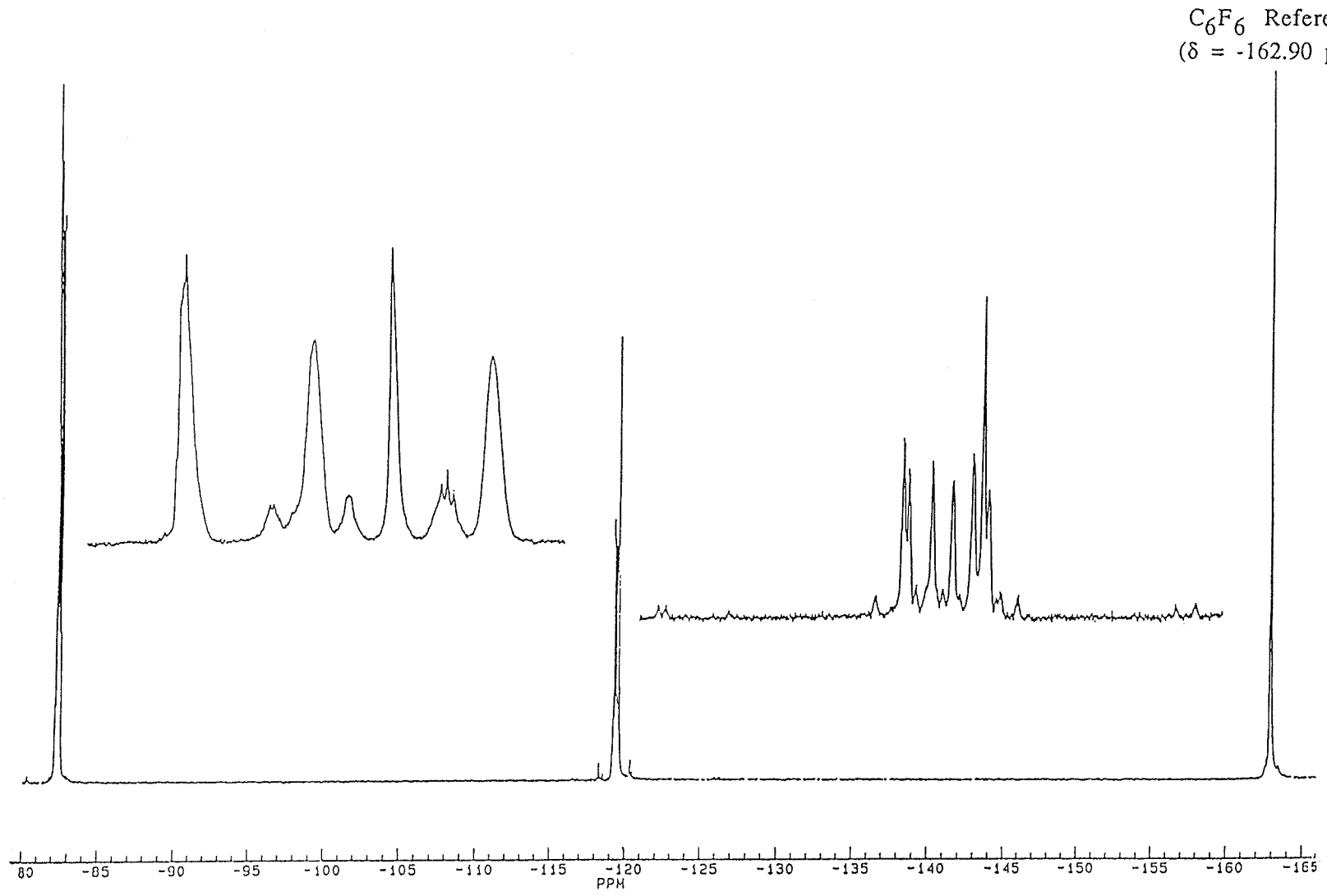

Figure 3.13 $\{^1H\}^{19}F$ NMR spectrum of $Rh(bzC_2F_5)_3$ recorded at 282.35 MHz in toluene at room temperature.

Three of these peaks, which are necessarily of equal intensity, may be assigned to the *mer* isomer and the fourth to the *fac* isomer. The relative areas of the shaded parts of the peaks (Figure 3.14), from low to high field, are 1.05:1.01:0.85:1.00 (acetone) and 1.05:1.00:0.85:1.01 (toluene). These results suggest that the third peak (counting from low field) can be assigned to the *fac* isomer, even though the intensities of the three remaining peaks (assigned to the *mer* isomer) are not exactly equal (due probably to interference from impurities).

Although no splitting of the four absorptions is apparent, the peak widths differ. Thus, for the spectrum recorded in acetone solution, the full width at half maximum height (FWHM) values are ~ 4.0, 4.7, 2.0 and 5.0 Hz, for the X_3 absorptions from low to high field, respectively. These widths place upper limits on the value of $J_{AX} + J_{BX}$ in each case. By noting that the FWHM value for the C_6F_6 absorption used for calibration is ~ 2 Hz then we find the respective values of $J_{AX} + J_{BX}$ to be ~ 2.0, 2.7, 0.0 and 3.0 Hz. If, in addition, $J_{AX} = J_{BX}$ then J_{AX} ~ 1.0, 1.4, 0.0 and 1.5 Hz, respectively. Based on the earlier discussion, these small coupling constants are as expected for coupling between vicinal fluorines.

In view of the foregoing, the CF_2 region of the spectrum, recorded in both solvents, should be interpreted as the AB parts of four ABX_3 spectra with small, or near zero, J_{AX} and J_{BX} coupling constants, i.e. approximately as four AB spectra. The presence of small amounts of impurities as well as overlapping of peaks made it impossible to measure accurately the relative intensities of peaks and associate them with a particular isomer. (As noted above, the

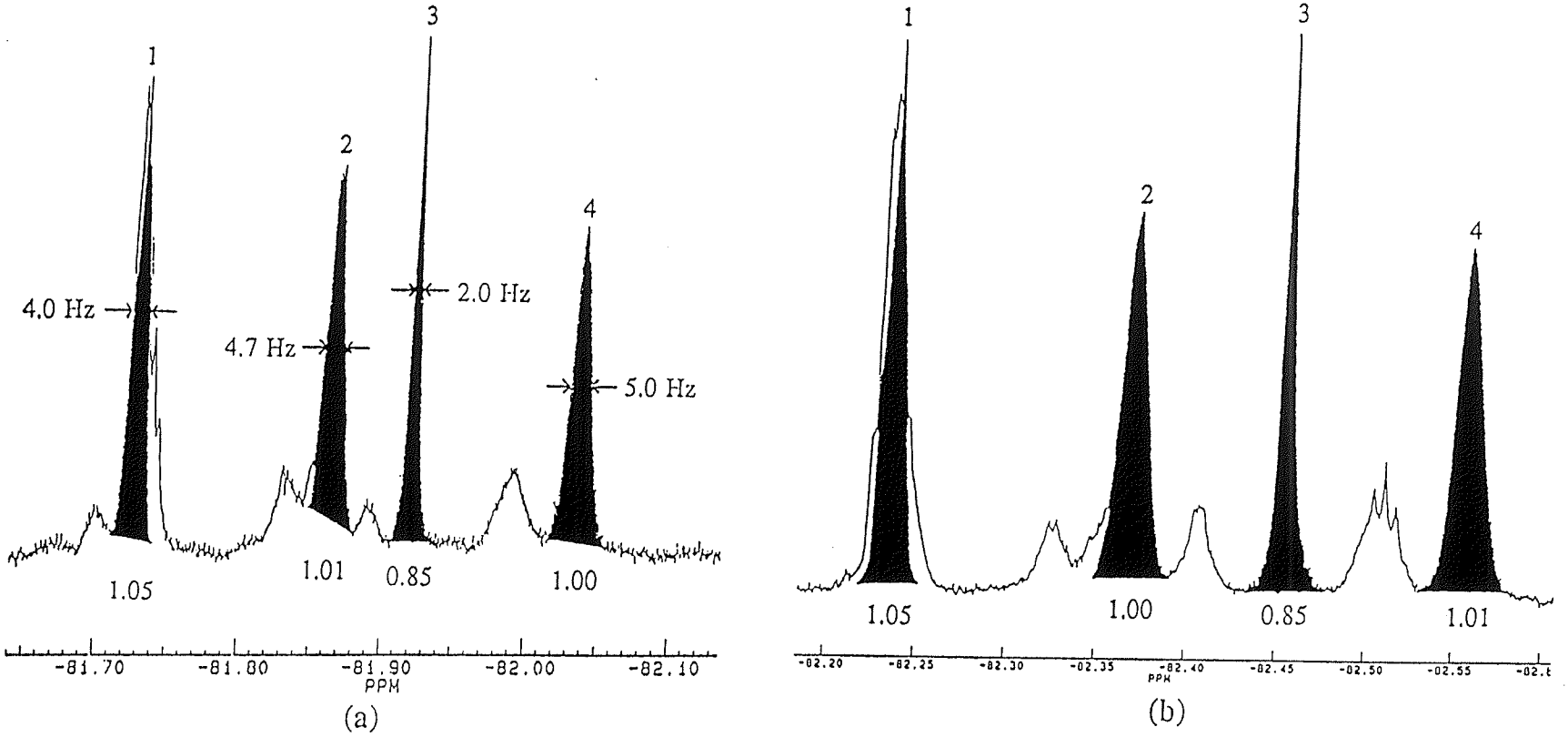

Figure 3.14 CF_3 (X_3) spectral regions of the $\{^1H\}^{19}F$ NMR spectra (with increased digital resolution) of *fac* and *mer* isomers of $Rh(bzC_2F_5)_3$ recorded at room temperature in (a) acetone and (b) toluene at 282.35 and 282.38 MHz, respectively. Relative areas of the peaks are determined from the shaded portions.

intensities of the three absorptions for the *mer* isomer should always be equal and therefore, if one of the four signals is smaller or larger than the other three it must be assigned to the *fac* isomer. If something such as this does not occur then it is not possible to assign signals to a particular isomer.) These AB spectra are therefore simply referred to as 1 to 4 (counting from low field).

Figures 3.15 and 3.16 show expanded views of the AB spectral regions recorded in acetone and toluene, respectively. As before, these spectra were simulated with the Numarit[83] program by using the NMR parameters and linewidth as input parameters that could be adjusted until a good match to the experimental spectrum could be obtained. This program can simulate four ABX_3 spectra but, in its present form, their intensities and linewidths must be equal. (This presents little difficulty in the present case because the four experimental signals for the C_2F_5 groups are of approximately equal intensity.) Comparison between the simulated, and experimental spectra recorded in acetone and toluene, are presented in Figures 3.17 and 3.18, while the NMR parameters and calculated peak positions and intensities are given in Tables 3.9 and 3.10 (spectra recorded in acetone) and Tables 3.11 and 3.12 (spectra recorded in toluene).

By referring to the experimental spectra in Figures 3.15 and 3.16 the results are now summarized. In acetone, the group of peaks between -118.35 and -118.45 ppm arises from partial overlap of the A parts of spectra 1 and 2, while the group between -118.50 and -118.54 ppm is due to partial overlap of the B part of 1 with the A part of 3. The single peak at -118.56 ppm, is actually the result of

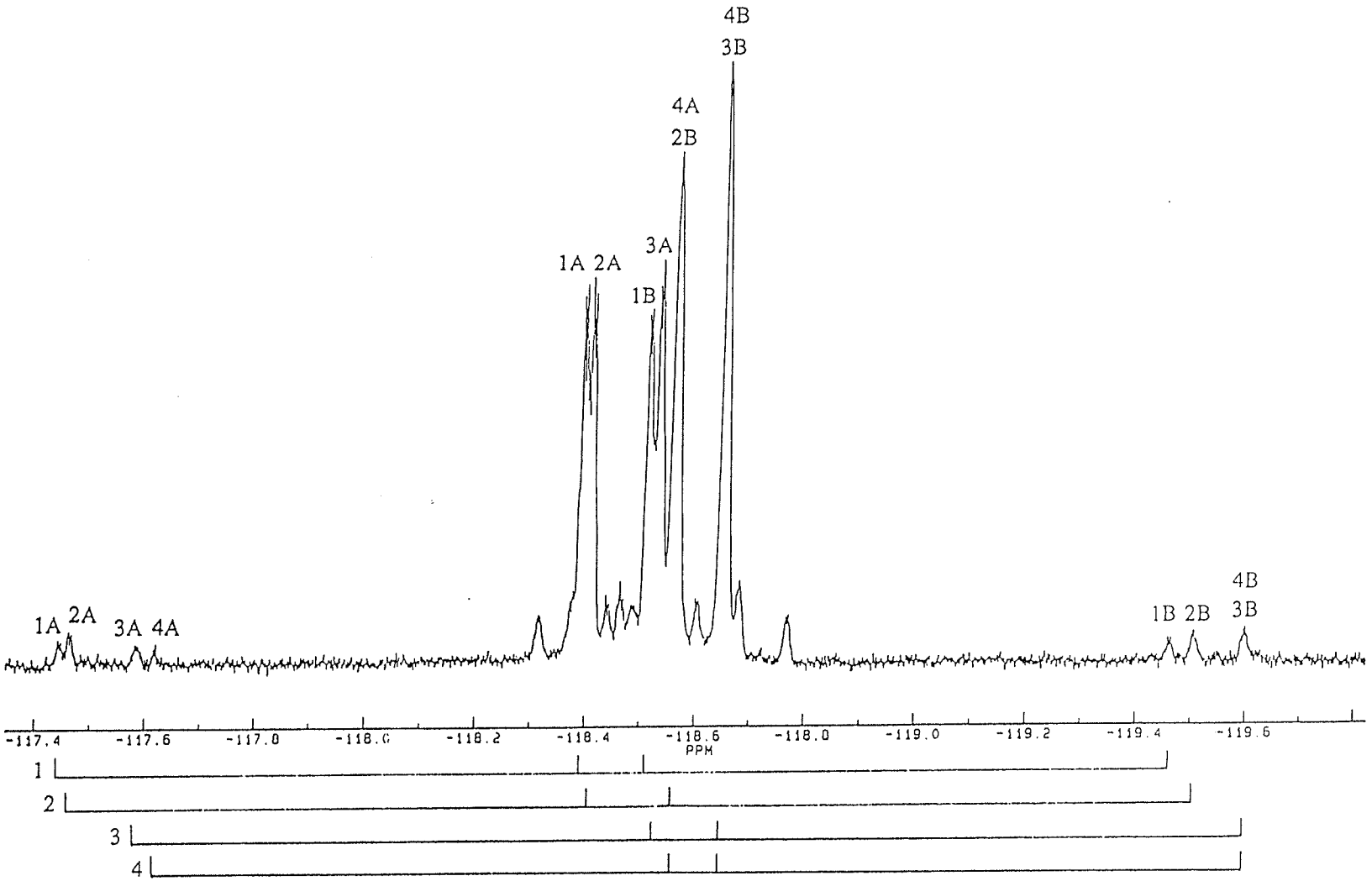

Figure 3.15 AB spectral region of the $\{^1H\}^{19}F$ NMR spectrum (with increased digital resolution) of $Rh(bzC_2F_5)_3$ recorded at 282.35 MHz in acetone at room temperature.

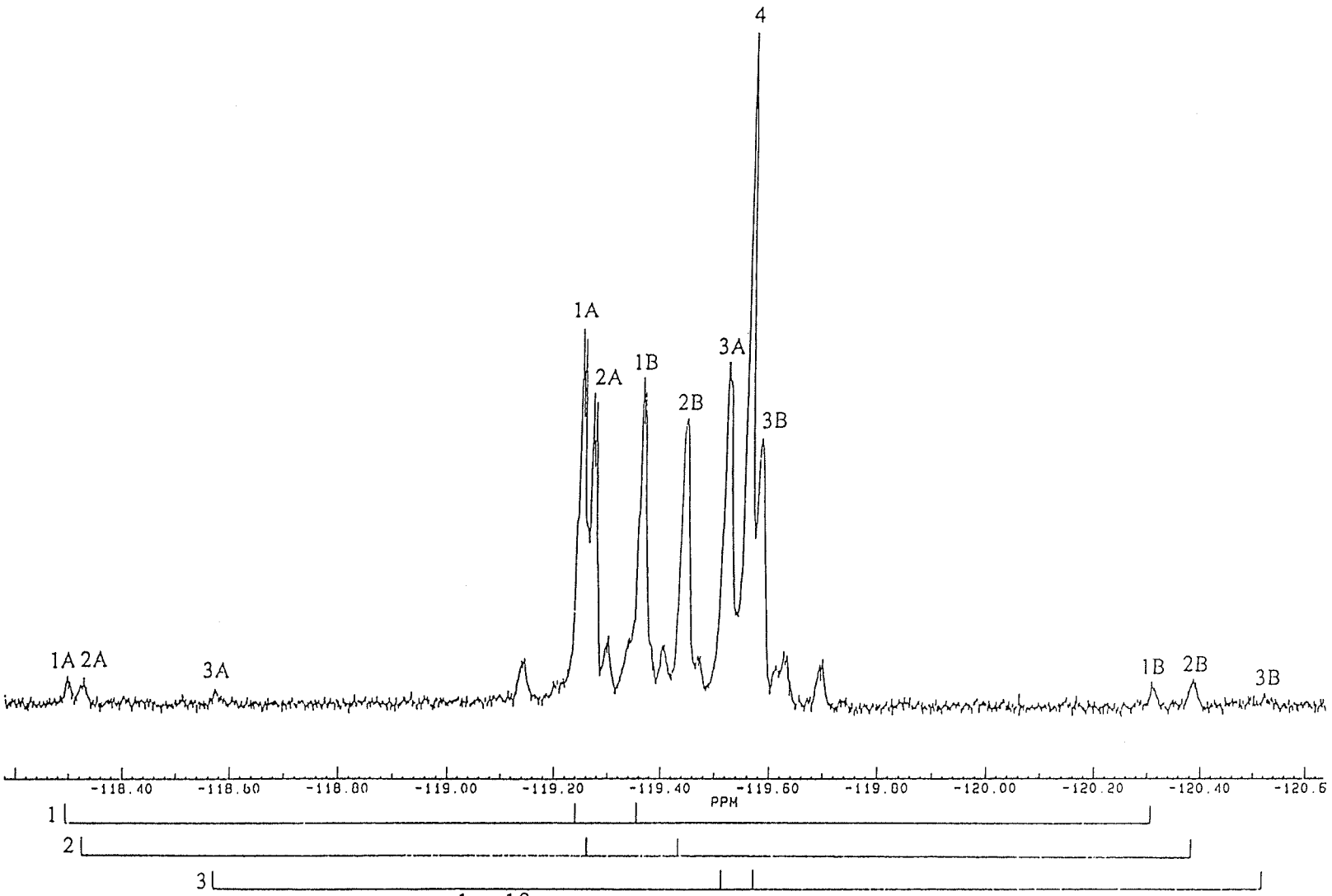

Figure 3.16 AB spectral region of the $\{^1H\}^{19}F$ NMR spectrum (with increased digital resolution) of $Rh(bzC_2F_5)_3$ recorded at 282.35 MHz in toluene at room temperature.

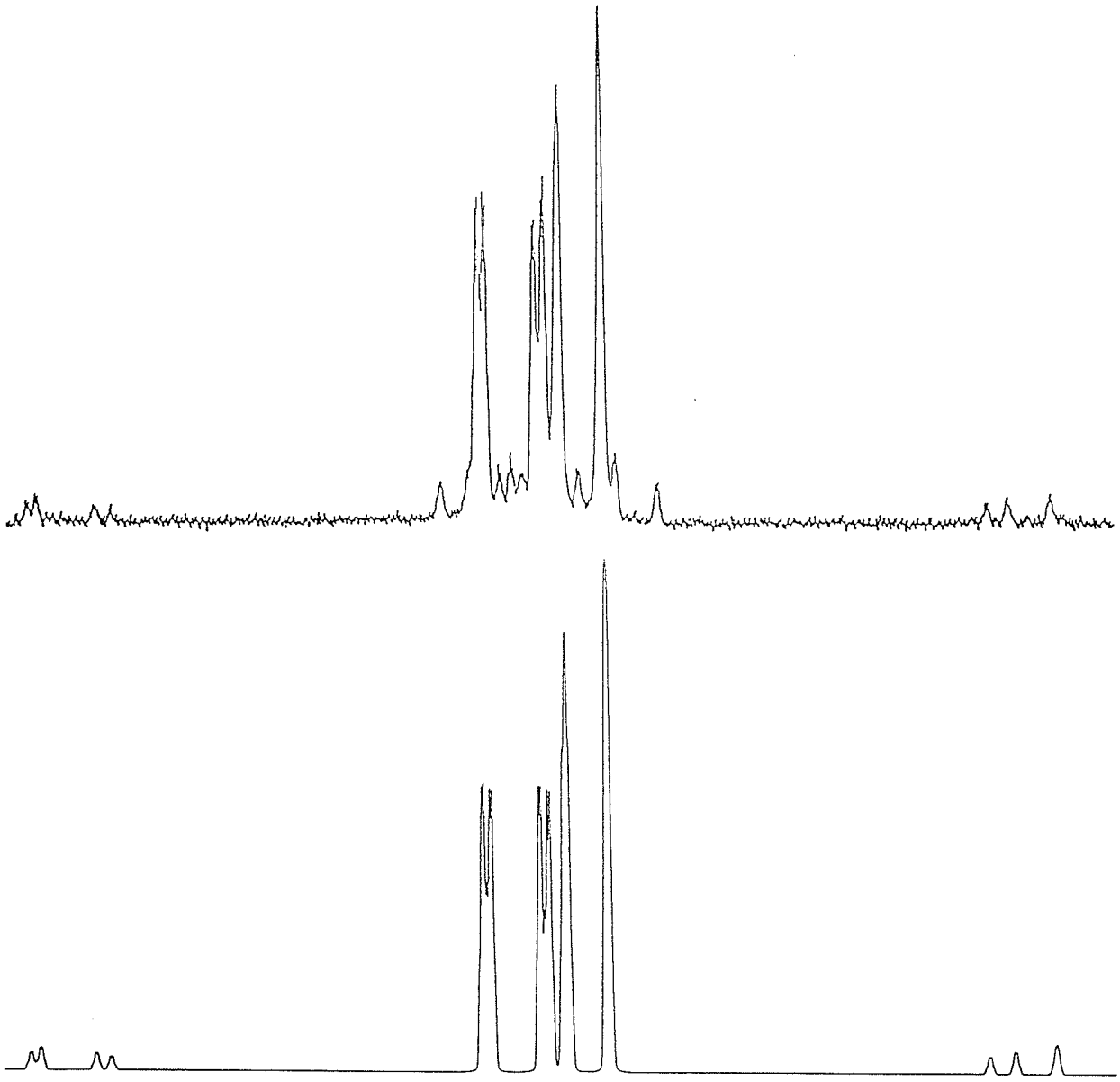

Figure 3.17 Comparison between experimental (upper) (recorded in acetone) and computer simulated (lower) $\{^1H\}^{19}F$ NMR spectra of the AB region of $Rh(bzC_2F_5)_3$.

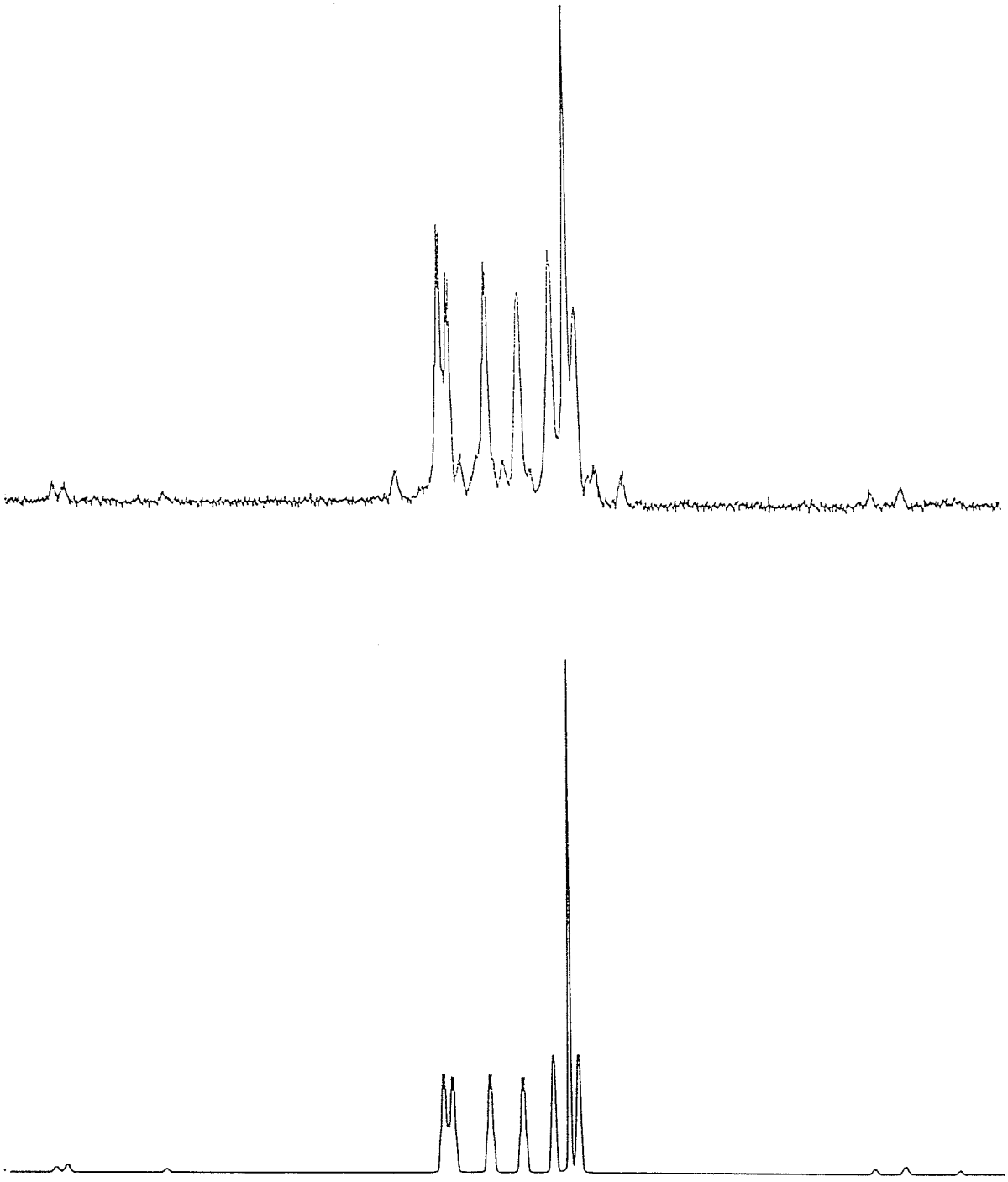

Figure 3.18 Comparison between experimental (upper) (recorded in toluene) and computer simulated (lower) $\{^1H\}^{19}F$ NMR spectra of the AB region of $Rh(bzC_2F_5)_3$.

Table 3.9 $\{^1H\}^{19}F$ NMR chemical shift (ppm) and coupling constant data (Hz) used in the best simulation of the AB region of $Rh(bzC_2F_5)_3$ in acetone.

Input parameters: J_{AB}, J_{AX}, J_{BX}, δ_A, δ_B, δ_X, LW = 1.5 Hz.

	J_{AB}	$J_{AX} = J_{BX}$	δ_A	δ_B	δ_X
Spectrum 1	268.1	1.5	-118.201	-118.697	-81.73
Spectrum 2	267.1	1.5	-118.197	-118.883	-81.86
Spectrum 3	268.6	1.5	-118.342	-118.837	-81.92
Spectrum 4	268.7	1.5	-118.391	-118.821	-82.04

Note:
(i) The uncertainties (see Table 3.8) are estimated to be 0.002 ppm for δ_A and δ_B, 0.01 ppm for δ_X and 0.3 Hz for J_{AX}, J_{BX} and J_{AB}.

(ii) Spectra are presented from low to high field (1 to 4, respectively). No relationship between a particular absorption occurring in the AB region with another in the CF_3 (X_3) region is implied.

Table 3.10 Calculated peak positions (± 0.002 ppm) and relative intensities* in the AB region of the $\{^1H\}^{19}F$ NMR spectrum of $Rh(bzC_2F_5)_3$ in acetone. (Input parameters used are given in Table 3.9.)

	A				B			
Spectrum 1	ppm	Int.	ppm	Int.	ppm	Int.	ppm	Int.
AB sub-spec 1	-117.431	0.114	-118.380	1.887	-118.502	1.887	-119.452	0.114
AB sub-spec 2	-117.436	0.341	-118.385	5.660	-118.507	5.660	-119.457	0.341
AB sub-spec 3	-117.441	0.341	-118.391	5.660	-118.513	5.660	-119.462	0.341
AB sub-spec 4	-117.447	0.114	-118.396	1.886	-118.518	1.886	-119.467	0.114

Spectrum 2	ppm	Int.	ppm	Int.	ppm	Int.	ppm	Int.
AB sub-spec 1	-117.451	0.147	-118.397	1.852	-118.561	1.852	-119.507	0.147
AB sub-spec 2	-117.456	0.442	-118.402	5.558	-118.566	5.558	-119.512	0.442
AB sub-spec 3	-117.462	0.442	-118.408	5.558	-118.571	5.558	-119.517	0.442
AB sub-spec 4	-117.467	0.147	-118.413	1.852	-118.576	1.852	-119.522	0.147

Spectrum 3	ppm	Int.	ppm	Int.	ppm	Int.	ppm	Int.
AB sub-spec 1	-117.569	0.113	-118.521	1.888	-118.642	1.888	-119.593	0.113
AB sub-spec 2	-117.575	0.339	-118.526	5.662	-118.647	5.662	-119.599	0.339
AB sub-spec 3	-117.580	0.339	-118.531	5.660	-118.653	5.660	-119.604	0.339
AB sub-spec 4	-117.585	0.113	-118.536	1.886	-118.658	1.886	-119.609	0.113

Spectrum 4	ppm	Int.	ppm	Int.	ppm	Int.	ppm	Int.
AB sub-spec 1	-117.600	0.089	-118.552	1.910	-118.644	1.912	-119.596	0.089
AB sub-spec 2	-117.606	0.266	-118.557	5.735	-118.650	5.735	-119.601	0.266
AB sub-spec 3	-117.611	0.266	-118.563	5.733	-118.655	5.733	-119.607	0.266
AB sub-spec 4	-117.617	0.089	-118.568	1.910	-118.661	1.912	-119.612	0.089

* Due to limitations of the spectral program Numarit[83], calculated intensity values assume the presence of equal amounts of spectra 1 to 4.

Table 3.11 $\{^1H\}^{19}F$ NMR chemical shift (ppm) and coupling constant data (Hz) used in the best simulation of the AB region of $Rh(bzC_2F_5)_3$ in toluene.

Input parameters: J_{AB}, J_{AX}, J_{BX}, δ_A, δ_B, δ_X, LW = 1.5 Hz.

	J_{AB}	$J_{AX} = J_{BX}$	δ_A	δ_B	δ_X
Spectrum 1	269.6	1.7	-119.064	-119.543	-82.24
Spectrum 2	268.0	1.7	-119.054	-119.656	-82.37
Spectrum 3	268.0	1.4	-119.374	-119.722	-82.56
Spectrum 4	-	< 1.0	-119.557	-119.557	-82.45

Note:
(i) The uncertainties (see Table 3.8) are estimated to be 0.002 ppm for δ_A and δ_B, 0.01 ppm for δ_X and 0.3 Hz for J_{AX}, J_{BX} and J_{AB}.

(ii) No relationship exists between a particular absorption occurring in the AB region with another in the CF_3 (X_3) region, with the exception of spectrum 4. The peak at -82.45 ppm, like the peak at -119.557 ppm, is thought to arise from the fluorines of the *fac* isomer. The remaining spectra are reported from low to high field (1 to 3, respectively).

Table **3.12** Calculated peak positions (± 0.002 ppm) and relative intensities* in the AB region of the $\{^1H\}^{19}F$ NMR spectrum of $Rh(bzC_2F_5)_3$ in toluene. (Input parameters used are given in Table 3.11.)

	A				B			
Spectrum 1	ppm	Int.	ppm	Int.	ppm	Int.	ppm	Int.
AB sub-spec 1	-118.282	0.106	-119.238	1.895	-119.351	1.895	-120.306	0.106
AB sub-spec 2	-118.287	0.319	-119.244	5.682	-119.357	5.682	-120.312	0.319
AB sub-spec 3	-118.295	0.319	-119.249	5.680	-119.364	5.680	-120.318	0.319
AB sub-spec 4	-118.301	0.106	-119.255	1.893	-119.369	1.893	-120.324	0.106

Spectrum 2	ppm	Int.	ppm	Int.	ppm	Int.	ppm	Int.
AB sub-spec 1	-118.310	0.155	-119.259	1.846	-119.433	1.846	-120.382	0.155
AB sub-spec 2	-118.316	0.466	-119.265	5.535	-119.439	5.535	-120.388	0.466
AB sub-spec 3	-118.322	0.466	-119.271	5.533	-119.445	5.533	-120.394	0.466
AB sub-spec 4	-118.328	0.155	-119.277	1.844	-119.451	1.844	-120.400	0.155

Spectrum 3	ppm	Int.	ppm	Int.	ppm	Int.	ppm	Int.
AB sub-spec 1	-118.561	0.061	-119.510	1.939	-119.572	1.939	-120.521	0.061
AB sub-spec 2	-118.566	0.184	-119.515	5.817	-119.577	5.817	-120.526	0.184
AB sub-spec 3	-118.570	0.184	-119.519	5.815	-119.581	5.815	-120.530	0.184
AB sub-spec 4	-118.575	0.061	-119.524	1.938	-119.586	1.938	-120.535	0.061

	ppm	Int.	ppm	Int.	ppm	Int.	ppm	Int.
Spectrum 4	-119.557	32.000	-	-	-	-	-	-

* Due to limitations of the spectral program Numarit[83], calculated intensity values assume the presence of equal amounts of spectra 1 to 4.

the B part of 2 lying almost directly over the A part of 4, while the remaining singlet at -118.65 ppm results from the overlap of the B parts of 3 and 4.

In toluene, the group of peaks between -119.20 and -119.30 ppm is due to partial overlap of the A parts of 1 and 2 and the peaks at -119.36 and -119.44 ppm to their B parts, respectively. The peaks at -119.52 and -119.58 ppm correspond to the A and B parts, respectively, of 3. Finally, the peak at -119.56 ppm corresponds to a CF_2 moiety, where no vicinal or geminal couplings are observed (i.e. for spectrum 4, $\delta_{AB} \sim 0$). (The fact that the ^{19}F NMR spectrum of the corresponding monothio analogue ($Rh(SbzC_2F_5)_3$), present only as the *fac* isomer, also shows no indication of vicinal or geminal couplings suggests that this peak arises from those of the *fac* isomer.)

The peak positions and relative areas of the unresolved peaks in the CF_3 (X_3) region, calculated from the values of J_{AX} and J_{BX} obtained in the AB region, are shown in Table 3.13. The four groups of signals are referred to as A to D rather than 1 to 4 as in the AB part so as not to suggest any relationship between them. However, the peak at -82.45 ppm in spectrum D recorded in toluene, like the peak at -119.56 ppm (spectrum 4) in the AB part, on the basis of relative intensities discussed earlier, is thought to arise from the fluorines of the *fac* isomer.

D) *$Rh(bzC_3F_7)_3$*

The ^{19}F NMR spectrum of $Rh(bzC_3F_7)_3$, recorded in acetone (Figure 3.19), consists of three groups of absorptions falling in the spectral regions centered on $\delta \sim 79.54$ ppm (relative intensity = 3),

Table 3.13 Calculated peak positions†, relative intensities* and coupling constants (± 0.3 Hz) of the unresolved peaks in the CF_3 (X_3) region of the $\{^1H\}^{19}F$ NMR spectrum of $Rh(bzC_2F_5)_3$ in (a) acetone, (b) toluene, using the optimized values of J_{AX} and J_{BX} determined in the AB spectral region.

Input parameters: J_{AX}, J_{BX}, δ_X, LW = 1.5 Hz.

(a)	ppm	Int.	ppm	Int.	ppm	Int.	δ_X	$J_{AX} = J_{BX}$
Spectrum A	-81.720	11.997	-81.726	24.000	-81.731	12.003	-81.726	1.5
Spectrum B	-81.858	11.997	-81.864	24.000	-81.869	12.003	-81.864	1.5
Spectrum C	-81.913	11.997	-81.919	24.000	-81.924	12.003	-81.919	1.5
Spectrum D	-82.039	11.997	-82.035	24.000	-82.040	12.003	-82.035	1.5

(b)	ppm	Int.	ppm	Int.	ppm	Int.	δ_X	$J_{AX} = J_{BX}$
Spectrum A	-82.230	11.996	-82.236	24.000	-82.242	12.004	-82.236	1.7
Spectrum B	-82.364	11.996	-82.370	24.000	-82.376	12.004	-82.370	1.7
Spectrum C	-82.552	11.996	-82.557	24.000	-82.562	12.004	-82.557	1.4
Spectrum D	-	-	-82.454	48.000	-	-	-82.454	-

† Because J_{AX} and J_{BX} are small, peak positions must be reported to three significant figures (1.6 Hz ~ 0.006 ppm). However, as for $Rh(SbzC_3F_7)_3$ (see Table 3.8), the input parameter, δ_X, corresponds to its experimental value, in this case to the centroid position of each unresolved triplet, and is therefore really only significant to two figures with an uncertainty of 0.01 ppm.

* Due to limitations of the spectral program Numarit[83], calculated intensity values assume the presence of equal amounts of spectra A to D.

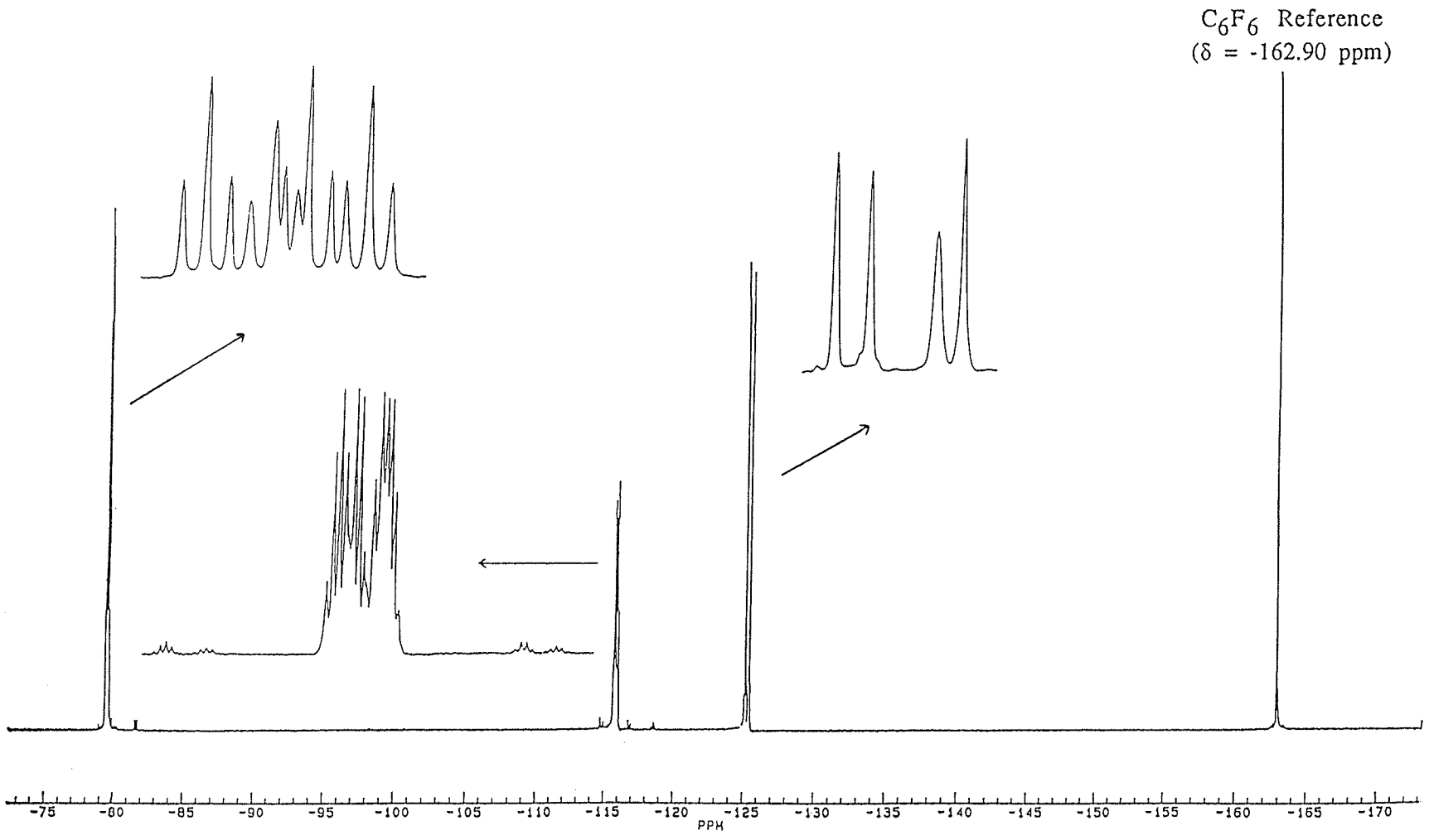

Figure 3.19 $\{^1H\}^{19}F$ NMR spectrum of $Rh(bzC_3F_7)_3$ recorded at 282.38 MHz in acetone at room temperature.

δ ~115.80 ppm (relative intensity = 2), and δ ~125.30 ppm (relative intensity = 2). Thus, the absorptions near δ ~ 79.54 ppm, which show twelve resolved or nearly resolved peaks, must be assigned to the fluorine atoms of the CF_3 group. The absorptions near δ ~115.80 ppm show evidence of 16 peaks in the central part and 16, or more, small peaks in the outer parts. These will be discussed later. The absorptions near δ ~125.30 ppm comprise four peaks, none of which shows evidence of splitting when the spectral region is expanded (Figure 3.20). These latter peaks must therefore be assigned to the fluorines of the β-CF_2 groups in a mixture of *fac* and *mer* isomers. As noted earlier, such fluorine atoms are expected to have zero, or near zero, coupling to vicinal fluorines of the CF_3 and α-CF_2 groups. From low to high field the FWHM values are 4.6, 4.6, 7.7 and 6.3 Hz, respectively. If we take the FWHM value of the C_6F_6 calibration peak as 2 Hz then the upper limits for the vicinal coupling constants are 1.3, 1.3, 2.9 and 2.2 Hz, respectively. (This is based on the assumption that the main broadening can be assigned to $J_{AX} + J_{BX}$ of the X_2 part of an ABX_2 spectrum. Of course, since the coupling is likely to be more complex than this then the upper limits for vicinal couplings should be reduced accordingly.) The relative areas of the four peaks (0.96:1.02:1.01:1.00 from low to high field) indicate that the *fac* and *mer* isomers are formed as a nearly statistical mixture.

The CF_3 region of the spectrum is shown in expanded form in Figure 3.21. The 12 peaks are easily analyzed as four symmetrical 1:2:1 triplets of nearly equal intensity. No further splitting of any of the peaks is apparent, but there are slight variations in peak width, which could be assigned to non-zero, but small, vicinal couplings. As

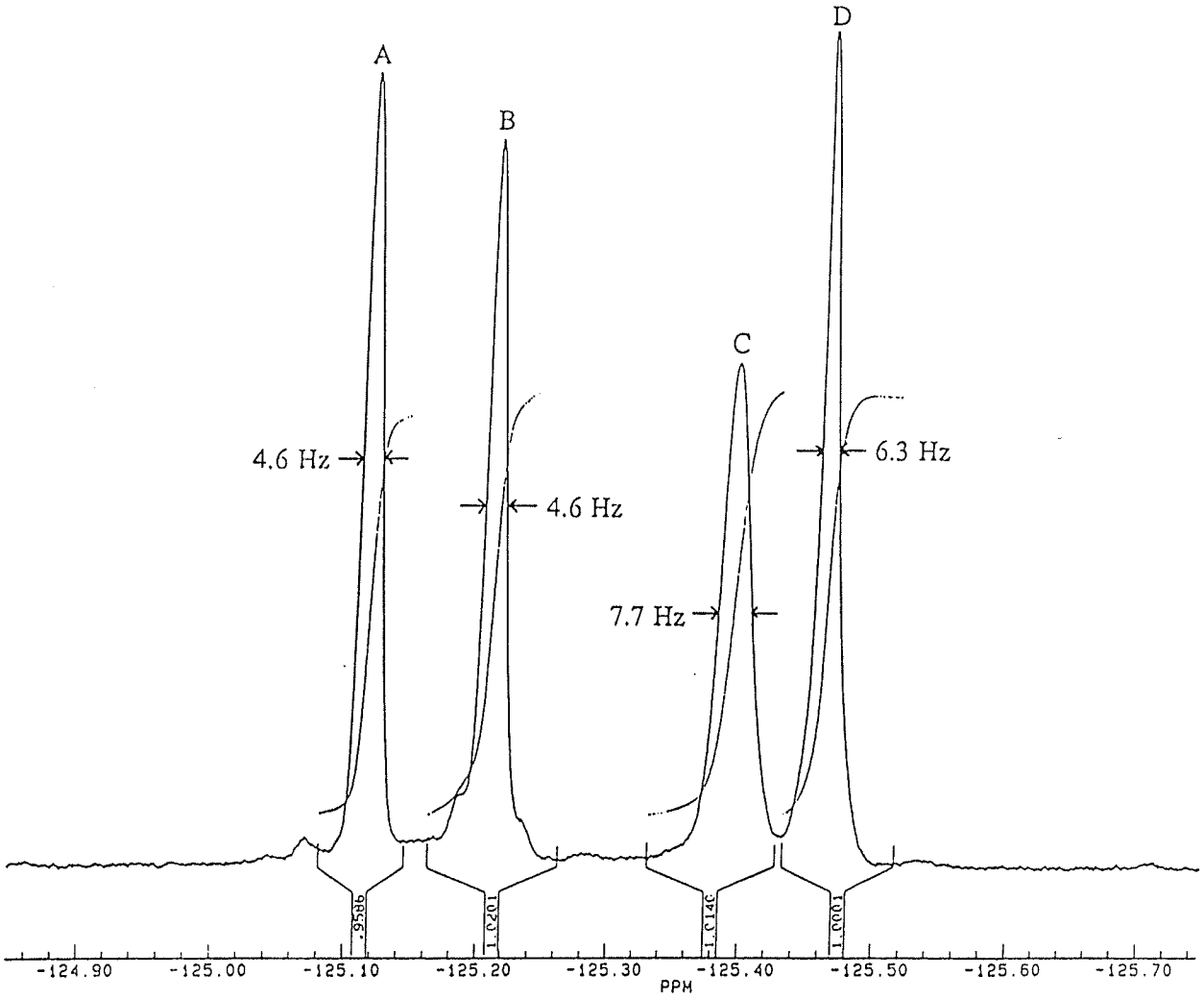

Figure 3.20 β-CF_2 spectral region of the $\{^1H\}^{19}F$ NMR spectrum (with increased digital resolution) of $Rh(bzC_3F_7)_3$ recorded at 282.38 MHz in acetone at room temperature.

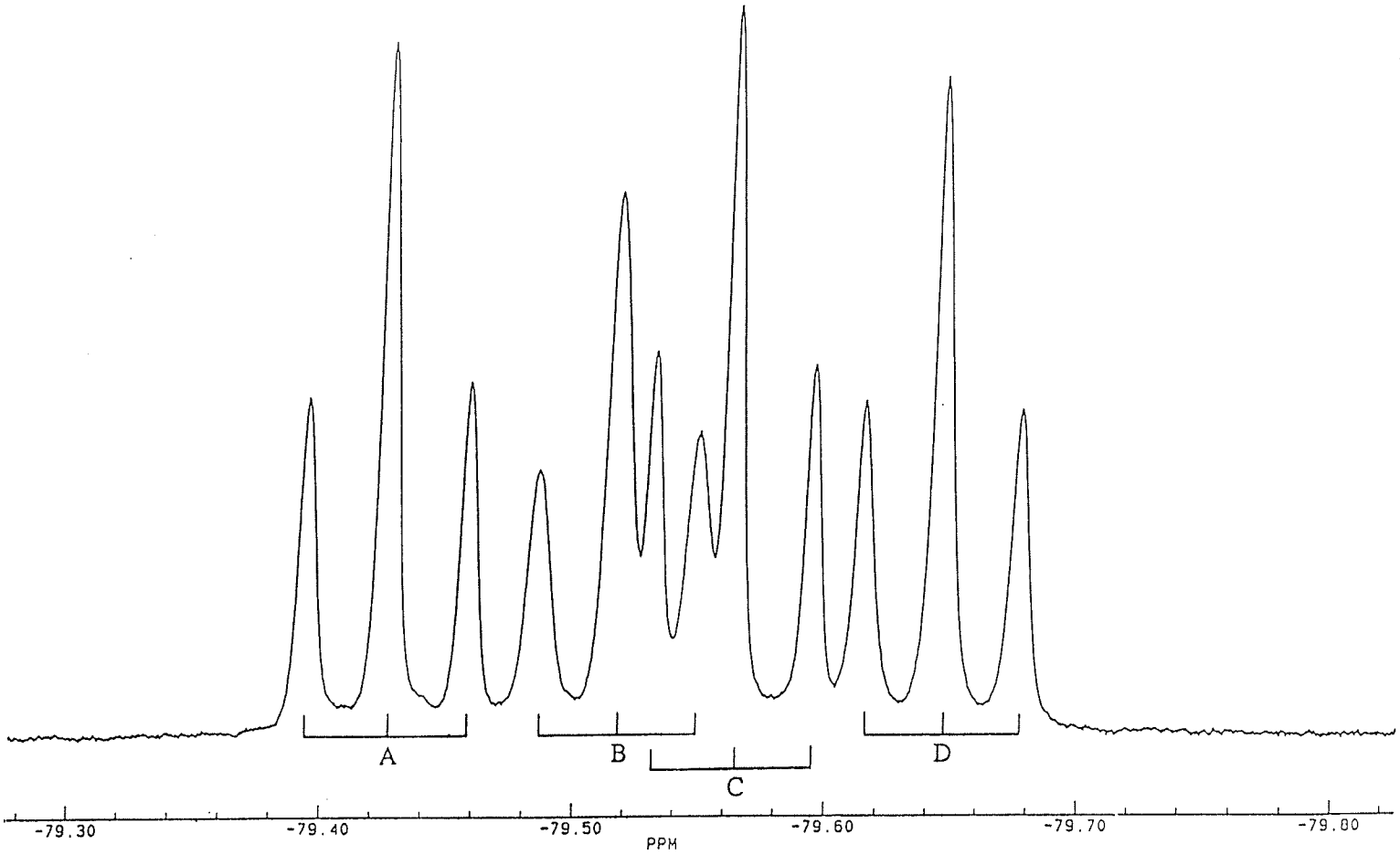

Figure 3.21 CF_3 (X_3) spectral region of the $\{^1H\}^{19}F$ NMR spectrum (with increased digital resolution) of $Rh(bzC_3F_7)_3$ recorded at 282.38 MHz in acetone at room temperature.

for $Rh(SbzC_3F_7)_3$, a four-bond coupling between the CF_3 group fluorines and the magnetically non-equivalent α-CF(A) and α-CF(B) fluorines results in an ABX_3-type spin system. When $J_{AX} = J_{BX}$ the X_3 spectrum collapses to the observed symmetrical 1:2:1 triplet. Peak positions and intensities in the CF_3 (X_3) and β-CF_2 regions are summarized in Table 3.14.

The α-CF_2 region of the spectrum (Figure 3.22) thus corresponds to the AB portions of four approximately equally intense ABX_3 spectra. In the general case, each of the AB regions contains 16 peaks, to make 64 in all. Of these, 32 occur in the central region, while 16 smaller peaks should be found on either side (assuming that all J_{AB} values are larger than any chemical shift differences). The number of peaks actually observed is much lower than the maximum. This can be attributed to accidental overlaps of different AB spectra and/or to $\Delta_{AB}/[(J_{AX}+J_{BX})/2]$ being accidentally equal to a small integer (as was the case for $Rh(SbzC_3F_7)_3$). We have seen above that when $J_{AX} = J_{BX}$ the four AB sub-spectra have relative intensities of 1:3:3:1. Thus if it were possible to record these as isolated NMR spectra each of the four AB resonance lines would be split into a 1:3:3:1 quartet of equal spacing, $(J_{AX} + J_{BX})/2$. Depending upon the value of Δ_{AB}, the two central quartets may overlap with one another. Thus, the complicated pattern of overlapping peaks observed in the central part of the experimental spectrum can be regarded as eight partially overlapping 1:3:3:1 quartets. Similarly, the outer peaks on both sides correspond to four overlapping 1:3:3:1 quartets. From the recognizable patterns associated with overlapping quartets of this type, along with the fact that each

Table 3.14 Calculated peak positions (± 0.01 ppm) and relative intensities* for the CF_3 (X_3) and β-CF_2 regions in the $\{^1H\}^{19}F$ NMR spectrum of $Rh(bzC_3F_7)_3$ using the optimized values of J_{AX} and J_{BX} determined in the AB spectral region. The experimental spectrum was recorded in acetone at room temperature.

Input parameters: J_{AX}, J_{BX}, δ_X, LW = 3.1 Hz

	CF_3 (X_3)								β-CF_2	
	ppm	Int.	ppm	Int.	ppm	Int.	$J_{AX}=J_{BX}$	δ_X	ppm	Int.
Spectrum A	-79.39	11.980	-79.43	24.000	-79.46	12.020	8.9	-79.43	-125.12	30.624
Spectrum B	-79.49	11.980	-79.52	24.000	-79.55	12.020	8.8	-79.52	-125.21	32.640
Spectrum C	-79.53	11.980	-79.56	24.000	-79.60	12.020	8.7	-79.56	-125.40	32.448
Spectrum D	-79.62	11.980	-79.65	24.000	-79.68	12.020	8.7	-79.65	-125.47	32.032

* Due to limitations of the spectral program Numarit[83], calculated intensity values assume the presence of equal amounts of spectra A to D.

Note:
(i) Spectra are presented from low to high field (A to D, respectively). No relationship between a particular absorption occurring in the β-CF_2 region with another in the CF_3 (X_3) region is implied.

(ii) The total signal intensity for one fluorine = 16.

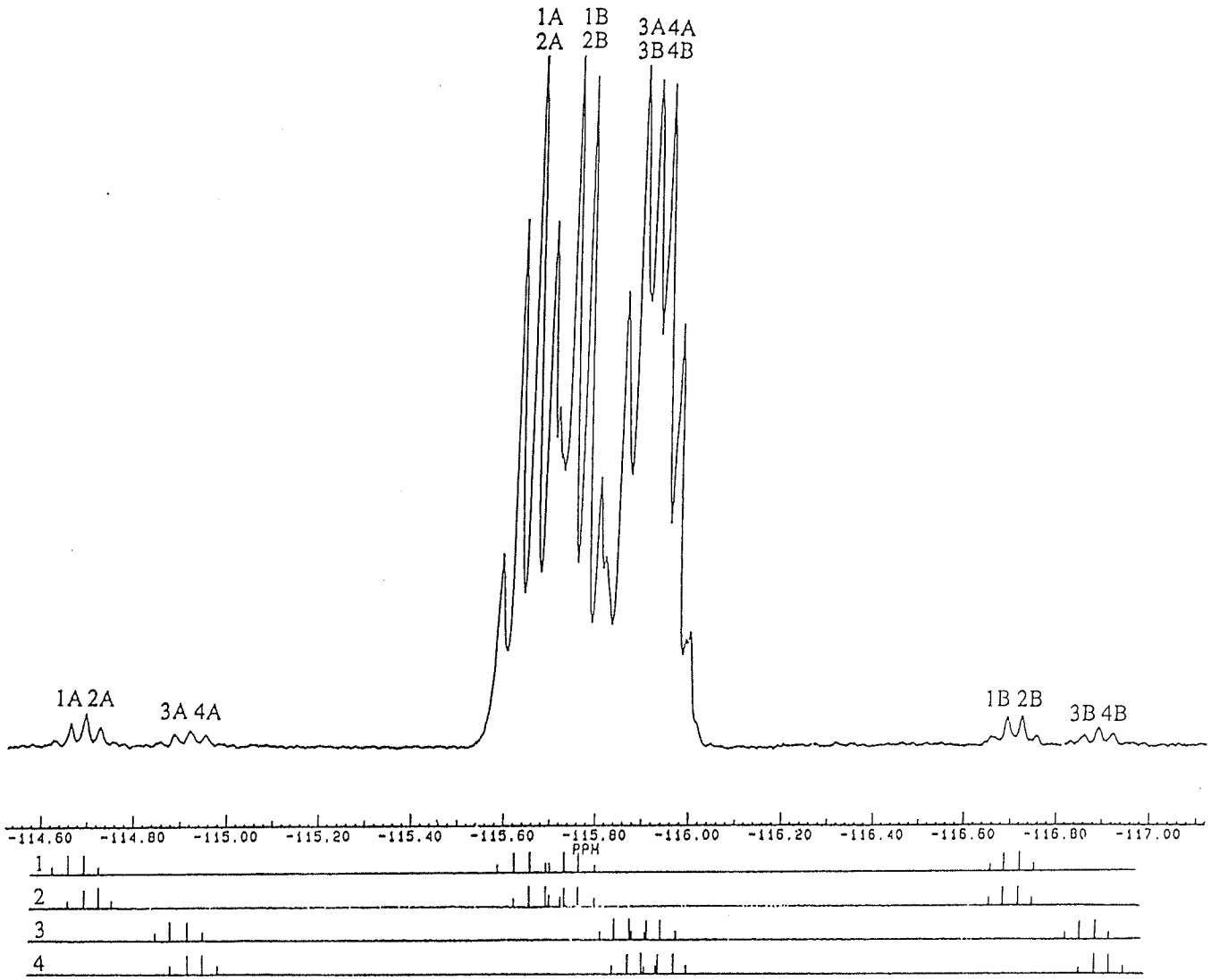

Figure 3.22 AB spectral region of the $\{^1H\}^{19}F$ NMR spectrum (with increased digital resolution) of $Rh(bzC_3F_7)_3$ recorded at 282.38 MHz in acetone at room temperature.

isomer has a distinct coupling constant J_{AB}, it was possible to simulate the spectrum and obtain the various chemical shifts and coupling constants. The results are presented in Tables 3.15 and 3.16, while Figure 3.23 shows both the computer simulated[83] and the experimental AB region of the spectrum. The peaks between -115.61 and -115.74 ppm arise from the partial overlap of the four central sub-spectra A group peaks of 1 and 2, while those lying between -115.74 and -115.84 ppm are due to the almost direct overlap of the central B group peaks of 1 and 2. Finally, the peaks occurring between -115.84 and -116.10 ppm are due to the closely overlapping central sub-spectra A and B group peaks of 3 and 4.

Table 3.15 $\{^1H\}^{19}F$ NMR shift (ppm) and coupling constant data (Hz) used in simulating the AB region of $Rh(bzC_3F_7)_3$ with the experimental spectrum recorded in acetone at room temperature.

Input parameters: J_{AB}, J_{AX}, J_{BX}, δ_A, δ_B, δ_X, LW = 3.1 Hz.

	J_{AB}	$J_{AX} = J_{AX}$	δ_A	δ_B	δ_X
Spectrum 1	270.8	8.9	-115.462	-115.942	-79.43
Spectrum 2	270.9	8.8	-115.518	-115.914	-79.52
Spectrum 3	270.4	8.7	-115.718	-116.078	-79.56
Spectrum 4	270.4	8.7	-115.743	-116.102	-79.45

Note:
(i) The uncertainties (see Table 3.8) are estimated to be 0.002 ppm for δ_A and δ_B, 0.01 for δ_X and 0.3 Hz for J_{AB}, J_{AX} and J_{BX}.

(ii) Spectra are presented from low to high field (1 to 4, respectively). No relationship between a particular absorption occurring in the AB region with another in the CF_3 (X_3) region is implied.

Table 3.16 Calculated peak positions (± 0.002 ppm) and relative intensities* in the AB region of the $\{^1H\}^{19}F$ NMR spectrum of $Rh(bzC_3F_7)_3$ in acetone. (Input parameters used are given in Table 3.15)

	A				B			
Spectrum 1	ppm	Int.	ppm	Int.	ppm	Int.	ppm	Int.
AB sub-spec 1	-114.639	0.106	-115.598	1.889	-115.711	1.889	-116.670	0.106
AB sub-spec 2	-114.670	0.318	-115.629	5.687	-115.743	5.687	-116.702	0.318
AB sub-spec 3	-114.702	0.317	-115.661	5.687	-115.774	5.678	-116.733	0.317
AB sub-spec 4	-114.733	0.106	-115.692	1.889	-115.806	1.889	-116.765	0.106

Spectrum 2	ppm	Int.	ppm	Int.	ppm	Int.	ppm	Int.
AB sub-spec 1	-114.670	0.076	-115.630	1.929	-115.708	1.919	-116.668	0.076
AB sub-spec 2	-114.701	0.227	-115.661	5.778	-115.739	5.778	-116.699	0.227
AB sub-spec 3	-114.733	0.227	-115.692	5.768	-115.771	5.768	-116.730	0.227
AB sub-spec 4	-114.764	0.076	-115.723	1.929	-115.802	1.919	-116.761	0.076

Spectrum 3	ppm	Int.	ppm	Int.	ppm	Int.	ppm	Int.
AB sub-spec 1	-114.861	0.064	-115.819	1.941	-115.884	1.931	-116.842	0.064
AB sub-spec 2	-114.892	0.193	-115.850	5.812	-115.915	5.812	-116.873	0.193
AB sub-spec 3	-114.923	0.193	-115.880	5.803	-115.946	5.803	-116.904	0.193
AB sub-spec 4	-114.954	0.064	-115.911	1.941	-115.977	1.931	-116.935	0.064

Spectrum 4	ppm	Int.	ppm	Int.	ppm	Int.	ppm	Int.
AB sub-spec 1	-114.886	0.064	-115.844	1.941	-115.909	1.931	-116.866	0.064
AB sub-spec 2	-114.917	0.192	-115.874	5.813	-115.940	5.813	-116.897	0.192
AB sub-spec 3	-114.947	0.191	-115.905	5.804	-115.970	5.804	-116.928	0.192
AB sub-spec 4	-114.978	0.064	-115.936	1.941	-116.001	1.931	-116.959	0.064

* Due to limitations of the spectral program Numarit[83], calculated intensity values assume the presence of equal amounts of spectra 1 to 4.

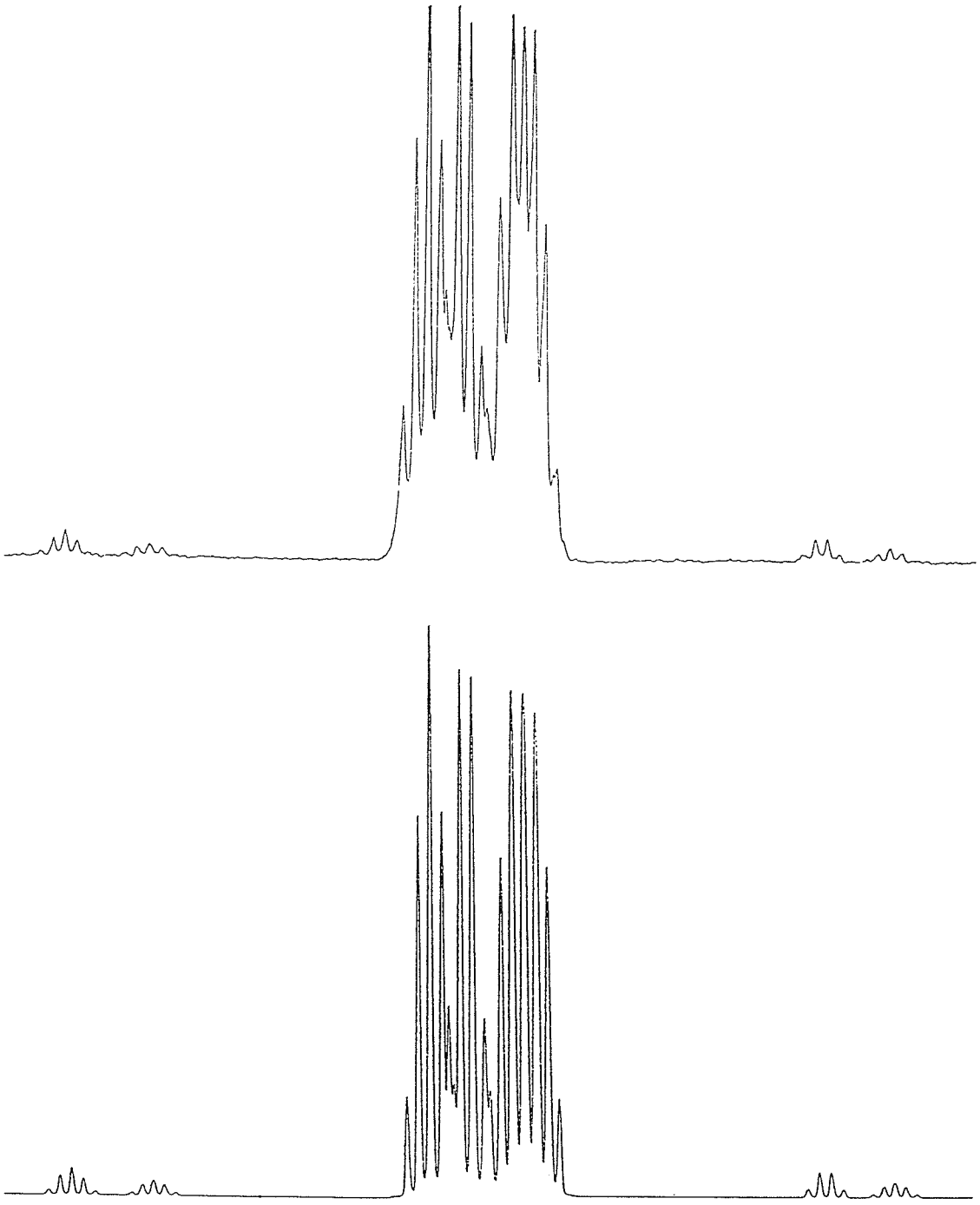

Figure 3.23 Comparison between experimental (upper) and computer simulated (lower) $\{^1H\}^{19}F$ NMR spectra of the AB region of $Rh(bzC_3F_7)_3$.

3.2 $Rh(Stfac)_3$ and $Rh(Sacac)_3$

3.2.1 Mass spectral studies

A) *General features*

The electron ionization (70 eV) positive ion mass spectra of $Rh(Stfa)_3$ and $Rh(Sacac)_3$ are shown in Figures 3.24 and 3.25, respectively. Tables 3.17 and 3.18 give the abundances of the characteristic ions as a percentage of that of the most abundant metal containing-ion (%RA). Figures 3.26 and 3.27 show the daughter ion spectra (B/E scan) of the RhL_2^+ ion for each complex, and fragmentation pathways are summarized in Schemes 3.24 and 3.25.

As observed in the mass spectra of $Rh(SbzC_2F_5)_3$ and $Rh(SbzC_3F_7)_3$ (see Section 3.1.1), and consistent with earlier reports on the mass spectra of other monothio-β-ketoenolate chelates of rhodium[69-71], RhL_3^+ corresponds to the most abundant metal-containing ion and L^+ to the base peak. With the exception of the loss of ·L from RhL_3^+, dissociation in the mass spectra of both complexes proceeds predominantly through elimination of even-electron neutrals such as CH_3CCH, CO and H_2S. In general, the observed fragmentations can be attributed to three known characteristics of rhodium. These are: its preference for the +III oxidation state[21,87], its ability to coordinate with soft bases (class (b) ligands) (see Section 1.2), and its tendency to form bonds with carbon[21,73,87].

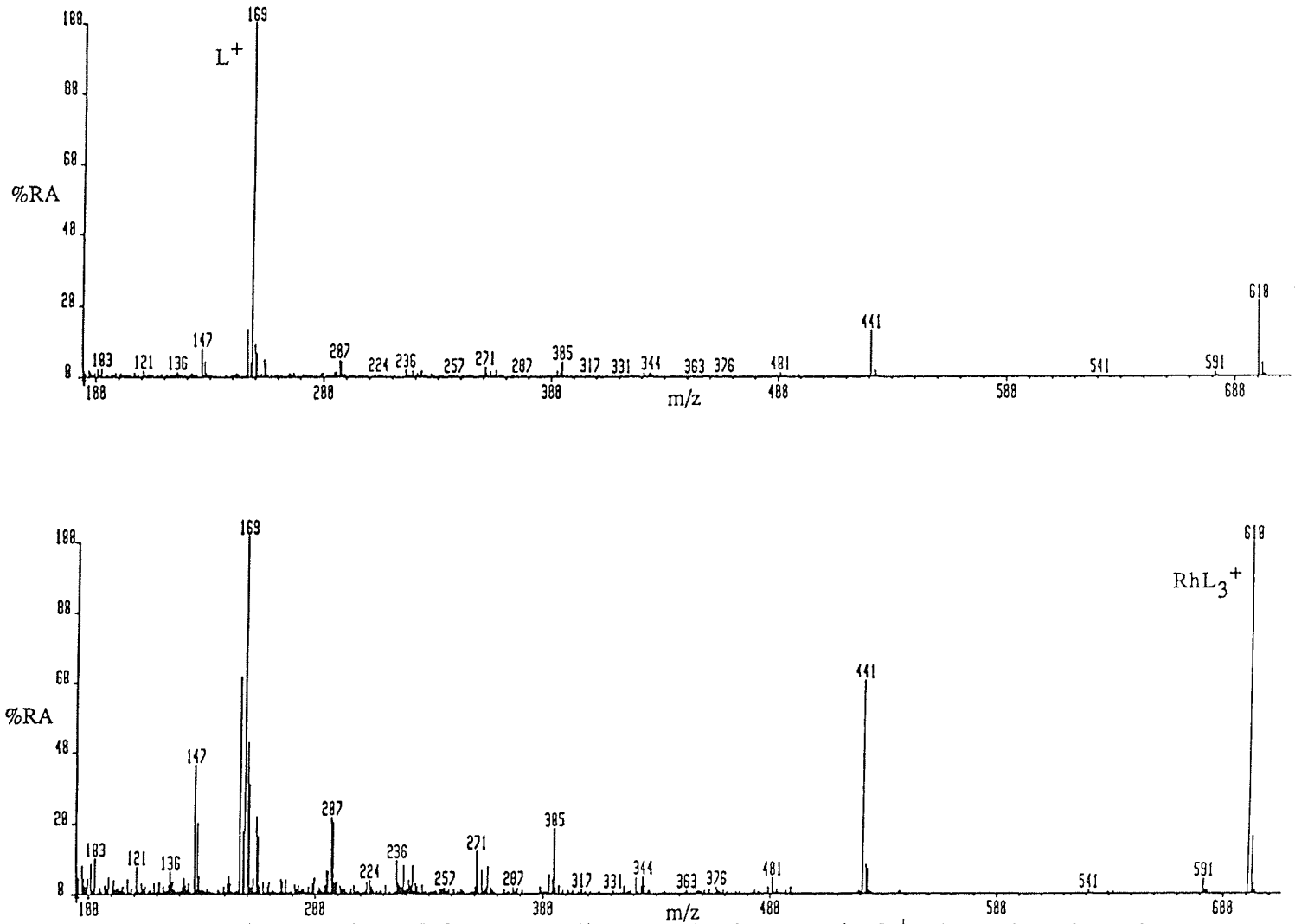

Figure 3.24 Mass spectrum of $Rh(Stfa)_3$ normalized to the base peak, L^+, (upper) and to the most abundant metal-containing ion, RhL_3^+, (lower).

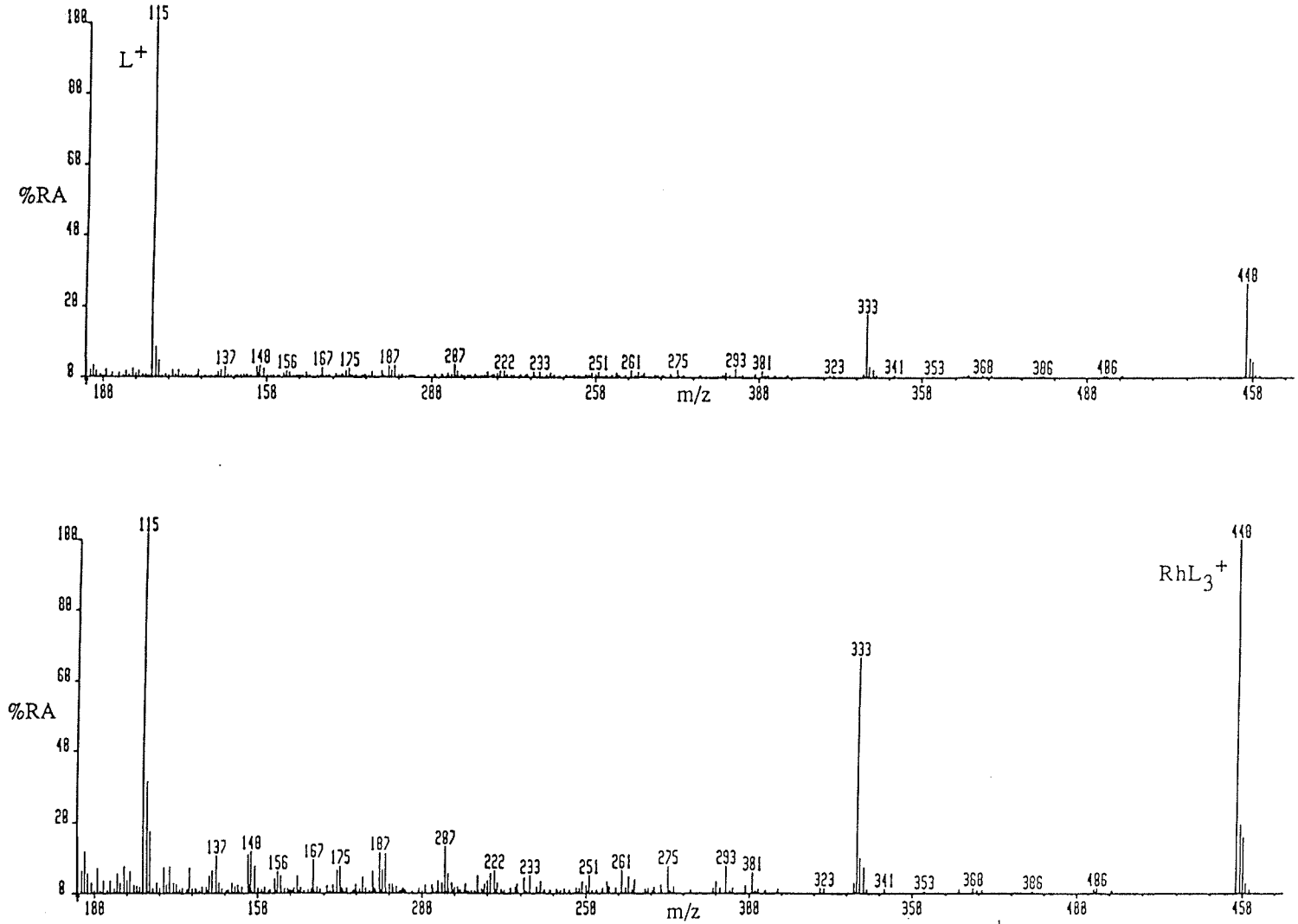

Figure 3.25 Mass spectrum of $Rh(Sacac)_3$ normalized to the base peak, L^+, (upper) and to the most abundant metal-containing ion, RhL_3^+, (lower).

Table 3.17 70 eV-EI mass spectrum of $Rh(Stfa)_3$. (L = Stfa)

Ion	m / z	%RA	Structure (Scheme 3.n)
RhL_3^+	610	100.0	
$[RhL_2(L\text{-}F)]^+$	591	3.9	
RhL_2^+	441	60.6	E441a(26-28,30-33),b(30)
$[RhL(L\text{-}S)]^+$	409	1.4	E409
$[RhL(L\text{-}H_2S)]^+$	407	<1.0	E407
$[RhL(L\text{-}CH_3CCH)]^+$	401	3.9	E401(26)
$[RhL(L\text{-}CH_2CO)]^+$	399	1.4	
$[SRhL(L\text{-}CF_3CO)]^+$	376	1.4	
$[LRh(S)(CF_3)]^+$	373	1.0	E373(26)
$[RhL(L\text{-}CF_3CO)]^+$	344	4.4	E344(28)
$LRhCF_3^+$	341	4.2	E341(26)
$RhC_5H_8OS_2^+$	305	17.5	E305a(27-29),b(27)
$LRhS^+$	304	3.4	E304(26,28)
$[SRh(L\text{-}H)]^+$	303	4.9	E303(30)
$[HSRh(L\text{-}CO)^+$	277	<1.0	E277(28)
$RhC_4H_4F_3S_2^+$	276	7.2	E276(26,28)
$[SRh(L\text{-}H\text{-}CO)]^+$	275	1.0	E275a(30),b(30)
$LRhH^+$	273	4.9	E273a(30),b(31),c(31),d(32)
RhL^+	272	1.4	E272(33)
$[Rh(L\text{-}H)]^+$	271	11.8	E271(29,30)
$[HSRh(L\text{-}CO\text{-}HF)]^+$	257	1.6	E257a(28),b(28)
$[SRh(L\text{-}H\text{-}CO\text{-}HF)]^+$	255	1.2	E255(30)
$[HRh(L\text{-}CO)]^+$	245	1.5	E245a(32),b(32)
$[Rh(L\text{-}CO)]^+$	244	2.1	E244(33)
$[Rh(L\text{-}H\text{-}CO)]^+$	243	7.4	E243(29)
$[HRh(L\text{-}S)]^+$	241	3.6	
$[Rh(L\text{-}HS)]^+$	239	7.6	E239a(31),b(31)
$CF_3RhS_2^+$	236	3.6	E236a(26)

Table 3.17 Continued

Ion	m / z	%RA	Structure (Scheme 3.n)
$[HSRh(L\text{-}CF_3)]^+$	236	5.5	E236b(28)
$[HRh(L\text{-}CO\text{-}HF)]^+$	225	1.3	E225a(32),b(32)
$[Rh(L\text{-}CO\text{-}HF)]^+$	224	3.4	E224(33)
$[Rh(L\text{-}H\text{-}CO\text{-}HF)]^+$	223	3.1	E223(29)
$[Rh(L\text{-}HS\text{-}CO)]^+$	211	2.0	E211(31)
$[HSRh(L\text{-}CF_3CO)]^+$	208	18.5	E208a(28),b(28),c(28)
$[SRh(L\text{-}CF_3CO)]^+$	207	21.0	E207a(26),b(26)
$[SRh(L\text{-}H\text{-}CF_3CO)]^+$	206	6.1	
$[Rh(L\text{-}CF_3CO)]^+$	175	15.4	E175a(33),b(33)
$RhC_3H_3S^+$	174	21.9	E174(28,29)
LH^+	170	11.2	
L^+	169	470.8	
$HSRhS^+$	168	16.6	E168(28)
RhS_2^+	167	61.5	E167(26,30)
$RhCHS^+$	148	19.5	
$RhCS^+$	147	36.2	
$HRhSH^+$	137	3.0	E137(32)
$RhSH^+$	136	5.8	E136(33)
RhS^+	135	2.5	E135(29,33)
Rh^+	103	9.7	E103(29)

Table 3.18 70 eV-EI mass spectrum of $Rh(Sacac)_3$. (L = Sacac)

Ion	m / z	%RA	Structure (Scheme 3.n)
RhL_3^+	448	100.0	F448(34)
$[RhL_2(L\text{-}CH_2CO)]^+$	406	1.2	
$[RhL_2(L\text{-}CH_3CO)]^+$	405	<0.1	
RhL_2^+	333	66.5	F333a(135-38,40),b(37)
$[SRhL(L\text{-}CH_2CO)]^+$	323	<1.0	
$[SRhL(L\text{-}CH_3CO)]^+$	322	1.1	
$[RhL(L\text{-}CO)]^+$	305	<1.0	
$[RhL(L\text{-}CH_2O)]^+$	303	<1.0	F303(38)
$[RhL(L\text{-}S)]^+$	301	5.4	F301(34)
$[RhL(L\text{-}H_2S)]^+$	299	1.9	F299a(40),b(40),c(40)
$[RhL(L\text{-}CH_3CCH)]^+$	293	7.3	F293(35)
$[RhL(L\text{-}CH_3CO)]^+$	290	3.1	
$[RhL_2\text{-}C_2H_4O]^+$	289	1.3	
$[Rh(L\text{-}CH_2O)(L\text{-}CO)]^+$	275	7.2	F275(38)
$LRhC_4H_7^+$	273	2.2	F273(34)
$[LRh(CH_3)(S)]^+$	265	3.1	F265(35)
$RhC_6H_8OS_2^+$	263	4.0	
$[LRh(CH_3)(CO)]^+$	261	6.1	F261(34)
$LRhSH^+$	251	4.2	F251(36)
$LRhS^+$	250	2.0	F250(39)
$[SRh(L\text{-}H)]^+$	249	3.0	F249(37)
$LRhCH_3^+$	233	4.4	F233(34)
$LRhCH^+$	231	4.2	F231(35)
$RhC_4H_8S_2^+$	223	2.2	F223(36)
$RhC_4H_7S_2^+$	222	5.5	F222(39)
$RhC_4H_6S_2^+$	221	5.2	F221a(37),b(37)
$[SRh(L\text{-}CH_2O)]^+$	220	3.3	
$HRhL^+$	218	1.3	

Table 3.18 Continued

Ion	m / z	%RA	Structure (Scheme 3.n)
$RhC_5H_6OS^+$	217	4.8	F217a(36),b(37)
$[SRh(L\text{-}CHCO)]^+$	209	1.2	
$[SRh(L\text{-}CH_2CO)]^+$	208	4.4	
$[SRh(L\text{-}CH_3CO)]^+$	207	12.5	F207a(38,39),b(38,39)
$[SRh(L\text{-}C_2H_4O)]^+$	206	2.5	
$[SRh(L\text{-}C_2H_5O)]^+$	205	3.1	
$RhC_5H_8S^+$	203	2.2	F203a(35),b(35)
$[Rh(L\text{-}CO)]^+$	190	1.5	
$RhC_4H_6S^+$	189	10.1	F189a(36),b(36),c(37)
$RhC_4H_5S^+$	188	5.9	
$RhC_5H_8O^+$	187	4.2	
$RhC_4H_4S^+$	187	6.7	
$[Rh(L\text{-}HS)]^+$	185	5.9	F185
$CH_3RhS_2^+$	182	3.8	
$[Rh(L\text{-}CH_3CO)]^+$	175	7.2	
$[Rh(L\text{-}C_2H_4O)]^+$	174	6.2	
$[Rh(L\text{-}C_2H_5O)]^+$	173	2.1	
RhS_2^+	167	9.1	F167(37-39)
$[Rh(L\text{-}HS\text{-}CO)]^+$	157	4.5	F157
$RhC_4H_5^+$	156	5.7	
$RhC_4H_4^+$	155	3.7	
$RhCHS^+$	148	11.4	
$RhCS^+$	147	10.6	
$RhC_3H_5^+$	144	2.1	
$RhC_3H_4^+$	143	1.7	
$RhC_2H_4^+$	131	1.2	
L^+	115	381.0	
Rh^+	103	3.3	

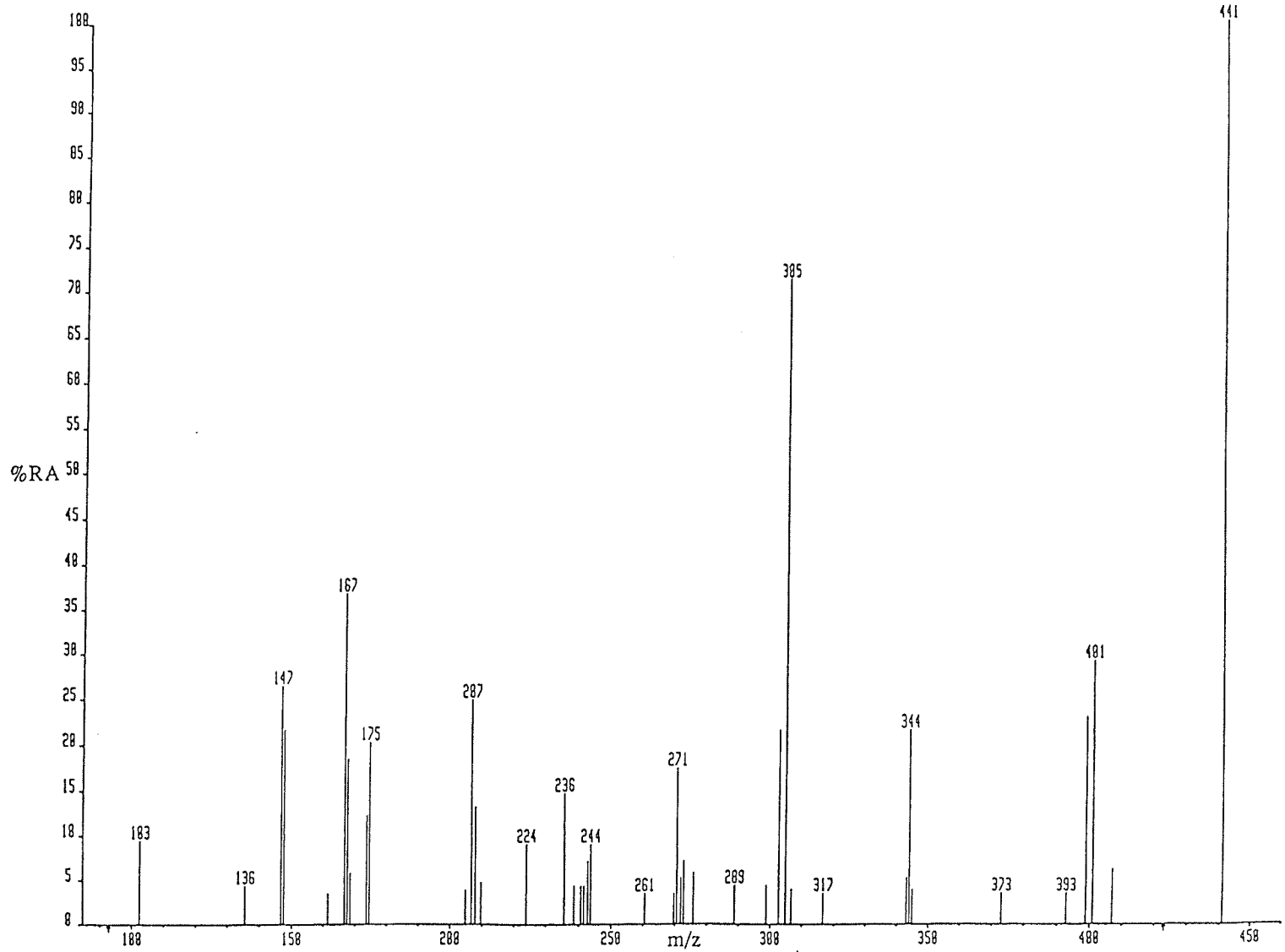

Figure 3.26 Daughter ion spectrum (B/E scan) of $Rh(Stfa)_2^+$ (Ion abundance x15 between arrows).

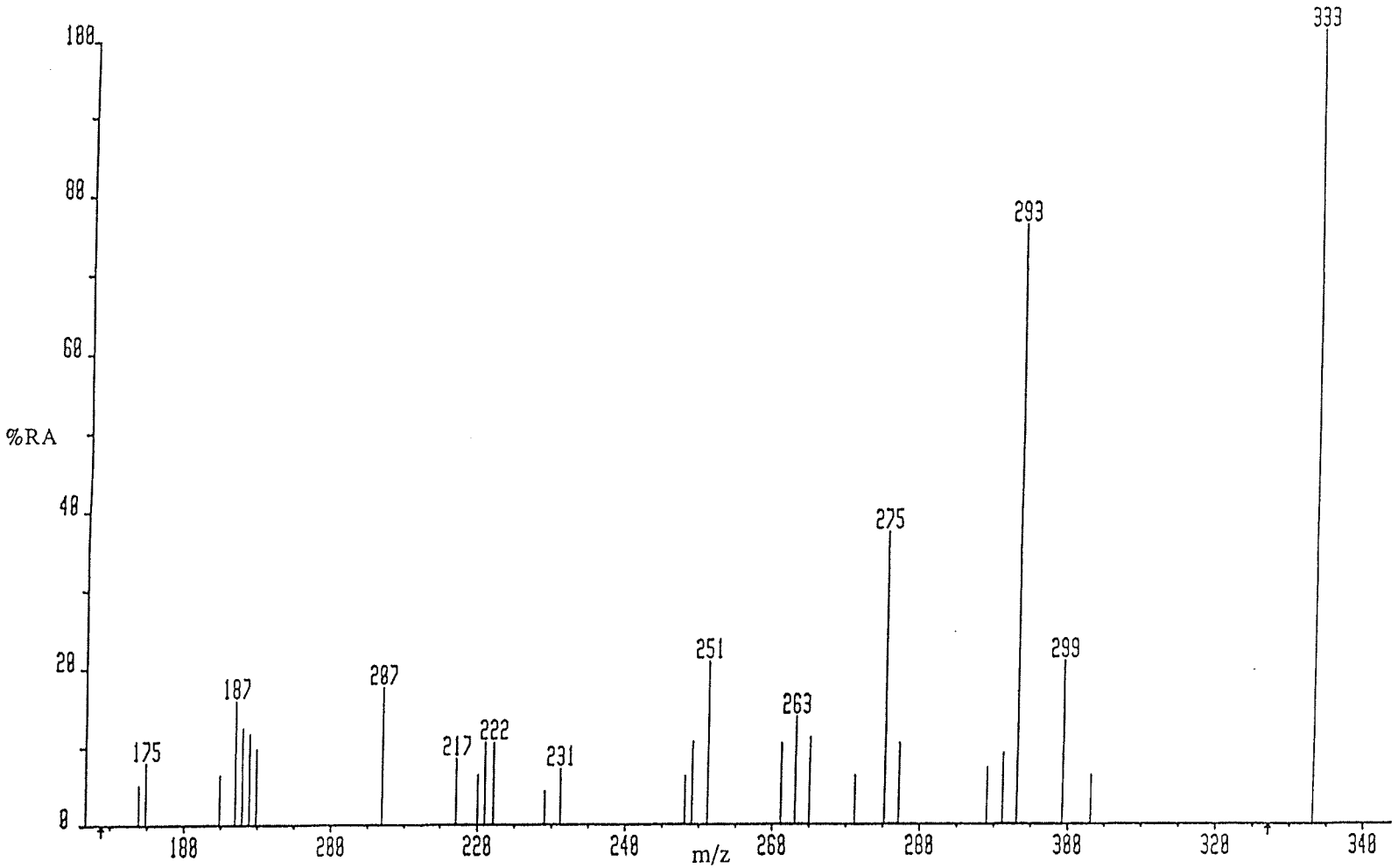

Figure 3.27 Daughter ion spectrum (B/E scan) of $Rh(Sacac)_2^+$ (Ion abundance x40 between arrows).

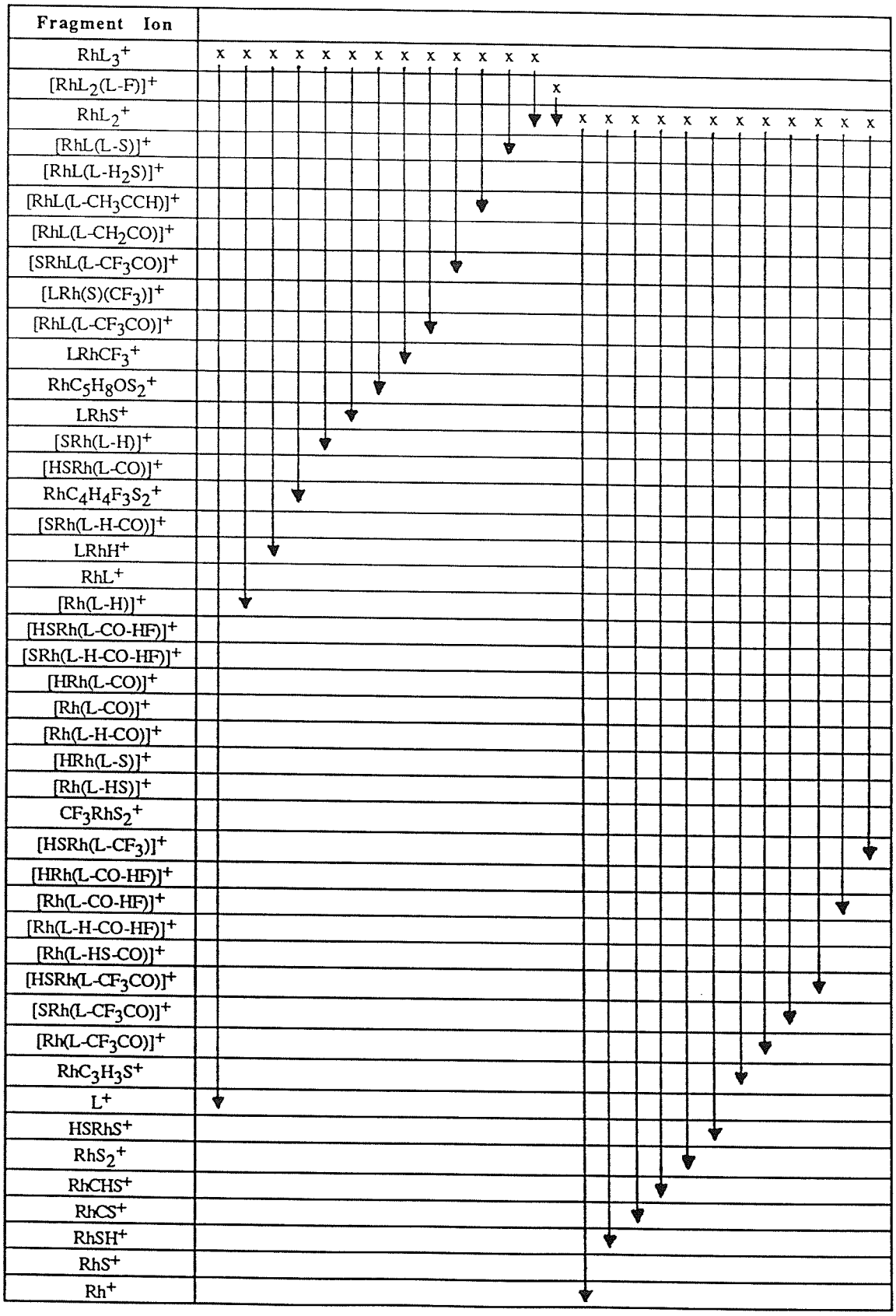

Scheme 3.24 Fragmentation pathways of $Rh(Stfa)_3$

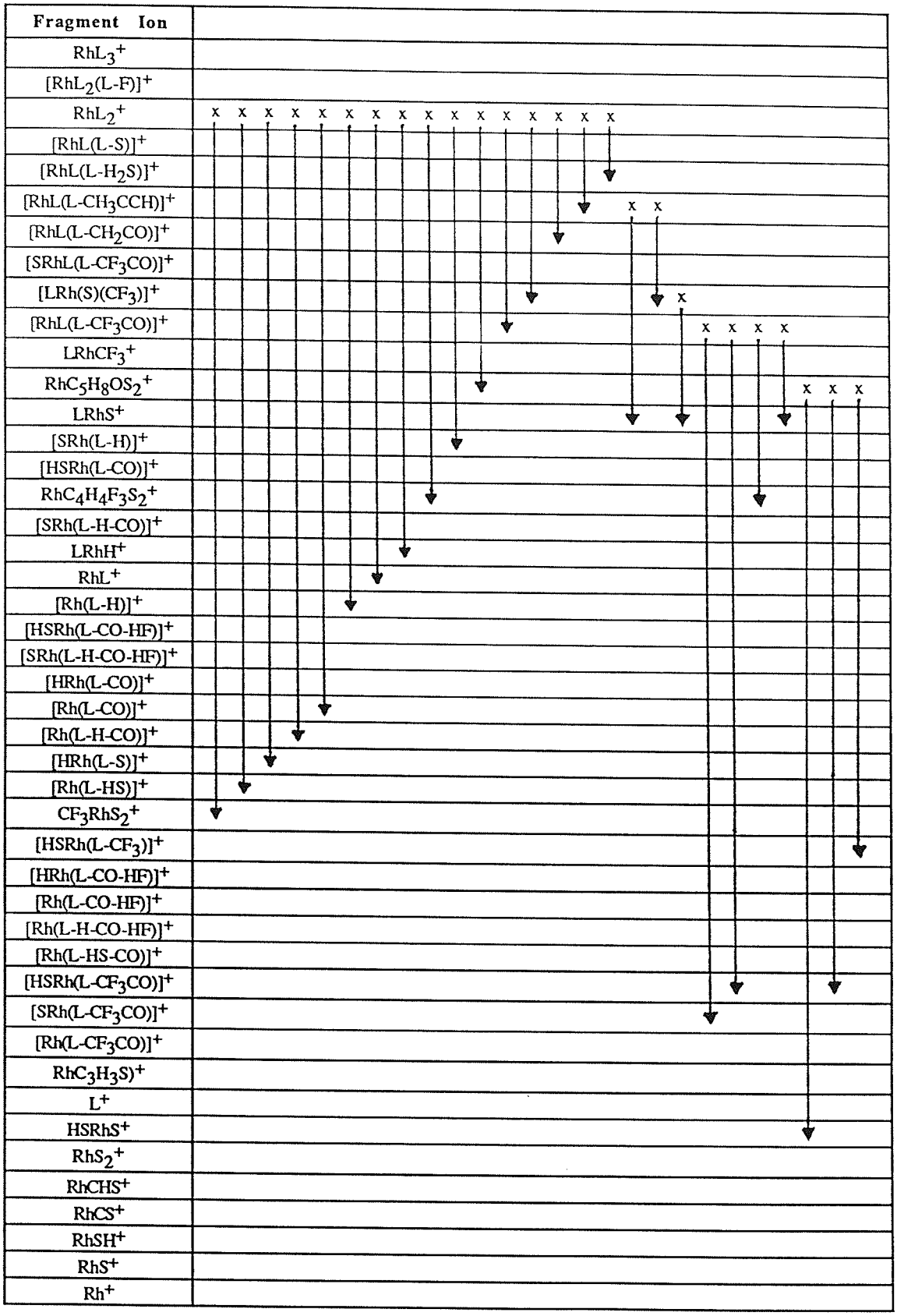

Scheme 3.24 Continued

Fragment Ion	
RhL_3^+	
$[RhL_2(L\text{-}F)]^+$	
RhL_2^+	
$[RhL(L\text{-}S)]^+$	
$[RhL(L\text{-}H_2S)]^+$	
$[RhL(L\text{-}CH_3CCH)]^+$	
$[RhL(L\text{-}CH_2CO)]^+$	
$[SRhL(L\text{-}CF_3CO)]^+$	
$[LRh(S)(CF_3)]^+$	
$[RhL(L\text{-}CF_3CO)]^+$	
$LRhCF_3^+$	
$RhC_5H_8OS_2^+$	
$LRhS^+$	
$[SRh(L\text{-}H)]^+$	
$[HSRh(L\text{-}CO)]^+$	
$RhC_4H_4F_3S_2^+$	
$[SRh(L\text{-}H\text{-}CO)]^+$	
$LRhH^+$	
RhL^+	
$[Rh(L\text{-}H)]^+$	
$[HSRh(L\text{-}CO\text{-}HF)]^+$	
$[SRh(L\text{-}H\text{-}CO\text{-}HF)]^+$	
$[HRh(L\text{-}CO)]^+$	
$[Rh(L\text{-}CO)]^+$	
$[Rh(L\text{-}H\text{-}CO)]^+$	
$[HRh(L\text{-}S)]^+$	
$[Rh(L\text{-}HS)]^+$	
$CF_3RhS_2^+$	
$[HSRh(L\text{-}CF_3)]^+$	
$[HRh(L\text{-}CO\text{-}HF)]^+$	
$[Rh(L\text{-}CO\text{-}HF)]^+$	
$[Rh(L\text{-}H\text{-}CO\text{-}HF)]^+$	
$[Rh(L\text{-}HS\text{-}CO)]^+$	
$[HSRh(L\text{-}CF_3CO)]^+$	
$[SRh(L\text{-}CF_3CO)]^+$	
$[Rh(L\text{-}CF_3CO)]^+$	
$RhC_3H_3S^+$	
L^+	
$HSRhS^+$	
RhS_2^+	
$RhCHS^+$	
$RhCS^+$	
$RhSH^+$	
RhS^+	
Rh^+	

Scheme 3.24 Continued

Fragment Ion	
RhL_3^+	
$[RhL_2(L\text{-}F)]^+$	
RhL_2^+	
$[RhL(L\text{-}S)]^+$	
$[RhL(L\text{-}H_2S)]^+$	
$[RhL(L\text{-}CH_3CCH)]^+$	
$[RhL(L\text{-}CH_2CO)]^+$	
$[SRhL(L\text{-}CF_3CO)]^+$	
$[LRh(S)(CF_3)]^+$	
$[RhL(L\text{-}CF_3CO)]^+$	
$LRhCF_3^+$	
$RhC_5H_8OS_2^+$	
$LRhS^+$	
$[SRh(L\text{-}H)]^+$	
$[HSRh(L\text{-}CO)]^+$	
$RhC_4H_4F_3S_2^+$	
$[SRh(L\text{-}H\text{-}CO)]^+$	
$LRhH^+$	
RhL^+	
$[Rh(L\text{-}H)]^+$	
$[HSRh(L\text{-}CO\text{-}HF)]^+$	
$[SRh(L\text{-}H\text{-}CO\text{-}HF)]^+$	
$[HRh(L\text{-}CO)]^+$	
$[Rh(L\text{-}CO)]^+$	
$[Rh(L\text{-}H\text{-}CO)]^+$	
$[HRh(L\text{-}S)]^+$	
$[Rh(L\text{-}HS)]^+$	
$CF_3RhS_2^+$	
$[HSRh(L\text{-}CF_3)]^+$	
$[HRh(L\text{-}CO\text{-}HF)]^+$	
$[Rh(L\text{-}CO\text{-}HF)]^+$	
$[Rh(L\text{-}H\text{-}CO\text{-}HF)]^+$	
$[Rh(L\text{-}HS\text{-}CO)]^+$	
$[HSRh(L\text{-}CF_3CO)]^+$	x x x x
$[SRh(L\text{-}CF_3CO)]^+$	x x x
$[Rh(L\text{-}CF_3CO)]^+$	x x
$RhC_3H_3S^+$	x x
L^+	
$HSRhS^+$	
RhS_2^+	
$RhHCS^+$	
$RhCS^+$	
$RhSH^+$	
RhS^+	
Rh^+	

Scheme 3.24 Continued

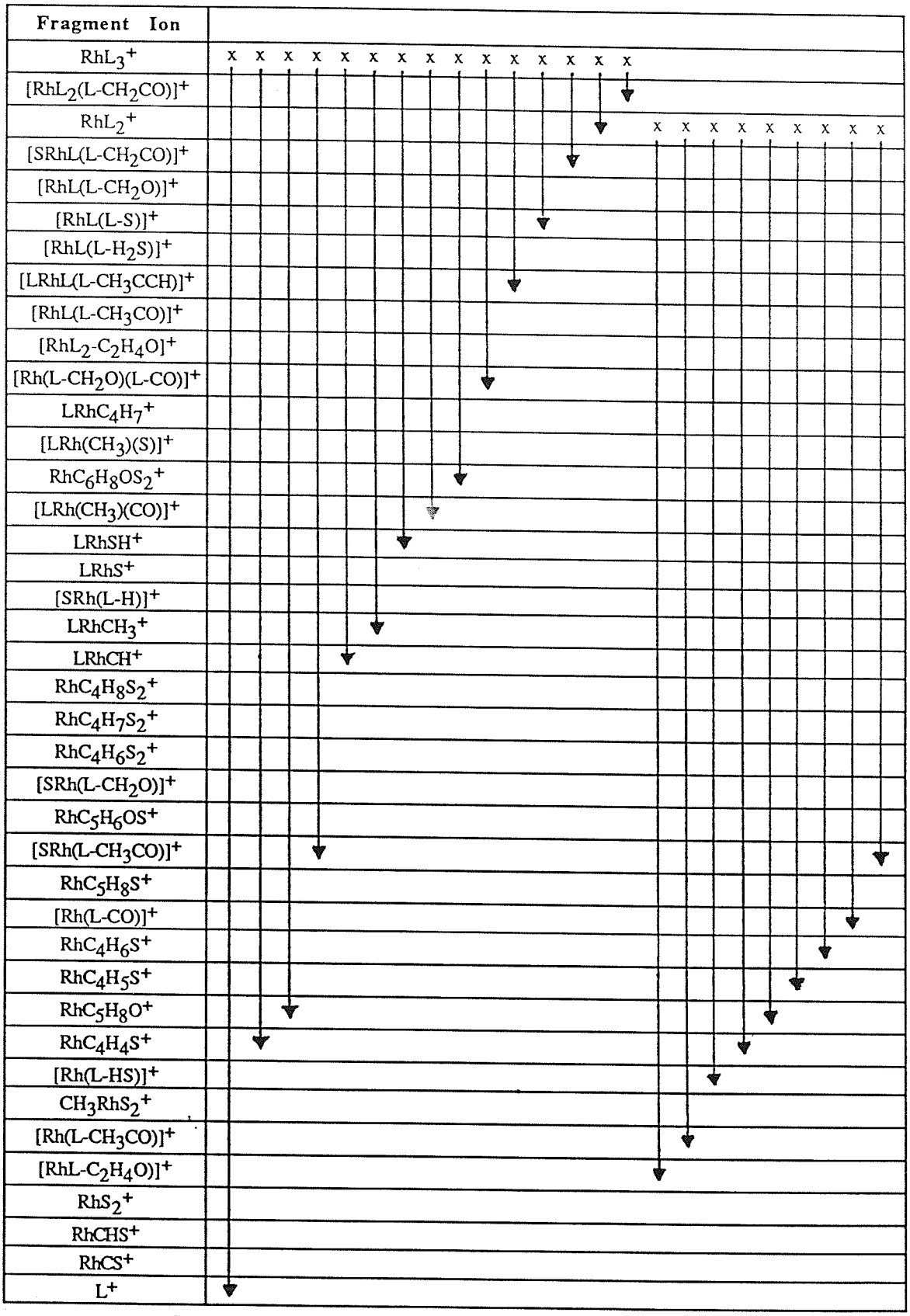

Scheme 3.25 Fragmentation pathways of $Rh(Sacac)_3$

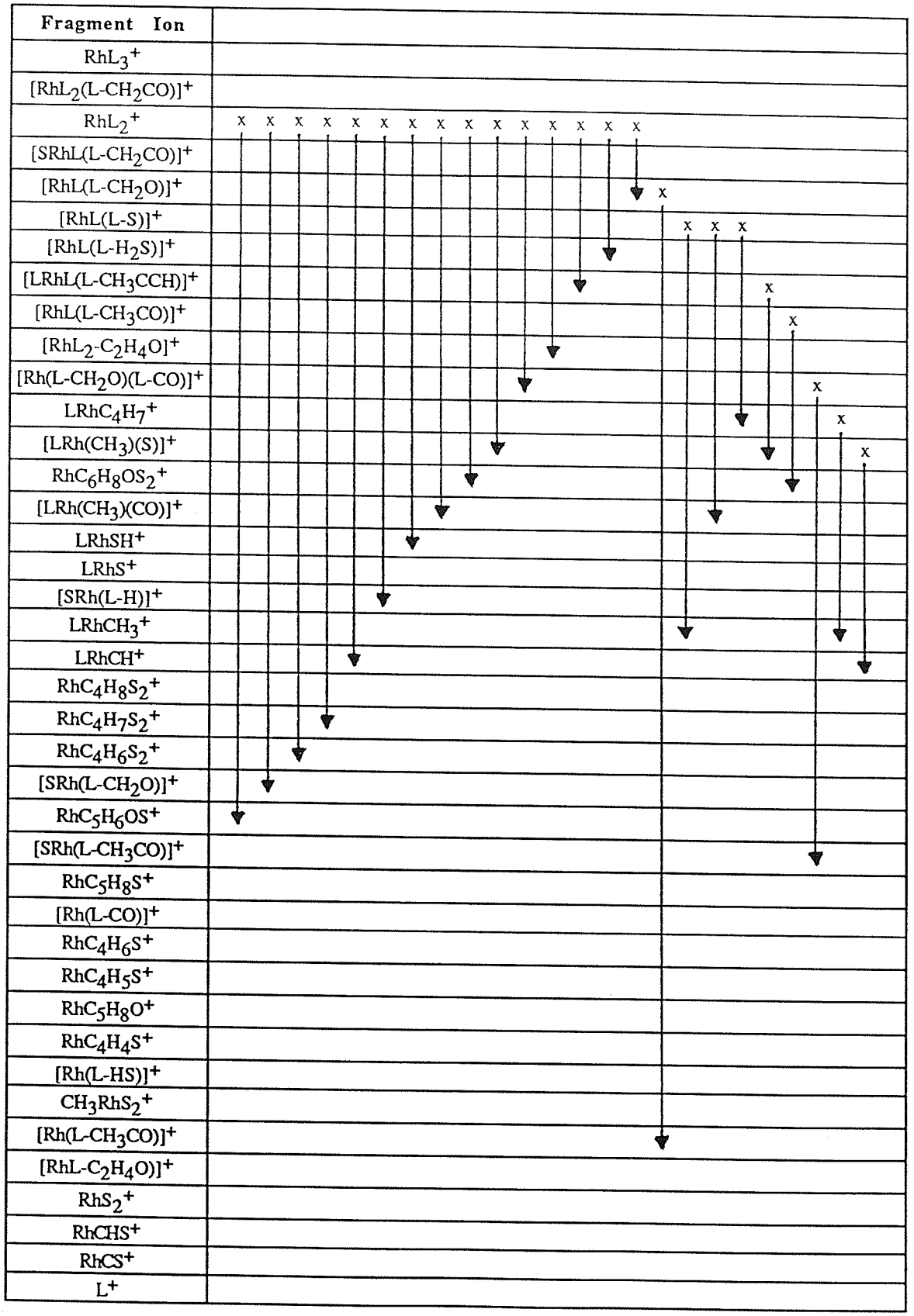

Scheme 3.25 Continued

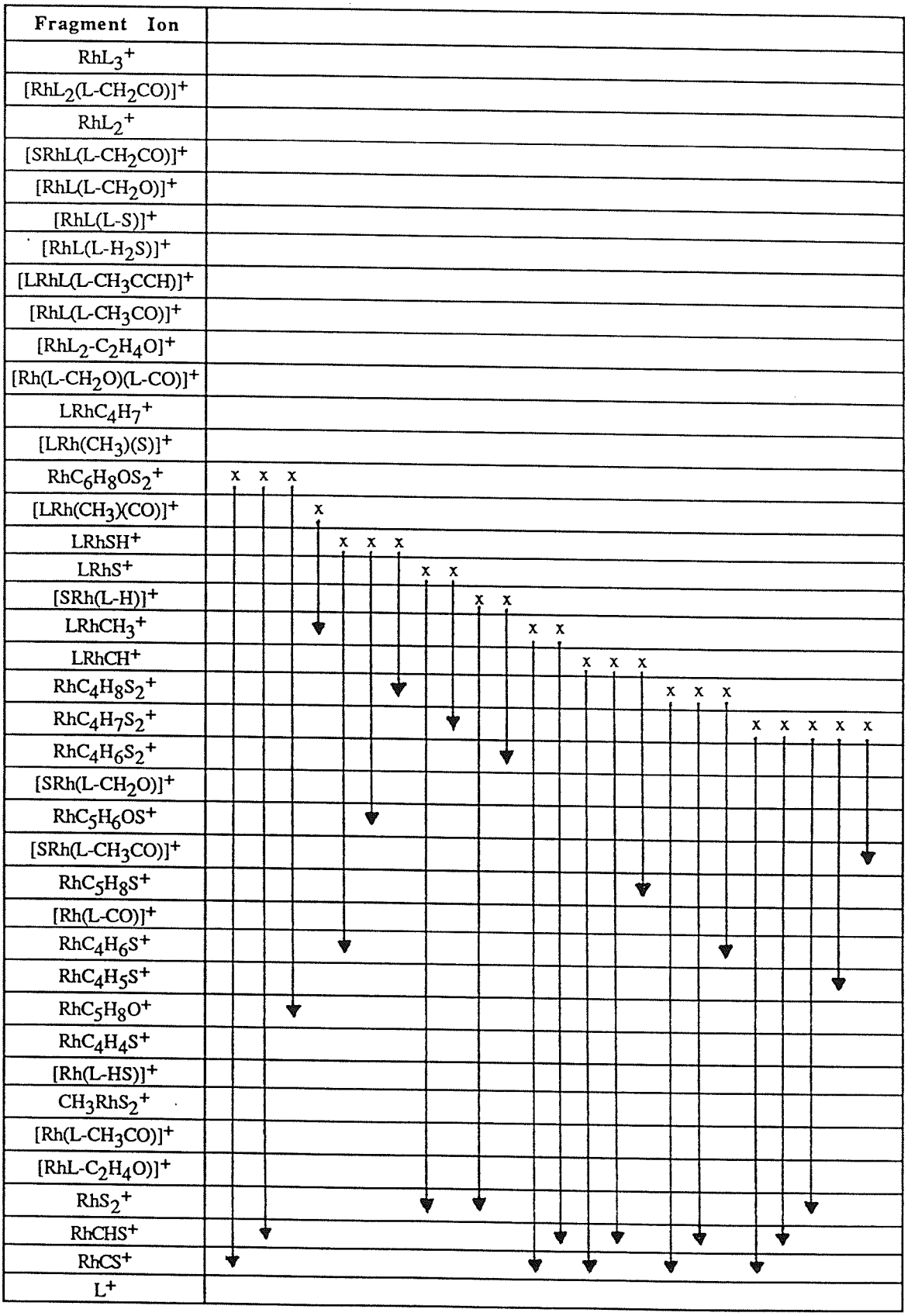

Scheme 3.25 Continued

Fragment Ion	
RhL_3^+	
$[RhL_2(L\text{-}CH_2CO)]^+$	
RhL_2^+	
$[SRhL(L\text{-}CH_2CO)]^+$	
$[RhL(L\text{-}CH_2O)]^+$	
$[RhL(L\text{-}S)]^+$	
$[RhL(L\text{-}H_2S)]^+$	
$[LRhL(L\text{-}CH_3CCH)]^+$	
$[RhL(L\text{-}CH_3CO)]^+$	
$[RhL_2\text{-}C_2H_4O]^+$	
$[Rh(L\text{-}CH_2O)(L\text{-}CO)]^+$	
$LRhC_4H_7^+$	
$[LRh(CH_3)(S)]^+$	
$RhC_6H_8OS_2^+$	
$[LRh(CH_3)(CO)]^+$	
$LRhSH^+$	
$LRhS^+$	
$[SRh(L\text{-}H)]^+$	
$LRhCH_3^+$	
$LRhCH^+$	
$RhC_4H_8S_2^+$	
$RhC_4H_7S_2^+$	
$RhC_4H_6S_2^+$	x x x x
$[SRh(L\text{-}CH_2O)]^+$	
$RhC_5H_6OS^+$	x x x
$[SRh(L\text{-}CH_3CO)]^+$	x x x
$RhC_5H_8S^+$	
$[Rh(L\text{-}CO)]^+$	
$RhC_4H_6S^+$	x x
$RhC_4H_5S^+$	x x
$RhC_5H_8O^+$	
$RhC_4H_4S^+$	
$[Rh(L\text{-}HS)]^+$	
$CH_3RhS_2^+$	x x x
$[Rh(L\text{-}CH_3CO)]^+$	x
$[RhL\text{-}C_2H_4O)]^+$	
RhS_2^+	
$RhCHS^+$	
$RhCS^+$	
L^+	

Scheme 3.25 Continued

B) *Rh(Stfa)$_3$*

Scheme 3.26 shows decomposition of RhL_2^+, **E441a**, by processes involving the formation of an Rh-CF_3 bond, with either simultaneous loss of the remaining portion of the ligand (L-CF_3) or subsequent formation of a Rh-CO bond and elimination of the neutral fragment CH_3CCH to produce the ions $LRhCF_3^+$, **E341**, and $[RhL(L\text{-}CH_3CCH)]^+$, **E401**, respectively. Consecutive losses of CO and $\cdot CF_3$ from **E401** yield $[LRh(S)(CF_3)]^+$, **E373**, and $LRhS^+$, **E304**, respectively; the latter ion can be written with rhodium in the +IV oxidation state. This ion then proceeds to lose a carbonyl group to give $RhC_4H_4F_3S_2^+$, **E276**; the mechanism, once again, involves migration of the $\cdot CF_3$ group to the metal. Consecutive losses of CH_3CCH and $\cdot CF_3$ (the latter indicating the reduction of Rh(IV) to Rh(III)) from **E276** lead to the formation of ions $CF_3RhS_2^+$, **E236a**, and RhS_2^+, **E167**, respectively. Alternatively, $\cdot CF_3$ can be lost first to yield $[SRh(L\text{-}CF_3CO)]^+$, **E207a**, for which the cyclic ion **E207b** should be the preferred structure. Loss of CH_3CCH from **E207a** gives, once again, **E167**.

Loss of the neutral fragment (L-SH) from **E441a** gives rise to one of the more abundant metal-containing ions in the mass spectrum of this complex, $RhC_5H_8OS_2^+$, **E305(a,b)**. I have proposed three mechanisms for the formation of this ion (Scheme 3.27). The first two (a,b) involve the migration of a methyl hydrogen or a bridging hydrogen, respectively, to the sulfur atom of the same ligand, yielding in both cases, $LRhSH^+$, **E305a**. The latter decomposition (c) involves migration of the bridging hydrogen to the metal to yield $LRhS(H)^+$, **E305b**. Although formation of **E305b**

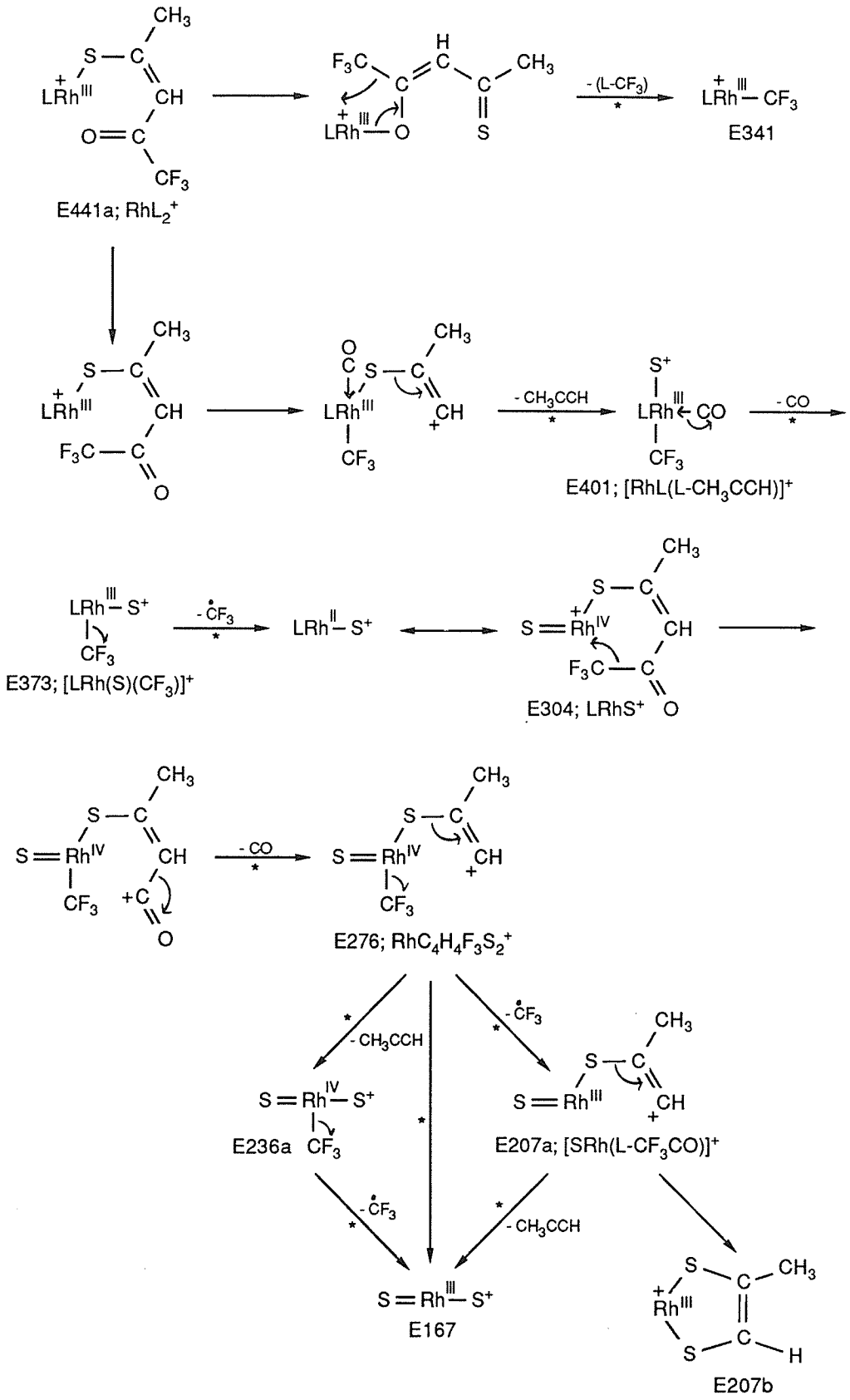
E441a; RhL2+
E341
E401; [RhL(L-CH3CCH)]+
E373; [LRh(S)(CF3)]+
E304; LRhS+
E276; RhC4H4F3S2+
E236a
E207a; [SRh(L-CF3CO)]+
E167
E207b

Scheme 3.26

a)

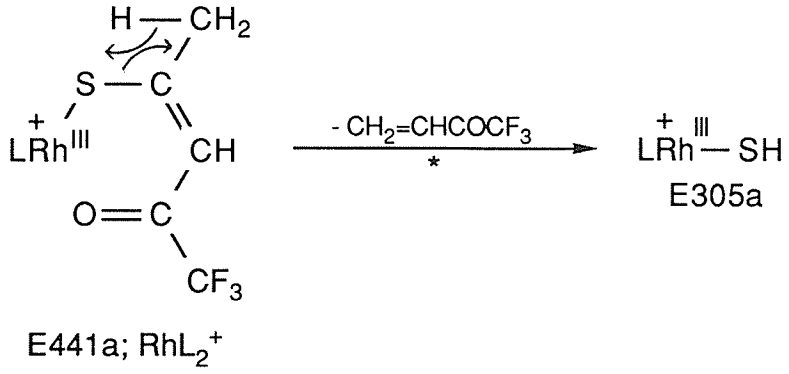

E441a; RhL_2^+ E305a

b)

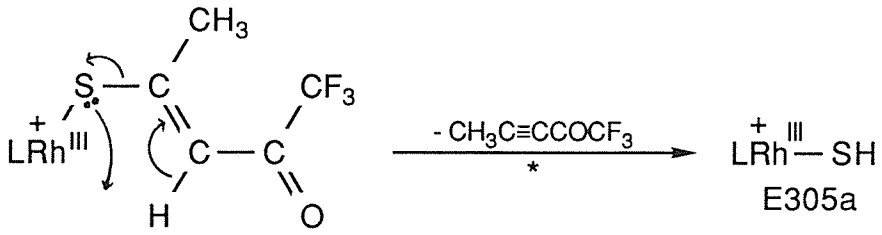

E441a; RhL_2^+ E305a

c)

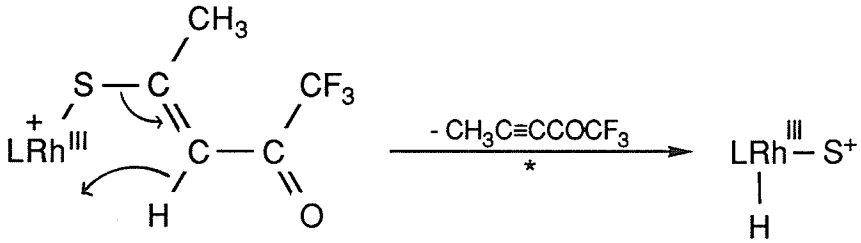

E441a; RhL_2^+ E305b

Scheme 3.27

cannot be ruled out, subsequent decompositions involving losses of $CF_3\dot{C}O$, $\cdot CF_3$, CO (Scheme 3.28) and H_2S (Scheme 3.29) are more readily explained if they occur from **E305a**, rather than from **E305b**.

From **E305a**, the neutral radical $CF_3\dot{C}O$ can be lost directly, giving rise to the ion $[HSRh(L\text{-}CF_3CO)]^+$, **E208a**, (Scheme 3.28), for which the cyclic ion, **E208b**, should be the preferred structure, or by a two step process involving first, the loss of $\cdot CF_3$ to give $[HSRh(L\text{-}CF_3)]^+$, **E236b**, which then can lose CO to yield, once again, **E208(a,b)**. Alternatively, **E208(a,b)**, can be formed by a process which first involves the loss of $CF_3\dot{C}O$ from **E441a**, giving rise to $[RhL(L\text{-}CF_3CO)]^+$, **E344**, which in turn, loses (L-SH). Consecutive eliminations of CH_3CCH and CO from **E344** yield $LRhS^+$, **E304**, and $RhC_4H_4F_3S_2^+$, **E276**, respectively. Decompositions of **E276** can be rationalized by mechanisms previously discussed in Scheme 3.26. Decomposition of **E305a** also occurs by consecutive losses of CO and HF to yield $[HSRh(L\text{-}CO)]^+$, **E277**, and $[HSRh(L\text{-}CO\text{-}HF)]^+$, **E257(a,b)**, respectively. (These processes, however, are not as significant as the losses of $CF_3\dot{C}O$, $\cdot CF_3$ or H_2S (to be discussed below, Scheme 3.29), evident from the corresponding daughter ion intensities and of those in the normal mass spectrum.) The proposed mechanism involves prior migration of the $\cdot CF_3$ group from the metal to the carbon atom from which the carbonyl group was previously lost. As mentioned in Section 3.1.1, when discussing the mass spectra of $Rh(SbzC_2F_5)_3$ and $Rh(SbzC_3F_7)_3$, the idea of a labile CF_3-Rh bond is strengthened by the existence of several compounds with a Rh-CF bond[72-74] (C_F = fluoroalkyl), and the presence of various ions such as $LRhCF_3^+$, **E341**,

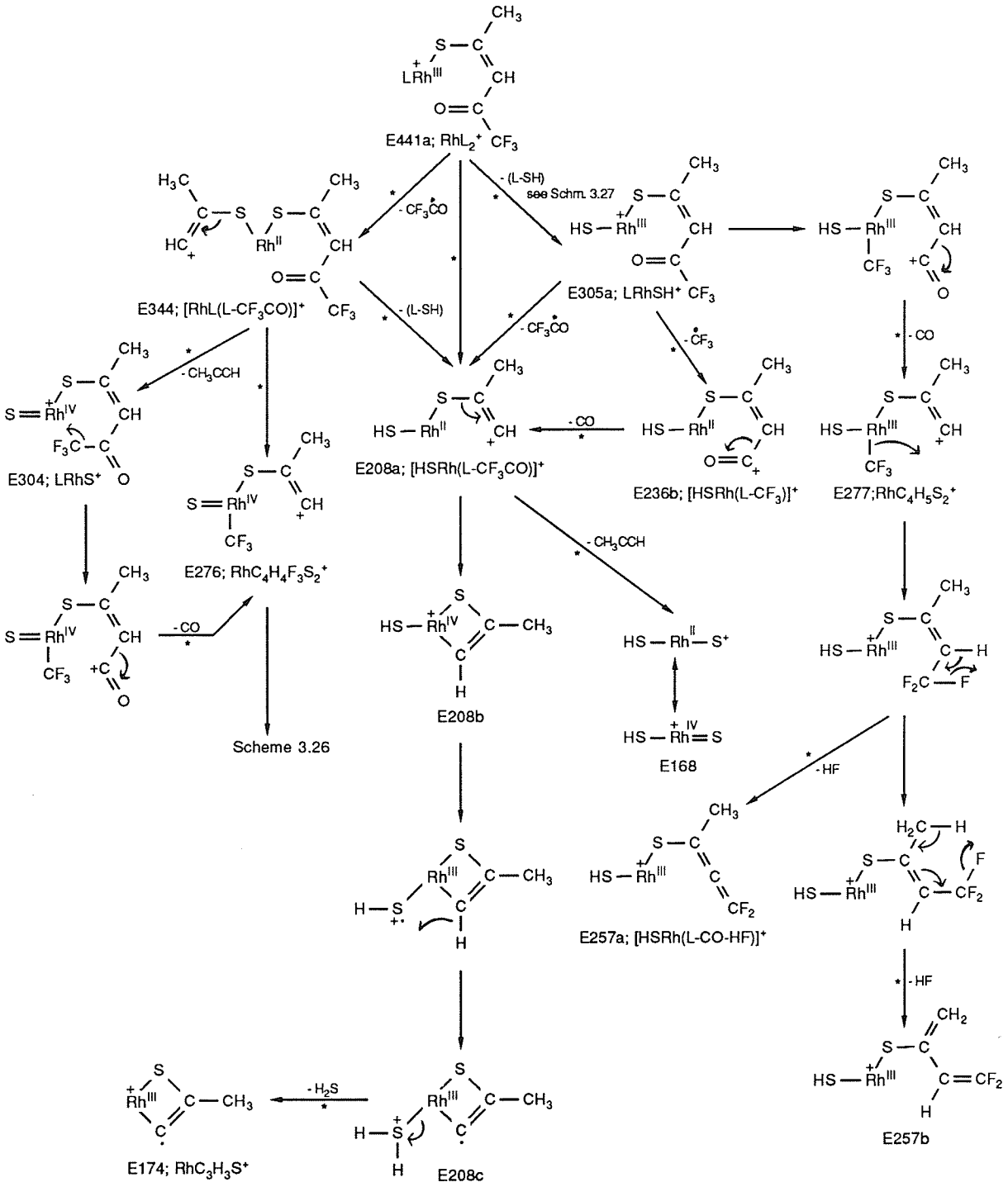
E441a; RhL2+ CF3
E344; [RhL(L-CF3CO)]+
E305a; LRhSH+ CF3
E304; LRhS+
E276; RhC4H4F3S2+
E208a; [HSRh(L-CF3CO)]+
E236b; [HSRh(L-CF3)]+
E277;RhC4H5S2+
E208b
E168
E257a; [HSRh(L-CO-HF)]+
E257b
E174; RhC3H3S+
E208c
Scheme 3.26
see Schm. 3.27
- (L-SH)
- CF3CO
- CH3CCH
- CO
- CF3
- HF
- H2S

Scheme 3.28

$[RhL(L\text{-}CH_3CCH)]^+$, **E401**, and $[LRh(S)(CF_3)]^+$, **E373** (all shown in Scheme 3.26). Failure to observe ions such as $LRhCH_3^+$ and $[RhL(L\text{-}CF_3CCH)]^+$ supports the idea of a strong Rh-S bond since their formation would require scission of this bond. The hydrogen atom transferred to the neutral product HF may originate from either the bridging carbon atom, giving rise to **E257a**, or from the methyl group *via* a six-membered cyclic transition state to give **E257b**. Elimination of H_2S from **E208b**, yielding the moderately abundant ion $RhC_3H_3S^+$, **E174**, is also described in Scheme 3.28. Following sulfur-to-metal electron transfer (i.e. reduction of Rh(IV) to Rh(III)) migration of the bridging hydrogen to the electron deficient sulfur atom of the other ligand yields **E208c**, which can then lose H_2S to give **E174**. Also observed is the elimination of CH_3CCH from **E208a** to give $HSRhS^+$, **E168**.

Loss of H_2S is also observed prior to the loss of $CF_3\dot{C}O$ from **E305a**, yielding $[Rh(L\text{-}H)]^+$, **E271** (Scheme 3.29). The proposed mechanism involves migration of hydrogen from the bridging carbon atom of the intact ligand to the electron deficient sulfur atom of the other ligand (following reduction of Rh(III) to Rh(II)) and is similar to that proposed for loss of H_2S from **E208b** (Scheme 3.28). Loss of $CF_3\dot{C}O$ from **E271** yields, once again, the cyclic radical ion **E174**. Scheme 3.29 also illustrates the postulated mechanism for the fragmentation sequence: $[Rh(L\text{-}H)]^+$ ---> $[Rh(L\text{-}H\text{-}CO)]^+$ ---> $[Rh(L\text{-}H\text{-}CO\text{-}HF)]^+$ ---> RhS^+. Elimination of the neutral fragment (L-H) from **E271** gives rise to the bare metal ion Rh^+, **E103**.

Simultaneous elimination of the even-electron neutral fragments $CH_3C{\equiv}CH$ and $HCOCF_3$ from **E441b** gives rise to $[SRh(L\text{-}H)]^+$, **E303**

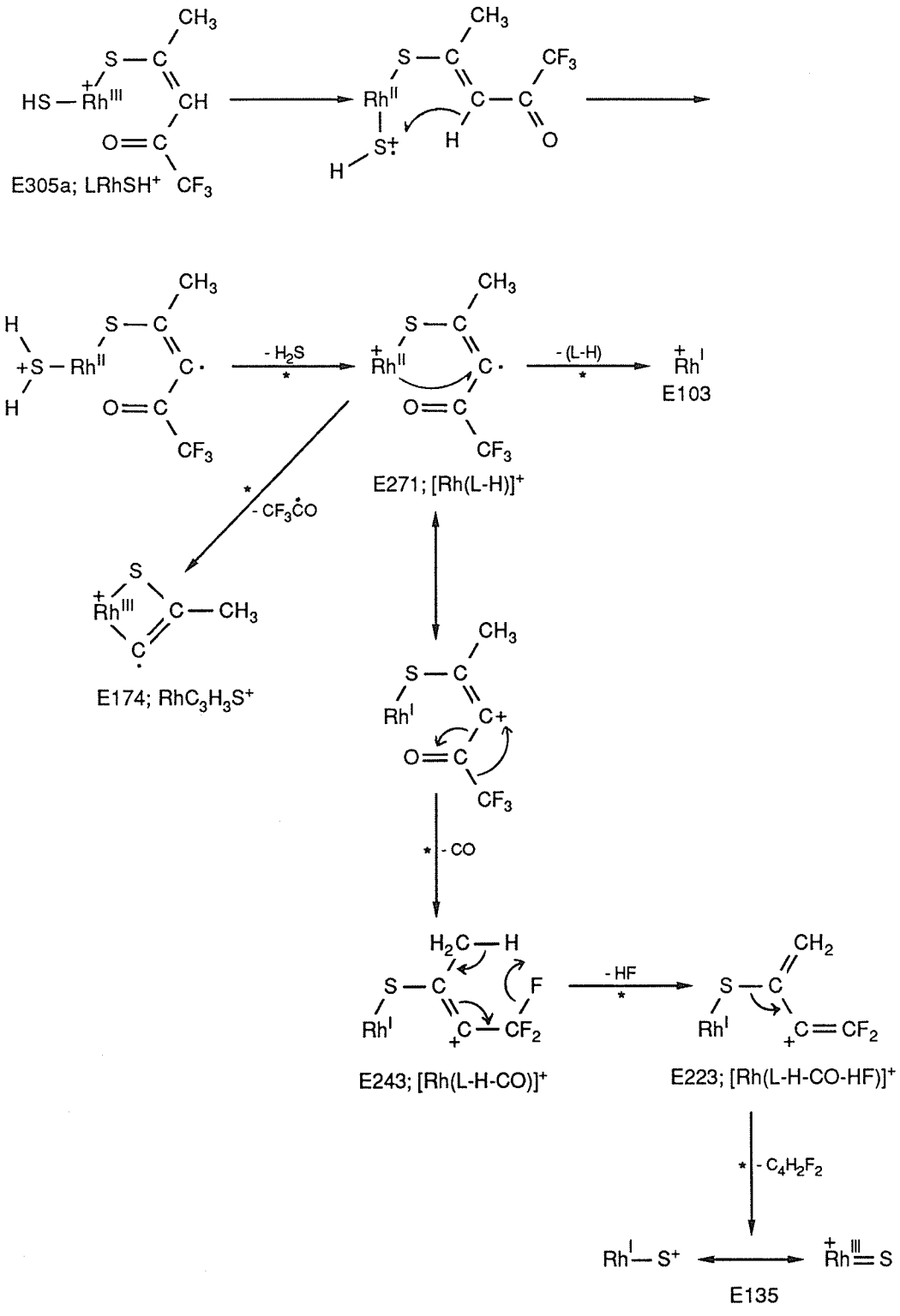
E305a; LRhSH+ CF3
E271; [Rh(L-H)]+
E103
E174; RhC3H3S+
E243; [Rh(L-H-CO)]+
E223; [Rh(L-H-CO-HF)]+
E135

Scheme 3.29

(Scheme 3.30). The postulated mechanism involves migration of the bridging hydrogen atom of one ligand to the oxygen atom of the other, followed by the loss of the above mentioned neutrals. Loss of CO from **E303** yields $[SRh(L\text{-}CO)]^+$, **E275a**, which in turn, can lose the even-electron neutral fragments $CH_3C{=}CCF_3$ or HF to give RhS_2^+, **E167**, and $[SRh(L\text{-}H\text{-}CO\text{-}HF)]^+$, **E255**, respectively, or undergo rearrangement to give the cyclic ion **E275b**. Loss of the neutral fragment $C_4H_2F_2$ from **E255** to give, once again, **E167** is postulated, but is not confirmed by metastable ion decomposition evidence. Elimination of the even-electron neutral fragment LH from **E441b** yields $[Rh(L\text{-}H)]^+$, **E271**, for which decomposition mechanisms have been rationalized previously (Scheme 3.29).

Decomposition leading to the formation of $[Rh(L\text{-}HS)]^+$, **E239a**, is of some interest. Metastable ion decomposition evidence indicates that this ion is formed by consecutive losses of the neutral fragments (L-H) and H_2S from RhL_2^+, **E441a** (Scheme 3.31). The postulated mechanism involves migration of the bridging hydrogen atom of one ligand to the electron deficient sulfur of the thiocarbonyl group on the other ligand followed by loss of (L-H) to give $RhC_5H_5F_3^+$, **E273b**. Loss of the stable even-electron neutral fragment H_2S from **E273c** gives the moderately abundant ion **E239a** (%RA = 7.6), which, can rearrange *via* a six-membered ring cyclic transition state to **E239b** which, on loss of CO yields $[Rh(L\text{-}HS\text{-}CO)]^+$, **E211**.

Elimination of the neutral fragments (L-H), CO and HF from **E441a** in the decomposition sequence: RhL_2^+ ---> $LRhH^+$ ---> $RhC_4H_5F_3S^+$ ---> $[HRh(L\text{-}CO\text{-}HF)]^+$ is described in Scheme 3.32. Migration of the hydrogen to the metal and not to the oxygen atom of

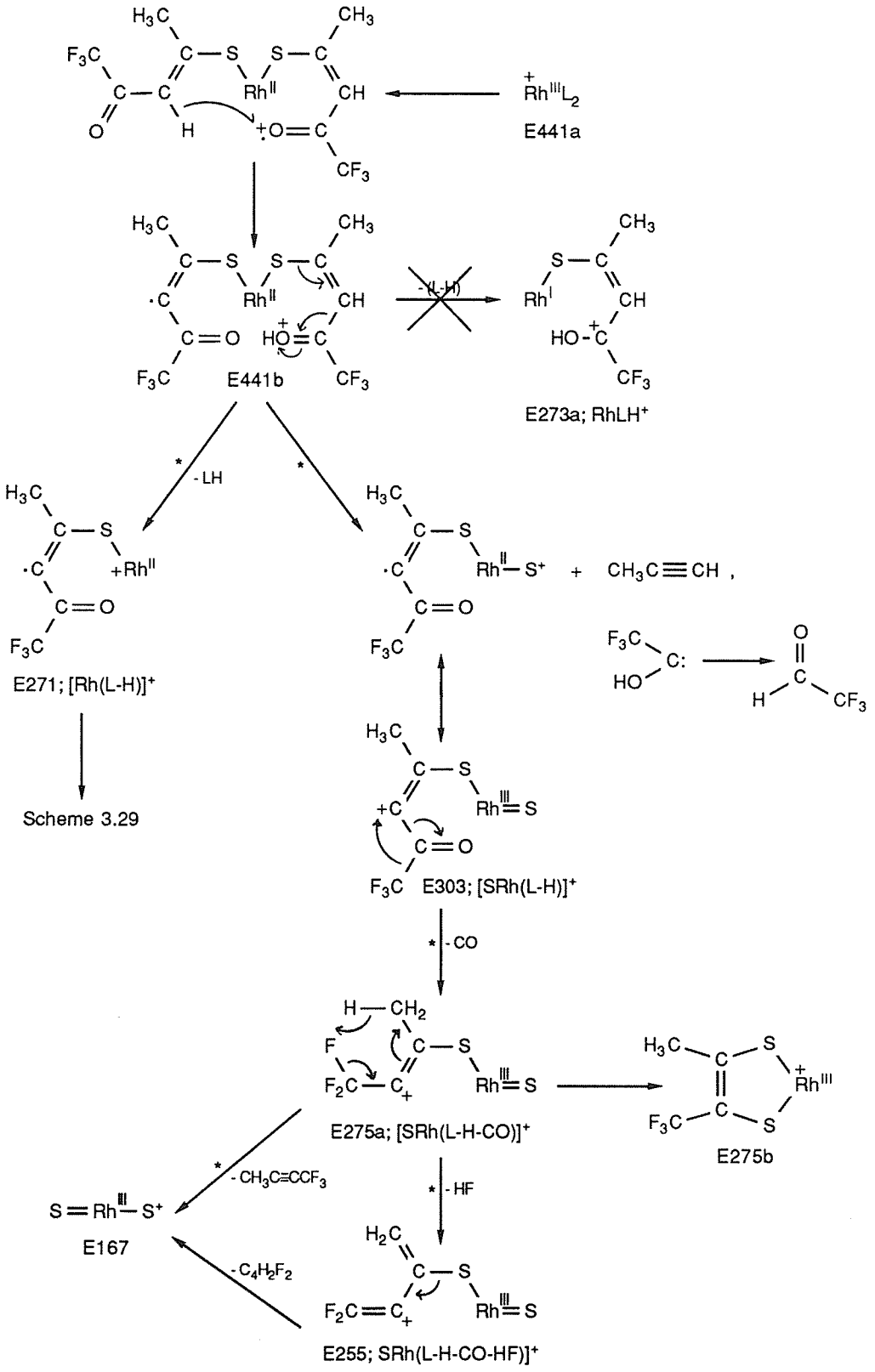
E441a
E441b
E273a; RhLH+
E271; [Rh(L-H)]+
Scheme 3.29
E303; [SRh(L-H)]+
E275a; [SRh(L-H-CO)]+
E275b
E167
E255; SRh(L-H-CO-HF)]+
- LH
- CO
- HF
- CH3C≡CCF3
- C4H2F2

Scheme 3.30

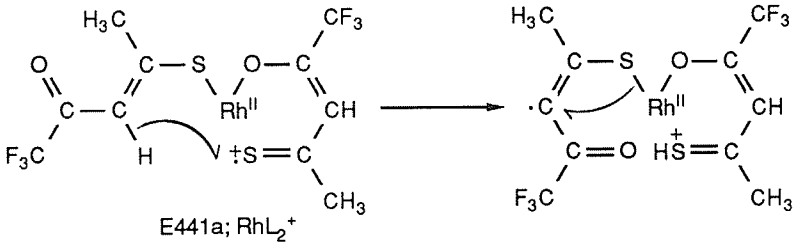

E441a; RhL_2^+

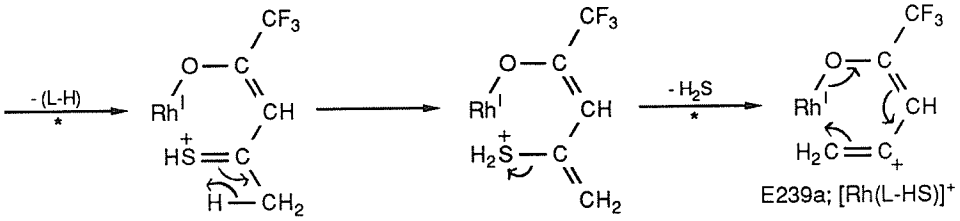

E273b; $RhC_5H_5F_3^+$ E273c E239a; $[Rh(L\text{-}HS)]^+$

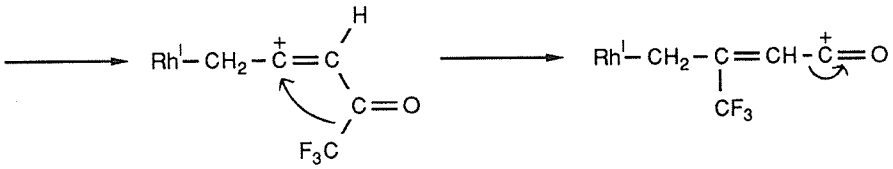

E239b

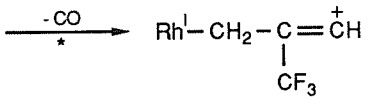

E211; $[Rh(L\text{-}HS\text{-}CO)]^+$

Scheme 3.31

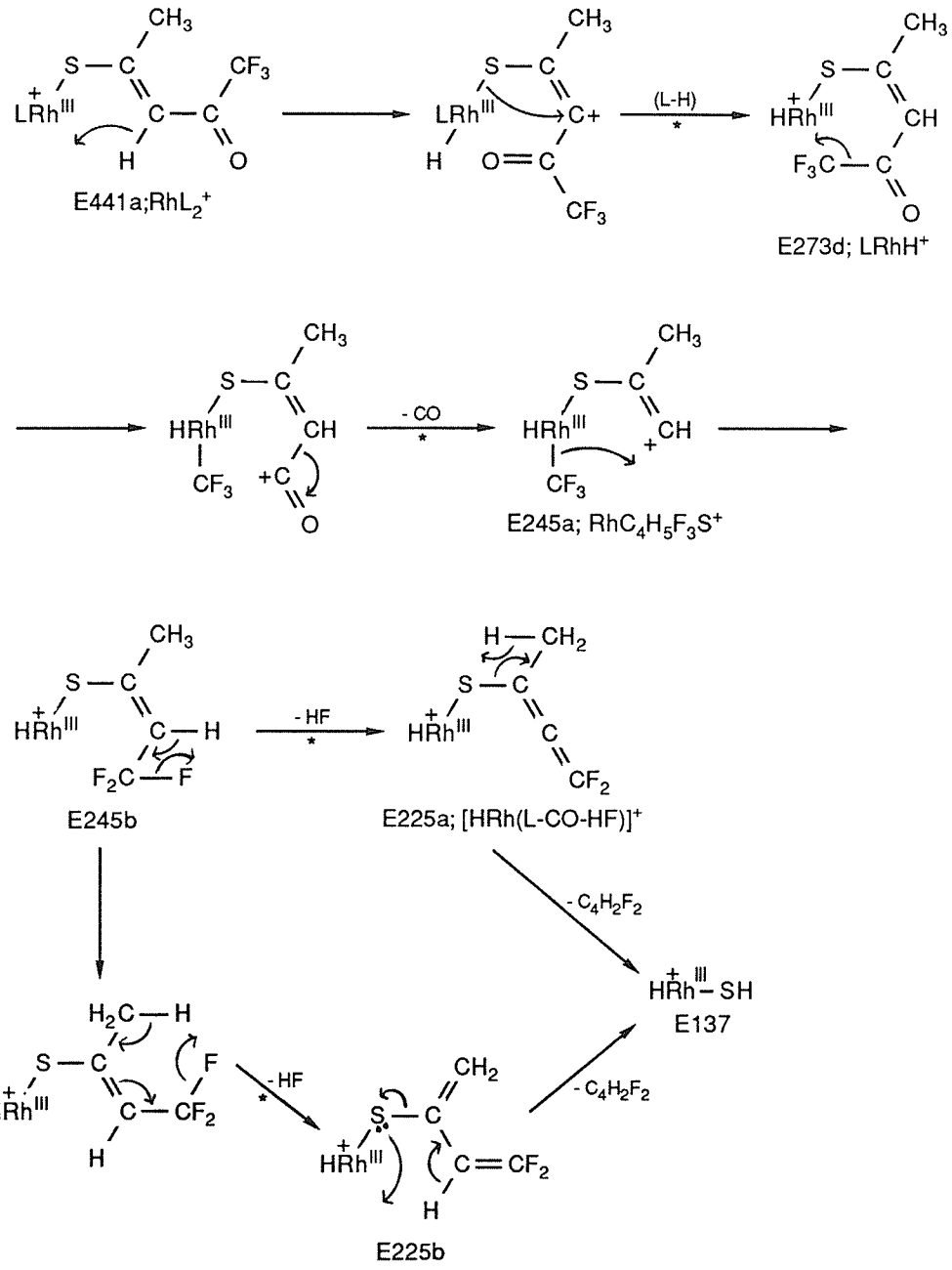
E441a;RhL2+
E273d; LRhH+
E245a; RhC4H5F3S+
E245b
E225a; [HRh(L-CO-HF)]+
E137
E225b
(L-H)
- CO
- HF
- C4H2F2

Scheme 3.32

another ligand, as proposed in Scheme 3.30, leading to the formation of $LRhH^+$, **E273d**, opposed to $RhLH^+$ **E273a**, is supported by the subsequent loss of CO to give $RhC_4H_5F_3S^+$, **E245(a,b)**. Loss of CO from **E273b** (Scheme 3.31) would be difficult to explain. The proposed mechanism for loss of HF from **E245b**, to give $[HRh(L\text{-}CO\text{-}HF)]^+$, **E225(a,b)**, is analogous to that proposed earlier for the formation of the ion $[HSRh(L\text{-}CO\text{-}HF)]^+$, **E257(a,b)**, from $RhC_4H_5S_2^+$, **E277** (Scheme 3.28). Although not supported by metastable ion decomposition evidence, loss of the neutral fragment $C_4H_2F_2$ from **E225(a,b)** could give rise to $HRhSH^+$, **E137**.

Consecutive losses of the neutral radicals ·L and CF_3CO from RhL_2^+, **E441a** (each indicating a reduction in the oxidation state of rhodium) yield the low abundance ion RhL^+, **E272**, and one of the more abundant metal-containing ions, $[Rh(L\text{-}CF_3CO)]^+$, **E175a**, respectively (Scheme 3.33). **E175a** can undergo either rearrangement, to give the cyclic ion **E175b**, or can lose the neutral fragment CH_3CCH to give RhS^+, **E135**. Consecutive losses of CO and HF from **E272**, following $\cdot CF_3$ migration to the metal, yield $[Rh(L\text{-}CO)]^+$, **E244**, and $[Rh(L\text{-}CO\text{-}HF)]^+$, **E224(a,b)**, respectively. The postulated mechanism is analogous to that proposed earlier for the loss of HF from **E277** (Scheme 3.28) and **E245b** (Scheme 3.32). Loss of the even-electron neutral $C_4H_2F_2$ from **E224(a,b)** (unsupported by metastable ion decomposition evidence) yields $RhSH^+$, **E136**.

C) *$Rh(Sacac)_3$*

In the mass spectra of $Rh(SbzC_2F_5)_3$ and $Rh(SbzC_3F_7)_3$, the ion $[RhL(L\text{-}S)]^+$ **(A633,B733)** is formed by the loss of ·L from

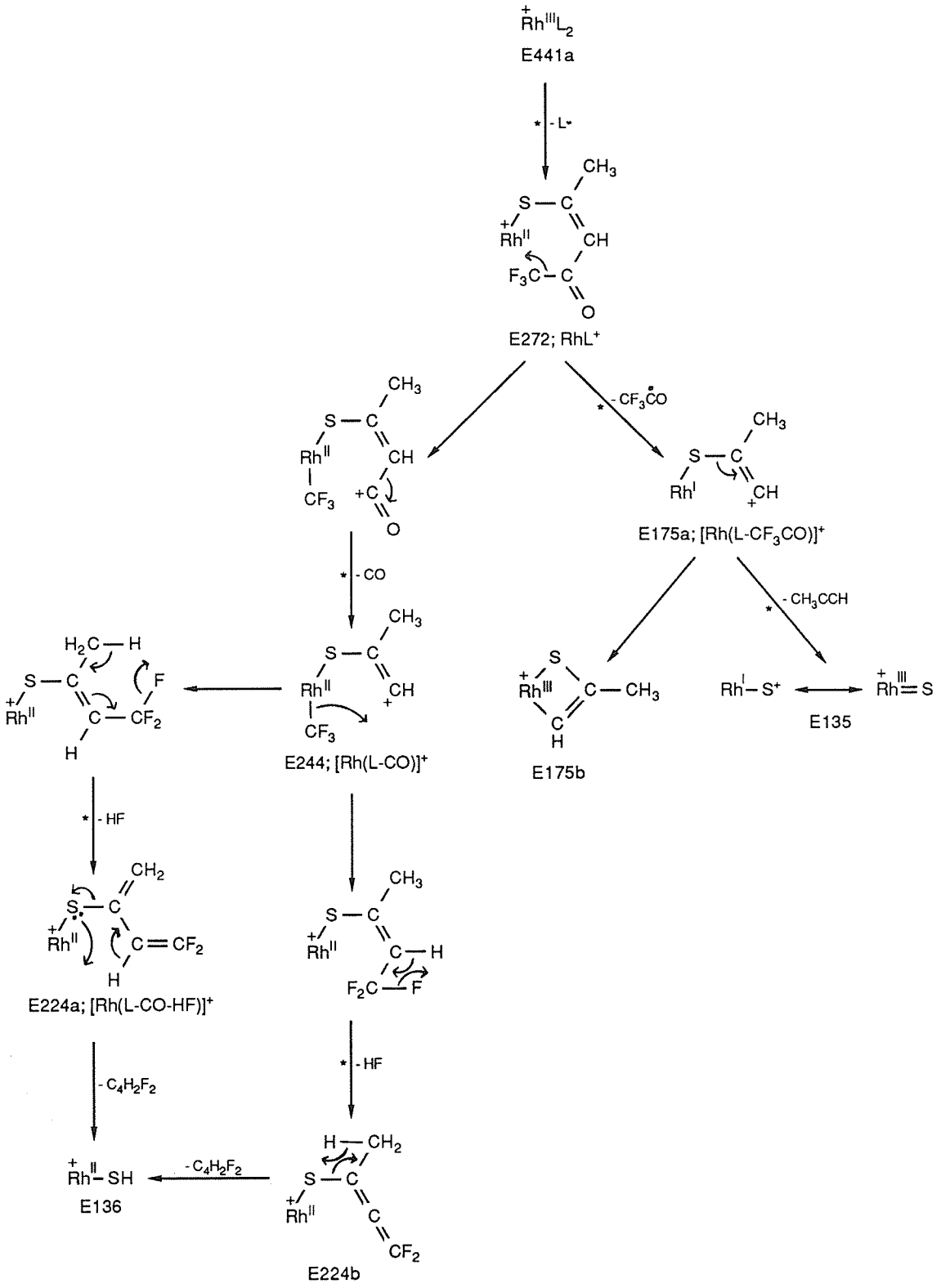
E441a
- L•
E272; RhL+
- CF3CO
E175a; [Rh(L-CF3CO)]+
- CO
E244; [Rh(L-CO)]+
- CH3CCH
E175b
E135
- HF
E224a; [Rh(L-CO-HF)]+
- HF
- C4H2F2
E136
- C4H2F2
E224b

Scheme 3.33

$[RhL_2(L\text{-}S)]^+$ **(A914,B1064)** (Section 3.1.1, Scheme 3.17). Direct loss of sulfur from their molecular ions and not from RhL_2^+, was rationalized by the decreased b-character of rhodium in the molecular ion, due to its higher oxidation state (+IV), and the competition of the three sulfur atoms for the available dπ-electrons. The ion $[RhL(L\text{-}S)]^+$, is also observed in the mass spectrum of $Rh(Sacac)_3$ and to a lesser extent in that of $Rh(Stfa)_3$. However, although metastable ion decompositions of RhL_3^+ **(E610,F448)** to $[RhL(L\text{-}S)]^+$ **(E409,F301)** are observed for both of the latter complexes, in neither case is the supposed precursor ion $[RhL_2(L\text{-}S)]^+$ observed in the normal mass spectrum. This implies, following the elimination of sulfur from the molecular ion (with rhodium in the +IV oxidation state), a rapid loss of ·L, and reflects rhodium's preference for the +III oxidation state. The observation of $[RhL_2(L\text{-}S)]^+$ in the mass spectra of $Rh(SbzC_2F_5)_3$ and $Rh(SbzC_3F_7)_3$ can be explained by an increase in stabilization of the molecular ion due to the presence of the aromatic substituents. Scheme 3.34, shows decomposition pathways proposed for formation of $[RhL(L\text{-}S)]^+$, **F301**, and its daughters. Consecutive losses of the even-electron neutral fragments CO and CH_3CCH from **F301** yield $LRhC_4H_7^+$, **F273**, and $LRhCH_3^+$, **F233**, respectively. Alternatively, CH_3CCH can be lost first to give $[LRh(CO)(CH_3)]^+$, **F261**, which in turn loses CO to yield, once again, **F233**. The existence of these ions, and others, (see Schemes 3.35, 3.36, 3.38, 3.39) reflect the relative importance played by pathways involving methyl migration to the metal in the fragmentation of this complex.

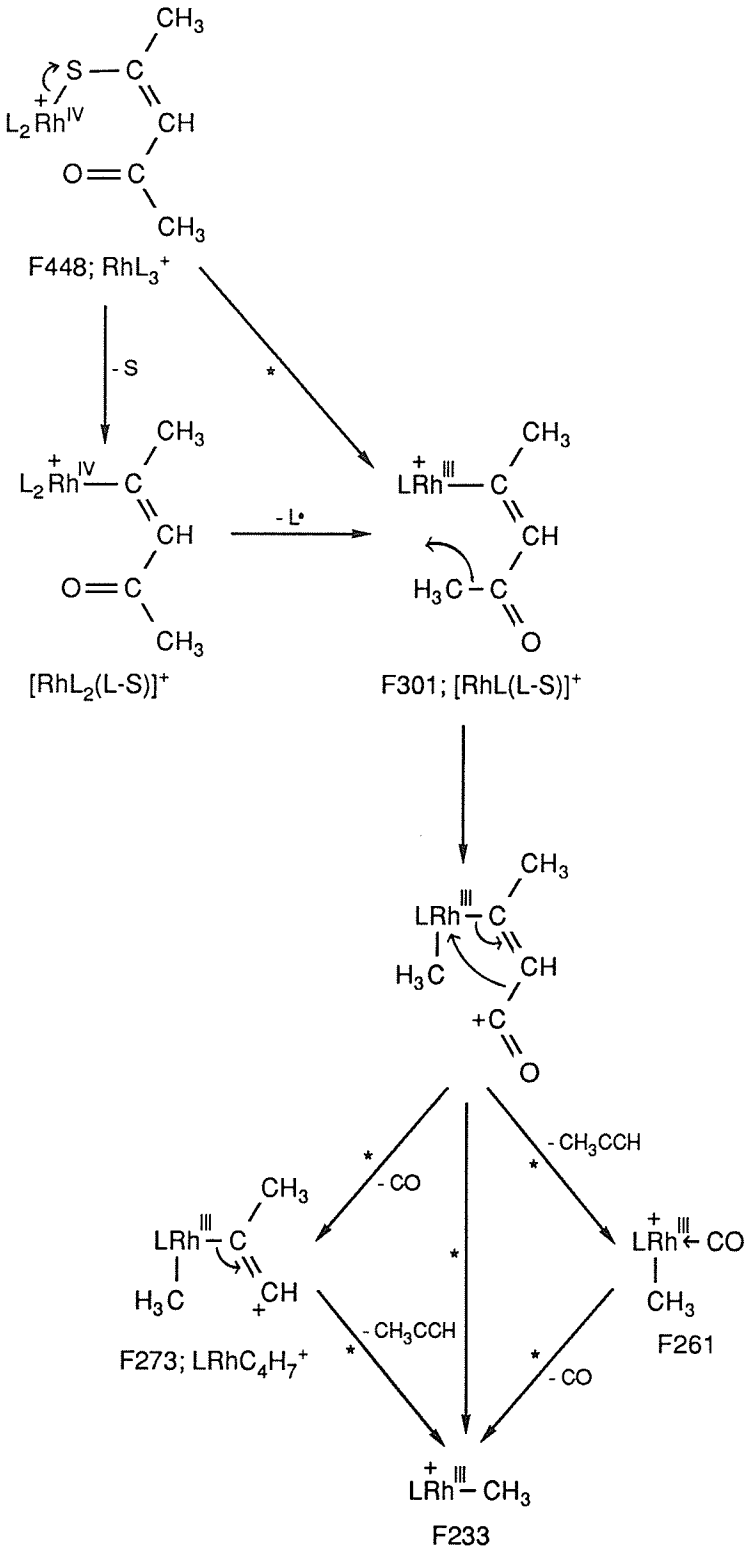
F448; RhL3+
- S
*
[RhL2(L-S)]+
- L•
F301; [RhL(L-S)]+
- CO
- CH3CCH
F273; LRhC4H7+
F261
F233

Scheme 3.34

Scheme 3.35 shows decomposition of RhL_2^+, **F333a**, by processes involving migration of both methyl and carbonyl groups to the metal. This is necessary to explain the loss of the neutral fragment CH_3CCH from **F333a**, to give $[RhL(L\text{-}CH_3CCH)]^+$, **F293**. Elimination of CO from **F293** yields $[LRh(S)(CH_3)]^+$, **F265**, which then loses H_2S to give the metal carbene ion $LRhCH^+$, **F231**. Following migration of the methyl group from the remaining intact ligand to the carbon residue of the fragmented ligand a second carbonyl group is lost, yielding $RhC_5H_8S^+$, **F203a**, for which the cyclic ion **F203b** should be the preferred structure.

Also observed in the mass spectrum of this complex is the ion $LRhSH^+$, **F251**. Its formation (Scheme 3.36) is exactly analogous to that proposed earlier for the corresponding ion, **E305(a,b)**, in the mass spectrum of $Rh(Stfa)_3$ (Scheme 3.27). Subsequent fragmentations of **F251** suggest that the mechanisms involving migration of hydrogen to the sulfur atom, rather than to the metal, is favored. Elimination of CO from **F251** yields $RhC_4H_8S_2^+$, **F223**, which can then lose H_2S to give the metal carbene ion $RhC_4H_6S^+$, **F189a**, for which the cyclic ion **F189b** should be the preferred stucture. Alternatively, H_2S can be lost first to give the ion $RhC_5H_6OS^+$, **F217a**, also a metal carbene ion, which can then lose CO to give, once again, **F189(a,b)**.

Scheme 3.37 illustrates the mechanisms proposed for the formation of $[SRh(L\text{-}H)]^+$, **F249**, and $[Rh(L\text{-}H)]^+$, **F217b**, from RhL_2^+, **F333(a,b)**, and their daughters. Migration of the bridging hydrogen atom of one ligand to the oxygen atom of the other, gives **F333b**, which can either lose the neutral fragment LH to yield **F217b** or can

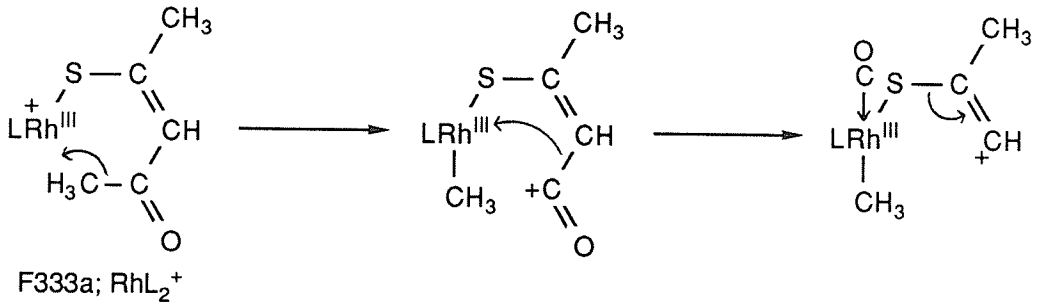

F333a; RhL_2^+

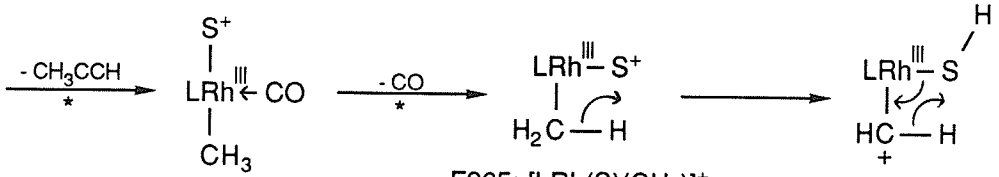

F293; $[RhL(L\text{-}CH_3CCH)]^+$

F265; $[LRh(S)(CH_3)]^+$

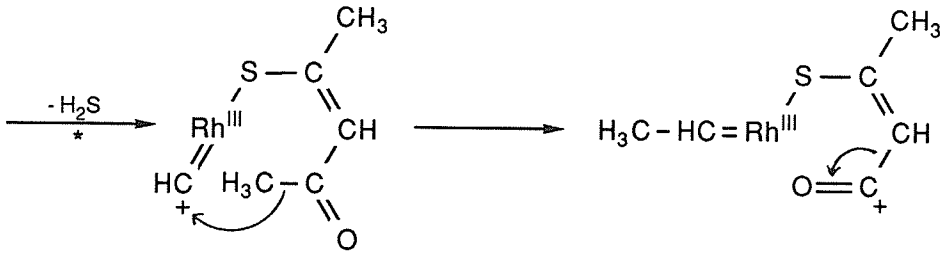

F231; $LRhCH^+$

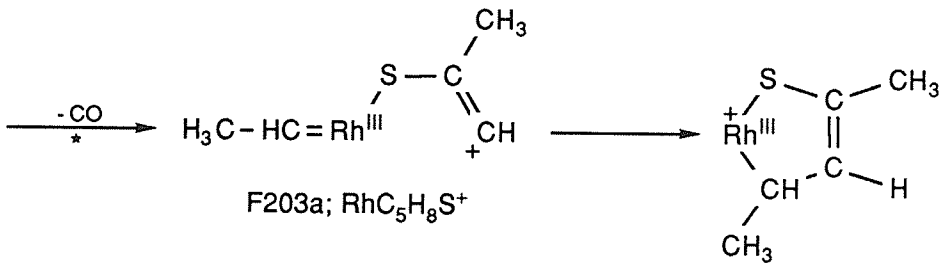

F203a; $RhC_5H_8S^+$

F203b

Scheme 3.35

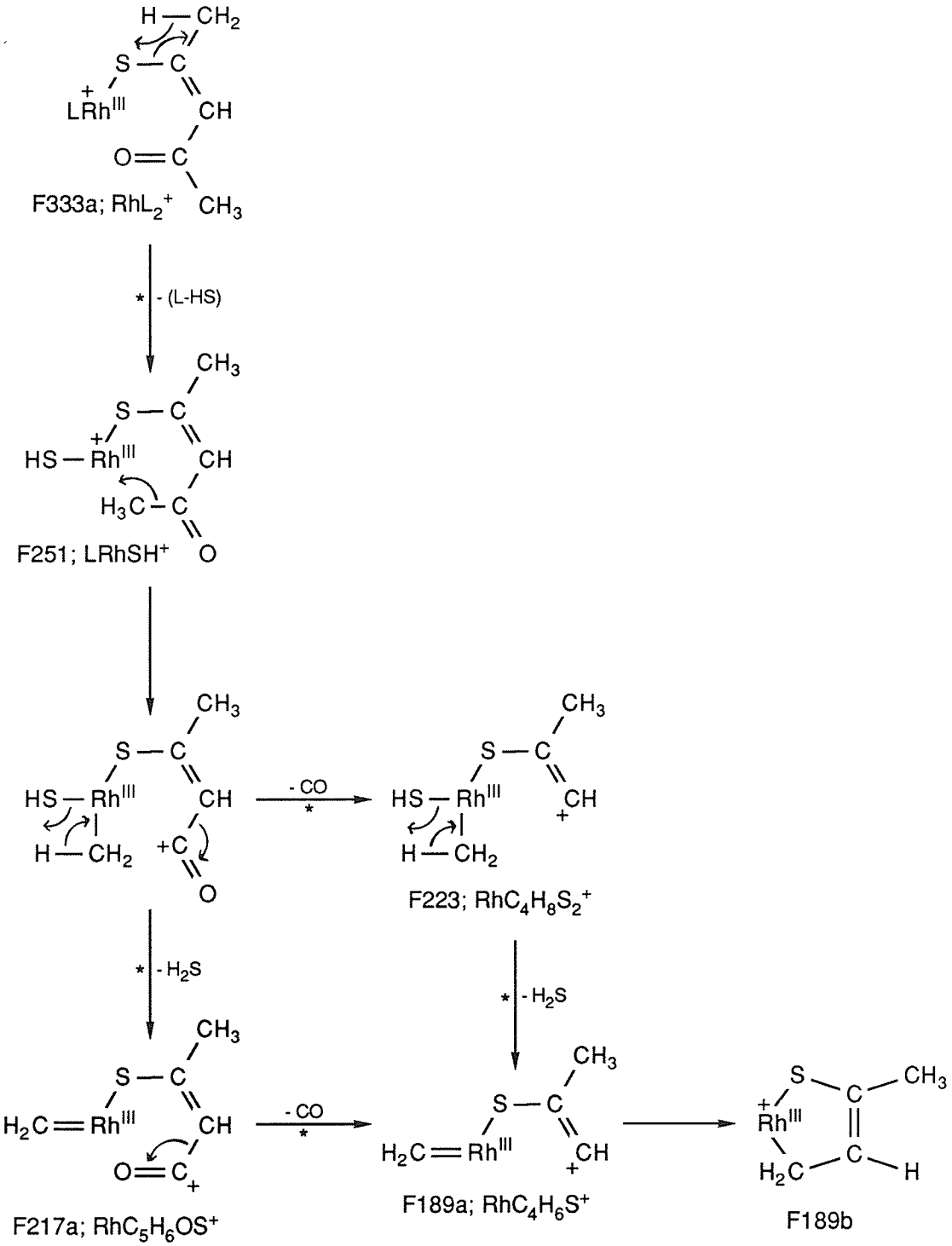
F333a; RhL2+
- (L-HS)
F251; LRhSH+
- CO
F223; RhC4H8S2+
- H2S
F217a; RhC5H6OS+
- CO
- H2S
F189a; RhC4H6S+
F189b

Scheme 3.36

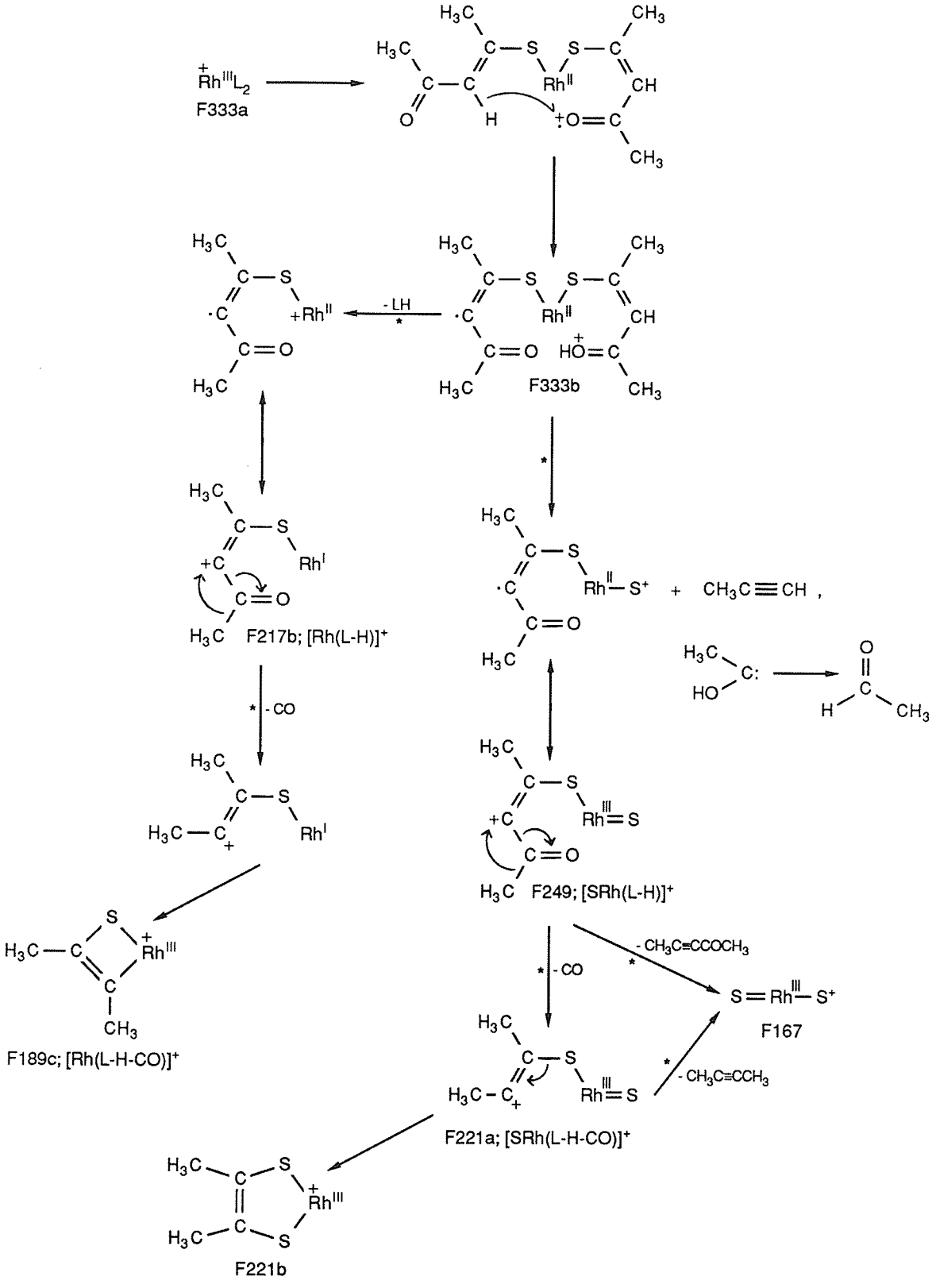
F333a
F333b
- LH
F217b; [Rh(L-H)]+
- CO
F189c; [Rh(L-H-CO)]+
+ CH3C≡CH ,
F249; [SRh(L-H)]+
- CH3C≡CCOCH3
F167
- CO
- CH3C≡CCH3
F221a; [SRh(L-H-CO)]+
F221b

Scheme 3.37

lose, simultaneously, the even-electron neutrals $CH_3C{\equiv}CH$ and CH_3CHO to give **F249**. Elimination of CO from **F217b** yields the cyclic ion $[Rh(L\text{-}H\text{-}CO)]^+$, **F189c**, while a similar loss from **F249** gives rise to $[SRh(L\text{-}H\text{-}CO)]^+$, **F221a**. This ion can then lose the even-electron neutral $CH_3C{\equiv}CCH_3$ to give RhS_2^+, **F167**, or undergo rearrangement to give the cyclic ion **F221b**. Loss of the even-electron neutral $CH_3C{\equiv}CCOCH_3$ from **F249** yields, once again, **F167**.

Elimination of the neutral fragments CH_2O, CO, C_5H_8 and CH_3CCH from **F333a** in the decomposition sequence RhL_2^+---> $[RhL(L\text{-}CH_2O)]^+$ ---> $[Rh(L\text{-}CH_2O)(L\text{-}CO)]^+$ ---> $[SRh(L\text{-}COCH_3)]^+$ ---> RhS_2^+ is described in Scheme 3.38. The proposed mechanism for the loss of formaldehyde from **F333a** to give $[RhL(L\text{-}CH_2O)]^+$, **F303**, involves an intermediate in which the bridging hydrogen moves to the metal, and back to the carbonyl group after migration of the methyl group to the bridging carbon has occurred. After loss of CH_2O, and following migration of the methyl group from the remaining intact ligand to the metal, a carbonyl group is lost to give the moderately abundant ion $[Rh(L\text{-}CH_2O)(L\text{-}CO)]^+$, **F275**. This ion, in turn, loses the even-electron neutral fragments C_5H_8 and CH_3CCH to give $[SRh(L\text{-}COCH_3)]^+$, **F207(a,b)**, and RhS_2^+, **F167**, respectively.

Although no metastable ion decompositions confirming the origin of $LRhS^+$, **F250**, are observed, its formation may be analogous to that proposed earlier for the corresponding ion, **E273**, in the mass spectrum of $Rh(Stfa)_3$ (see Schemes 3.26 and 3.28). Scheme 3.39 shows the proposed mechanisms for decomposition of this ion and its daughters. Elimination of CO from **F250**, following methyl migration to the metal, yields $RhC_4H_7S_2^+$, **F222**. This ion then loses a methyl

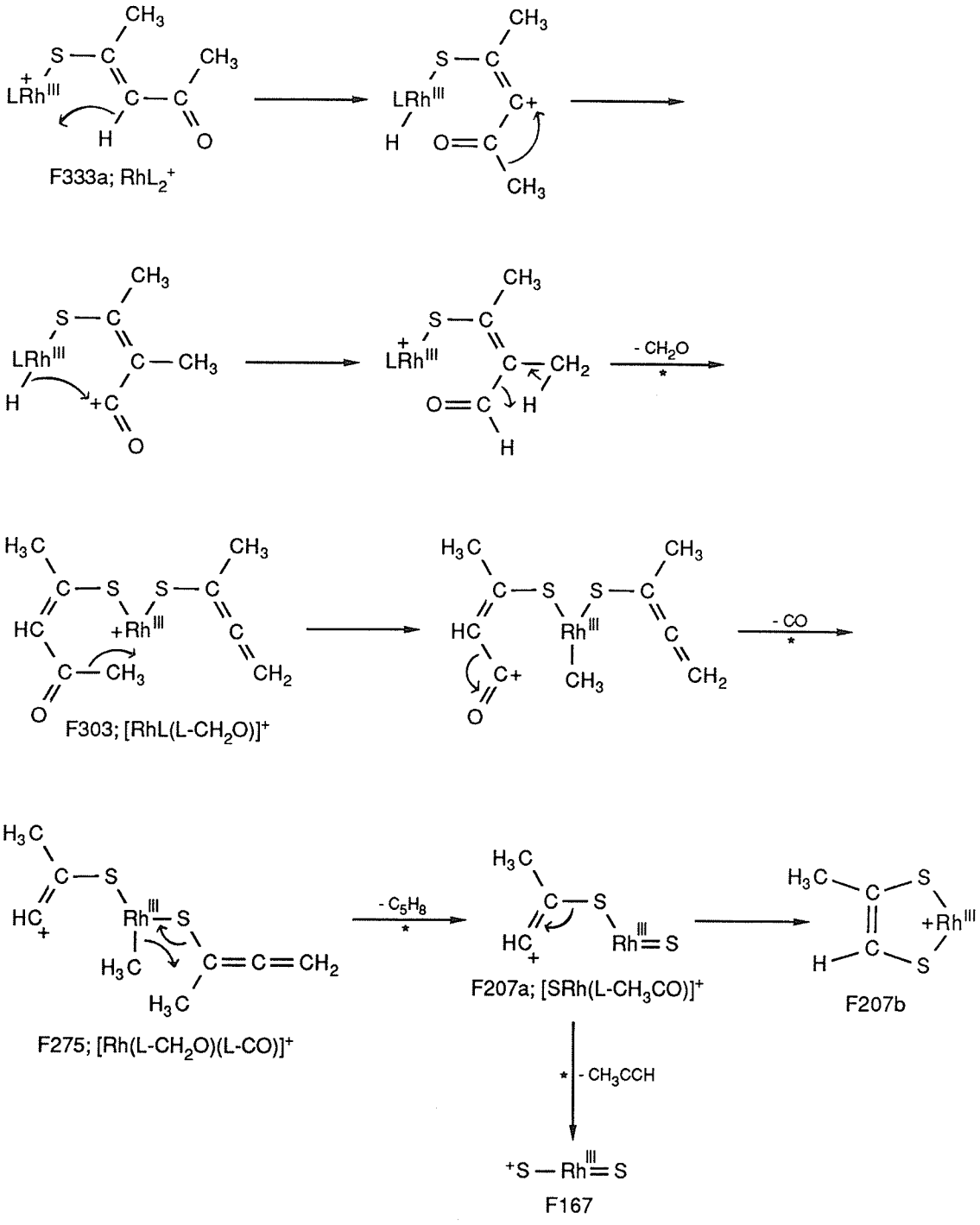
F333a; RhL_2^+
F303; $[RhL(L\text{-}CH_2O)]^+$
F275; $[Rh(L\text{-}CH_2O)(L\text{-}CO)]^+$
F207a; $[SRh(L\text{-}CH_3CO)]^+$
F207b
F167
$-C_5H_8$
$-CH_2O$
$-CO$
$-CH_3CCH$

Scheme 3.38

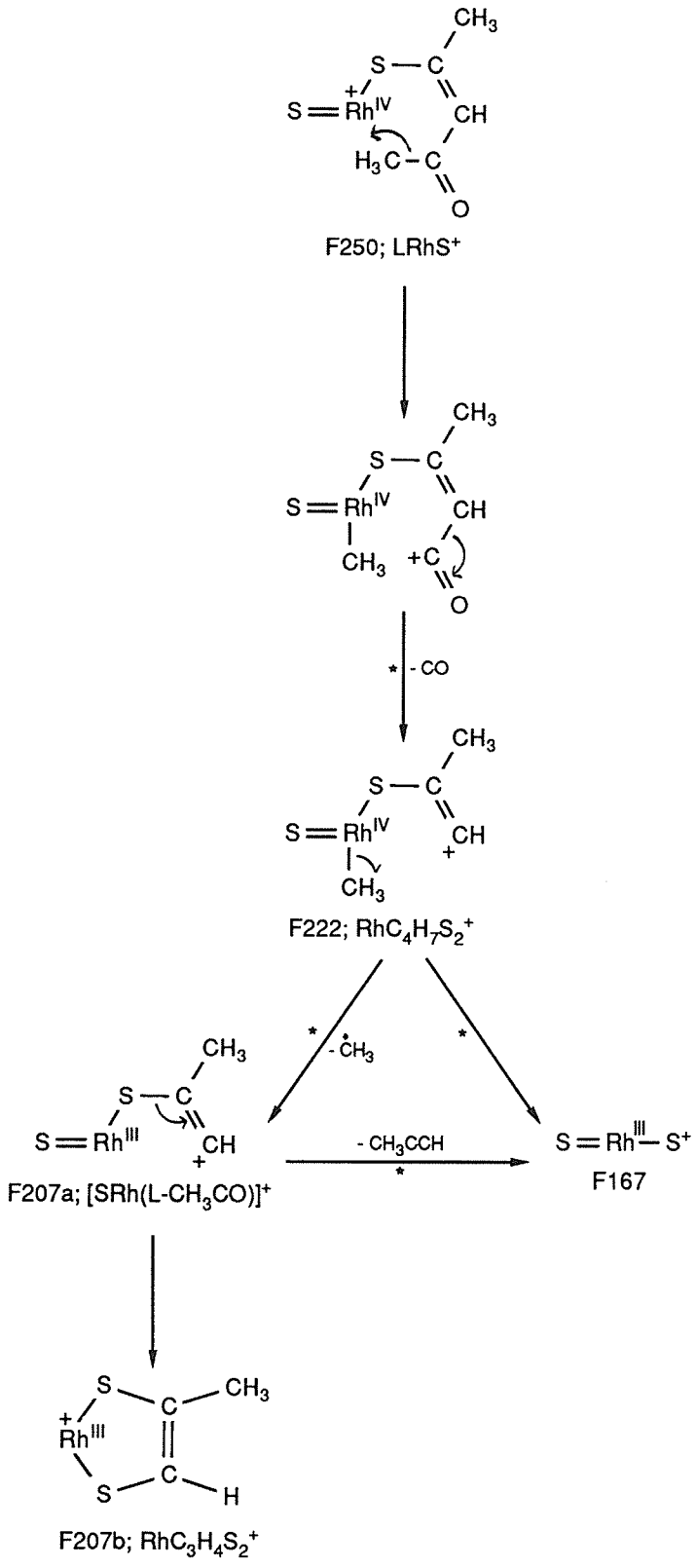
F250; LRhS+
F222; RhC4H7S2+
- CO
- CH3
- CH3CCH
F207a; [SRh(L-CH3CO)]+
F167
F207b; RhC3H4S2+

Scheme 3.39

radical (indicating reduction of Rh(IV) to Rh(III)) to give $[SRh(L\text{-}COCH_3)]^+$, **F207a**, which in turn, can either lose the neutral fragment CH_3CCH to give RhS_2^+, **F167**, or undergo rearrangement to yield the cyclic ion $RhC_3H_4S_2^+$, **F207b**. The sequence of neutral losses from **F222** supports the idea that the methyl group lost originates from the metal and not from the remaining portion of the ligand.

Scheme 3.40 shows the proposed mechanisms for the observed loss of H_2S from RhL_2^+, **F333(c,d)**. Migration of a hydrogen atom, originating from either the methyl group on the oxygen side (Pathway a) or from the sulfur side (Pathway b) of the ligand, to the sulfur atom of the same ligand gives rise to the intermediate ions **F333c** and **F333d**, respectively. Depending on the origin of the second hydrogen transfered to the sulfur atom, loss of H_2S from **F333d** gives rise to either **F299b** or **F299c**, while elimination of H_2S from **F333c** yields **F299a**, which in turn, may undergo rearrangement to give, once again, **F299b**. This ion, $[RhL(L\text{-}H_2S)]^+$, is also observed in the mass spectrum of $Rh(Stfa)_3$. However, its low relative abundance (<1%) is reflected, at least partially, by the fact that its formation from RhL_2^+ (supported by metastable ion decomposition evidence) can only occur *via* Pathway b.

Consecutive losses of H_2S and CO from $LRhH^+$, **F218**, lead to formation of the ions $[Rh(L\text{-}HS)]^+$, **F185** and $[Rh(L\text{-}HS\text{-}CO)]^+$, **F157**, respectively. These can be formed by mechanisms analogous to those proposed earlier for formation of corresponding ions in the mass spectrum of $Rh(Stfa)_3$ (Scheme 3.31).

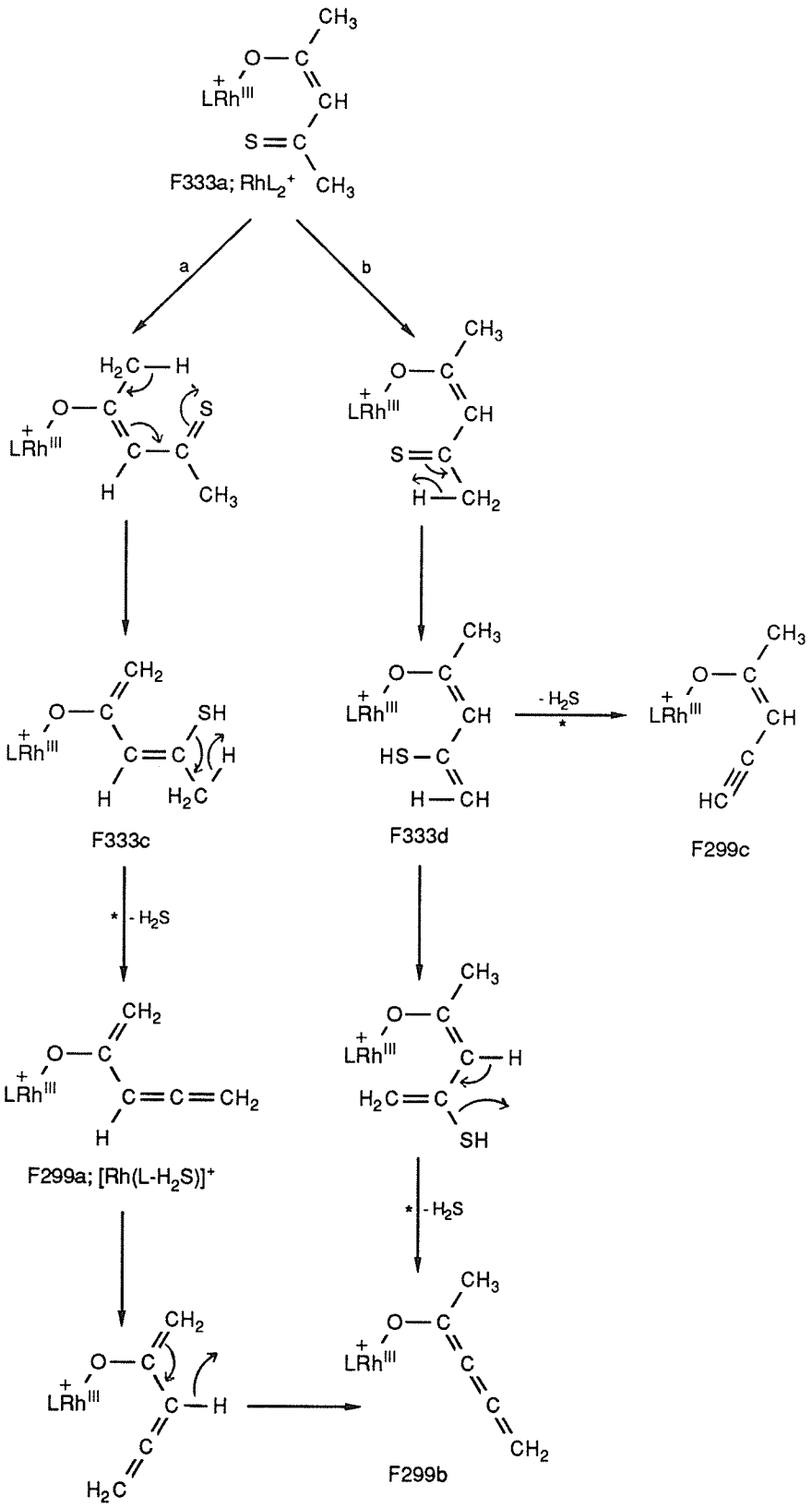
F333a; RhL2+
a
b
F333c
F333d
F299c
F299a; [Rh(L-H2S)]+
F299b
- H2S
- H2S
- H2S

Scheme 3.40

3.2.2 ^{1}H and ^{19}F NMR studies

A) *General features*

In Table 3.19, the ^{1}H and ^{19}F NMR spectra of $Rh(Sacac)_3$ and $Rh(Stfa)_3$ are summarized. These spectra support a *facial* octahedral geometry, as corroborated by X-ray studies of the latter complex[61] (see Section 3.2.3), and in agreement with our earlier results for $Rh(SbzC_2F_5)_3$ and $Rh(SbzC_3F_7)_3$ (see Section 3.1.1).

B) *$Rh(Sacac)_3$*

The ^{1}H NMR spectrum of $Rh(Sacac)_3$, recorded in $CDCl_3$, consists of three absorptions with relative intensities of 1:3:3 (counting from low field) (Figure 3.28). The signal occurring at 6.374 ppm must be assigned to the methine proton and the remaining two absorptions, occurring at 2.295 and 2.225 ppm, to the two methyl groups, the first of which appears as a doublet (Figure 3.29). The splitting of this signal was not reported by Kawanishi *et al*[65] in an earlier study of this complex. This signal is assigned to the protons of the methyl group on the sulfur side of the chelate ring; the down-field shift (with respect to the protons of the methyl group on the oxygen side) was attributed to the long range deshielding effect of the sulfur containing group[88], and the splitting (0.5 Hz) we attribute to coupling of the protons with the rhodium atom (^{103}Rh has a nuclear spin of 1/2 and a natural abundance of 100%). The observed coupling of the methyl group protons with rhodium on the sulfur side of the chelate ring and not on the oxygen side can be related to rhodium's greater affinity towards sulfur ($d\pi$-$d\pi$ bonding). Since irradiation of the methine resonance (double resonance experiment) did not have an

Table 3.19 ^{1}H and ^{19}F NMR chemical shift (ppm), coupling constant (Hz) and intensity data for the NMR spectra of $Rh(Sacac)_3$ and $Rh(Stfa)_3$.

Complex	Solvent	δ_{CH}	Int.	δ_{CH_3}	Int.	δ_{CF_3}
*$Rh(Sacac)_3$	$CDCl_3$	6.25(s)	1	2.25(s)	3	-
				2.20(s)	3	-
$Rh(Sacac)_3$	$CDCl_3$	6.374(s)	0.998	2.295(d), $J_{CH_3\text{-}Rh}$ = 0.5 Hz	3.160	-
				2.225(s)	3.249	-
$Rh(Stfa)_3$	CD_2Cl_2	6.681(q), $J_{CH\text{-}CF_3}$ = 0.4 Hz	0.911	2.495(d), $J_{CH_3\text{-}Rh}$ = 0.3 Hz	3.123	-74.981(t), $J_{CF_3\text{-}CH}$ = 0.4 Hz $J_{CF_3\text{-}Rh}$ = 0.4 Hz
$Rh(Stfa)_3$	$CDCl_3$	6.631(q), $J_{CH\text{-}CF_3} \leq$ 0.2 Hz	0.998	2.476(d), $J_{CH_3\text{-}Rh}$ = 0.2 Hz	3.127	-

* Results taken from Kawanishi *et al*[65].
Chemical shift and coupling constant data are believed to be accurate to ± 0.001 ppm and ± 0.1 Hz, respectively.

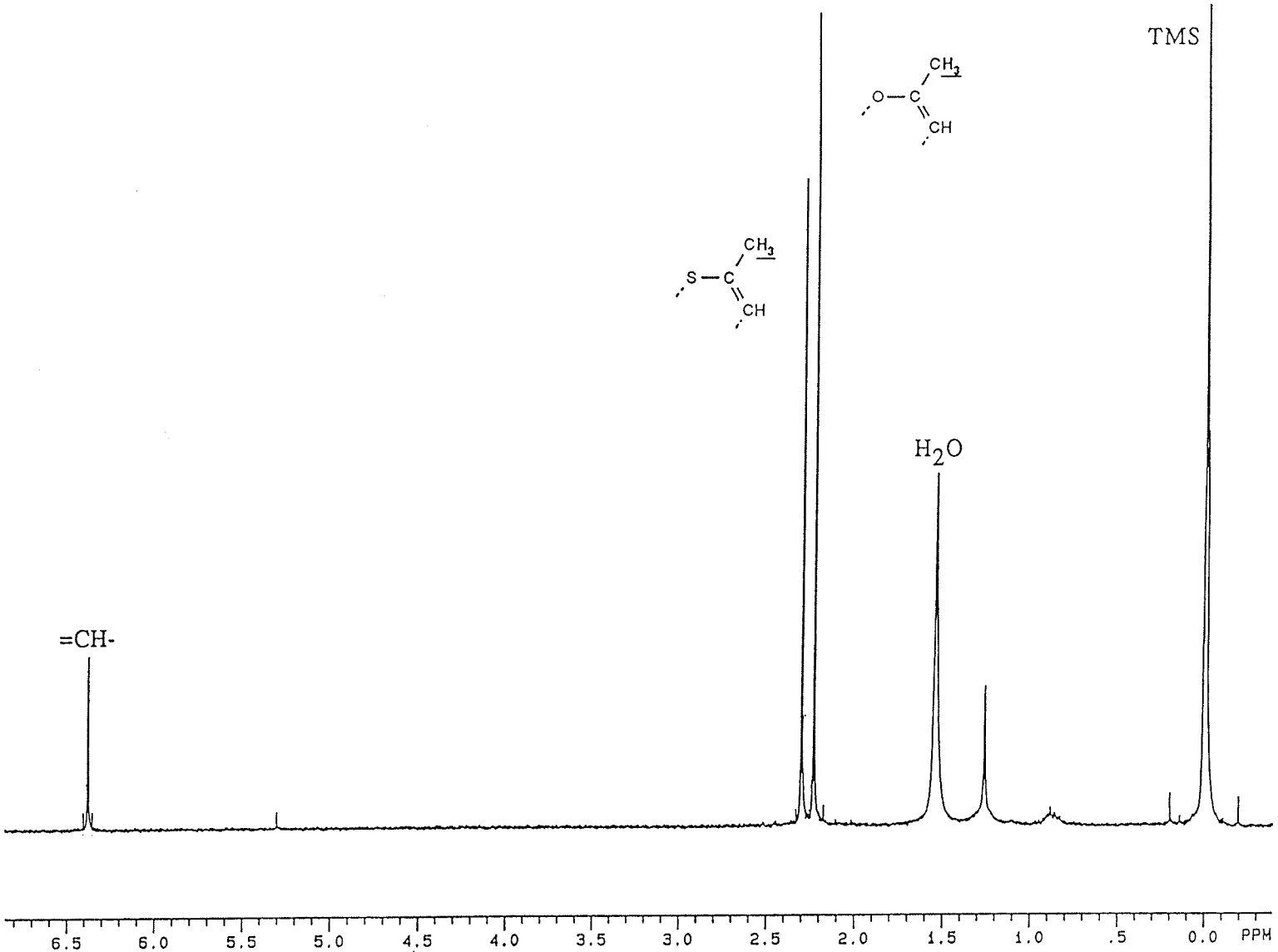

Figure 3.28 ^1H NMR spectrum of $Rh(Sacac)_3$ recorded at 300.13 MHz in $CDCl_3$ at room temperature.

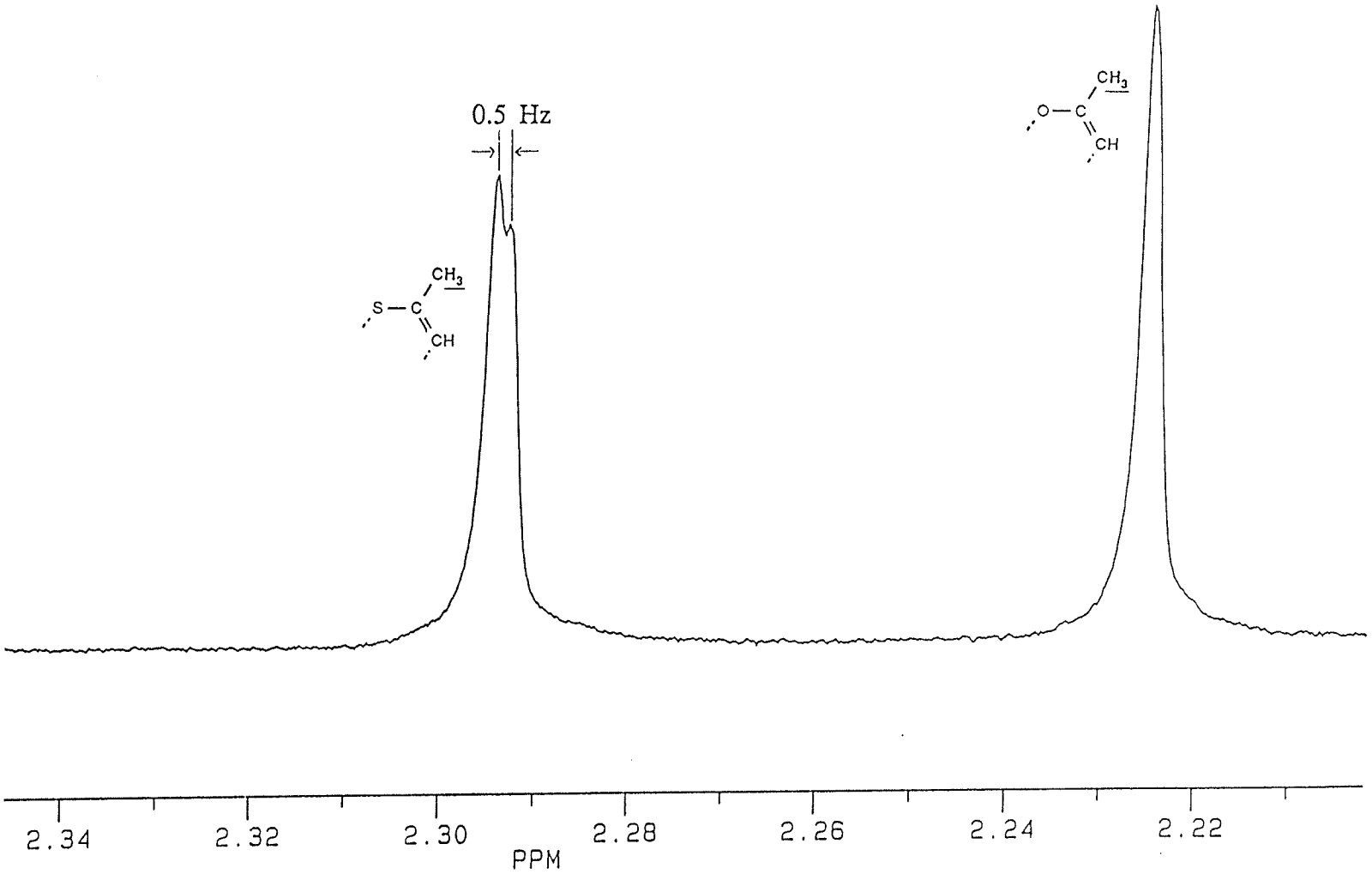

Figure 3.29 $-CH_3$ spectral region of the ^1H NMR spectrum (with increased digital resolution) of $Rh(Sacac)_3$ recorded at 300.13 MHz in $CDCl_3$ at room temperature.

effect on the observed methyl doublet the alternative possibility that the observed splitting is the result of coupling between the methyl and methine protons can be ignored. As well, if the splitting of the methyl resonance was due to coupling between the methyl and methine protons, one would also have expected the methine resonance to be split into a quartet. This, however, was not observed.

C) *Rh(Stfa)$_3$*

The ^{19}F NMR spectrum of $Rh(Stfa)_3$, recorded in CD_2Cl_2, consists of a single absorption split into a triplet, with peak intensity ratios 1:2:1 (Figure 3.30(a)). In the proton decoupled spectrum, the triplet is reduced to a doublet (Figure 3.30(b)). Thus, the triplet is actually two overlapping doublets, due to coupling of the fluorines of the trifluoromethyl group with the methine proton ($J_{CF_3\text{-}CH}$ = ~0.4 Hz) and with rhodium ($J_{CF_3\text{-}Rh}$ = ~0.4 Hz). Our X-ray structure of this complex[61] showed an average separation of 2.26 Å between the methine proton and a fluorine atom lying in the plane of each chelate ring; this is 0.44 Å less than the sum of the van der Waals radii of the two atoms[89]. The long range coupling mechanism between fluorines, referred to as "fragment coupling", discussed earlier in Section 1.6, is also valid when considering long range F-H couplings[37,38]. The close proximity of the above nuclei and the fact that coupling between the methyl and methine protons is not observed suggest that fragment coupling may be the working mechanism.

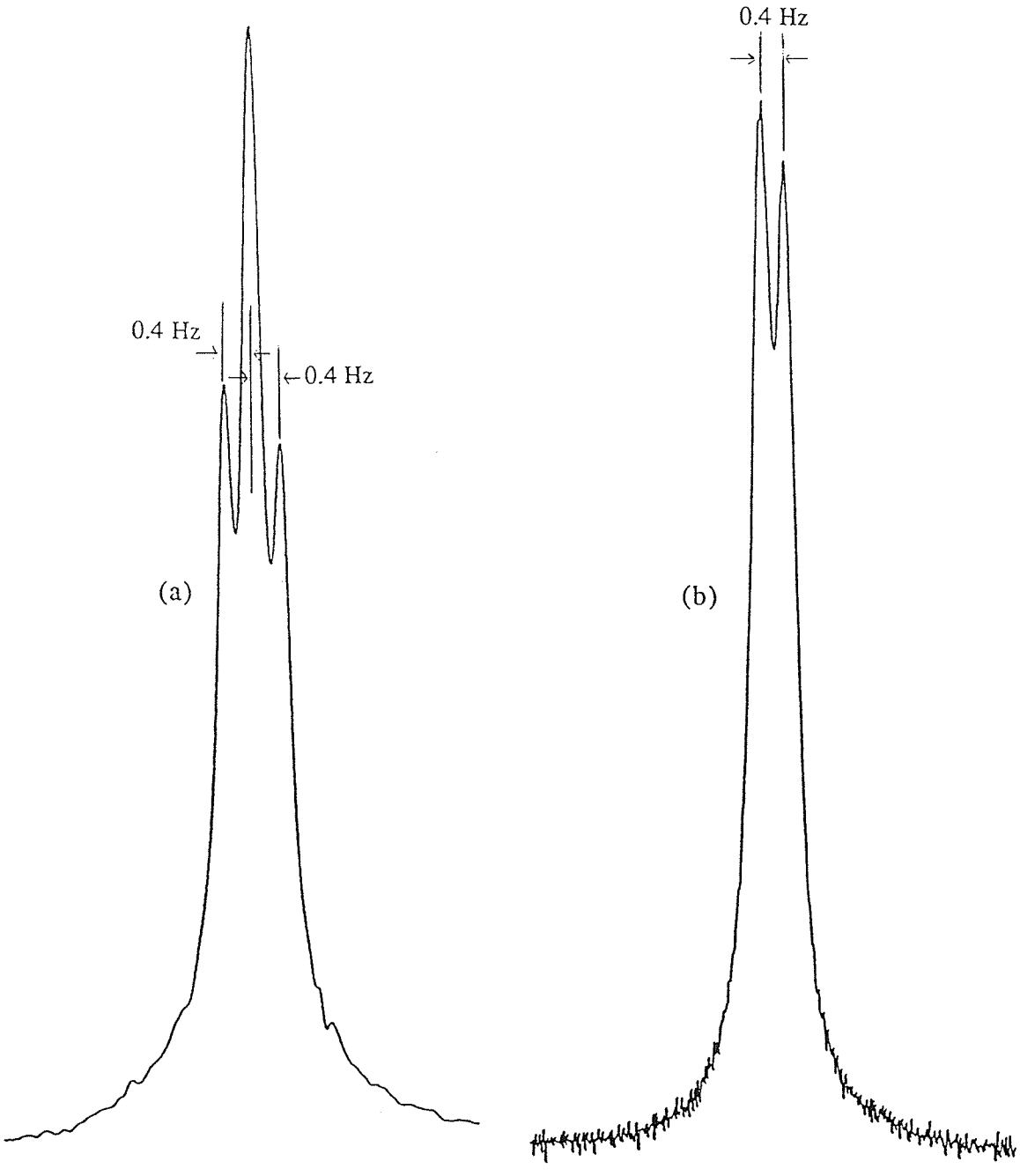

Figure 3.30 -CF_3 resonance in the ^{19}F (a) and $\{^1H\}^{19}F$ (b) NMR spectra (with increased digital resolution) of $Rh(Stfa)_3$ recorded at 282.41 MHz in CD_2Cl_2 at room temperature.

The ^1H NMR spectrum of $Rh(Stfa)_3$, recorded in both CD_2Cl_2 and $CDCl_3$ (Figures 3.31-3.34), consist of two absorptions appearing as a doublet and a quartet with relative intensities 3:1, respectively. In CD_2Cl_2 these multiplets are resolved to a greater extent. These signals are assigned to the methyl and methine protons, respectively. As in the ^1H NMR spectrum of $Rh(Sacac)_3$ the splitting of the methyl signal is due to coupling of ^1H with rhodium ($J_{CH_3\text{-}Rh}$ = 0.3 and 0.2 Hz in CD_2Cl_2 and $CDCl_3$, respectively). In agreement with the ^{19}F NMR spectrum of this complex, coupling between the methine proton and the trifluoromethyl fluorines gives rise to the observed quartet ($J_{CH\text{-}CF_3}$ = 0.4 Hz).

3.2.3 Crystal Structure of $Rh(Stfa)_3$

To complement our other studies (mass and NMR spectroscopies) we have determined the crystal stucture of $Rh(Stfa)_3$[61], which was shown by the NMR studies (see Section 3.2.2) to exist as the *facial* isomer in organic solvents. This result is confirmed by the crystal structure, which also provides insights into the bonding in the chelate ring, and between rhodium and the ligand. Table 3.20 lists all determined bond lengths and angles of this complex, and the resulting ORTEP diagram is shown in Figure 3.35.

Mean bond lengths in the chelate rings of the present rhodium complex and monothio-β-ketoenolates of other metal ions are given in Table 3.21. Each of the $MetL_3$ complexes is pseudo-octahedral, with a *facial* arrangement of S atoms. The data have been arranged so that, on proceeding from left to right across the table, the

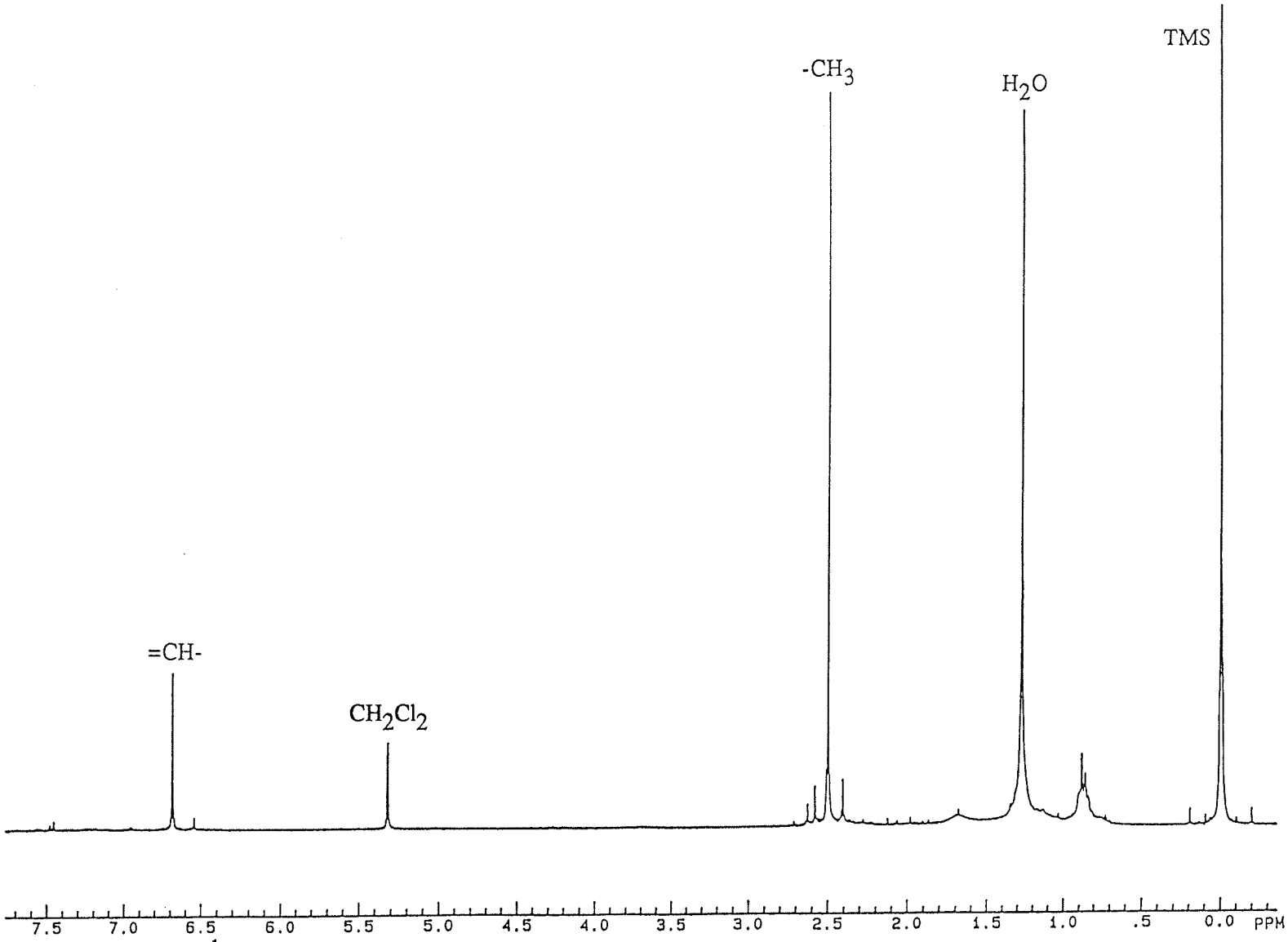

Figure 3.31 ^{1}H NMR spectrum of $Rh(Stfa)_3$ recorded at 300.13 MHz in CD_2Cl_2 at room temperature.

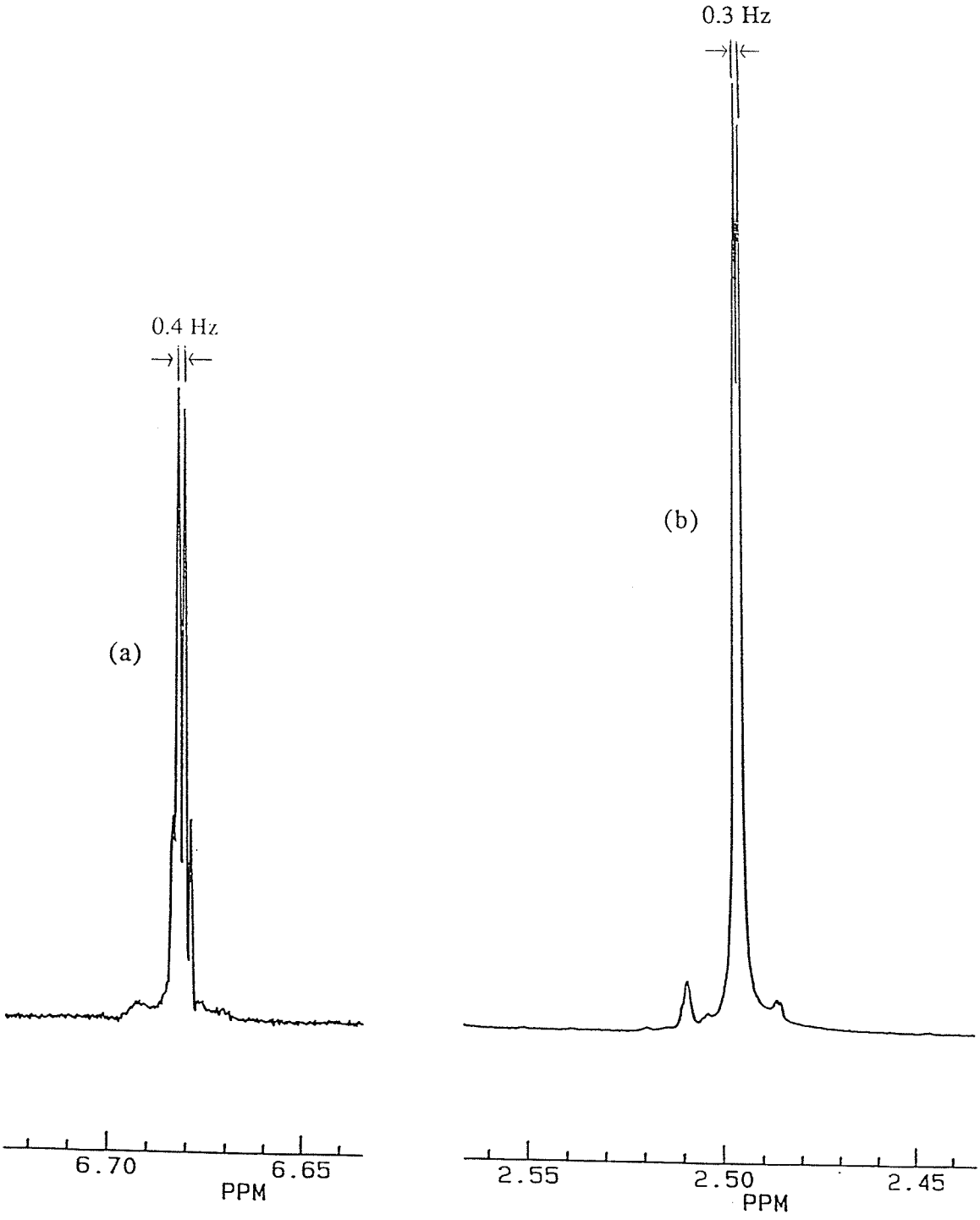

Figure 3.32 =CH- (a) and $-CH_3$ (b) spectral regions of the ^1H NMR spectrum (with increased digital resolution) of $Rh(Stfa)_3$ recorded at 300.13 MHz in CD_2Cl_2 at room temperature.

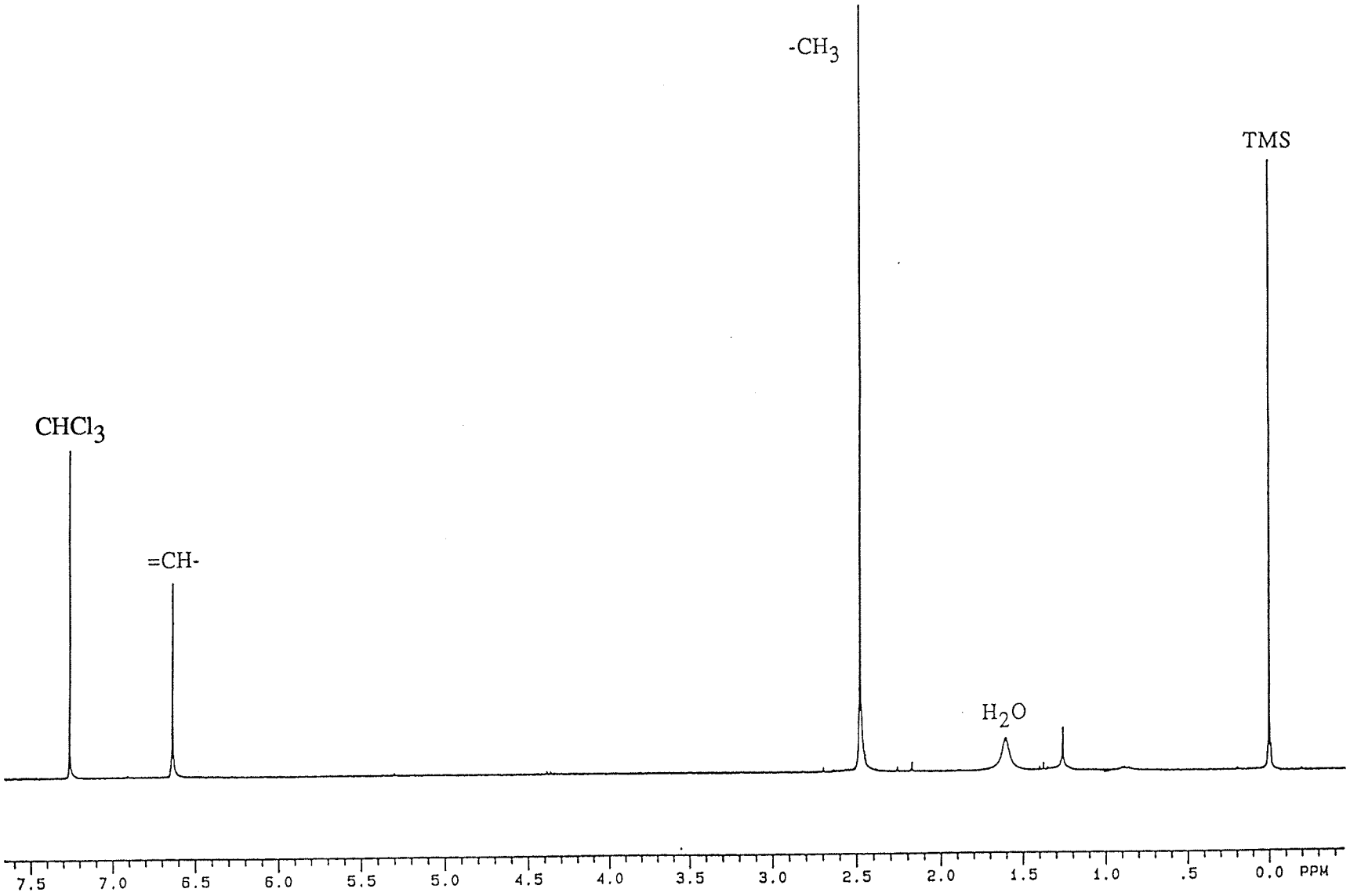

Figure 3.33 ^{1}H NMR spectrum of $Rh(Stfa)_3$ recorded at 300.13 MHz in $CDCl_3$ at room temperature.

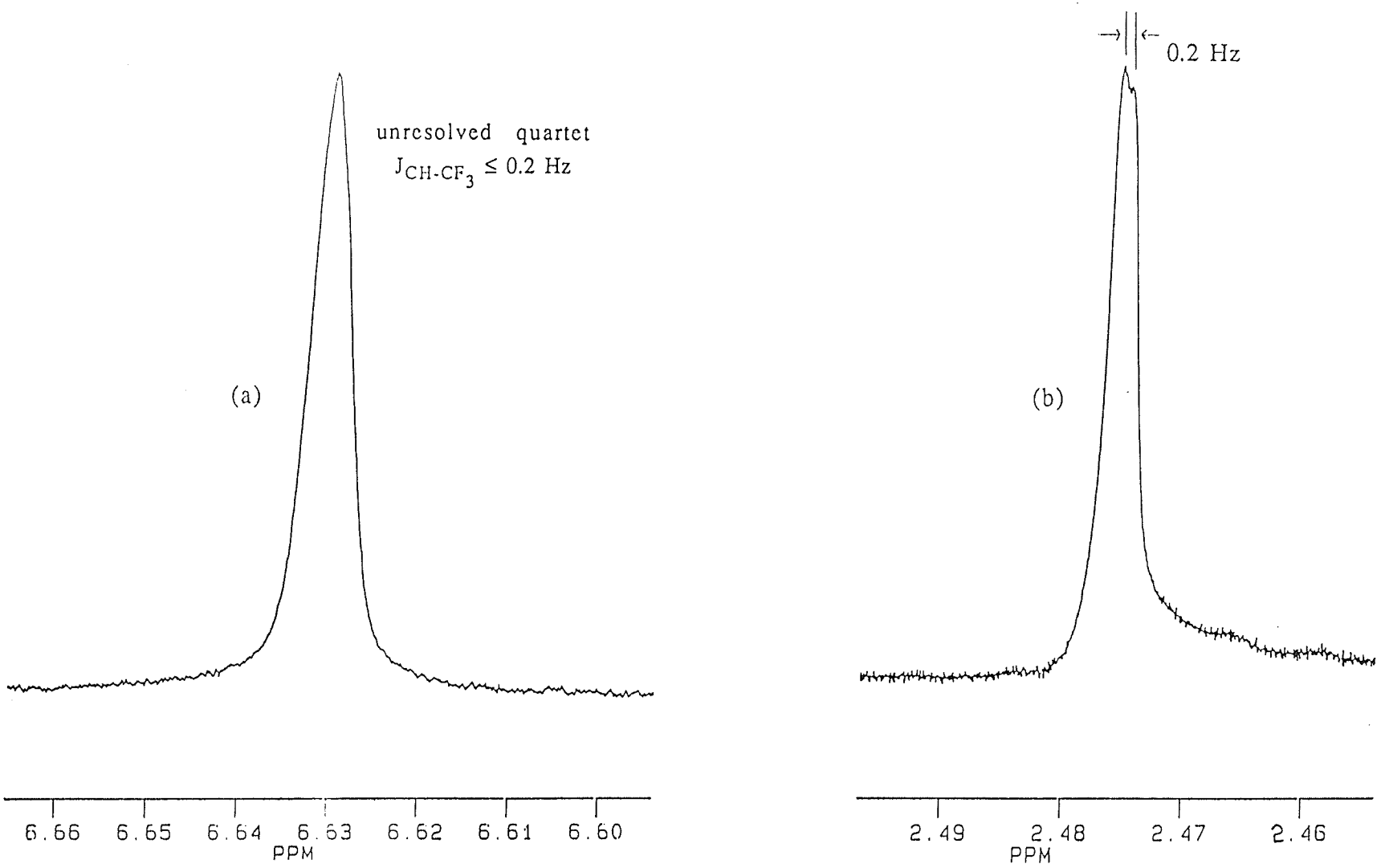

Figure 3.34 =CH- (a) and $-CH_3$ (b) spectral regions of the ^1H NMR spectrum (with increased digital resolution) of $Rh(Stfa)_3$ recorded at 300.13 MHz in $CDCl_3$ at room temperature.

Table 3.20 Bond lengths (Å) and angles (°) with their estimated standard deviations[61].

Rh(1)—S(1)	2·256 (2)	C(9)—C(8)	1·373 (9)
Rh(1)—S(2)	2·254 (2)	C(10)—F(10*a*)	1·311 (9)
Rh(1)—S(3)	2·259 (2)	C(10)—F(10*b*)	1·313 (9)
Rh(1)—O(1)	2·091 (4)	C(10)—F(10*c*)	1·304 (9)
Rh(1)—O(2)	2·073 (5)	C(11)—C(13)	1·385 (10)
Rh(1)—O(3)	2·081 (4)	C(11)—C(12)	1·514 (10)
S(1)—C(1)	1·661 (8)	C(13)—C(14)	1·388 (9)
S(2)—C(6)	1·678 (8)	C(14)—C(15)	1·530 (10)
S(3)—C(11)	1·676 (7)	C(14)—O(3)	1·246 (7)
C(1)—C(3)	1·377 (10)	C(15)—F(15*a*)	1·317 (10)
C(1)—C(2)	1·519 (10)	C(15)—F(15*b*)	1·311 (9)
C(3)—C(4)	1·375 (10)	C(15)—F(15*c*)	1·259 (9)
O(1)—C(4)	1·244 (8)	F(5a)—C(5)	1·286 (10)
C(6)—C(8)	1·383 (9)	F(5b)—C(5)	1·279 (10)
C(6)—C(7)	1·503 (9)	F(5c)—C(5)	1·275 (10)
C(9)—C(10)	1·543 (11)	C(4)—C(5)	1·522 (11)
C(9)—O(2)	1·255 (8)		
S(1)—Rh(1)—S(2)	88·55 (8)	C(9)—C(10)—F(10*b*)	113·3 (8)
S(1)—Rh(1)—S(3)	88·66 (8)	C(9)—C(10)—F(10*c*)	112·4 (7)
S(1)—Rh(1)—O(1)	94·95 (14)	F(10*a*)—C(10)—F(10*b*)	106·2 (8)
S(1)—Rh(1)—O(2)	174·53 (14)	F(10*a*)—C(10)—F(10*c*)	108·0 (9)
S(1)—Rh(1)—O(3)	91·71 (14)	F(10*b*)—C(10)—F(10*c*)	106·9 (9)
S(2)—Rh(1)—S(3)	87·38 (7)	Rh(1)—O(2)—C(9)	124·1 (5)
S(2)—Rh(1)—O(1)	89·38 (13)	S(3)—C(11)—C(13)	128·6 (6)
S(2)—Rh(1)—O(2)	96·17 (14)	S(3)—C(11)—C(12)	113·2 (6)
S(2)—Rh(1)—O(3)	176·22 (14)	C(13)—C(11)—C(12)	118·2 (7)
S(3)—Rh(1)—O(1)	175·08 (14)	C(11)—C(13)—C(14)	129·0 (7)
S(3)—Rh(1)—O(2)	88·78 (13)	C(13)—C(14)—C(15)	117·9 (7)
S(3)—Rh(1)—O(3)	96·40 (14)	C(13)—C(14)—O(3)	130·6 (7)
O(1)—Rh(1)—O(2)	87·9 (2)	C(15)—C(14)—O(3)	111·5 (7)
O(1)—Rh(1)—O(3)	86·8 (2)	C(14)—C(15)—F(15*a*)	109·0 (8)
O(2)—Rh(1)—O(3)	83·8 (2)	C(14)—C(15)—F(15*b*)	113·6 (8)
Rh(1)—S(1)—C(1)	109·0 (3)	C(14)—C(15)—F(15*c*)	114·0 (7)
Rh(1)—S(2)—C(6)	108·7 (3)	F(15*a*)—C(15)—F(15*b*)	103·1 (7)
Rh(1)—S(3)—C(11)	108·6 (3)	F(15*a*)—C(15)—F(15*c*)	106·5 (9)
S(1)—C(1)—C(3)	128·6 (6)	F(15*b*)—C(15)—F(15*c*)	109·7 (8)
S(1)—C(1)—C(2)	113·4 (7)	Rh(1)—O(3)—C(14)	126·1 (5)
C(3)—C(1)—C(2)	118·0 (8)	C(3)—C(4)—O(1)	130·5 (8)
C(1)—C(3)—C(4)	128·6 (8)	C(3)—C(4)—C(5)	117·5 (8)
Rh(1)—O(1)—C(4)	125·5 (5)	O(1)—C(4)—C(5)	112·0 (8)
S(2)—C(6)—C(8)	128·4 (6)	C(6)—C(8)—C(9)	127·9 (7)
S(2)—C(6)—C(7)	113·7 (6)	F(5*a*)—C(5)—F(5*b*)	103·0 (10)
C(8)—C(6)—C(7)	117·8 (7)	F(5*a*)—C(5)—F(5*c*)	106·2 (9)
C(10)—C(9)—O(2)	109·8 (7)	F(5*a*)—C(5)—C(4)	112·0 (8)
C(10)—C(9)—C(8)	118·2 (8)	F(5*b*)—C(5)—F(5*c*)	105·4 (9)
O(2)—C(9)—C(8)	132·0 (7)	F(5*b*)—C(5)—C(4)	112·7 (8)
C(9)—C(10)—F(10*a*)	109·7 (8)	F(5*c*)—C(5)—C(4)	116·3 (9)

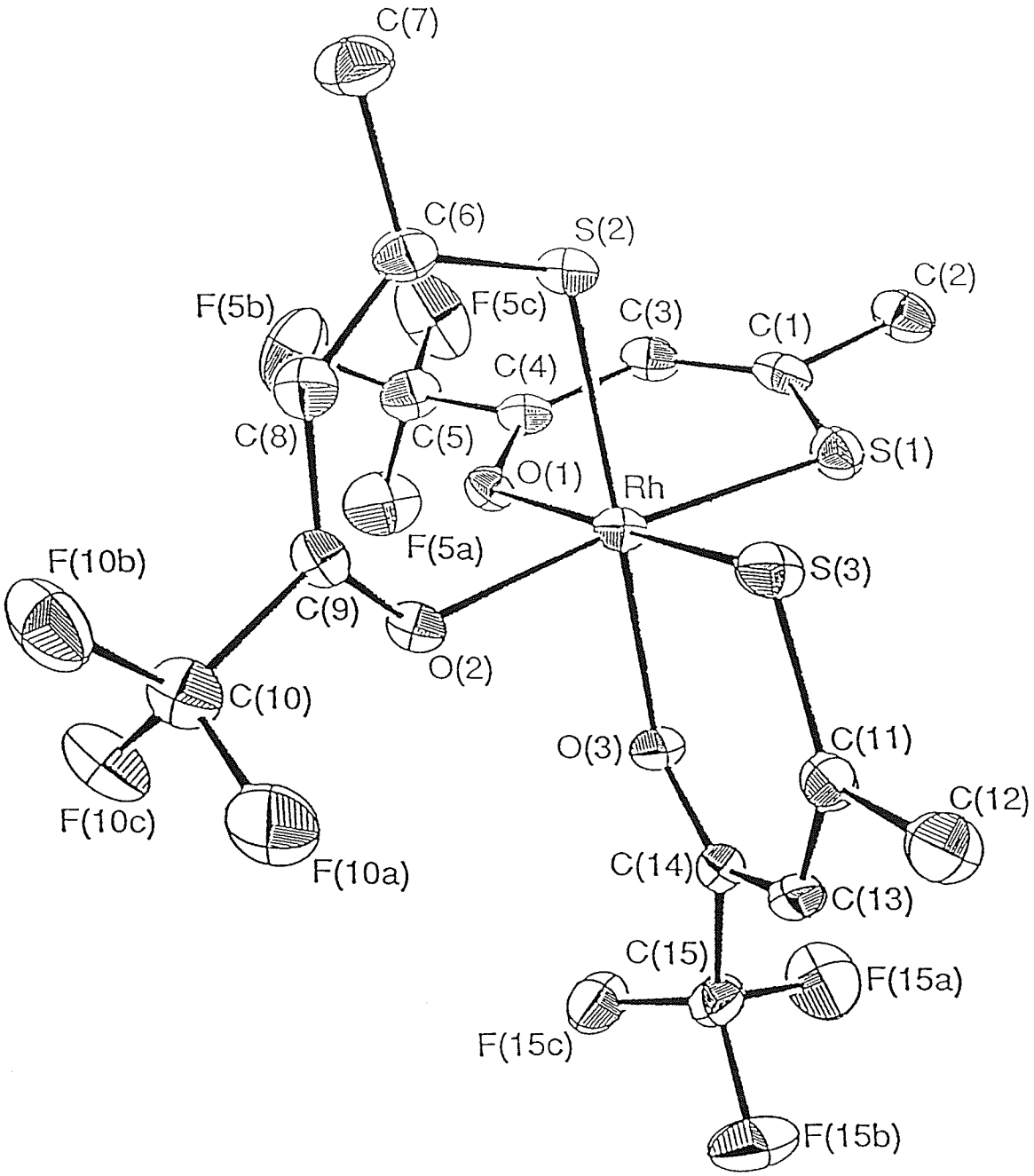

Figure 3.35 ORTEP diagram of $Rh(Stfa)_3$[61].

Table 3.21 Mean bond lengths and related lengths (Å) in chelate rings of monothio-β-ketoenolates, $M(R_SCSCHCOR_O)_n$

R_S, R_O Configuration Reference	$Fe^{III}L_3$ C_6H_5, CH_3 $(t_{2g})^3(e_g)^2$ 90	$In^{III}L_3$ C_6H_5, CH_3 d^{10} 91	$Fe^{III}L_3$ C_6H_5, CF_3 $(t_{2g})^5$ 90	$Te^{III}L_3$† C_6H_5, C_6H_5 $(t_{2g})^4$ 92	$Co^{III}L_3$ CH_3, CF_3 $(t_{2g})^6$ 93	$Rh^{III}L_3$ CH_3, CF_3 $(t_{2g})^6$ 61
M–S(a)	2.368(2)	2.527(3)	2.239(2)	2.330(4)	2.195(1)	2.256(2)
M–O(b)	1.988(4)	2.205(3)	1.942(4)	2.053(4)	1.944(2)	2.082(4)
C_S–S	1.705(4)	1.728(4)	1.693(6)	1.707(10)	1.703(3)	1.672(8)
C_O–O	1.259(6)	1.257(4)	1.260(7)	1.267(20)	1.253(3)	1.248(8)
C_S–C	1.378(7)	1.369(5)	1.380(8)	1.360(20)	1.372(4)	1.382(10)
C_O–C	1.403(7)	1.432(5)	1.382(8)	1.427(20)	1.393(4)	1.379(10)
a-b	0.380(5)	0.322(5)	0.297(5)	0.277(6)	0.251(3)	0.174(5)
r*	0.79	0.94	0.69	(0.79)	0.69	0.81
a-r	1.58	1.59	1.55	(1.54)	1.51	1.45
b-r	1.20	1.27	1.25	(1.26)	1.25	1.27

The subsripts S and O identify atoms and groups on the S and O sides of the chelate ring respectively.

* Ionic radii (r) are from Cotton and Wilkinson[21].

† Values in parentheses for Tc^{III} are derived by assuming that b-r = 1.26 Å, for consistency with values for the other complexes.

difference between metal-sulfur and metal-oxygen bond length decreases.

In the following discussion we consider that variation of the metal ion plays the major role in effecting changes in the chelate ring because any *d* electrons that the metal possesses are *directly* involved in the metal-ring bonding. Substituents attached to the chelate ring could also have some influence, but their effects (inductive and mesomeric) are probably less important. The metal-sulfur and metal-oxygen bond lengths in these complexes can be compared by attempting to remove the effects of differing sizes of the metal ions by assuming that the metal ion sizes are proportional to tabulated ionic radii. The values given in Table 3.21 are ionic radii of metal ions in a similar coordination environment and high/low-spin state to those in the corresponding complexes. When these radii are subtracted from the metal-oxygen bond lengths a nearly constant value (1.26±0.01 Å) for the difference is obtained (with the exception of high-spin Fe(III), for which a significantly lower value is given). The value of 1.26±0.01 Å is somewhat larger than the 1.19±0.01 Å value that results from a similar treatment of β-ketoenolate complexes[94-103] and implies that, in the monothio complexes, there is little shortening of the metal-oxygen bond due to covalency and that metal-ligand π bonding makes a minor contribution to the metal-oxygen bonding. On the other hand, when the ionic radii are subtracted from the metal-sulfur bond lengths there is a significant decrease in the resulting differences for ML_3 complexes on proceeding from left to right of Table 3.21. The shortening of the metal-sulfur bond implied by this decrease can be assigned to

increasing metal->sulfur $d\pi$ bonding in this sequence. Such bonding requires the presence of electrons in the metal t_{2g} orbitals (in O_h symmetry) but their bonding effects are reduced by the presence of electrons in metal e_g orbitals. Furthermore, metal->ligand π bonding is stronger for second- than for first-series transition elements. Thus it is possible to predict that metal->ligand π bonding should increase according to: high spin Fe(III) < [low-spin Fe(III), Tc(III)] < Co(III) < Rh(III), an order consistent with the trends in Table 3.21 and with known trends in the properties of this set of transition metals. It is also possible to predict that metal->sulfur π bonding should make a minor contribution in the case of In(III) complexes, again in agreement with the trends observed in Table 3.21.

The carbon-oxygen bond lengths in the monothio complexes (Table 3.21) fall in the narrow range 1.26±0.01 Å and are only slightly longer than that typical for a double bond (1.24 Å). In contrast, the carbon-sulfur bond length in the Rh(III) complex is significantly shorter than in the other ML_3 complexes, reflecting an increase in the metal->sulfur π bonding. Furthermore, in the RhL_3 complex the carbon-carbon bond lengths are equal. These observations are all consistent with the following qualitative description of the bonding in the metal-chelate ring. The inequality of the two carbon-carbon bond lengths for some ML_3 complexes is usually explained by predominance of the canonical form, A. With increasing π-electron density in the ring, caused by enhanced metal --> ligand π bonding, the increased carbon-sulfur bond order results in bond shortening. On the other hand, there is little more scope for shortening the carbon-oxygen bond, which has an order of two in the

predominating canonical form. Also to be expected, the chelate ring becomes more aromatic, i.e. both carbon-carbon lengths approach 1.39 Å, the value in benzene, as the ring π-electron density increases.

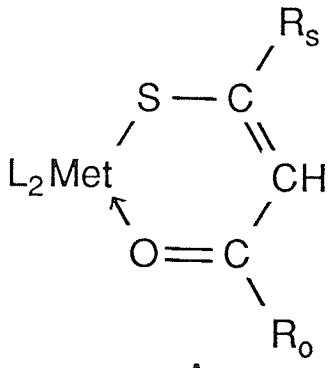

A

3.3 $Ir(hfa)_3$, $Ir(acac)_3$ and $Ir(tfa)_3$

3.3.1 Mass spectral studies

A) *General features*

The electron ionization (70 eV) positive ion mass spectra of $Ir(hfa)_3$, $Ir(acac)_3$ and $Ir(tfa)_3$ are shown in Figures 3.36-3.38, respectively. Tables 3.22-3.24 give the abundances of the characteristic ions as a percentage of that of the most abundant metal-containing ion (%RA). Figures 3.39-3.41 show the daughter ion spectra (B/E scans) of the IrL_2^+ ion for each complex, and fragmentation pathways are summarized in Schemes 3.41-3.43.

The two most intense peaks in each spectrum correspond to the molecular ion, IrL_3^+, and the fragment ion IrL_2^+; the base peak corresponds to the former ion for $Ir(acac)_3$ and $Ir(tfa)_3$ and to the latter ion for $Ir(hfa)_3$. (Even though IrL_3^+ is not the base peak ion for $Ir(hfa)_3$, its abundance is high (%RA = 80.9), suggesting appreciable stability.) Of the generalizations postulated by Westmore[4], regarding the relationship between metal oxidation states and molecular ion stabilities (see Section 1.1), these iridium complexes fall into generalization 1, which states that the molecular ion will be stabilized if metal to ligand π-donation readily occurs, i.e. if a facile increase of oxidation state can occur. This observation is consistent with iridium's known preference for the +III and +IV oxidation states and with the ease with which Ir(III) <--> Ir(IV) interconversion can occur[21,87]. In the mass spectra of the analogous rhodium complexes[68,104], RhL_2^+ corresponds to the base peak ion in all three cases, reflecting the fact that, compared to iridium, the +IV

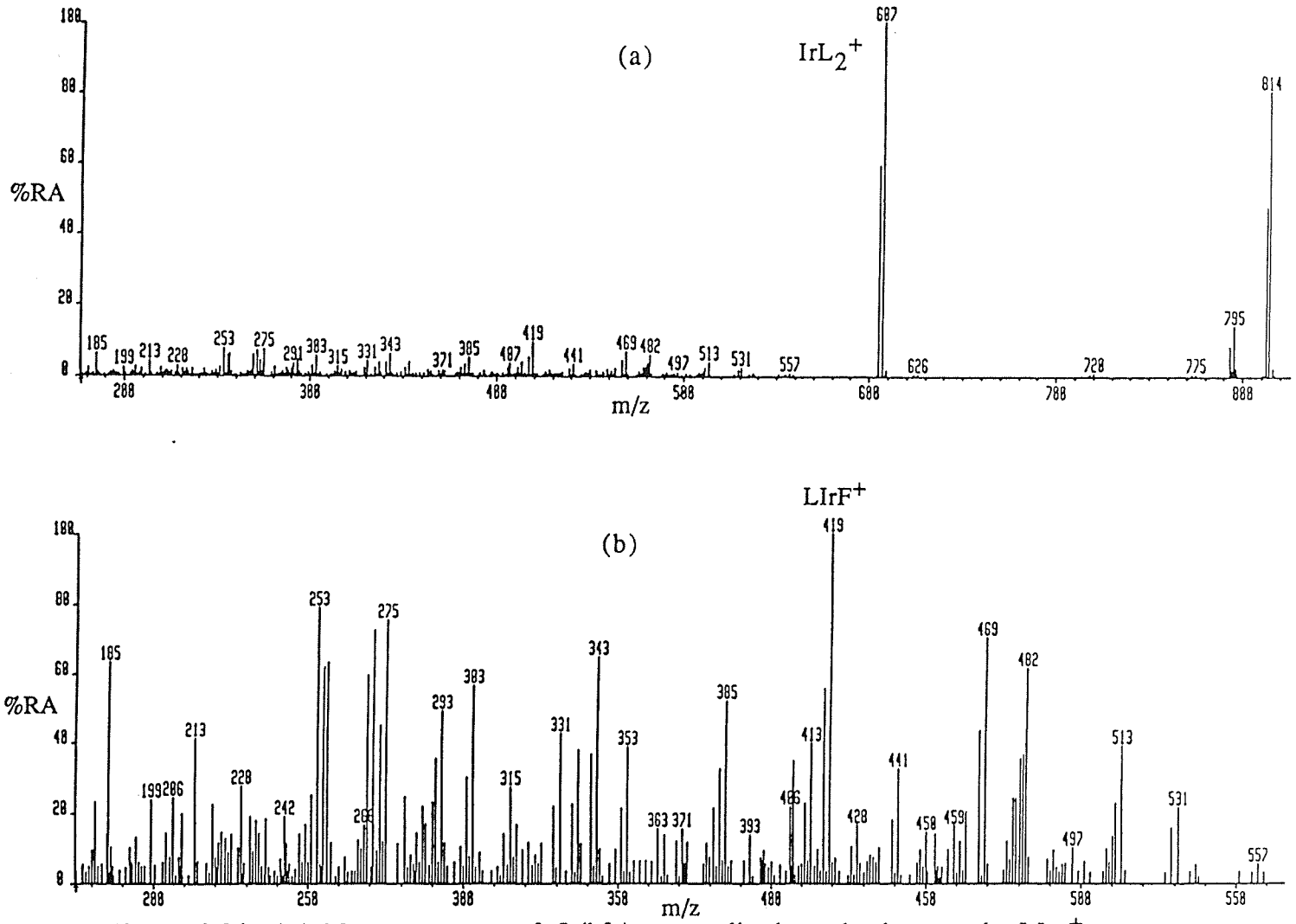

Figure 3.36 (a) Mass spectrum of $Ir(hfa)_3$ normalized to the base peak, IrL_2^+.
(b) Region of (a) between m/z 175 and m/z 560, normalized to m/z 419, $LIrF^+$.

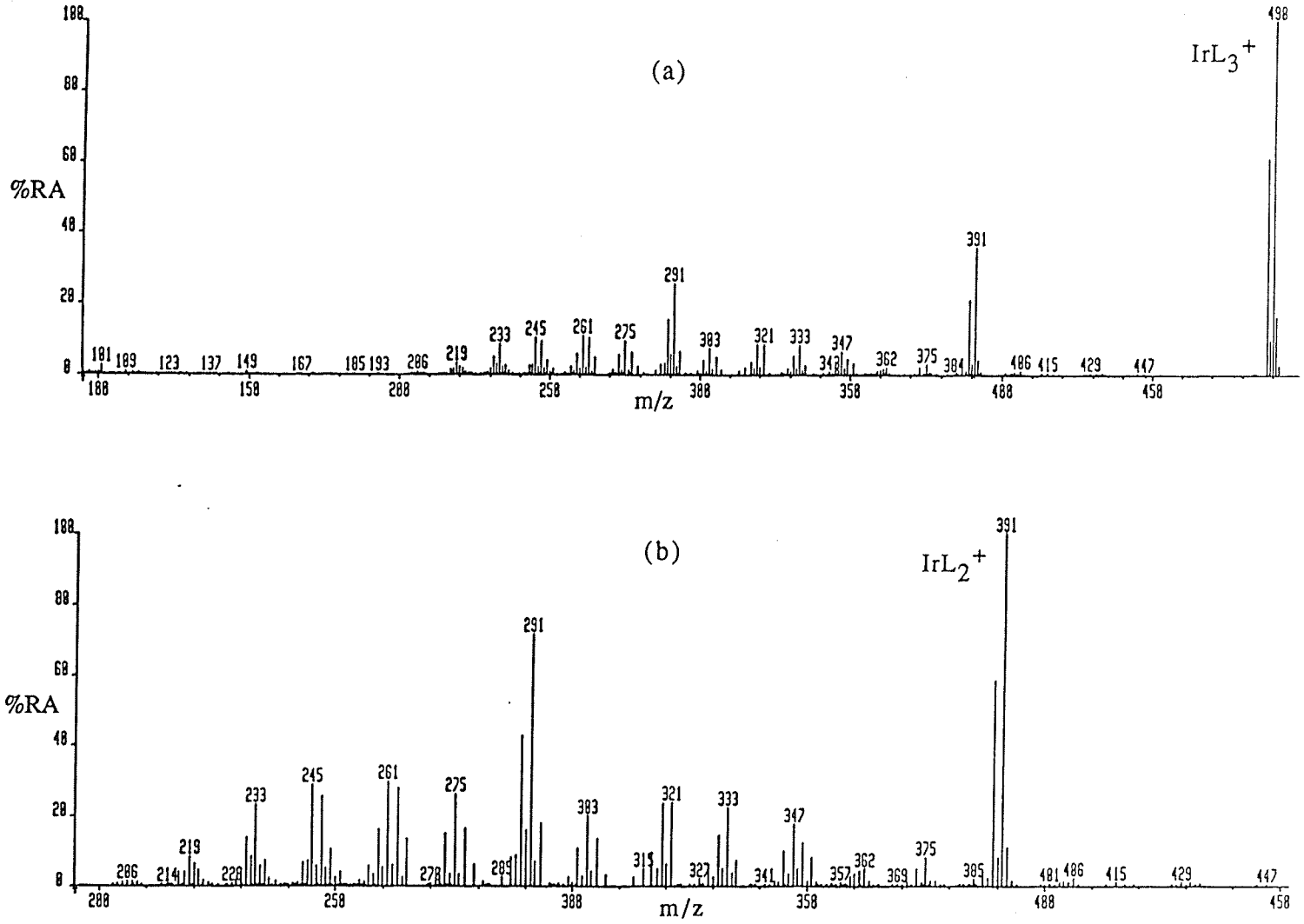

Figure 3.37 (a) Mass spectrum of $Ir(acac)_3$ normalized to the base peak, IrL_3^+.
(b) Region of (a) between m/z 200 and m/z 450, normalized to m/z 391, IrL_2^+.

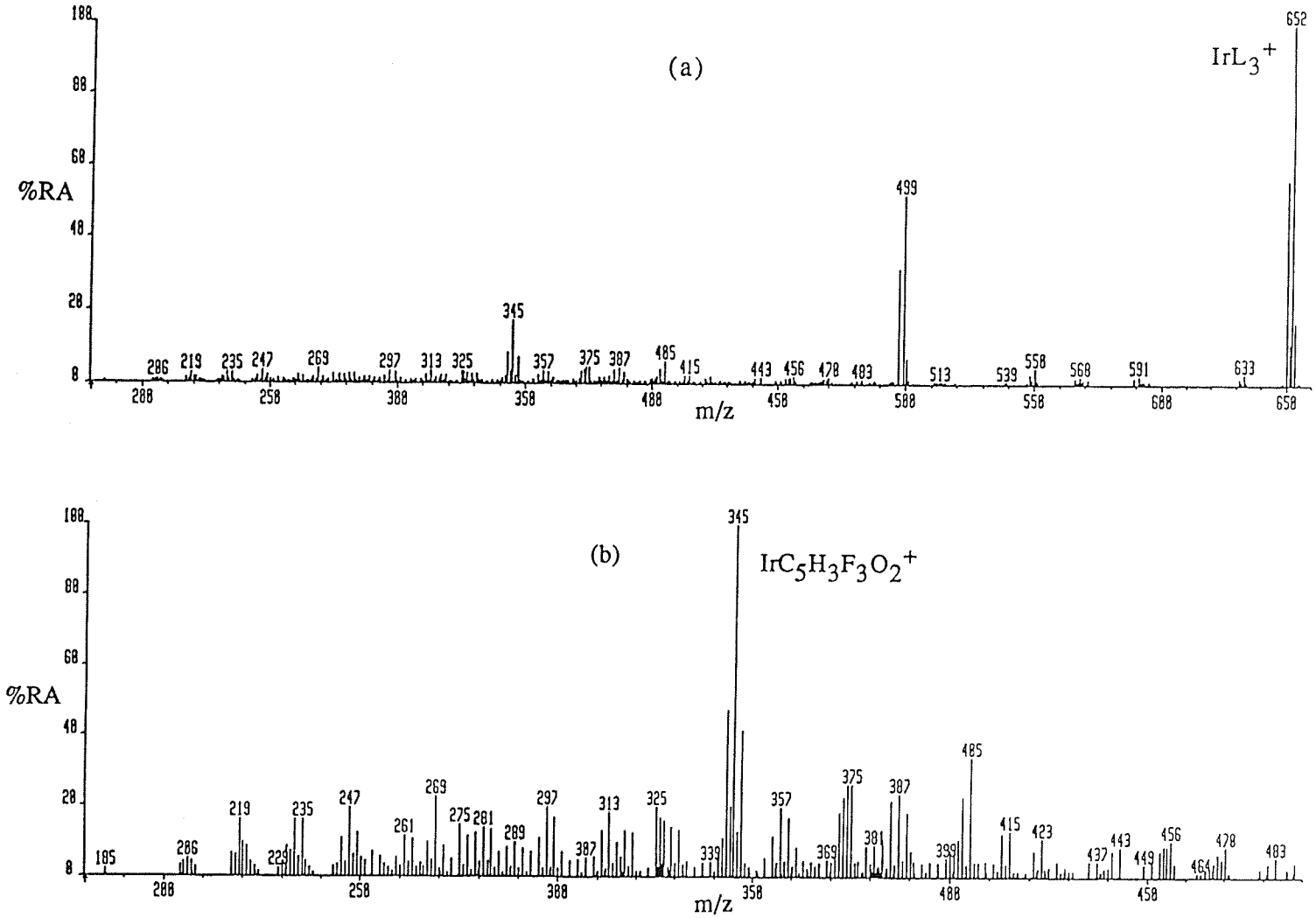

Figure 3.38 (a) Mass spectrum of $Ir(tfa)_3$ normalized to the base peak, IrL_3^+.
(b) Region of (a) between m/z 180 and m/z 490, normalized to m/z 345, $IrC_5H_3F_3O_2^+$.

Table 3.22 70 eV-EI mass spectrum of $Ir(hfa)_3$. (L = hfa)

Ion	m / z	%RA	Structure (Scheme 3.n)
IrL_3^+	814	80.9	G814(44)
$[IrL_2(L\text{-}F)]^+$	795	13.4	G795(44)
IrL_2^+	607	100.0	G607(44-47,50)
$[LIr(CO_2)(CF_3)]^+$	513	3.6	G513(45)
$[IrL(L\text{-}CF_3CO)]^+$	510	1.2	G510a(47),b(47,48),c(47)
$[LIr(CO)(CF_3)]^+$	497	<1.0	G497(46)
$[IrL(L\text{-}CF_3CO\text{-}CO)]^+$	482	5.7	G482a(47),b(47)
$[LIr(CO)(CF_2)]^+$	478	2.2	G478(46)
$LIrCF_3^+$	469	6.5	G469(46)
$[LIr(CO_2)F]^+$	463	1.9	G463(45)
$LIrCF_2^+$	450	1.4	G450(46)
$[IrL(L\text{-}CF_3CO\text{-}CF_3)]^+$	441	3.0	G441a(47),b(48)
$LIrCO^+$	428	1.5	G428(50)
$LIrF^+$	419	9.3	G419(45,50)
$IrC_6H_2F_6O_2^+$	413	3.7	G413a(47),b(47),c(47,48),d(48)
IrL^+	400	<1.0	G400a(45,50,51),b(51)
$IrC_6HF_5O_2^+$	393	1.3	G393a(47,48),b(47)
$IrC_5H_2F_6O^+$	385	4.8	G385(47,49)
$IrC_5HF_5O_2^+$	381	2.0	G381a(46),b(46)
$[Ir(L\text{-}CHO)]^+$	371	1.4	G371(51)
$IrC_5HF_5O^+$	365	1.3	G365(47,49)
$[Ir(CO)(L\text{-}CF_3)]^+$	359	<1.0	G359(50)
$IrC_4HF_5O^+$	353	3.6	G353a(46),b(46),c(46)
$IrC_5HF_3O_2^+$	343	6.0*	G343a(48)
$IrC_3F_6^+$	343		G343b(51)

* Relative contributions to m/z 343 from $IrC_5HF_3O_2^+$ and $IrC_3F_6^+$ could not be determined due to the high resolution required for separation ($m/\Delta m$=145,000).

Table 3.22 Continued

Ion	m / z	%RA	Structure (Scheme 3.n)
$IrC_4HF_5^+$	337	3.5	G337(49)
$IrC_4HF_3O_2^+$	331	3.9	G331a(50),b(50),c(50)
$IrC_3HF_5^+$	325	1.0	G325(46)
$IrC_2F_4CO^+$	321	1.1	G321(51)
$IrC_4F_4^+$	317	1.5	G317(49)
$IrC_4HF_3O^+$	315	1.7	G315a(48),b(48,49)
$IrC_3F_4^+$	305	<1.0	G305(46)
$IrC_3HF_3O^+$	303	4.8	G303a(45,46,50),b(45,50), c(45,50),d(50)
$IrC_2F_4^+$	293	4.5	G293a(51),b(51)
$COIrCF_3^+$	290	2.1	G290(46)
$IrC_3HF_3^+$	287	2.0	G287(48,49)
$IrCHCF_3^+$	275	7.0	G275a(45,50),b(45,46,50)
$COIrCF_2^+$	271	6.7	G271(46)
$IrC_3HF_2^+$	268	1.5	
$IrCF_3^+$	262	<1.0	G262(46)
$IrC_2F_2^+$	255	5.7	G255(46)
IrC_2HFO^+	253	4.0	
$IrCF_2^+$	243	1.0	G243(46,51)
IrC_2HO^+	234	1.3	
$IrCCO^+$	233	1.6	
$IrCHF^+$	225	1.3	
$IrCF^+$	224	<1.0	G224(46,51)
$IrCO^+$	221	1.1	G221(50)
$IrCH^+$	206	2.2	
Ir^+	193	<1.0	G193(51)
$C_5HF_4O_2^+$	169	3.3	G169(45)

Table 3.23 70 eV-EI mass spectrum of $Ir(acac)_3$. (L = acac)

Ion	m / z	%RA	Structure (Scheme 3.n)
IrL_3^+	490	100.0	
$CH_3IrL_2^+$	406	<1.0	
IrL_2^+	391	35.6	H391a(52,53,55,58),b(55)
$[IrL(L\text{-}CH_4)]^+$	375	2.8	H375(55)
$[IrL(L\text{-}CHO)]^+$	362	1.6	H362(55)
$[LIr(CO_2)(CH_3)]^+$	351	2.8	H351(58)
$[IrL(L\text{-}CH_2CO)]^+$	349	2.6	H349(53,57)
$[IrL(L\text{-}CH_3CO)]^+$	348	1.2	
$LIrC_3H_3O^+$	347	4.7	H347a(55),b(55)
$[LIr(CO)(CH_3)]^+$	335	2.5	H335a(52),b(52)
$[LIr(CO)(CH)]^+$	333	6.4	H333(55,57)
$IrC_7H_6O_3^+$	331	1.2	
$[LIr(CO)H]^+$	321	8.3	H321a(53),b(53)
$LIrCO^+$	320	1.5	
$IrC_6H_6O_3^+$	319	2.1	H319a(52)
$LIrC_2H_3^+$	319	1.2	H319b(55,56)
$LIrCH_3^+$	307	<1.0	H307(58)
$IrC_6H_8O_2^+$	305	4.7	H305(57)
$IrC_6H_6O_2^+$	303	4.2	H303(56)
$LIrH^+$	293	6.3	H293(53,54)
IrL^+	292	1.0	
$IrC_5H_6O_2^+$	291	21.7	H291a(52,57,58),b(58)
$IrC_5H_5O_2^+$	290	4.1	
$IrC_5H_4O_2^+$	289	2.4	H289(57)
$IrC_5H_{10}O^+$	279	2.1	H279(58)
$IrC_4H_4O_2^+$	277	2.8	H277a(54),b(57)

Table 3.23 Continued

Ion	m / z	%RA	Structure (Scheme 3.n)
$IrC_5H_8O^+$	277	1.7	H277c(57)
$IrC_5H_6O^+$	275	6.6	H275a(56),b(56)
$IrC_4H_8O^+$	265	4.7	H265a(54)
$IrC_4H_6O^+$	263	7.1	H263a(52,58),b(52)
$IrC_4H_5O^+$	262	1.8	
$IrC_4H_4O^+$	261	6.3	H261(57)
$IrC_3H_4O^+$	249	2.9	H249a(54),b(54),c(57)
$IrC_4H_6^+$	247	3.3	H247a(56)
$IrC_3H_2O^+$	247	4.0	H247b(56)
$[Ir(CO)(CH_2)]^+$	235	1.1	H235a(52)
$IrC_3H_6^+$	235	1.4	H235b(52)
$IrC_3H_4^+$	233	6.8	H233(57)
$IrC_3H_3^+$	232	1.9	
$IrC_2H_4^+$	221	1.6	H221(54)
$IrC_2H_3^+$	220	2.2	
$IrC_2H_2^+$	219	2.1	H219(56)

Table 3.24 70 eV-EI mass spectrum of $Ir(tfa)_3$. (L = tfa)

Ion	m / z	%RA	Structure (Scheme 3.n)
IrL_3^+	652	100.0	I652(59,60)
$[IrL_2(L\text{-}F)]^+$	633	3.5	I633(60)
$[IrL_3\text{-}F\text{-}CH_2CO)]^+$	591	1.1	I591a(60),b(60)
$CF_3IrL_2^+$	568	1.9	I568(59)
$[CF_3IrL(L\text{-}H_2O)]^+$	550	3.9	I550(59)
IrL_2^+	499	44.9	I499(60,63,64,66,67,69)
$[IrL(L\text{-}CHO)]^+$	470	1.3	I470(66)
$[IrL(L\text{-}CH_3CO)]^+$	456	1.8	I456a(61),b(61),c(61)
$[IrL(L\text{-}CHO\text{-}CH_3)]^+$	455	1.4	I445(66)
$[LIr(CO)(CF_3)]^+$	443	1.1	I443(64)
$LIrC_2F_3^+$	427	<1.0	I427(66)
$LIrCF_3^+$	415	1.7	I415(64)
$[LIr(CO_2)(CH_3)]^+$	405	4.4	I405(69)
$[IrL(L\text{-}CF_3CO)]^+$	402	1.2	I402a(61),b(61),c(61)
$[LIr(CO)(CH_3)]^+$	389	2.7	I389(63)
$LIrCHCO^+$	387	1.7	I387(61)
$LIrC_3H_3^+$	385	1.6	
$IrC_5HF_5O_2^+$	381	1.1	I381(64)
$[Ir(CO)H]^+$	375	3.0	I375(67)
$LIrCO^+$	374	3.4	I374(61,63)
$LIrCH_3^+$	361	1.0	I361a(63,69),b(63)
$LIrCH^+$	359	1.4	I359a(61,62),b(62),c(62)
$IrC_6H_3F_3O_2^+$	357	1.7	
$IrC_4HF_5O^+$	353	<1.0	I353(64)
$LIrH^+$	347	6.0	I347(67,68)
$IrC_5H_3F_3O_2^+$	345	10.8	I345a(63,65,69),b(63,65)

Table 3.24 Continued

Ion	m / z	%RA	Structure (Scheme 3.n)
$IrC_5H_3F_3O^+$	331	1.6	I331a(62),b(62),c(62)
$IrC_5H_4F_2O_2^+$	327	1.1	I327a(64),b(68)
$IrC_5H_2F_2O_2^+$	325	1.0	I325(65)
$IrC_4H_5F_3O^+$	319	1.3	I319(68)
$IrC_4H_3F_3O^+$	317	1.6	I317a(65),b(65)
$IrC_4H_2F_2O_2^+$	313	2.7	
$IrC_5H_4F_2O^+$	311	<1.0	I311a(62),b(62)
$IrC_4H_4F_2O^+$	299	2.2	I299a(64,67),b(68)
$IrC_4H_2F_2O^+$	297	1.7	I297a(65),b(65)
$IrC_4H_4F_2^+$	283	2.5	I283(62)
$IrC_4H_4O_2^+$	277	1.3	
$IrC_2HF_3^+$	275	1.8	
$IrC_3H_4F_2^+$	271	1.7	I271(68)
$IrC_3H_2F_2^+$	269	3.6	I269(65)
$IrC_4H_3F^+$	263	2.0	
$IrCCF_2^+$	255	<1.0	I255(62)
$IrC_3H_4O^+$	249	2.1	I249(68)
$IrCF_2^+$	243	<1.0	I243(68)
CH_2IrCO^+	235	3.1	I235(69)
$IrC_2H_4^+$	221	1.1	
LH^+	154	13.3	

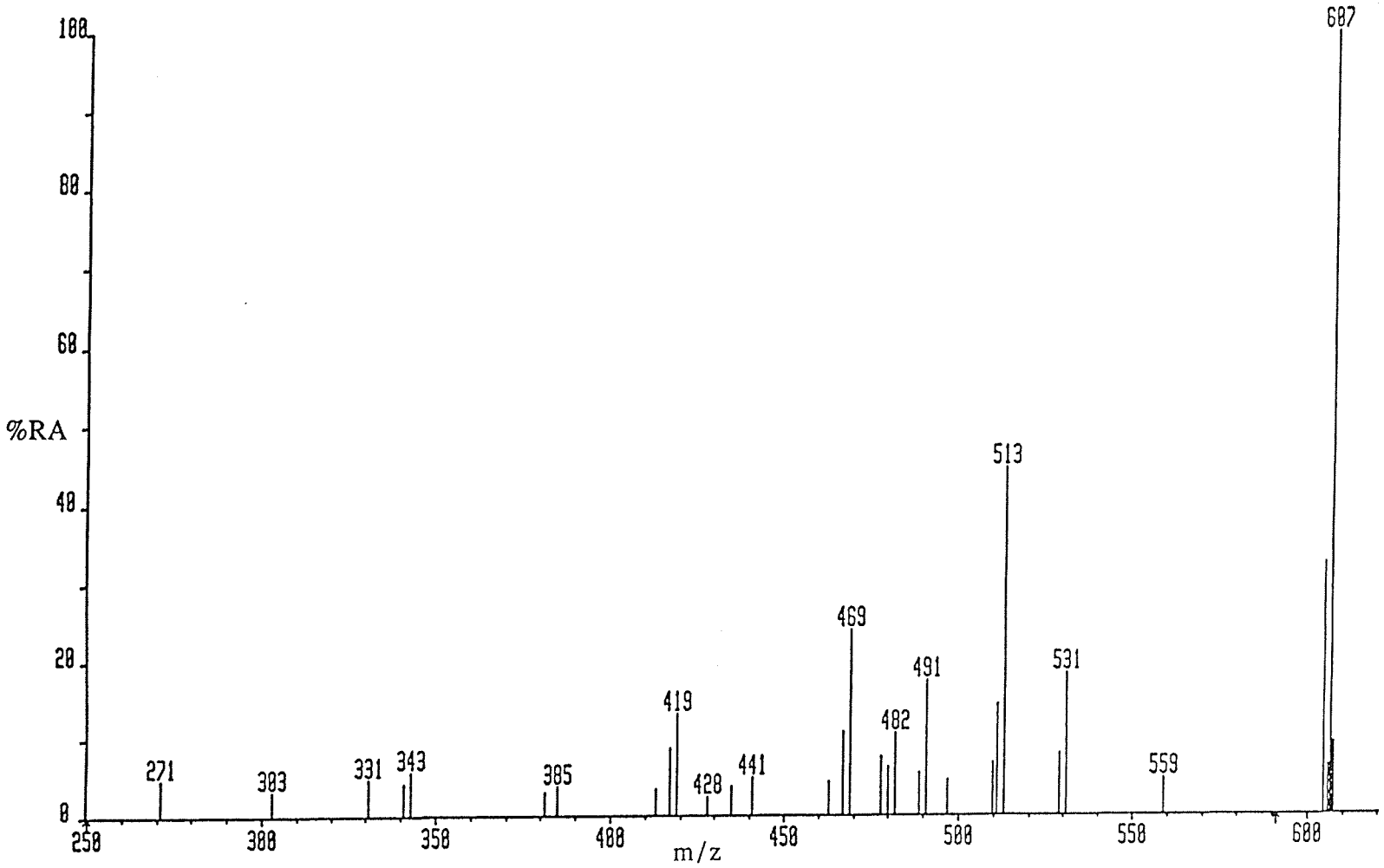

Figure 3.39 Daughter ion spectrum (B/E scan) of $Ir(hfa)_2^+$ (Ion abundance x100 between arrows).

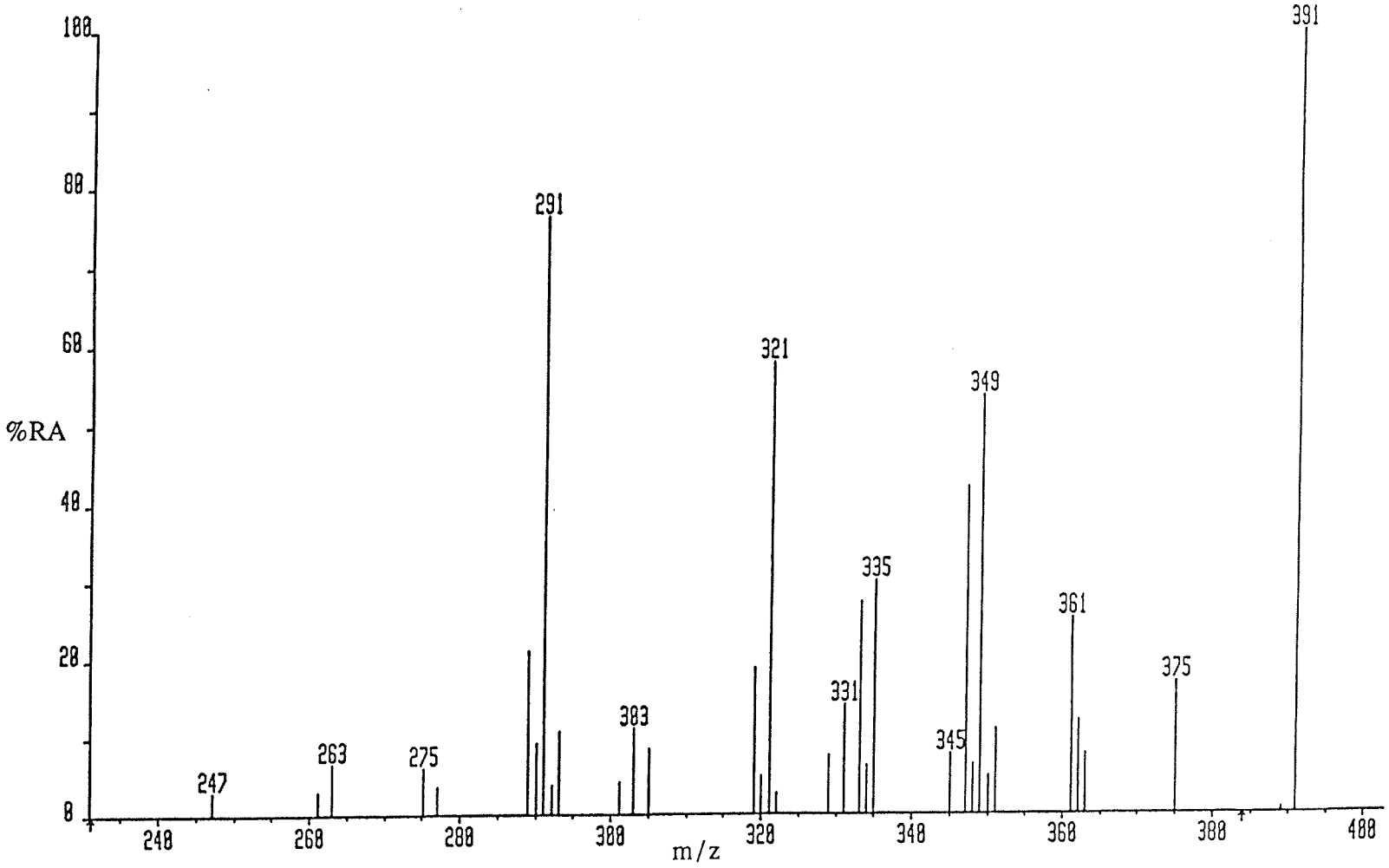

Figure 3.40 Daughter ion spectrum (B/E scan) of $Ir(acac)_2^+$ (Ion abundance x50 between arrows).

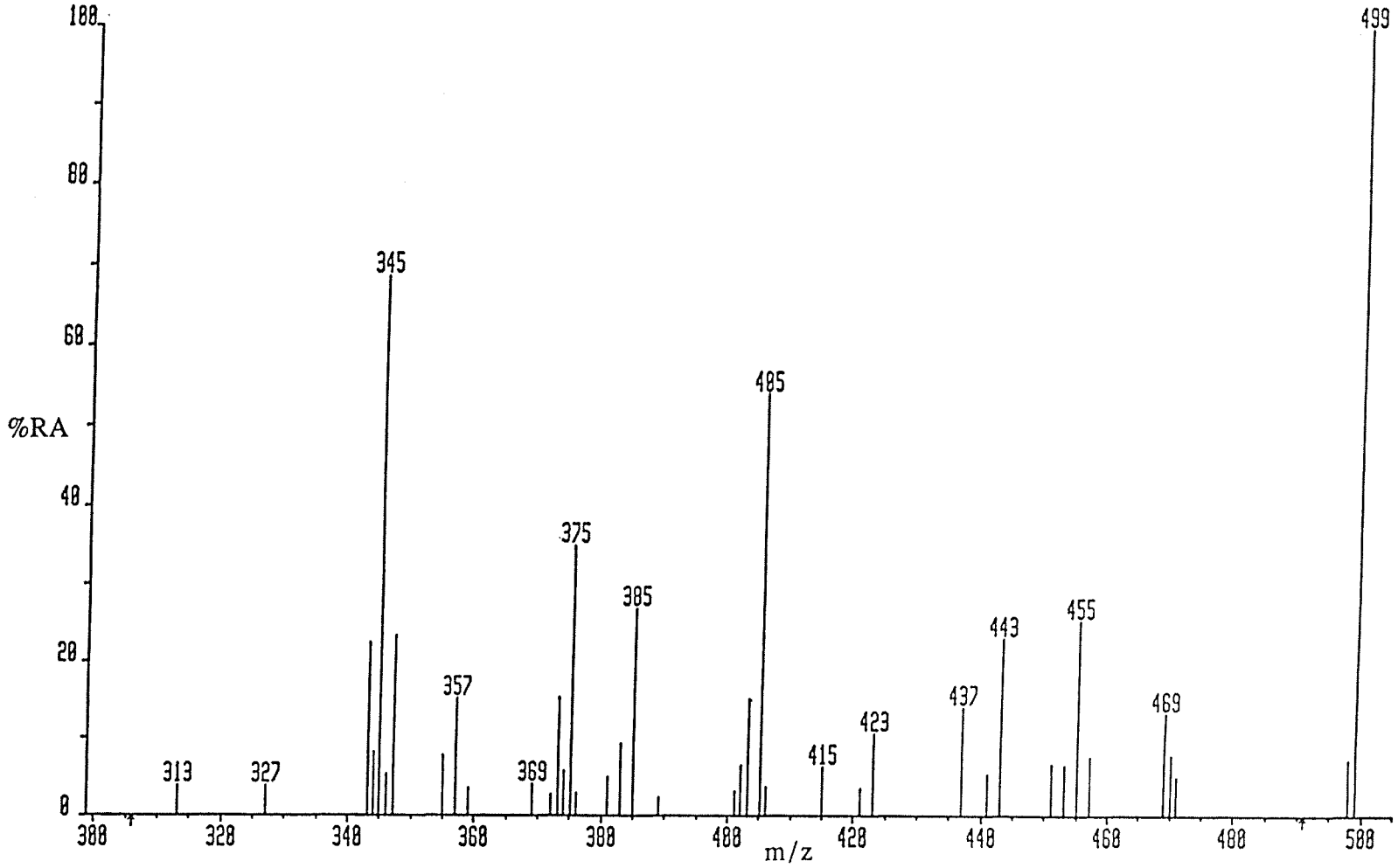

Figure 3.41 Daughter ion spectrum (B/E scan) of $Ir(tfa)_2^+$ (Ion abundance x80 between arrows).

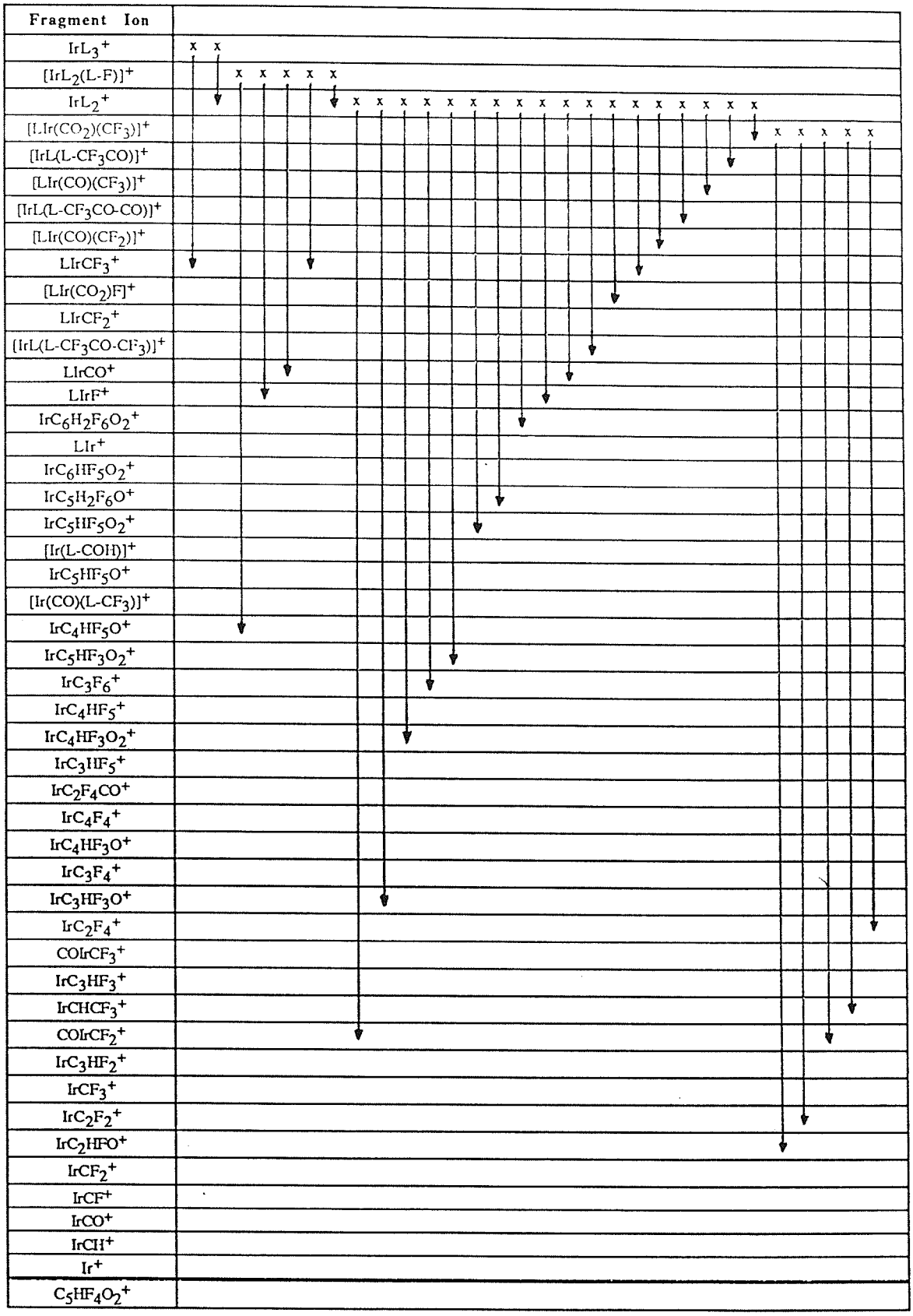

Scheme 3.41 Fragmentation pathways of $Ir(hfa)_3$

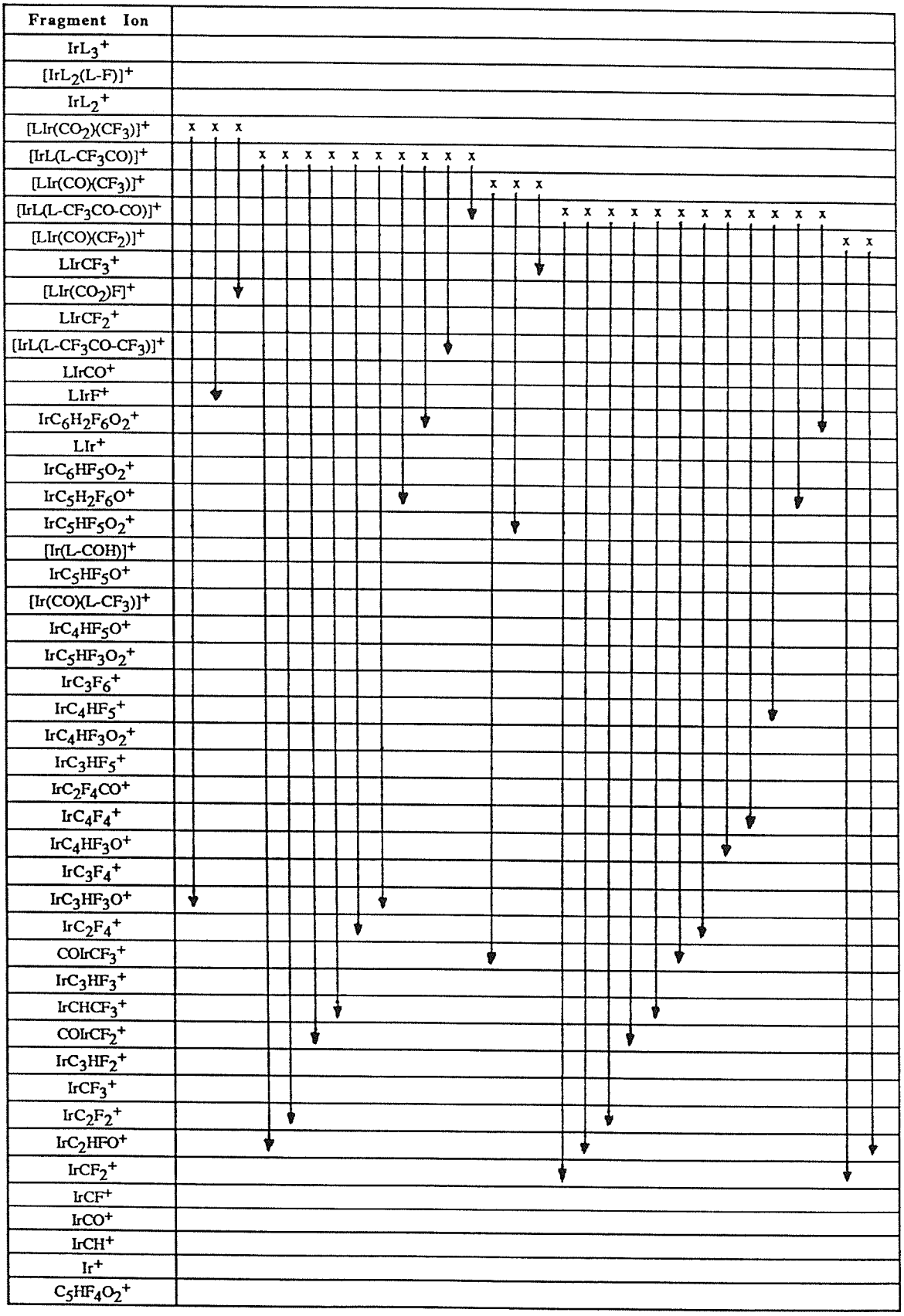

Scheme 3.41 (Continued)

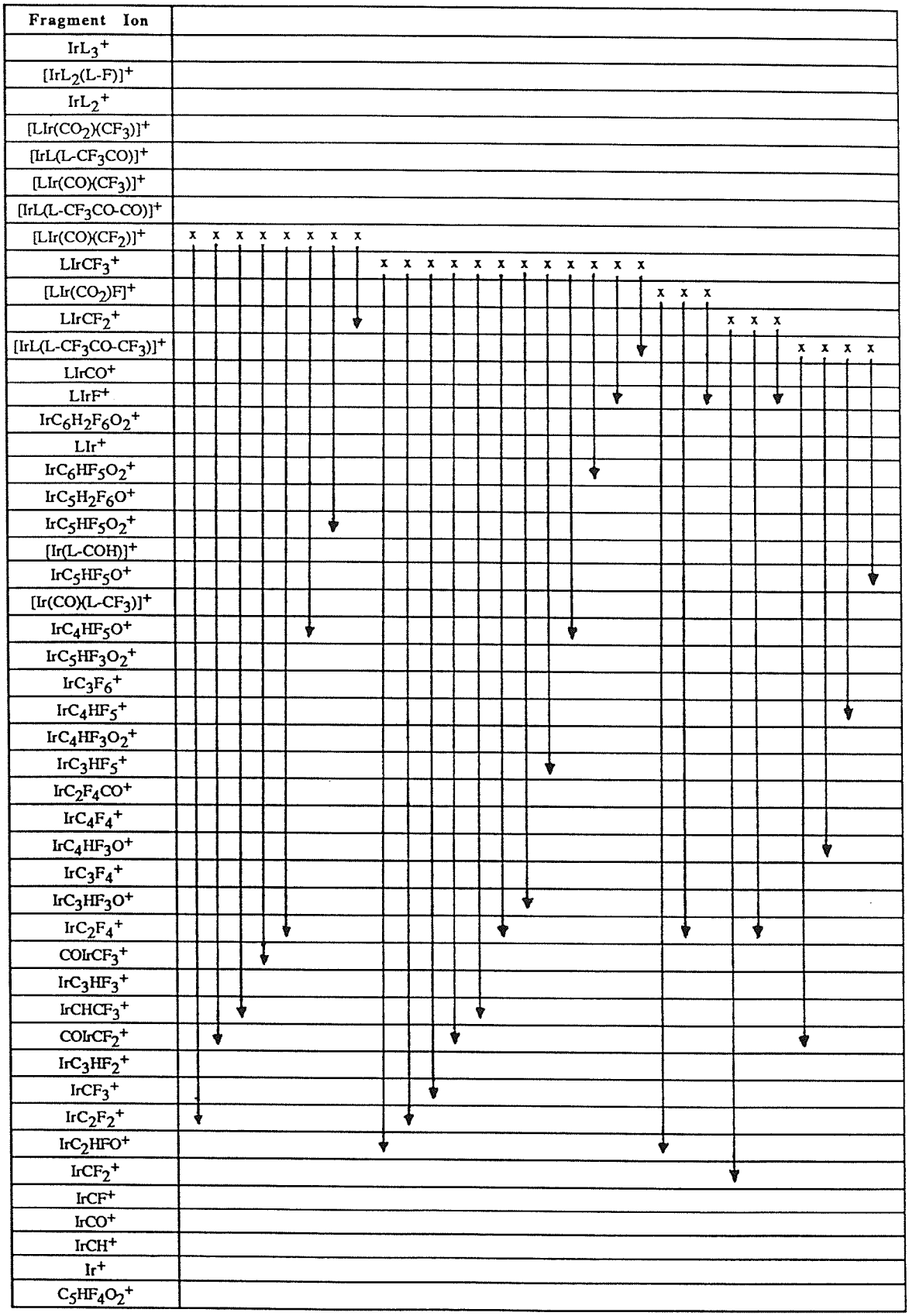

Scheme 3.41 (Continued)

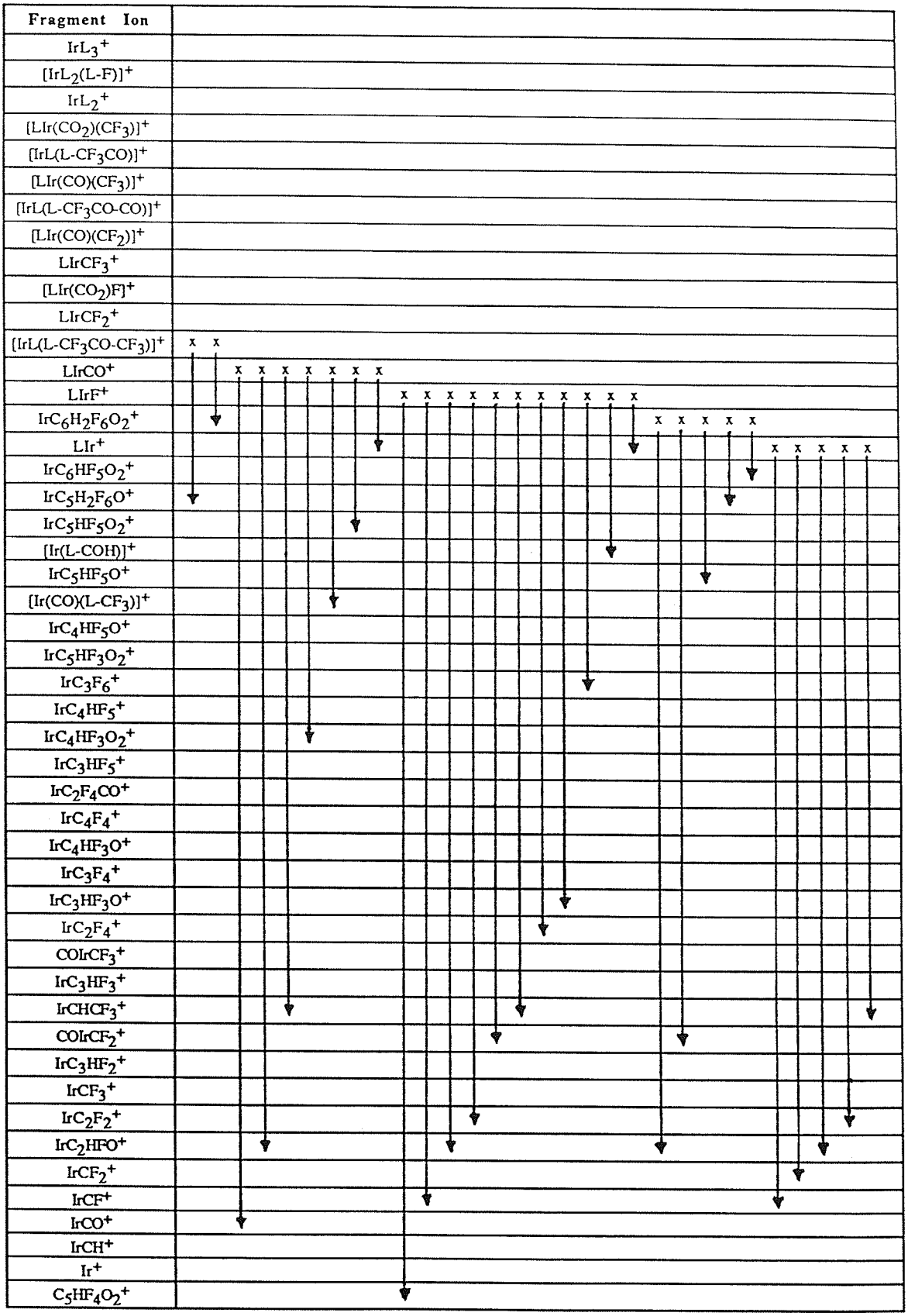

Scheme 3.41 (Continued)

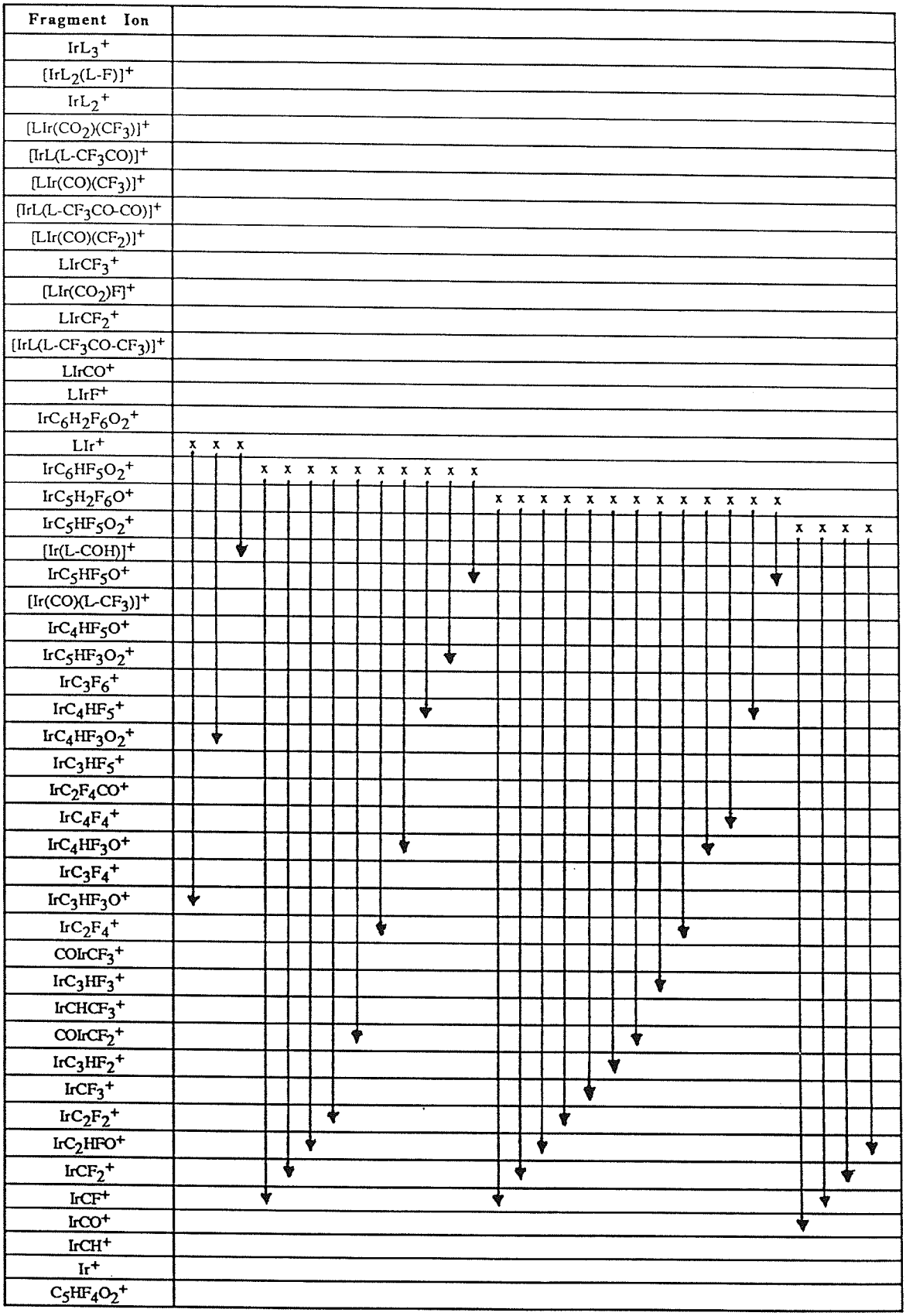

Scheme 3.41 (Continued)

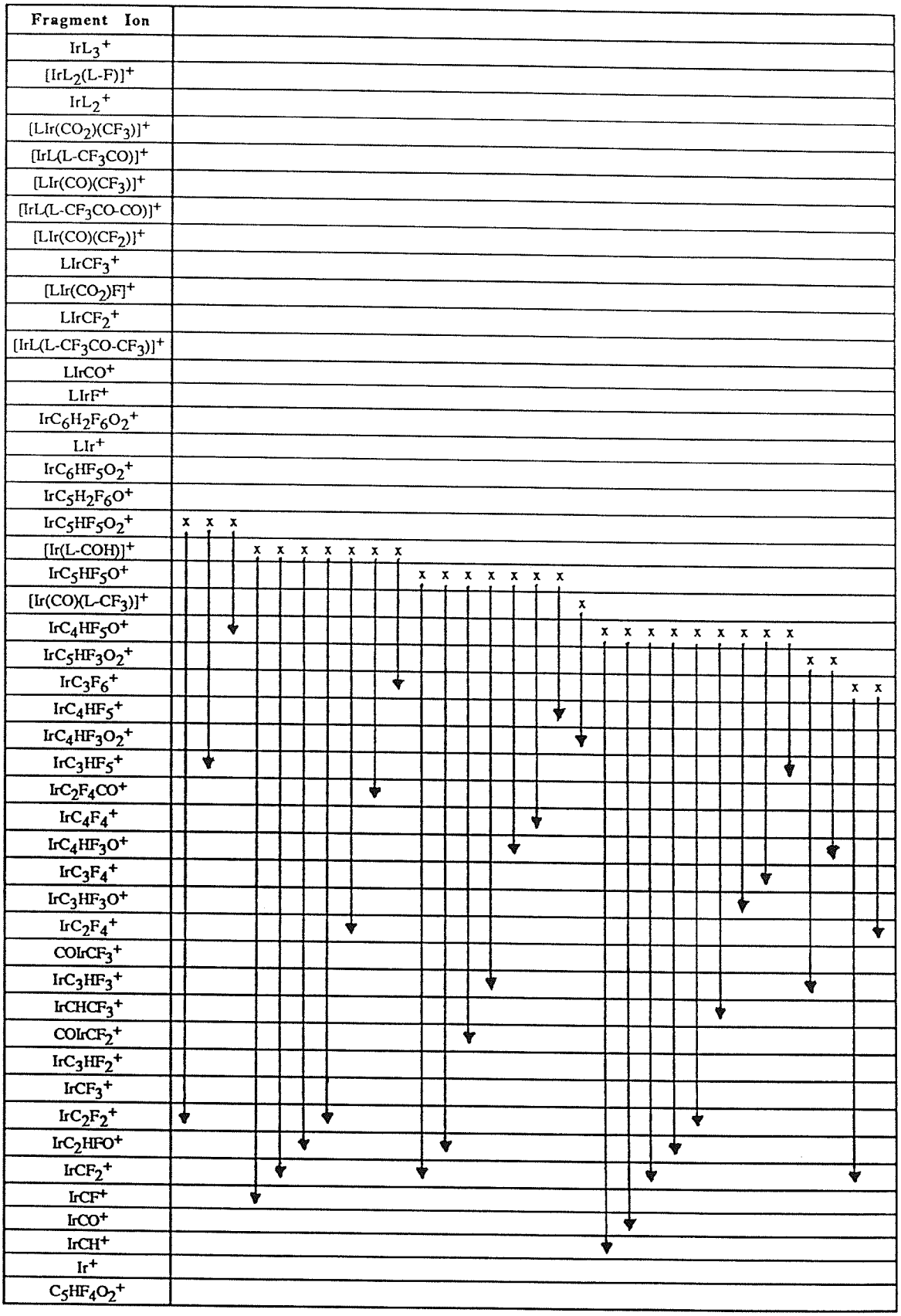

Scheme 3.41 (Continued)

Fragment Ion	
IrL_3^+	
$[IrL_2(L\text{-}F)]^+$	
IrL_2^+	
$[LIr(CO_2)(CF_3)]^+$	
$[IrL(L\text{-}CF_3CO)]^+$	
$[LIr(CO)(CF_3)]^+$	
$[IrL(L\text{-}CF_3CO\text{-}CO)]^+$	
$[LIr(CO)(CF_2)]^+$	
$LIrCF_3^+$	
$[LIr(CO_2)F]^+$	
$LIrCF_2^+$	
$[IrL(L\text{-}CF_3CO\text{-}CF_3)]^+$	
$LIrCO^+$	
$LIrF^+$	
$IrC_6H_2F_6O_2^+$	
LIr^+	
$IrC_6HF_5O_2^+$	
$IrC_5H_2F_6O^+$	
$IrC_5HF_5O_2^+$	
$[Ir(L\text{-}COH)]^+$	
$IrC_5HF_5O^+$	
$[Ir(CO)(L\text{-}CF_3)]^+$	
$IrC_4HF_5O^+$	
$IrC_5HF_3O_2^+$	
$IrC_3F_6^+$	
$IrC_4HF_5^+$	x x x x x x
$IrC_4HF_3O_2^+$	x
$IrC_3HF_5^+$	x x x
$IrC_2F_4CO^+$	x
$IrC_4F_4^+$	
$IrC_4HF_3O^+$	x
$IrC_3F_4^+$	x
$IrC_3HF_3O^+$	x
$IrC_2F_4^+$	x x x
$COIrCF_3^+$	x x x x
$IrC_3HF_3^+$	
$IrCHCF_3^+$	x
$COIrCF_2^+$	
$IrC_3HF_2^+$	
$IrCF_3^+$	
$IrC_2F_2^+$	
IrC_2HFO^+	
$IrCF_2^+$	
$IrCF^+$	
$IrCO^+$	
$IrCH^+$	
Ir^+	
$C_5HF_4O_2^+$	

Scheme 3.41 (Continued)

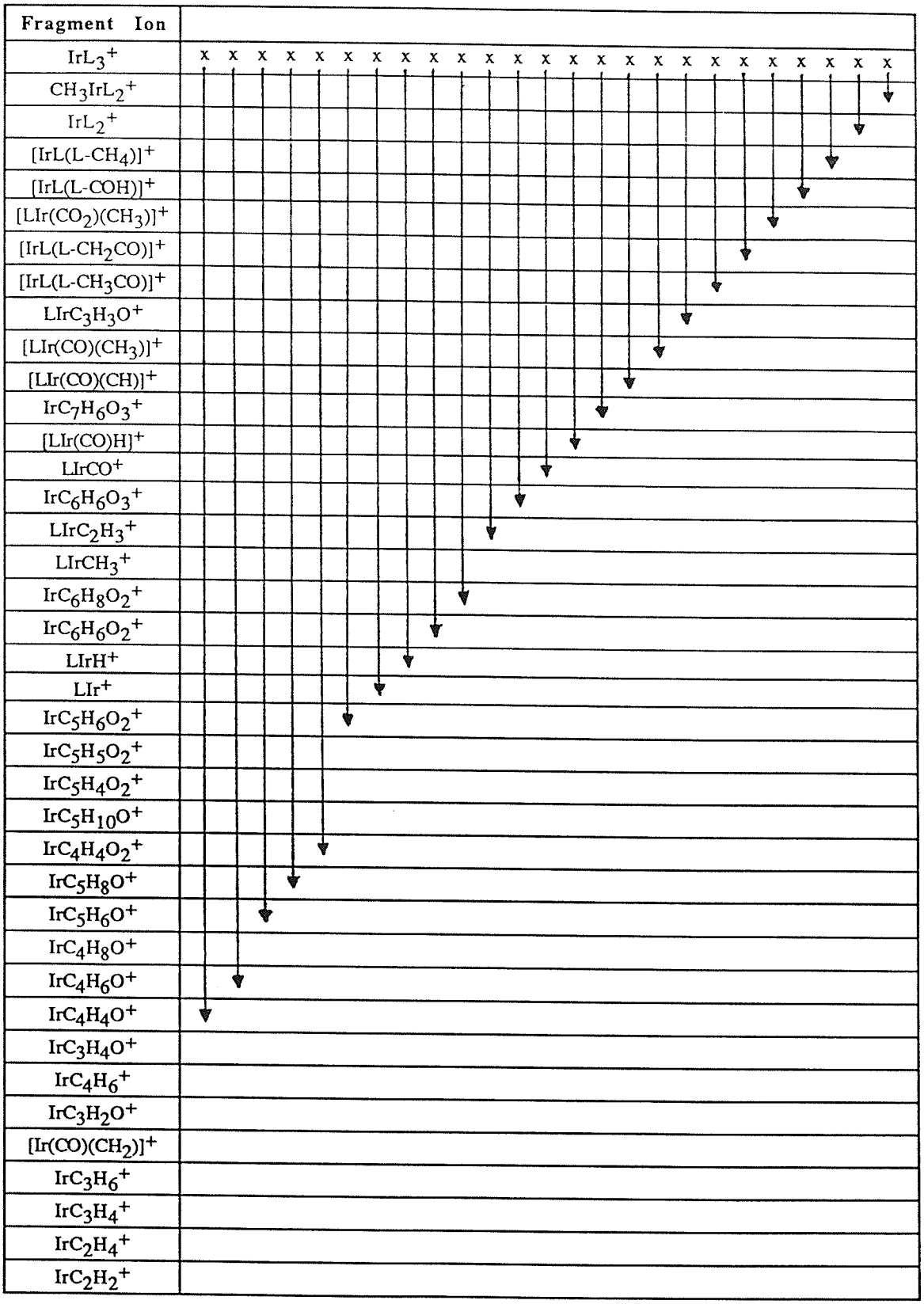

Scheme 3.42 Fragmentation pathways of $Ir(acac)_3$

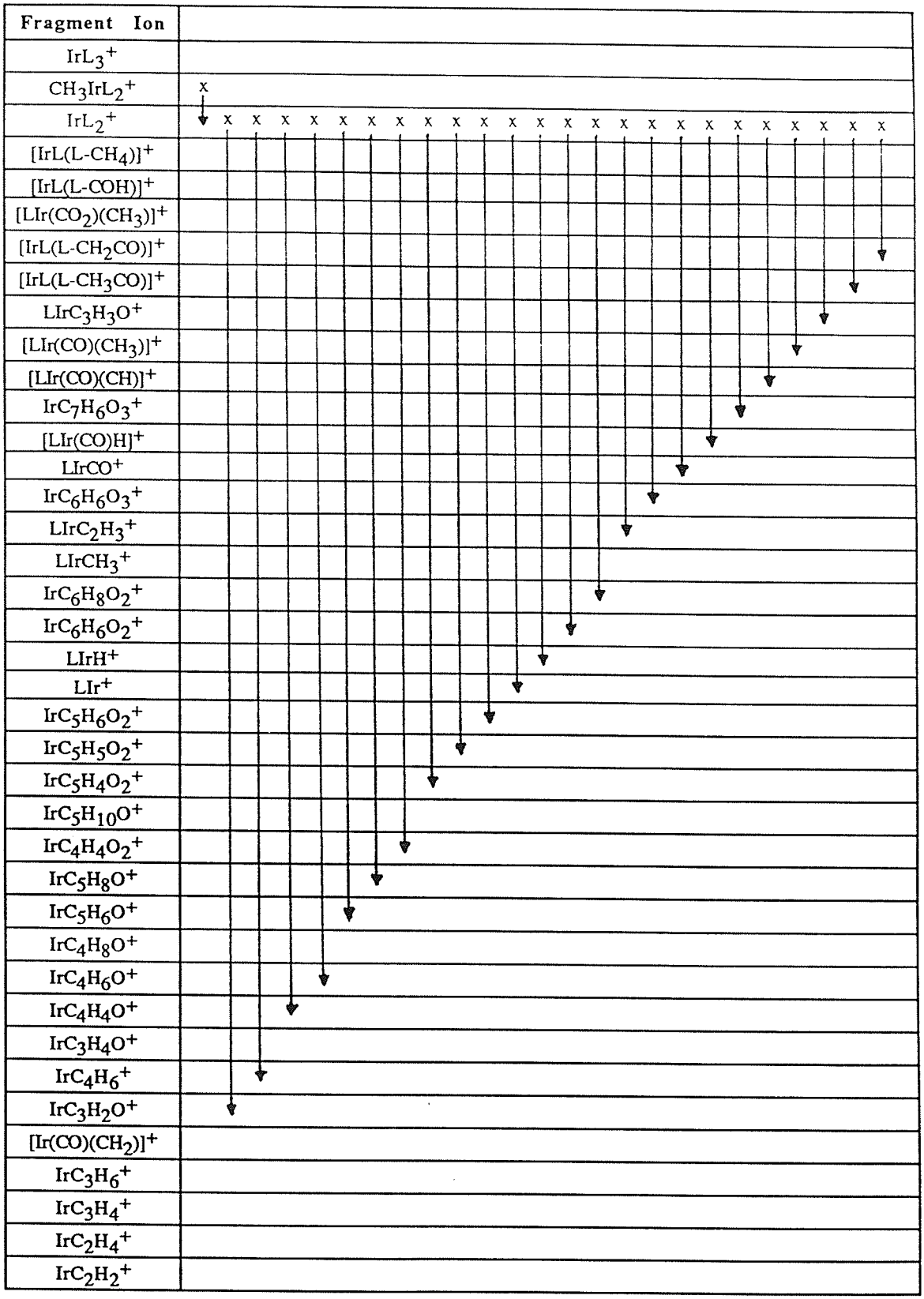

Scheme 3.42 (Continued)

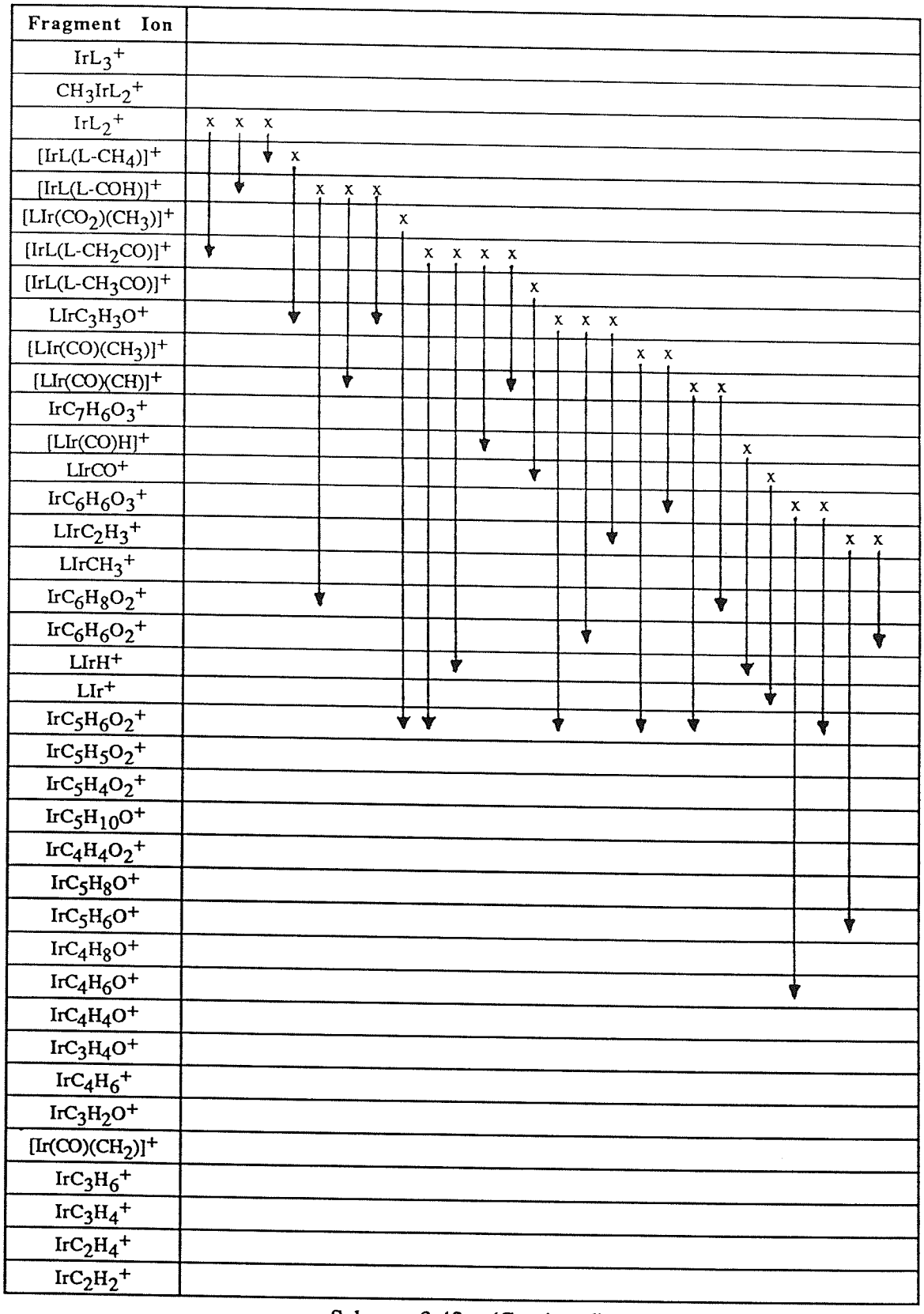

Scheme 3.42 (Continued)

Fragment Ion	
IrL_3^+	
$CH_3IrL_2^+$	
IrL_2^+	
$[IrL(L\text{-}CH_4)]^+$	
$[IrL(L\text{-}COH)]^+$	
$[LIr(CO_2)(CH_3)]^+$	
$[IrL(L\text{-}CH_2CO)]^+$	
$[IrL(L\text{-}CH_3CO)]^+$	
$LIrC_3H_3O^+$	
$[LIr(CO)(CH_3)]^+$	
$[LIr(CO)(CH)]^+$	
$IrC_7H_6O_3^+$	
$[LIr(CO)H]^+$	
$LIrCO^+$	
$IrC_6H_6O_3^+$	
$LIrC_2H_3^+$	
$LIrCH_3^+$	x x
$IrC_6H_8O_2^+$	x x x
$IrC_6H_6O_2^+$	x
$LIrH^+$	x x
LIr^+	
$IrC_5H_6O_2^+$	x x x
$IrC_5H_5O_2^+$	
$IrC_5H_4O_2^+$	x
$IrC_5H_{10}O^+$	x
$IrC_4H_4O_2^+$	x
$IrC_5H_8O^+$	x
$IrC_5H_6O^+$	x
$IrC_4H_8O^+$	x
$IrC_4H_6O^+$	
$IrC_4H_4O^+$	x
$IrC_3H_4O^+$	x x
$IrC_4H_6^+$	x
$IrC_3H_2O^+$	
$[Ir(CO)(CH_2)]^+$	
$IrC_3H_6^+$	
$IrC_3H_4^+$	
$IrC_2H_4^+$	
$IrC_2H_2^+$	

Scheme 3.42 (Continued)

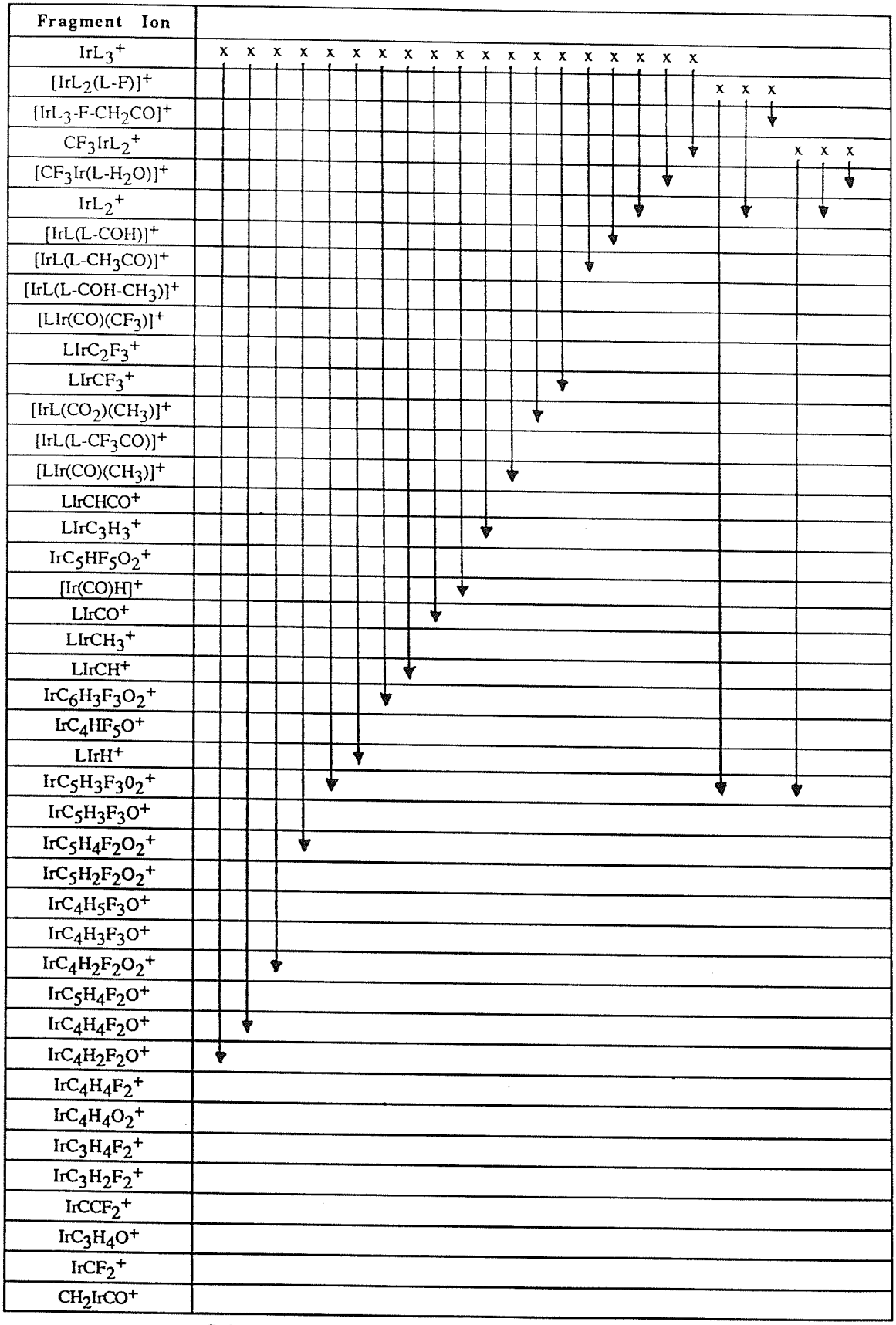

Scheme 3.43 Fragmentation pathways of $Ir(tfa)_3$

Fragment Ion	
IrL_3^+	
$[IrL_2(L\text{-}F)]^+$	
$[IrL_3\text{-}F\text{-}CH_2CO]^+$	
$CF_3IrL_2^+$	
$[CF_3Ir(L\text{-}H_2O)]^+$	
IrL_2^+	
$[IrL(L\text{-}COH)]^+$	
$[IrL(L\text{-}CH_3CO)]^+$	
$[IrL(L\text{-}COH\text{-}CH_3)]^+$	
$[LIr(CO)(CF_3)]^+$	
$LIrC_2F_3^+$	
$LIrCF_3^+$	
$[IrL(CO_2)(CH_3)]^+$	
$[IrL(L\text{-}CF_3CO)]^+$	
$[LIr(CO)(CH_3)]^+$	
$LIrCHCO^+$	
$LIrC_3H_3^+$	
$IrC_5HF_5O_2^+$	
$[Ir(CO)H]^+$	
$LIrCO^+$	
$LIrCH_3^+$	
$LIrCH^+$	
$IrC_6H_3F_3O_2^+$	
$IrC_4HF_5O^+$	
$LIrH^+$	
$IrC_5H_3F_3O_2^+$	
$IrC_5H_3F_3O^+$	
$IrC_5H_4F_2O_2^+$	
$IrC_5H_2F_2O_2^+$	
$IrC_4H_5F_3O^+$	
$IrC_4H_3F_3O^+$	
$IrC_4H_2F_2O_2^+$	
$IrC_5H_4F_2O^+$	
$IrC_4H_4F_2O^+$	
$IrC_4H_2F_2O^+$	
$IrC_4H_4F_2^+$	
$IrC_4H_4O_2^+$	
$IrC_3H_4F_2^+$	
$IrC_3H_2F_2^+$	
$IrCCF_2^+$	
$IrC_3H_4O^+$	
$IrCF_2^+$	
CH_2IrCO^+	

Scheme 3.43 Continued

Fragment Ion	
IrL_3^+	
$[IrL_2(L\text{-}F)]^+$	
$[IrL_3\text{-}F\text{-}CH_2CO]^+$	
$CF_3IrL_2^+$	
$[CF_3Ir(L\text{-}H_2O)]^+$	
IrL_2^+	
$[IrL(L\text{-}COH)]^+$	
$[IrL(L\text{-}CH_3CO)]^+$	
$[IrL(L\text{-}COH\text{-}CH_3)]^+$	
$[LIr(CO)(CF_3)]^+$	
$LIrC_2F_3^+$	
$LIrCF_3^+$	
$[IrL(CO_2)(CH_3)]^+$	
$[IrL(L\text{-}CF_3CO)]^+$	
$[LIr(CO)(CH_3)]^+$	
$LIrCHCO^+$	
$LIrC_3H_3^+$	
$IrC_5HF_5O_2^+$	
$[Ir(CO)H]^+$	
$LIrCO^+$	
$LIrCH_3^+$	
$LIrCH^+$	
$IrC_6H_3F_3O_2^+$	
$IrC_4HF_5O^+$	
$LIrH^+$	
$IrC_5H_3F_3O_2^+$	
$IrC_5H_3F_3O^+$	
$IrC_5H_4F_2O_2^+$	
$IrC_5H_2F_2O_2^+$	
$IrC_4H_5F_3O^+$	
$IrC_4H_3F_3O^+$	
$IrC_4H_2F_2O_2^+$	
$IrC_5H_4F_2O^+$	
$IrC_4H_4F_2O^+$	
$IrC_4H_2F_2O^+$	
$IrC_4H_4F_2^+$	
$IrC_4H_4O_2^+$	
$IrC_3H_4F_2^+$	
$IrC_3H_2F_2^+$	
$IrCCF_2^+$	
$IrC_3H_4O^+$	
$IrCF_2^+$	
CH_2IrCO^+	

Scheme 3.43 Continued

Fragment Ion	
IrL_3^+	
$[IrL_2(L\text{-}F)]^+$	
$[IrL_3\text{-}F\text{-}CH_2CO]^+$	
$CF_3IrL_2^+$	
$[CF_3Ir(L\text{-}H_2O)]^+$	
IrL_2^+	
$[IrL(L\text{-}COH)]^+$	
$[IrL(L\text{-}CH_3CO)]^+$	
$[IrL(L\text{-}COH\text{-}CH_3)]^+$	
$[LIr(CO)(CF_3)]^+$	
$LIrC_2F_3^+$	
$LIrCF_3^+$	
$[IrL(CO_2)(CH_3)]^+$	
$[IrL(L\text{-}CF_3CO)]^+$	
$[LIr(CO)(CH_3)]^+$	
$LIrCHCO^+$	
$LIrC_3H_3^+$	
$IrC_5HF_5O_2^+$	
$[Ir(CO)H]^+$	
$LIrCO^+$	
$LIrCH_3^+$	
$LIrCH^+$	
$IrC_6H_3F_3O_2^+$	
$IrC_4HF_5O^+$	
$LIrH^+$	
$IrC_5H_3F_302^+$	
$IrC_5H_3F_3O^+$	x x
$IrC_5H_4F_2O_2^+$	x
$IrC_5H_2F_2O_2^+$	
$IrC_4H_5F_3O^+$	x
$IrC_4H_3F_3O^+$	x x
$IrC_4H_2F_2O_2^+$	
$IrC_5H_4F_2O^+$	x
$IrC_4H_4F_2O^+$	x x x
$IrC_4H_2F_2O^+$	x x
$IrC_4H_4F_2^+$	x
$IrC_4H_4O_2^+$	
$IrC_3H_4F_2^+$	
$IrC_3H_2F_2^+$	
$IrCCF_2^+$	
$IrC_3H_4O^+$	
$IrCF_2^+$	
CH_2IrCO^+	

Scheme 3.43 Continued

oxidation state in rhodium is relatively less stable. The lack of importance generally assigned to the +II oxidation state of iridium is consistent with the very minor presence, if any, of the ion IrL^+. The loss of two complete ligand radicals from the molecular ion would have indicated that iridium had undergone reduction from the +III to the +II oxidation state. Instead, IrL_2^+ decomposes mainly by loss of even-electron neutral species, consistent with the discussion in Section 1.1.

One further characteristic of iridium that greatly influences the mass spectra of these complexes is iridum's demonstrated ability to form single and multiple bonds with carbon[21,73,87,105]. In the Co, Rh and Ir triad the metal-carbon bond strength increases in the order Co < Rh < Ir[87].

B) *Ir(hfa)*

Loss of ·F from the molecular ion yields $[IrL_2(L\text{-}F)]^+$, **G795**, the third most abundant peak in the mass spectrum. A similar loss has been observed for a wide range of fluorine-substituted acetylacetonates[68,104,106,107]; its relative importance reflects the stability of the molecular ion and, of course, the number of fluorines present per ligand (Tables 3.25 and 3.26). The daughter ion spectrum of **G795** indicates that this ion loses the remaining portion of the ligand to give IrL_2^+, **G607**, and a neutral fragment assigned as the stable species (L-F), **G188** (Scheme 3.44).

IrL_2^+, **G607**, undergoes fragmentation to yield many of the major metal-containing ions in the mass spectrum. Some proposed

Table 3.25 Relative abundances (%) of the molecular ion and $[MetL_2(L\text{-}F)]^+$ ions in the mass spectra of various trivalent fluorine-substituted acetylacetonates.

	L = hfa		L = tfa	
	$MetL_3^+$	$[MetL_2(L\text{-}F)]^+$	$MetL_3^+$	$[MetL_2(L\text{-}F)]^+$
Al(III)[106]	5	1	3	-
Cr(III)[106]	20	4	24	2
Fe(III)[106]	18	2	10	-
Co(III)[104]	21	-	34	4
Rh(III)[104]	33	8	47	3
Rh(III)[68]	100	20	NR	NR
Re(III)[107]	100	36	NR	NR
Ir(III)†	81	13	100	4

NR Value not reported in reference.

† This work.

Table 3.26 Relative abundances (%) of the molecular ion and $[MetL(L\text{-}F)]^+$ ions in the mass spectra of various divalent fluorine-substituted acetylacetonates.

	L = hfa		L = tfa	
	$MetL_2^+$	$[MetL(L\text{-}F)]^+$	$MetL_2^+$	$[MetL(L\text{-}F)]^+$
Fe(II)[106]	83	4	100	-
Ni(II)[104]	43	10	54	5
Cu(II)[106]	9	-	5	-
Zn(II)[106]	9	-	44	-
Zn(II)[104]	27	3	100	-
Pd(II)[104]	75	15	100	5

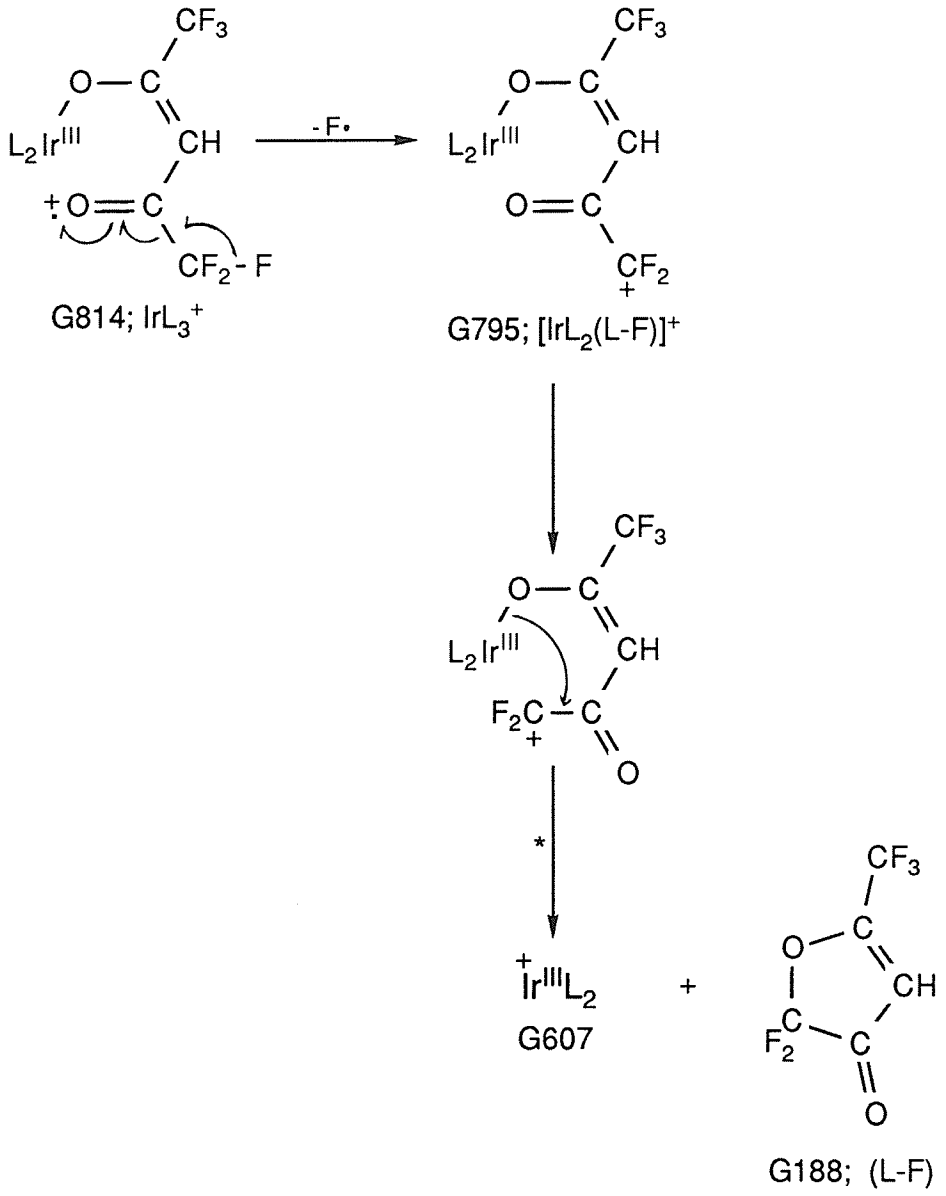
CF3
O—C
L2Ir(III)
CH
+O=C
CF2- F
G814; IrL3+
- F•
CF3
O—C
L2Ir(III)
CH
O=C
CF2
+
G795; [IrL2(L-F)]+
CF3
O—C
L2Ir(III)
CH
F2C—C
+
O
*
+
Ir(III)L2
G607
+
CF3
C
O
CH
F2C
C
O
G188; (L-F)

Scheme 3.44

mechanisms for formation of these ions, and of subsequent daughter ions, are shown in Schemes 3.45 to 3.51.

Scheme 3.45 shows decomposition of **G607** in a reaction sequence involving formation of an Ir-CF_3 bond, migration of the now free carbonyl group to the other oxygen of the ligand, and elimination of CF_3CCH to give $[LIr(CO_2)(CF_3)]^+$, **G513**. Consecutive losses of CF_2 and CO_2 from **G513** involve the formation of an Ir-F bond to yield ions $[LIr(CO_2)F]^+$, **G463**, and $LIrF^+$, **G419**, respectively. Ir(III) is considered to be a borderline acid while fluorine can be classified as a hard base. The formation of an Ir-F bond is therefore in keeping with the HSAB theory discussed earlier (see Section 1.2). In addition, the two electron withdrawing CF_3 groups in the remaining intact ligand of **G513**, would further increase the hardness of iridium making it even more receptive to a fluorine transfer. Migration of ·F to ruthenium was also observed in the mass spectrum of $Ru(hfa)_3$[68] but proceeded by the direct dissociation of RuL_2^+ to $LRuF^+$. In contrast, fluorine migration to the metal in the analogous rhodium complex[68,104] was not observed, the difference being attributed to rhodium's preference (in this complex) to undergo reduction. That Ir-F bonds are indeed formed was confirmed by the observed loss of the neutral fragment, IrF_3 from **G419** to yield the organic ion $[L-2F]^+$, **G169**. Ion **G419** also decomposes by successive losses of the neutral radicals ·F and $CF_3\dot{C}O$, yielding the low abundance ion IrL^+, **G400a**, and $[Ir(L-CF_3CO)]^+$, **G303a**, respectively. The loss of each of these neutrals is an indicator that iridium has undergone a decrease in oxidation state. The +II oxidation state as mentioned earlier, does not occur to any

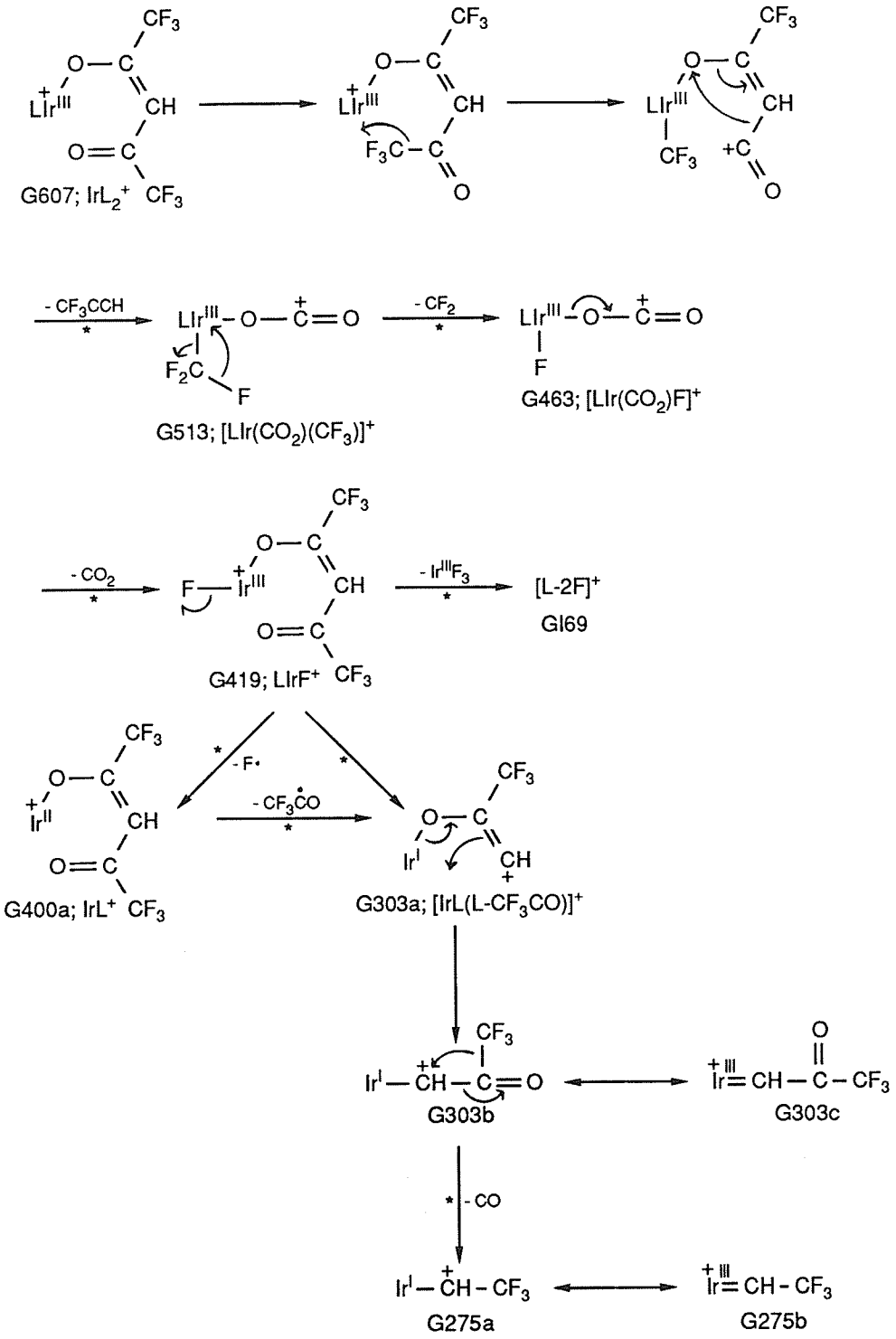
G607; IrL2+ CF3
- CF3CCH
G513; [LIr(CO2)(CF3)]+
- CF2
G463; [LIr(CO2)F]+
- CO2
G419; LIrF+ CF3
- IrIIIF3
[L-2F]+
GI69
- F•
- CF3CO
G400a; IrL+ CF3
G303a; [IrL(L-CF3CO)]+
G303b
G303c
- CO
G275a
G275b

Scheme 3.45

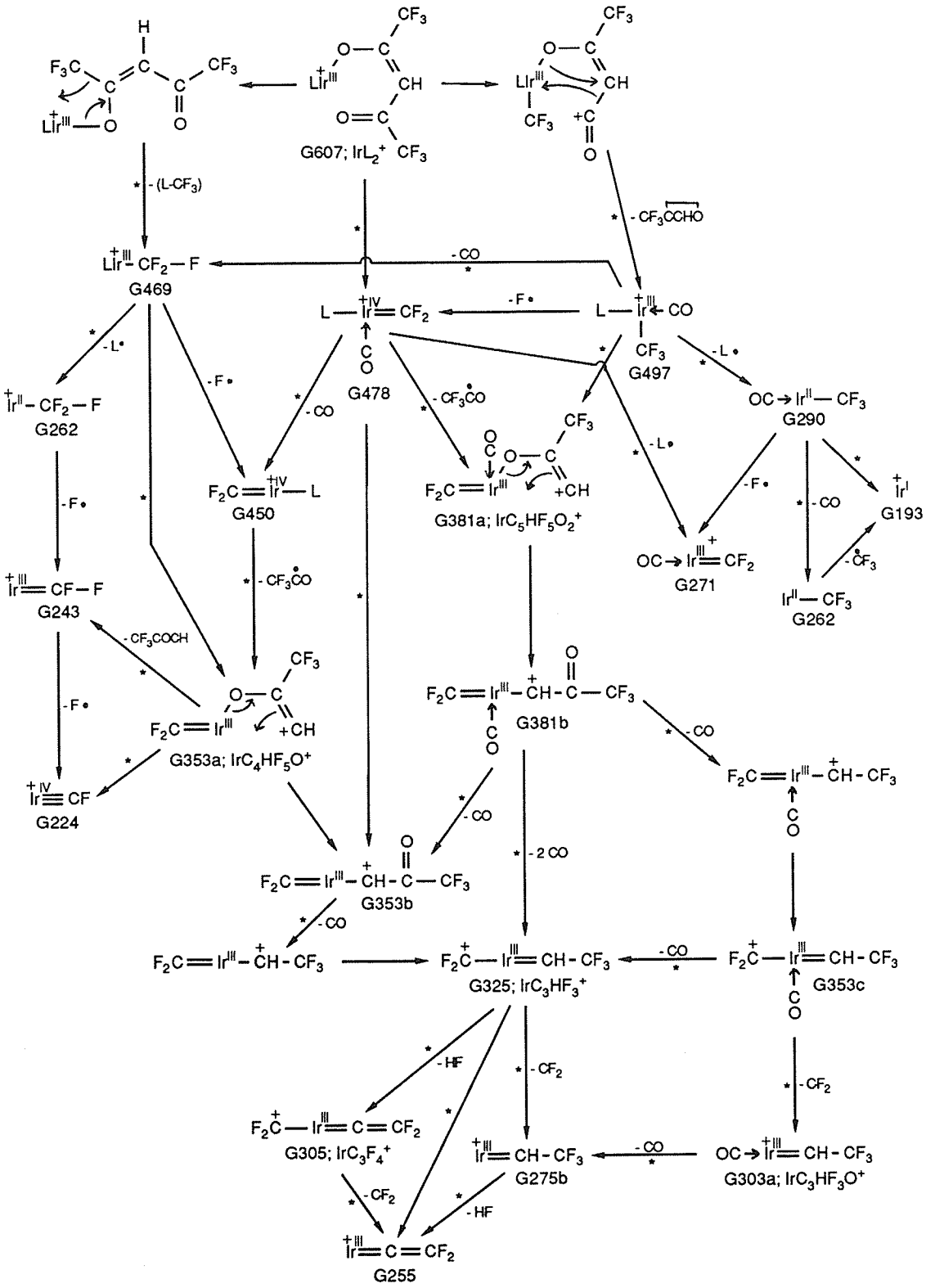
G607; IrL2+ CF3
- (L-CF3)
- CF3CCHO
- CO
G469
- F•
- L•
G497
G478
- CF3CO
G262
G450
G290
G381a; IrC5HF5O2+
G193
G271
G262
G243
- CF3COCH
G353a; IrC4HF5O+
G381b
G224
- 2 CO
G353b
G325; IrC3HF3+
G353c
- HF
- CF2
G305; IrC3F4+
G275b
G303a; IrC3HF3O+
G255

Scheme 3.46

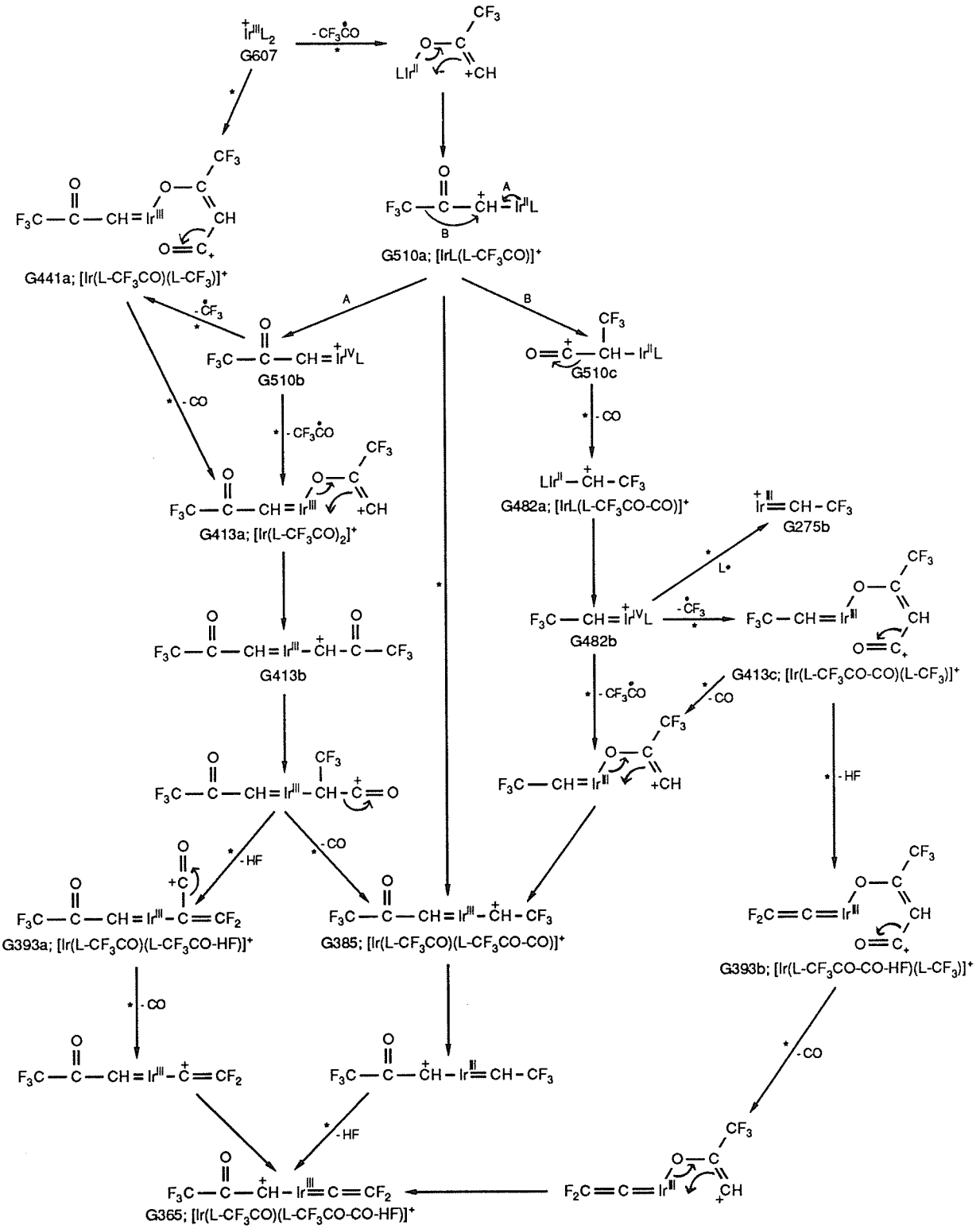
G607
G441a; [Ir(L-CF3CO)(L-CF3)]+
G510a; [IrL(L-CF3CO)]+
G510b
G510c
G413a; [Ir(L-CF3CO)2]+
G482a; [IrL(L-CF3CO-CO)]+
G275b
G482b
G413b
G413c; [Ir(L-CF3CO-CO)(L-CF3)]+
G393a; [Ir(L-CF3CO)(L-CF3CO-HF)]+
G385; [Ir(L-CF3CO)(L-CF3CO-CO)]+
G393b; [Ir(L-CF3CO-CO-HF)(L-CF3)]+
G365; [Ir(L-CF3CO)(L-CF3CO-CO-HF)]+

Scheme 3.47

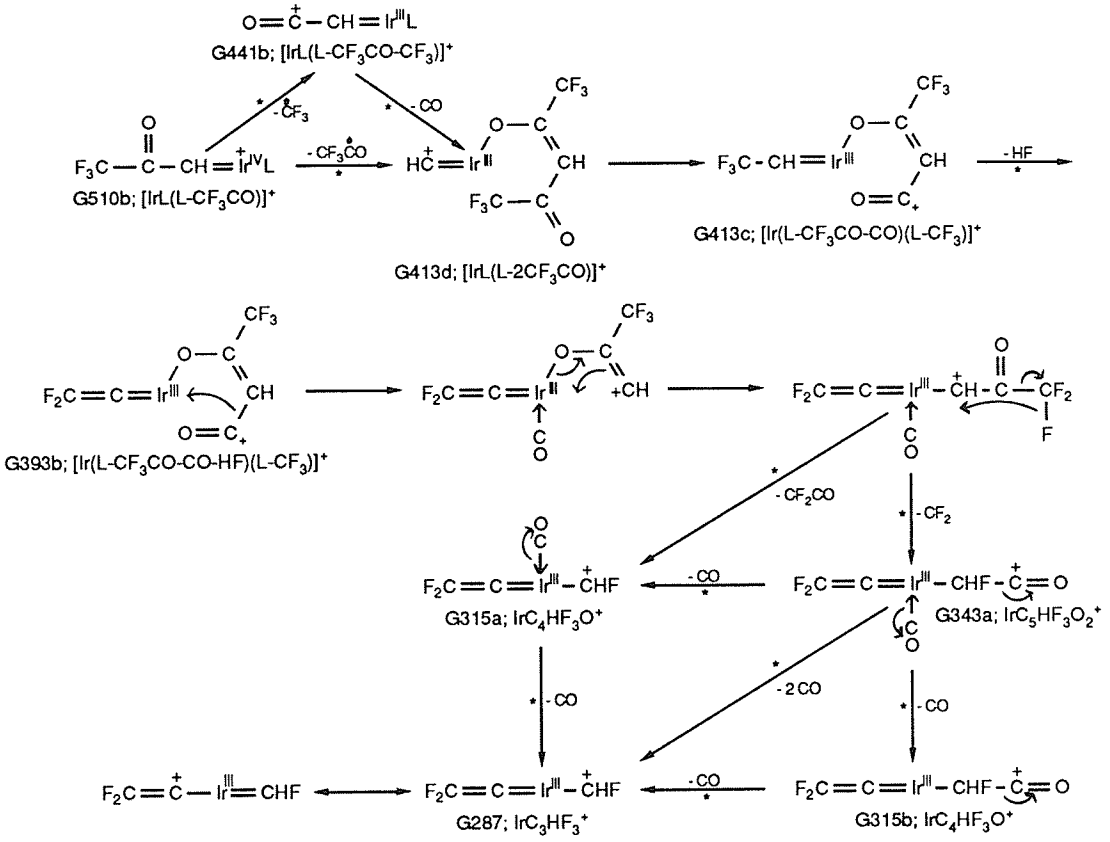

Scheme 3.48

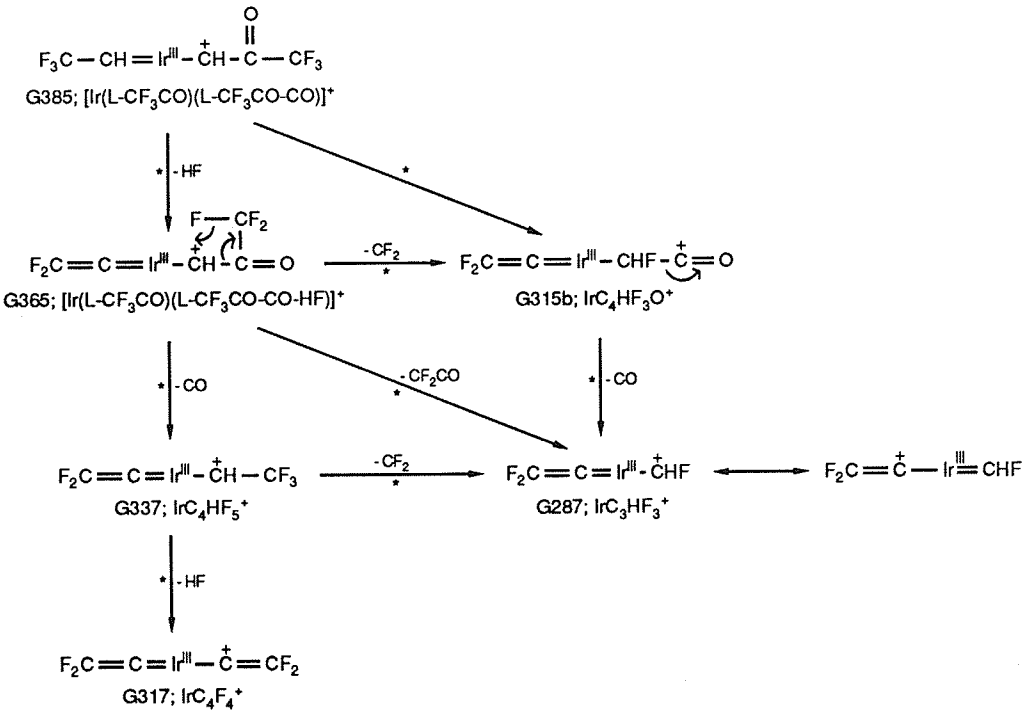

Scheme 3.49

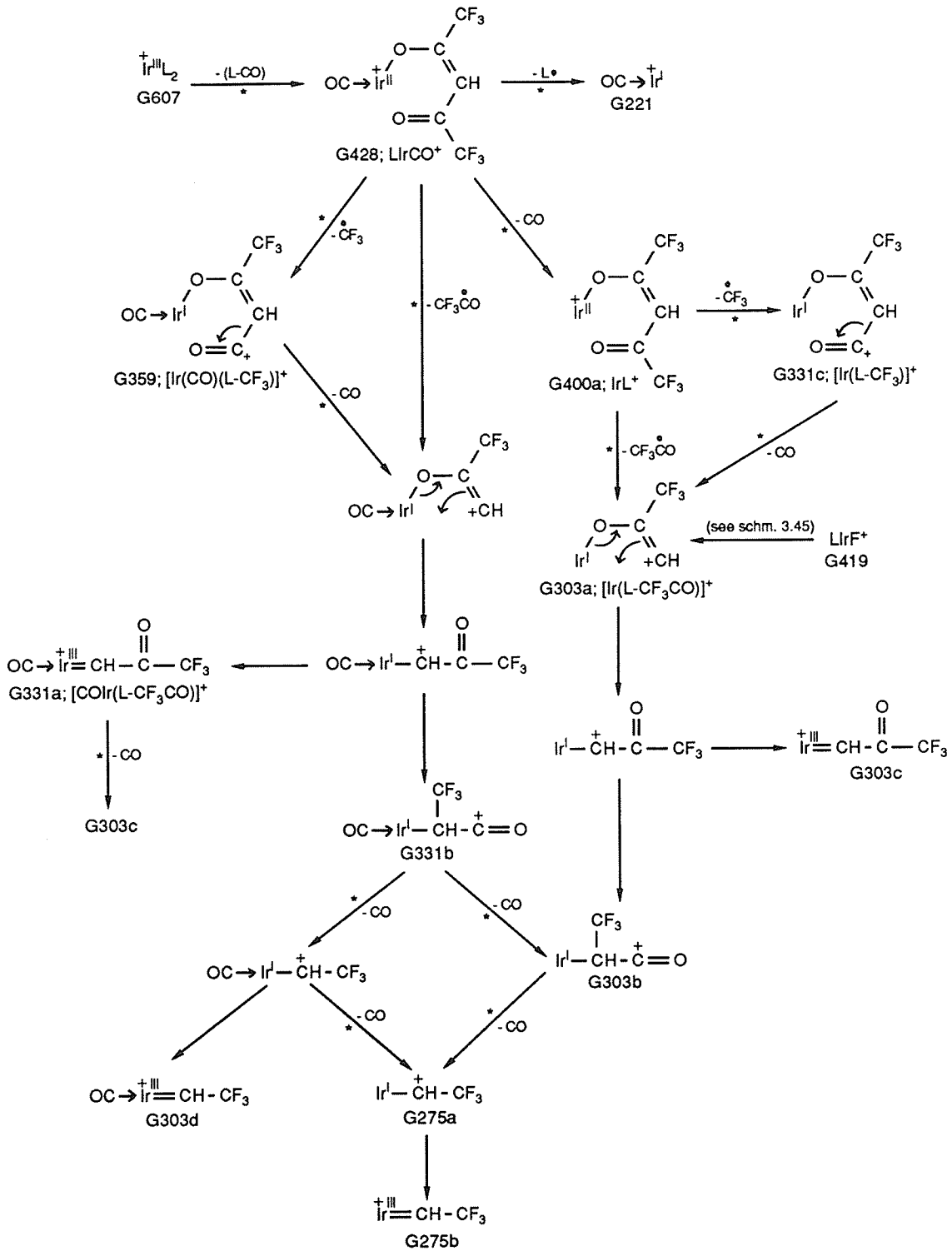
G607
- (L-CO)
G428; LIrCO+ CF3
- L•
G221
- CF3•
- CF3CO•
- CO
G359; [Ir(CO)(L-CF3)]+
G400a; IrL+ CF3
- CF3•
G331c; [Ir(L-CF3)]+
- CF3CO•
- CO
(see schm. 3.45)
LIrF+
G419
G303a; [Ir(L-CF3CO)]+
G331a; [COIr(L-CF3CO)]+
- CO
G303c
G331b
G303c
- CO
- CO
G303b
- CO
- CO
G303d
G275a
G275b

Scheme 3.50

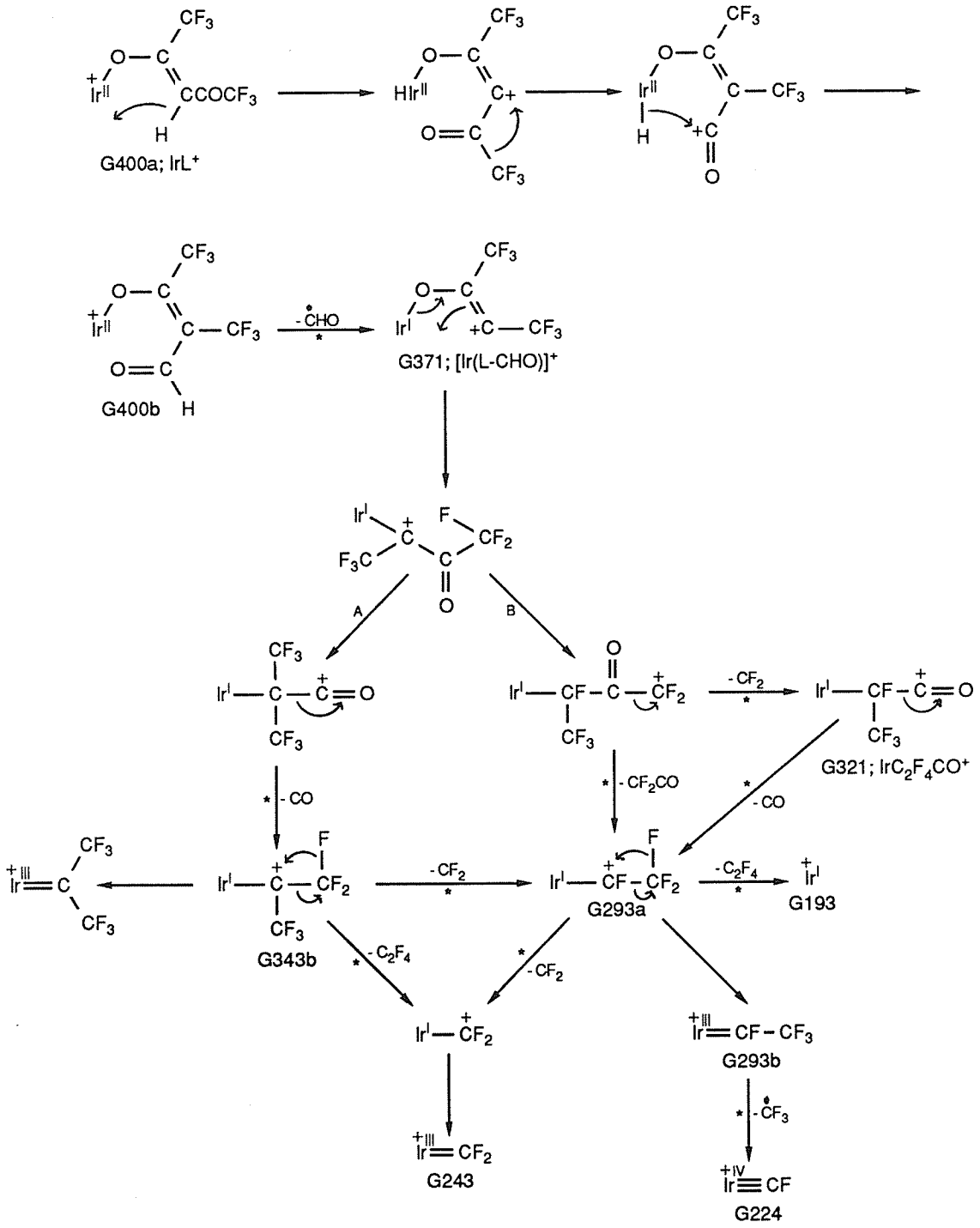
G400a; IrL+
G400b
G371; [Ir(L-CHO)]+
G321; IrC2F4CO+
G343b
G293a
G193
G293b
G243
G224
A
B
- CHO
- CO
- CF2CO
- CF2
- C2F4
- CF3

Scheme 3.51

appreciable extent in iridum compounds and oxidation states lower than this require the stabilizing effect of a π-acceptor ligand, such as a carbonyl group[21,87]. The driving force behind this reaction is therefore thought to be the formation of the iridium(III) carbene ion, **G303c**. Formation of this ion from **G303a** involves breaking the remaining Ir-O bond with concurrent formation of an Ir-C bond. Loss of a carbonyl group from **G303b** gives $IrCHCF_3^+$, **G275a**, which can also be written with iridium in the preferred +III oxidation state, **G275b**.

Scheme 3.46 shows decomposition of **G607** by a process involving formation of an Ir-CF_3 bond, with either simultaneous loss of the remaining portion of the ligand (L-CF_3) or by subsequent loss of the neutral fragment, $CF_3\overline{CCHO}$, and formation of an Ir-CO bond, to produce the ions $LIrCF_3^+$, **G469**, and $[LIr(CO)(CF_3)]^+$, **G497**, respectively. The abundances of **G469** and **G497** in the normal mass spectrum (6.5 and <1.0 %RA, respectively) and in the daughter ion spectrum of IrL_2^+, **G607**, (5.4:1.0), indicate higher stability for the former ion. This result may be rationalized as follows. It is well accepted that a carbonyl ligand bonds to a transition metal by synergic σ-π bonds[21]. When the relatively electronegative trifluoromethyl group is bonded to iridium, electron density available for π back-bonding to the carbonyl group is reduced. Consequently, formation of an Ir-CO bond will be less favorable.

Because $LIrCF_3^+$ is isobaric with $[Ir(L\text{-}CF_3)_2]^+$, which would most likely be formed by successive losses of $\cdot CF_3$ from IrL_3^+, care was taken to confirm that the former assignment is the correct one. Its experimentally determined accurate mass (468.9460u) compares

well with its calculated value (468.9462u). This is consistent with iridium's ability to form bonds with carbon, and more specifically with perfluoroalkyl groups[73,105,108,109], and with failure to observe a peak corresponding to the ion $[IrL(L\text{-}CF_3)]^+$.

Although not directly confirmed by metastable evidence, loss of ·F from ions $LIrCF_3^+$, **G469**, $[LIr(CO)(CF_3)]^+$, **G497**, $[Ir(CF_3)(CO)]^+$, **G290**, and $IrCF_3^+$, **G262**, yielding the iridium-fluorocarbene ions $LIrCF_2^+$, **G450**, $[LIr(CO)(CF_2)]^+$, **G478**, $[Ir(CO)(CF_2)]^+$, **G271**, and $IrCF_2^+$, **G243**, respectively, is postulated. The proposal that fluorine is lost from the trifluoromethyl group bonded to the iridium atom and not from the remaining intact ligand is strengthened by the observed loss of ·L from ions **G469** and **G497**. Loss of ·F from **G243** to give the iridium-fluorocarbyne ion $IrCF^+$, **G224**, is also postulated. Ion **G290** can alternatively decompose by losses of CO and $\cdot CF_3$ in successive steps to give, once again, **G262**, and the bare metal ion Ir^+, **G193**, respectively.

Consecutive losses of CO and $CF_3\dot{C}O$ from ion **G478** yield ions **G450** and $IrC_4HF_5O^+$, **G353(a,b)**, respectively. Alternatively, $CF_3\dot{C}O$ can be lost first to give $IrC_5HF_5O_2^+$, **G381(a,b)**, which, in turn, can lose CO to give, once again, **G353b**. Loss of the neutral radical $CF_3\dot{C}O$, indicates that iridium undergoes reduction from +IV to +III in the first step. The rearrangement **G303a** ---> **G303b** postulated above (Scheme 3.45) is also proposed for ions **G353a** and **G381a**, leading to preferred stuctures **G353b** and **G381b**, respectively. These ions, and their subsequent daughters, undergo numerous decompositions involving, almost exclusively, losses of the even-electron neutral fragments CO, CF_2 and HF.

Loss of $CF_3\dot{C}O$ from IrL_2^+, **G607**, gives rise to the ion $[IrL(L\text{-}COCF_3)]^+$, **G510a**, with iridium in the +II oxidation state (Scheme 3.47). This ion can then undergo decomposition *via* pathway A or B. The first pathway initially involves a rearrangement in which simultaneous formation of an iridium-carbon double bond and oxidation of iridium from +II to +IV yields ion **G510b**. From the remaining intact ligand $CF_3\dot{C}O$ can be lost directly, to yield the ion $[Ir(L\text{-}CF_3CO)_2]^+$, **G413a**, for which **G413b** is the preferred structure, or by a two step process involving initial loss of $\cdot CF_3$ to give $[Ir(L\text{-}CF_3CO)(L\text{-}CF_3)]^+$, **G441a**, and then loss of CO to yield, once again, **G413(a,b)**. Consecutive losses of CO and HF from ion **G413b** lead to the formation of the ions $[Ir(L\text{-}CF_3CO)(L\text{-}CF_3CO\text{-}CO)]^+$, **G385**, and $[Ir(L\text{-}CF_3CO)(L\text{-}CF_3CO\text{-}CO\text{-}HF)]^+$, **G365**, respectively. Alternatively, HF can be lost first, to yield $[Ir(L\text{-}CF_3CO)(L\text{-}CF_3CO\text{-}HF)]^+$, **G393a**, which can, in turn, lose a carbonyl group to give, once again, ion **G365**.

Pathway B differs from A because it involves loss of CO from **G510a** prior to oxidation, subsequently yielding $[IrL(L\text{-}CF_3CO\text{-}CO)]^+$, **G482a**, for which **G482b** is the preferred structure. Losses of $\cdot CF_3$, $CF_3\dot{C}O$ or ·L from **G482b**, yield the ions $[Ir(L\text{-}CF_3CO\text{-}CO)(L\text{-}CF_3)]^+$, **G413c**, **G385** and $IrCHCF_3^+$, **G275b**, respectively. In all three cases, iridium undergoes reduction from +IV to +III. Consecutive losses of HF and CO from **G413c**, yield the ions $[Ir(L\text{-}CF_3CO\text{-}CO\text{-}HF)(L\text{-}CF_3)]^+$, **G393b** and **G365**, respectively.

In pathway A of Scheme 3.47, the proposed origin of the $\cdot CF_3$ and $CF_3\dot{C}O$ groups lost from **G510b** is the remaining intact ligand. However, it is also conceivable that these fragments can be lost from

the residue of the incomplete ligand, to yield ions $[IrL(L\text{-}CF_3CO\text{-}CF_3)]^+$, **G441b** and $[IrL(L\text{-}2CF_3CO)]^+$, **G413d**, respectively (Scheme 3.48). Migration of a CF_3 group from the intact ligand to the carbon residue of the other ligand gives rise, once again, to **G413c**. Ion **G393b**, resulting from the loss of HF from **G413c** (see also Scheme 3.47), might then decompose by two subsequent rearrangements followed by loss of CF_2, to yield $IrC_5HF_3O_2^+$, **G343a**, which, in turn, can undergo decomposition by successive losses of CO to yield $IrC_4HF_3O^+$, **G315(a,b)** (depending on which carbonyl group is lost first) and $IrC_3F_3H^+$, **G287**.

Decomposition of ion **G365** (Scheme 3.49) involves consecutive losses of CO and CF_2 yielding $IrC_4HF_5^+$, **G337**, and **G287**, respectively, or in reverse order to give ion **G315b** and then ion **G287**. Finally, loss of HF from **G337** yields the ion $IrC_4F_4^+$, **G317**.

A first field-free region metastable ion decomposition of IrL_2^+, **G607**, to $LIrCO^+$, **G428**, is observed (Scheme 3.50). This decomposition probably occurs in two or more steps but is not confirmed by evidence from decomposition of metastable ions. However, a possible intermediate in this decomposition reaction might be the ion $[LIr(CO)(CF_3)]^+$, **G497** (Scheme 3.46), from which $\cdot CF_3$ can then be lost to give **G428**, with iridium in the +II oxidation state (loss of CO from **G497** is expected to be the preferred process, for reasons discussed earlier, i.e. inductive effects of the CF_3 group and iridium's preference for the higher oxidation states.). Subsequent losses of $\cdot CF_3$, $CF_3\dot{C}O$ or $\cdot L$ from **G428** (indicating the reduction of iridium to the +I oxidation state in each case), yield $[Ir(CO)(L\text{-}CF_3)]^+$, **G359**, $[Ir(CO)(L\text{-}CF_3CO)]^+$, **G331(a,b)**, and $IrCO^+$,

G221, respectively. Loss of CO from **G331b**, depending on the site of elimination, yields the ions $IrC_3HF_3O^+$, **G303(b,d)**. Loss of a second CO group results in the formation of $IrCHCF_3^+$, **G275(a,b)**. An alternative decomposition pathway for ion **G428** invokes the loss of a carbonyl group prior to the loss of $\cdot CF_3$ and $CF_3\dot{C}O$ to give ion IrL^+, **G400a**. Losses of $\cdot CF_3$ or $CF_3\dot{C}O$ from this ion give rise to $[Ir(L\text{-}CF_3)]^+$, **G331c**, or **G303a** (for which **G303c** is the preferred structure, see also Scheme 3.45), respectively. Ion **G303c** can also be formed from **G331a** by loss of CO.

Scheme 3.51 shows the proposed mechanism for the loss of the odd-electron neutral fragment $\cdot CHO$ from IrL^+, **G400a.** It invokes hydrogen movement to the metal and back to the carbonyl carbon after migration of the trifluoromethyl group to the bridging carbon has occurred, yielding ion **G400b**. This is followed by loss of $\cdot CHO$, an indication that iridium has undergone reduction from +II to +I, to yield $[Ir(L\text{-}CHO)]^+$, **G371**. This ion, after rearrangement, can decompose via pathway A or B, both of which involve consecutive losses of CO and CF_2, the difference being the order in which they are lost. In both cases $IrC_2F_4^+$, **G293(a,b)**, is the resulting ion. Losses of CF_2 or C_2F_4 from **G293a** yield the iridium fluorocarbene ion **G243**, or the bare metal ion Ir^+, **G193**, respectively, while loss of $\cdot CF_3$ from **G293b** yields the iridium fluorocarbyne ion $IrCF^+$, **G224**.

C) *Ir(acac)$_3$*

Decompositions involving the loss of neutral radicals play a very minor role in the mass spectrum of $Ir(acac)_3$ (unlike in that of

$Ir(hfa)_3$). Dissociation proceeds predominantly through losses of even-electron neutral fragments CH_2CO, CO, C_2H_4 and CH_4.

Both methyl and hydrogen migration from the ligand to the metal, substantiated by the presence of ions such as $CH_3IrL_2^+$, **H406**, $[LIr(CO)(CH_3)]^+$, **H335(a,b)**, $[LIr(CO)H]^+$, **H321(a,b)**, and $HIrL^+$, **H293**, (to be described below) are thought to play a major role in the fragmentation of this complex. The formation of **H335a** from IrL_2^+, **H391a**, involves successive migrations of CH_3 and CO to the metal (Scheme 3.52) followed by the loss of the remainder of the ligand. Migration of a second methyl group to the metal is then postulated (structure **H335b**), followed by loss of CH_4, yielding the iridium carbene ion $IrC_6H_6O_3^+$, **H319**, which in turn loses CO to give $IrC_5H_6O_2^+$, **H291a**. This ion can decompose by the loss of $CH_3\overline{CCHO}$ to yield $[Ir(CH_2)(CO)]^+$, **H235a**, or by consecutive losses of 28 Da fragments. Thus successive losses of CO yield ions $IrC_4H_6O^+$, **H263(a,b)** (depending on which carbonyl group is lost first) and $IrC_3H_6^+$, **H235b**, while losses of CO followed by C_2H_4 yield ions $IrC_4H_6O^+$, **H263b**, and **H235a**, respectively. Rearrangement of **H291a**, as shown in Scheme 3.52, prior to the loss of these fragments will, as postulated earlier when discussing the mass spectrum of $Ir(hfa)_3$, facilitate their release. All the above pathways were supported by results from daughter ion linked scannning.

Our deuterium-labelling studies show that ~69 and 72% of the hydrogen retained in $[LIr(CO)H]^+$, **H321(a,b)**, and $HIrL^+$, **H293** respectively, originate from the methyl substituent. Three pathways, A, B and C, leading to their formation have been postulated, all of which involve prior loss of CH_2CO from IrL_2^+, **H391a**, to give

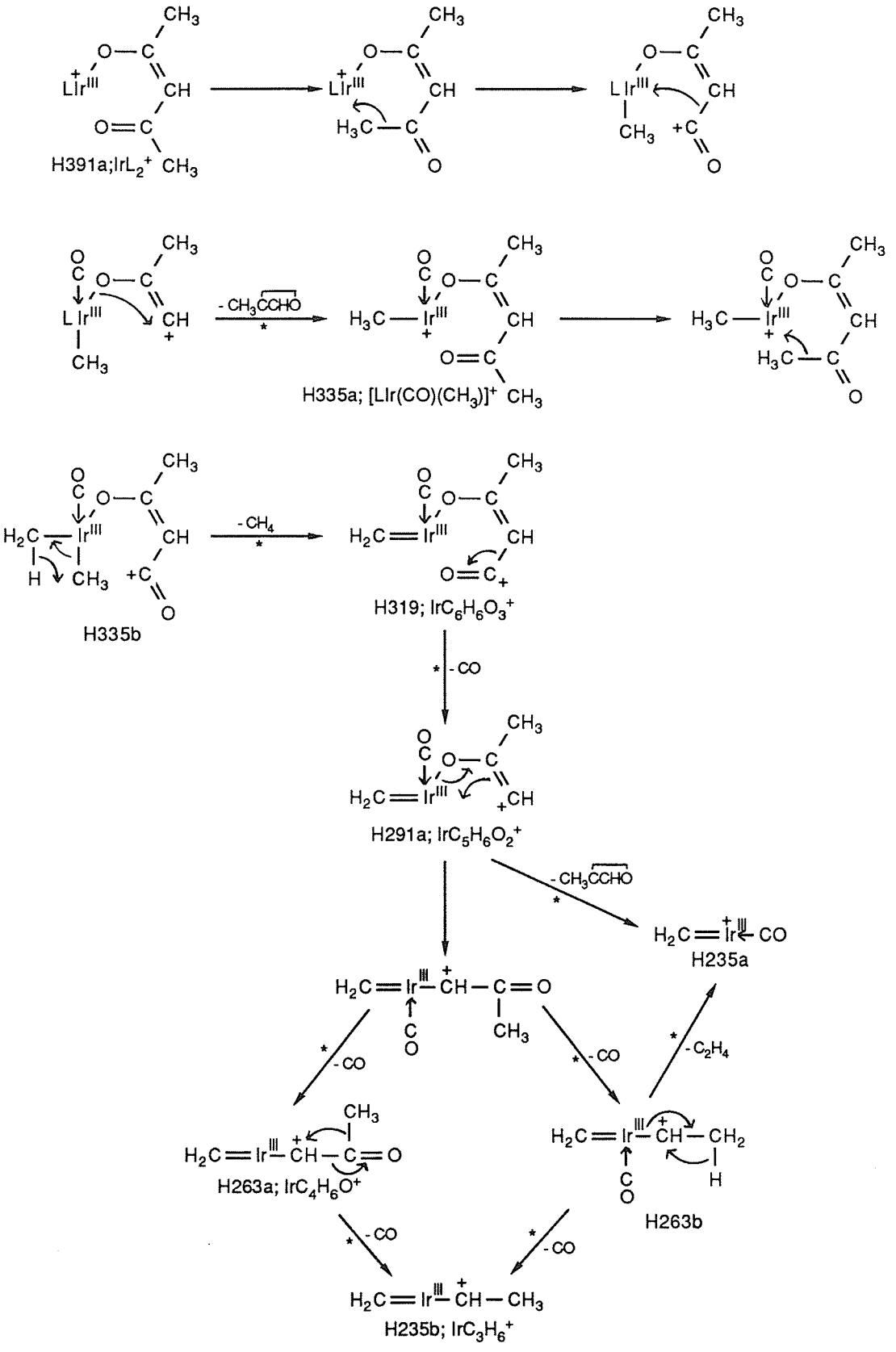
H391a;IrL2+
H335a; [LIr(CO)(CH3)]+
H335b
H319; IrC6H6O3+
H291a; IrC5H6O2+
H235a
H263a; IrC4H6O+
H263b
H235b; IrC3H6+
- CH3CCHO
- CH4
- CO
- C2H4

Scheme 3.52

$Ir[L(L\text{-}CH_2CO)]^+$, **H349**, (Scheme 3.53). Pathway A differs from B and C since CH_2CO is lost *prior* to hydrogen rearrangement to the metal.

Two mechanisms have been suggested for release of C_2H_4 from **H349**. The first, yielding **H321a**, was originally proposed by MacDonald and Shannon[1] and later by Fraas *et al*[110] to explain a similar loss from the ion $[Met(L\text{-}COCH_3)]^+$, where Met = Al, Cr, Co and Ni. Here the carbonyl group is bonded to the iridium atom through oxygen, leaving the carbon atom two electrons shy of an octet and the positive charge on the electronegative oxygen atom. The alternative mechanism leads to a more stable structure, **H321b**, for this ion, which has the carbonyl group bound through the carbon atom. As verified by linked scanning, **H293**, is formed either by loss of CO from **H321** or by loss of the even-electron neutral fragment $CH_3\overline{CCHO}$ from **H349**. Ions **H321** and **H293** can also be formed directly from **H391a** by losses of the even-electron neutrals (L-H-CO) or (L-H), respectively (see Scheme 3.67 below, for analogous decompositions).

Mechanisms proposed for the fragmentation of **H293** and its daughters are shown in Scheme 3.54. Following methyl migration to the metal, decomposition of this ion involves the sequential losses, in a variety of permutations, of two carbonyl groups and a methane molecule, all sequences terminating at $IrC_2H_4^+$, **H221**.

Scheme 3.55 shows the mechanisms proposed for the formation of ions $[IrL(L\text{-}COH)]^+$, **H362**, and $[IrL(L\text{-}CH_4)]^+$, **H375**, and their daughters from IrL_2^+, **H391a**. These ions are unique to this acetylacetonate complex, and imply an important role for iridium in

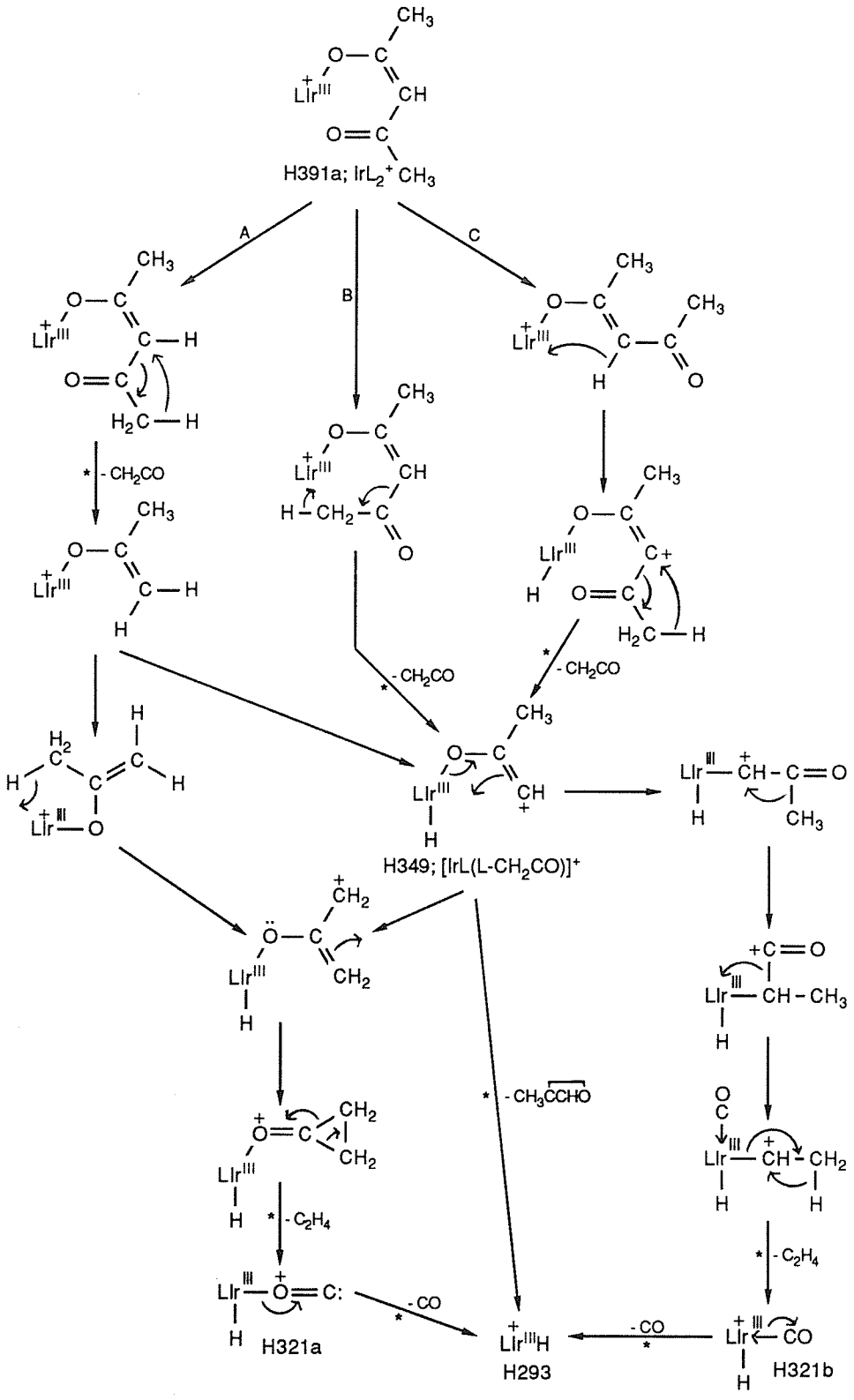
H391a; IrL2+ CH3
A
B
C
- CH2CO
- CH2CO
- CH2CO
H349; [IrL(L-CH2CO)]+
- CH3CCHO
- C2H4
- C2H4
- CO
- CO
H321a
H293
H321b

Scheme 3.53

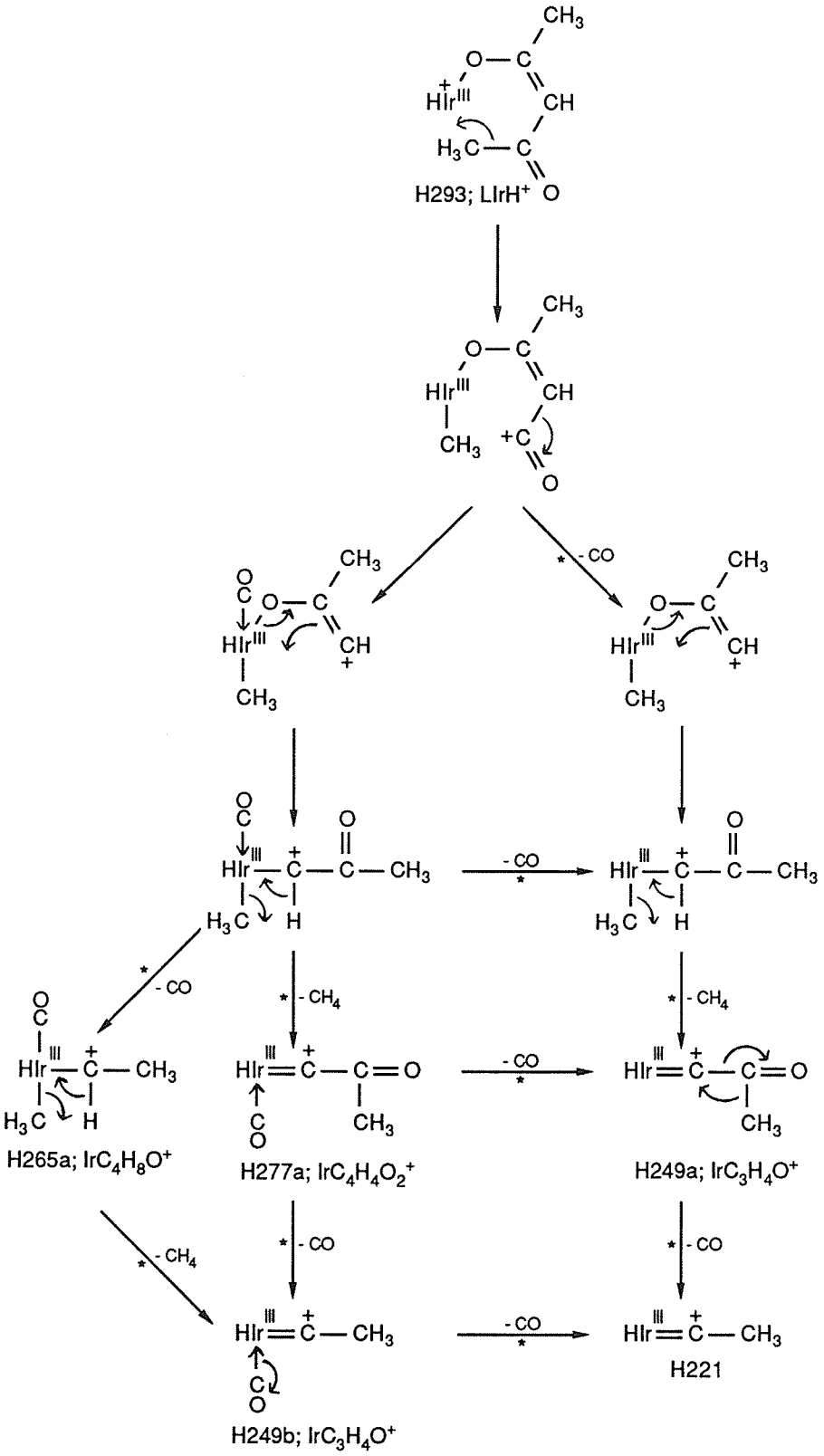
H293; LIrH+
H265a; IrC4H8O+
H277a; IrC4H4O2+
H249a; IrC3H4O+
H249b; IrC3H4O+
H221
- CO
- CH4

Scheme 3.54

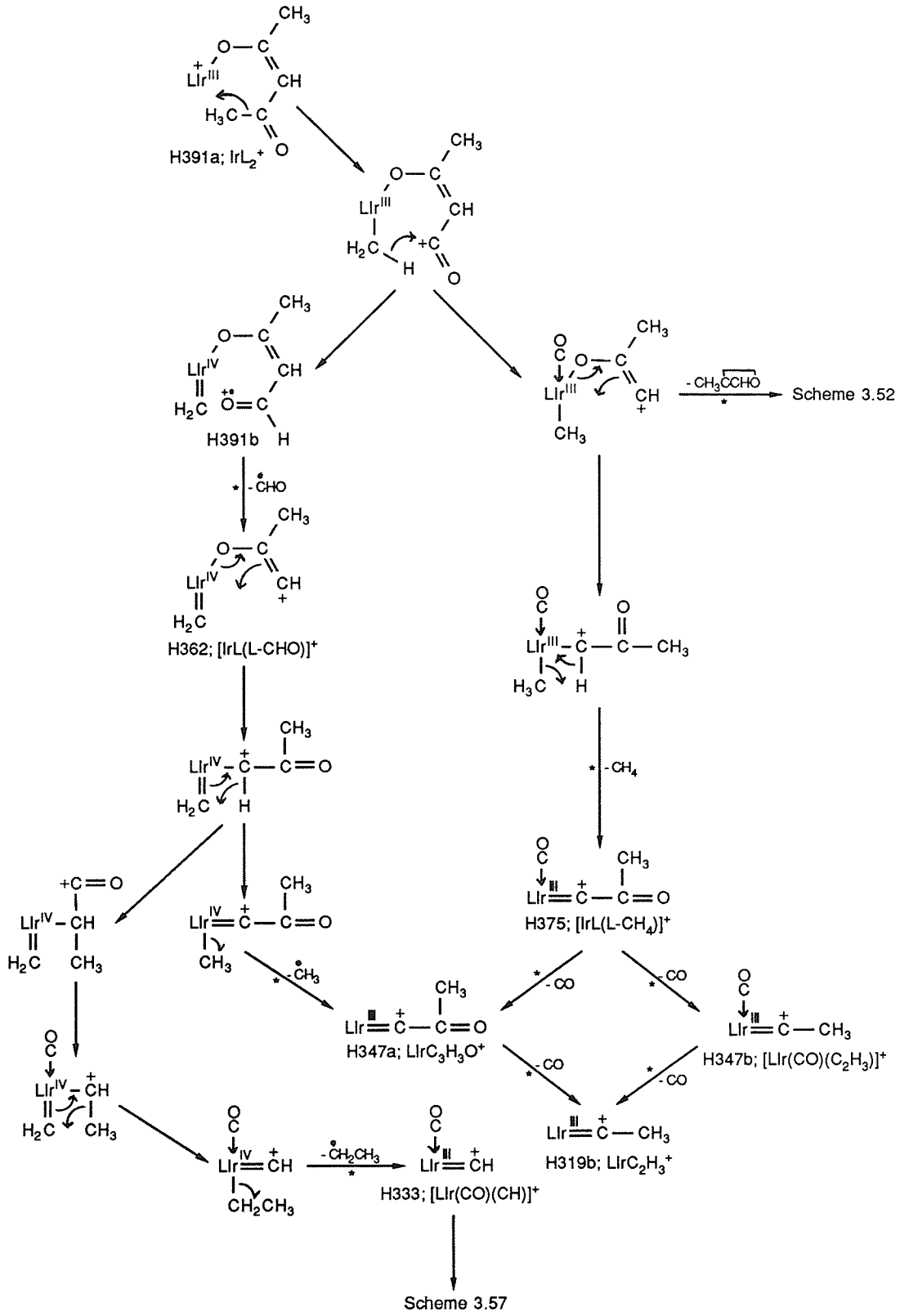
H391a; IrL2+
H391b
H362; [IrL(L-CHO)]+
H375; [IrL(L-CH4)]+
H347a; LIrC3H3O+
H347b; [LIr(CO)(C2H3)]+
H319b; LIrC2H3+
H333; [LIr(CO)(CH)]+
Scheme 3.52
Scheme 3.57

Scheme 3.55

their formation. Labelling results indicate that a majority of the hydrogen transferred to the eliminated neutral species ·CHO and $CH_3(H)$ originates from the methyl substituent (*ca* 77%) and bridging carbon atom (*ca* 74%), respectively. Following methyl migration to the metal one of the methyl hydrogens migrates back to the carbonyl group from which the methyl group was originally lost to yield the odd-electron iridium(IV) carbene ion **H391b**. This intermediate ion subsequently loses ·CHO to give **H362**, which, in turn, loses the neutral radical $\cdot CH_3$ or $\cdot CH_2CH_3$ (indicating that Ir(IV) has undergone reduction to Ir(III)) to yield ions $LIrC_3H_3O^+$, **H347a** and $[LIr(CO)(CH)]^+$, **H333**, respectively. An alternative decomposition of **H391a** involves migration of CO to the metal (after methyl migration) followed by loss of CH_4 to give **H375**. Two consecutive losses of CO from this ion yield **H347(a,b)** (depending on which carbonyl group is lost first) and $LIrC_2H_3^+$, **H319b**.

As verified by results from linked scanning and exact mass determinations, **H319b** loses CH_4 to give $IrC_6H_6O_2^+$, **H303**, (Scheme 3.56). The proposed mechanism involves migration of a methyl group from the intact ligand to the carbon of the residue of the other ligand. Ion **H303** then loses three successive neutral 28 Da fragments. The presence of ions $IrC_5H_6O^+$ (**H275(a,b)**), and the absence of isobaric $IrC_4H_2O_2^+$, indicates that fragmentation proceeds initially by the elimination of CO. The presence of both $IrC_4H_6^+$ (**H247a**) and $IrC_3H_2O^+$ (**H247b**) however, indicates that the decomposition of **H275(a,b)** occurs by means of competitive eliminations of CO and C_2H_4. The %RA of **H247a** and **H247b** are 3.3 and 4.0%, respectively, indicating that neither process dominates.

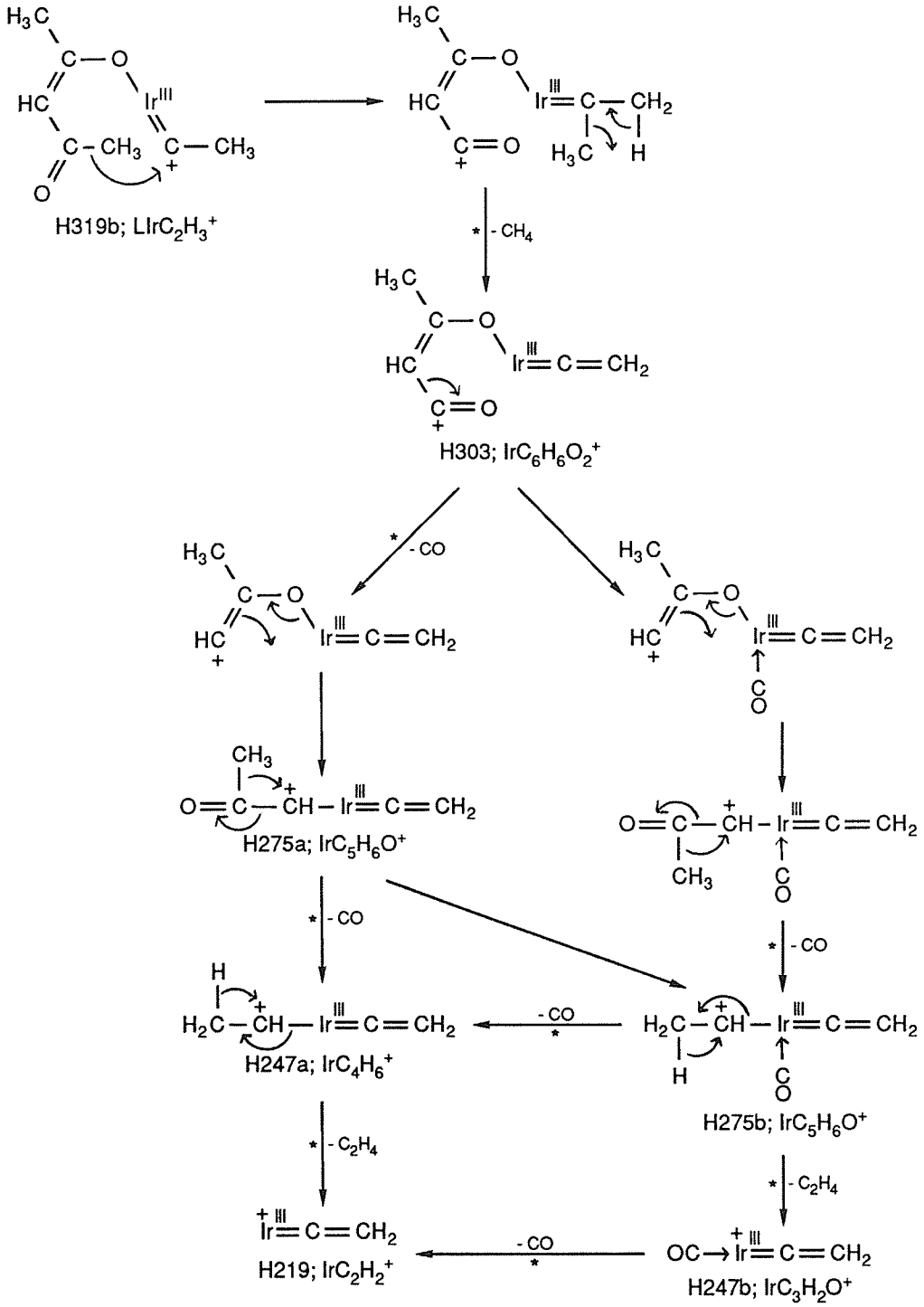
H319b; $LIrC_2H_3^+$
H303; $IrC_6H_6O_2^+$
H275a; $IrC_5H_6O^+$
H247a; $IrC_4H_6^+$
H275b; $IrC_5H_6O^+$
H219; $IrC_2H_2^+$
H247b; $IrC_3H_2O^+$
- CO
- C_2H_4

Scheme 3.56

Finally, **H247a** and **H247b** lose C_2H_4 and CO, respectively, yielding in both cases, $IrC_2H_2^+$, **H219**.

In Scheme 3.53, a mechanism was proposed for the observed loss of C_2H_4 from $[IrL(L\text{-}CH_2CO)]^+$, **H349**, to yield $[LIr(CO)H]^+$, **H321(a,b)**. An alternative decomposition of **H349**, verified by linked scanning and exact mass determinations, involves loss of CH_4 to give $[LIr(CO)(CH)]^+$, **H333** (Scheme 3.57). Migration of a hydrogen or a methyl group from the remaining intact ligand to the carbon residue of the fragmented ligand is postulated in the formation of $IrC_5H_6O_2^+$, **H291a**, or $IrC_6H_8O_2^+$, **H305**, from **H333**, respectively. Decomposition routes originating from **H305** involve the elimination of the even-electron neutrals CO, C_2H_4 and CH_4 in a variety of permutations yielding the ions $IrC_5H_4O_2^+$ **(H289)**, $IrC_4H_4O_2^+$ **(H277b)**, $IrC_5H_8O^+$ **(H277c)**, $IrC_4H_4O^+$ **(H261)**, $IrC_3H_4O^+$ **(H249c)**, and $IrCCO^+$ **(H233)**, while those from **H291a** have been rationalized in Scheme 3.52 by mechanisms discussed above.

The reaction sequence corresponding to the loss of the even-electron neutral fragment CH_3CCH from IrL_2^+, **H391**, to yield $[LIr(CO_2)(CH_3)]^+$, **H351**, followed by the losses of CO_2 and CH_4 to give the low abundance ions $LIrCH_3^+$, **H307**, and $IrC_5H_6O_2^+$, **H291(a,b)**, respectively, is shown in Scheme 3.58. With the exception of the loss of CO_2 from **H351**, this reaction pathway is entirely supported by metastable ion decompositions and is further strengthened by the occurrence of analogous fragmentations in the mass spectrum of $Ru(acac)_3$[68]. Consecutive eliminations of CO and CH_4 from **H307** are also observed (and supported by metastable ion

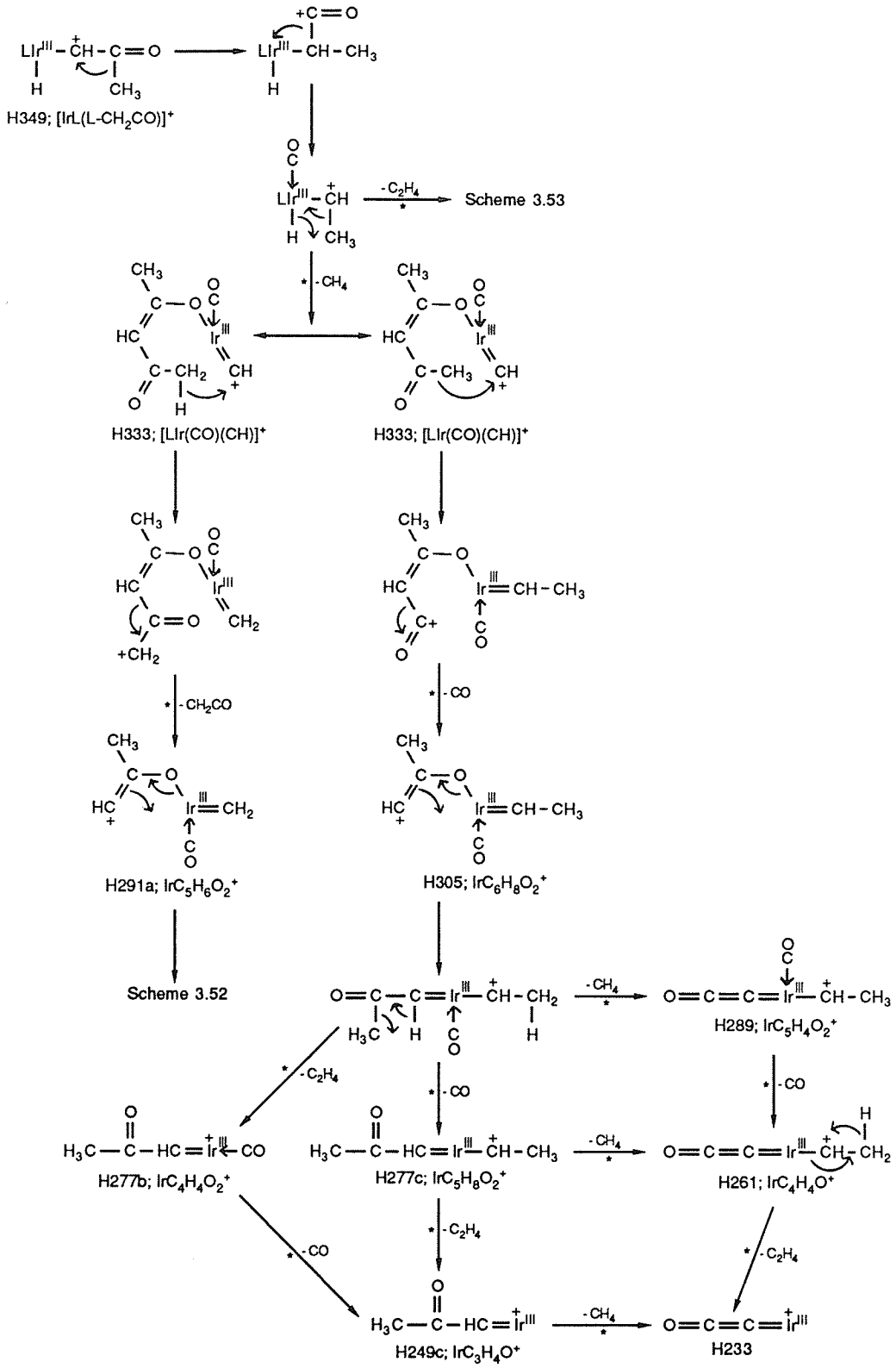
H349; [IrL(L-CH2CO)]+
Scheme 3.53
H333; [LIr(CO)(CH)]+
H333; [LIr(CO)(CH)]+
H291a; IrC5H6O2+
H305; IrC6H8O2+
Scheme 3.52
H289; IrC5H4O2+
H277b; IrC4H4O2+
H277c; IrC5H8O2+
H261; IrC4H4O+
H249c; IrC3H4O+
H233

Scheme 3.57

decompositions), and yield $IrC_5H_{10}O^+$, **H279**, and $IrC_4H_6O^+$, **H263a**, respectively.

D) *Ir(tfa)$_3$*

The mass spectrum of $Ir(tfa)_3$, not surprisingly, is characterized by decompositions common to both $Ir(hfa)_3$ and $Ir(acac)_3$. Migrations of hydrogen, methyl and trifluoromethyl groups are found, once again, to play a major role in observed fragmentations. Numerous losses of neutral radicals are observed, usually occurring prior to, and after, oxidation of Ir(II) to Ir(IV), while CO and HF are the most commonly lost even-electron neutral fragments.

Although decomposition of the molecular ion IrL_3^+, **I652**, occurs mainly by loss of the ligand radical to give the bis complex ion IrL_2^+, **I499**, other reaction sequences are also observed. Scheme 3.59 shows the decomposition of the molecular ion by a process involving formation of an Ir-CF_3 bond with simultaneous loss of the remainder of the ligand (exactly analogous to the mechanism proposed earlier for the reaction: $Ir(hfa)_2^+$ ----> $(hfa)IrCF_3^+$ (see Scheme 3.46)) to give $L_2IrCF_3^+$, **I568**, followed by the loss of H_2O to give $[CF_3IrL(L\text{-}H_2O)]^+$, **I550**. Because loss of a neutral fragment from an even-electron ion is more favorable than is loss from an odd-electron ion (see Section 1.1) the molecular ion is written as an even-electron ion with iridium in the +IV oxidation state. Loss of $\cdot CF_3$ from **I568** to yield IrL_2^+, **I499**, is also observed.

The elimination of the neutral fragments ·F and CH_2CO from the molecular ion in the decomposition sequence: IrL_3^+ ----> $[IrL_2(L\text{-}F)]^+$ ----> $[IrL_3\text{-}F\text{-}COCH_2]^+$ is described in Scheme 3.60. Loss of CH_2CO

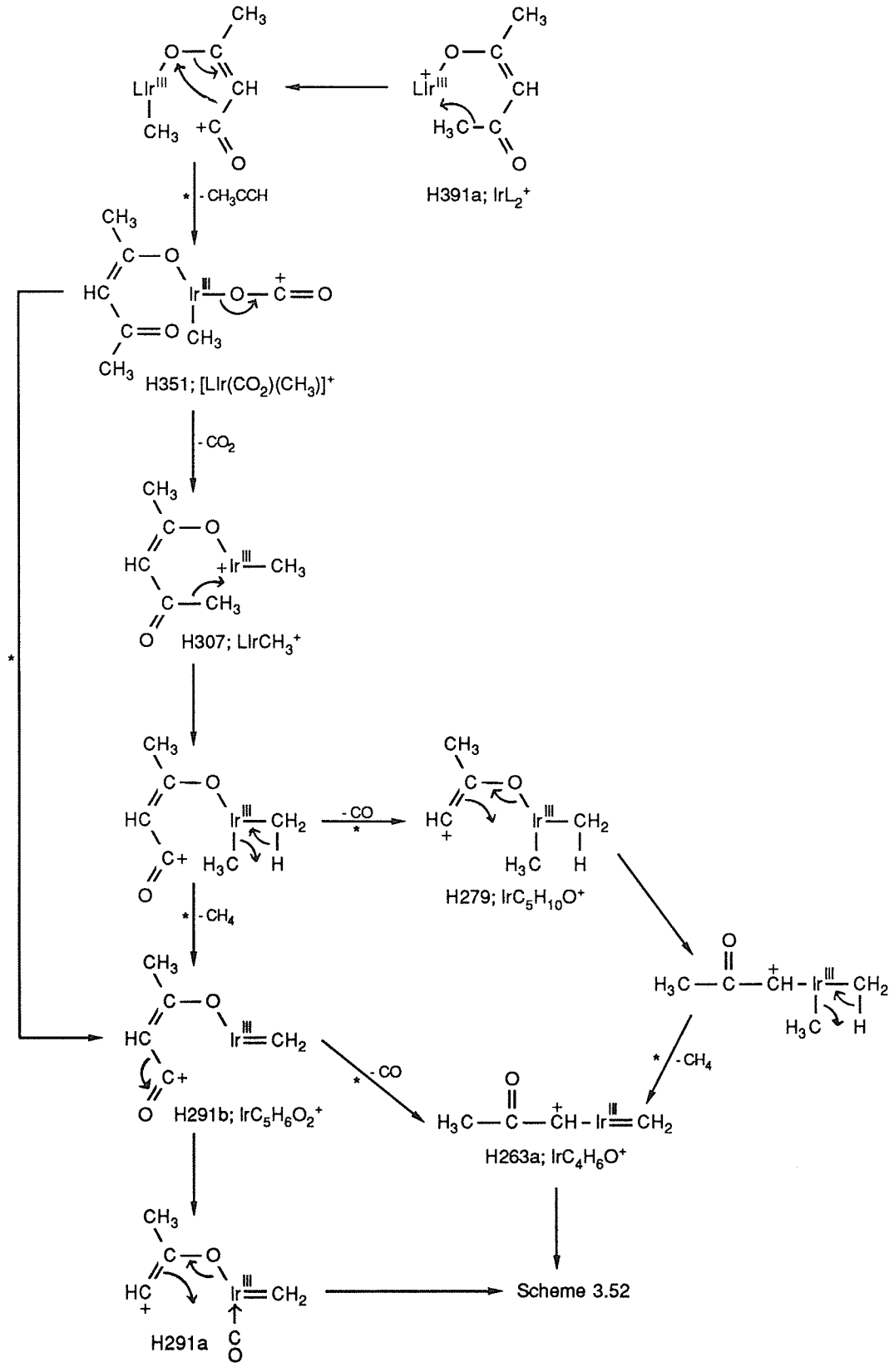
H391a; IrL_2^+
- CH_3CCH
H351; $[LIr(CO_2)(CH_3)]^+$
- CO_2
H307; $LIrCH_3^+$
- CO
H279; $IrC_5H_{10}O^+$
- CH_4
H291b; $IrC_5H_6O_2^+$
- CO
H263a; $IrC_4H_6O^+$
- CH_4
H291a
Scheme 3.52

Scheme 3.58

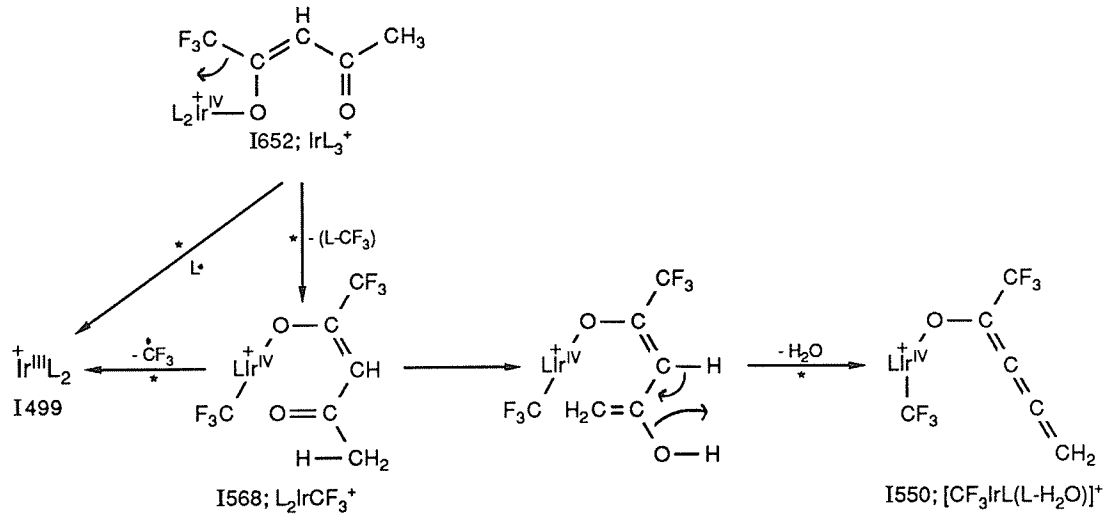

Scheme 3.59

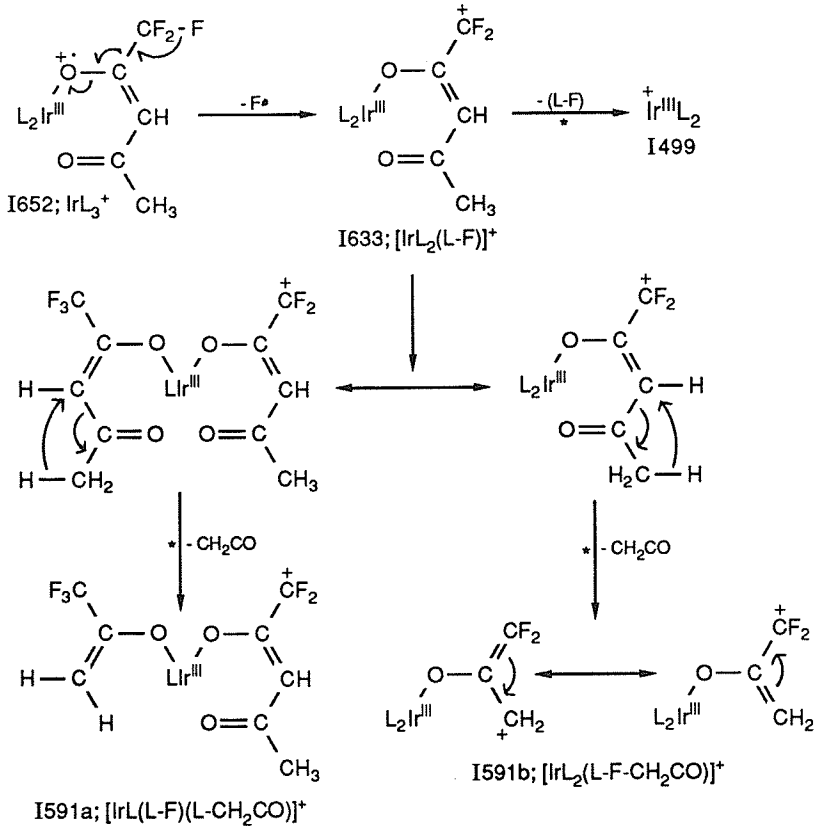

Scheme 3.60

may occur from one of the two intact ligands to yield **I591a** or from the ligand which has lost a fluorine to give **I591b**. An analogous reaction sequence was previously reported in the mass spectrum of both $In(tfa)_3$ and $Ga(tfa)_3$[111].

Losses of the neutral radicals $CF_3\dot{C}O$ and $CH_3\dot{C}O$ from IrL_2^+, **I499**, (indicating that Ir(III) has undergone reduction to Ir(II)) yield the ions $[IrL(L\text{-}CF_3CO)]^+$, **I402a**, and $[IrL(L\text{-}CH_3CO)]^+$, **I456a**, respectively, for which **I402c** and **I456c** (with iridium in the +IV oxidation state) are the preferred structures (Scheme 3.61). Elimination of $\cdot CH_3$ from **I402c** or $\cdot CF_3$ from **I456c** (indicating reduction of Ir(IV) to Ir(III)) yield, in both cases, the ion $LIrCHCO^+$, **I387**, which, in turn, loses CO to give $LIrCH^+$, **I359a**. The proposal that $\cdot CH_3$ and $\cdot CF_3$ are lost from the partly fragmented ligand and not from the intact ligand, is supported by the fact that losses of these fragments have not been observed from an ion such as IrL_2^+, **I499**, and more importantly, that the daughter ion spectra of **I402** and **I456** do not show evidence for loss of $\cdot CF_3$ and $\cdot CH_3$, respectively. Loss of C_2H_4 from **I402b** to yield $LIrCO^+$, **I374**, is also observed. Iridium in this case must be in the +II oxidation state. Loss of C_2H_4, and not CO, is verified by accurate mass studies. Loss of the neutral fragment CH_2CO from **I387** to yield $IrC_5H_3F_3O_2^+$, **345a**, involves prior migration of the methyl group (from the remaining intact ligand) to iridium.

Postulated mechanisms for decomposition of **I359a** and its daughters are shown in Scheme 3.62. Following scission of an iridium-oxygen bond, rotation about a OC-CH bond can bring either the CH_3 or CF_3 substituent (depending on which Ir-O bond is broken)

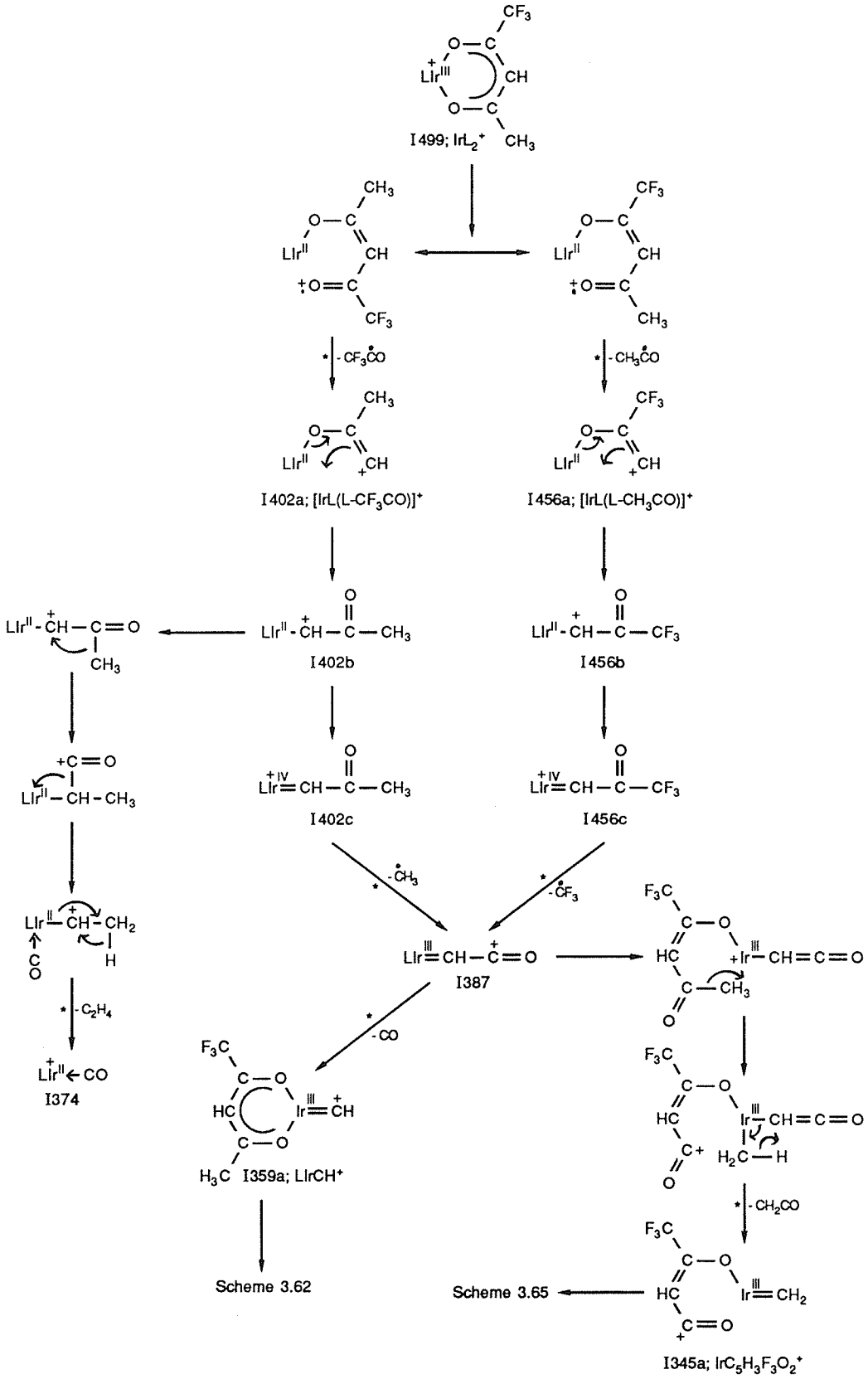
I499; IrL2+
I402a; [IrL(L-CF3CO)]+
I456a; [IrL(L-CH3CO)]+
I402b
I456b
I402c
I456c
I387
I374
I359a; LIrCH+
I345a; IrC5H3F3O2+
Scheme 3.62
Scheme 3.65

Scheme 3.61

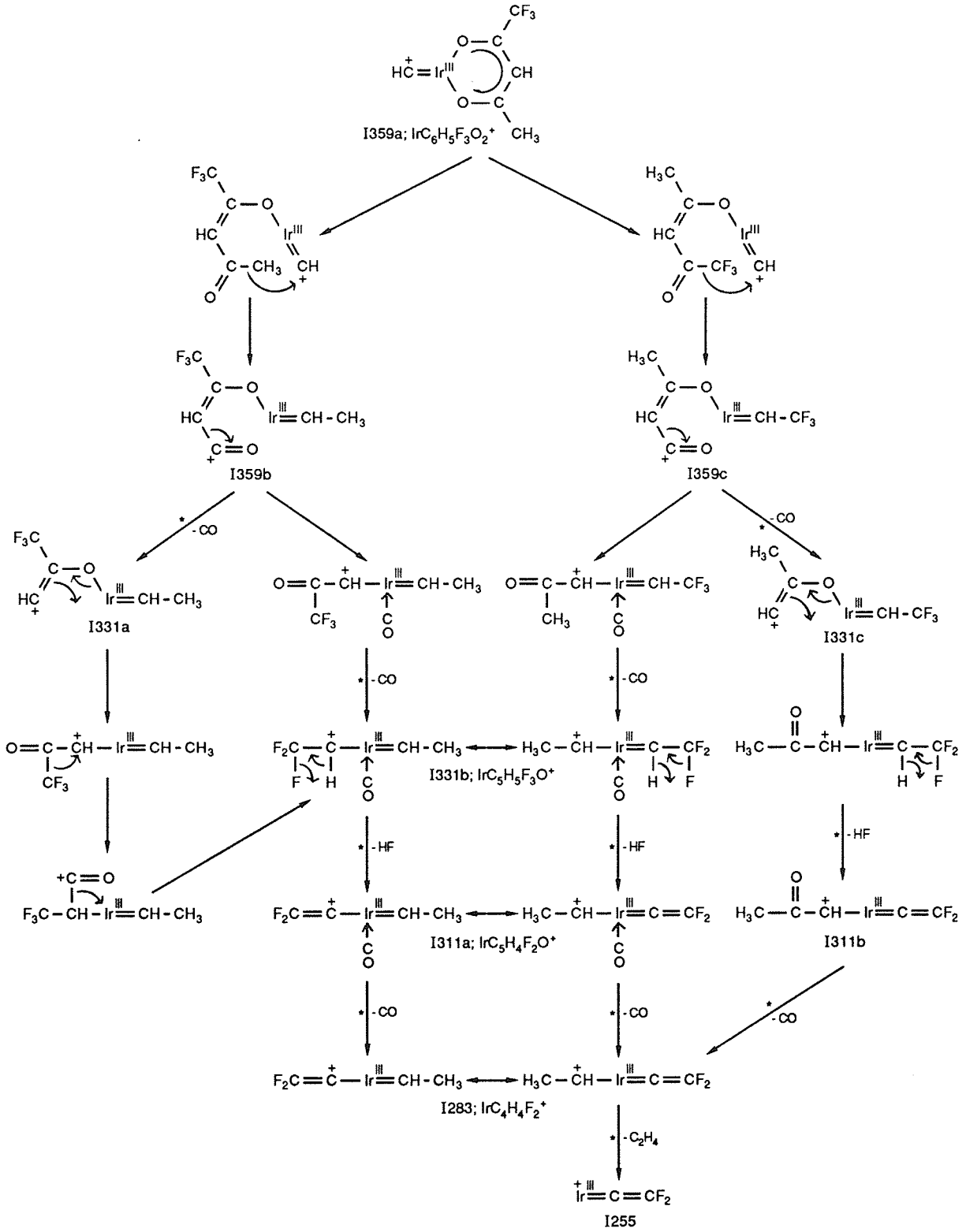
I359a; $IrC_6H_5F_3O_2^+$
I359b
I359c
I331a
I331c
I331b; $IrC_5H_5F_3O^+$
I311a; $IrC_5H_4F_2O^+$
I311b
I283; $IrC_4H_4F_2^+$
I255
-CO
-HF
$-C_2H_4$

Scheme 3.62

close enough to the carbon residue of the fragmented ligand so that migration can occur and yield the structures **I359b** and **I359c**, respectively. An analogous mechanism was proposed above to rationalize the observed loss of CO from the ion $IrC_7H_8O_3^+$, **H333**, in the mass spectrum of $Ir(acac)_3$ (Scheme 3.49). The carbonyl group from which these migrating groups originated can then either (a) be lost directly to yield $IrC_5H_5F_3O^+$, **I331(a,c)**, or (b) undergo migration to iridium, after which the remaining CO group of that ligand is lost, yielding in this case, ion **I331b**. Eliminations of HF from **I331b** and **I331c** give rise to the fluorocarbene ions $IrC_5H_4F_2O^+$, **I311a** and **I331b**, respectively, from which the remaining carbonyl group is lost yielding, in both cases, $IrC_4H_4F_2^+$, **I283**. Loss of C_2H_4 from **I283** yields $IrC_2F_2^+$, **I255**.

Migrations of CF_3 and CH_3 to iridium, both evident by the presence of ions such as $[LIr(CO)(CH_3)]^+$, **I389**, $[LIr(CO)(CF_3)]^+$, **I443**, $LIrCF_3^+$, **I415** and $LIrCH_3^+$, **I361**, are observed in the mass spectrum of this complex, and as noted above in the mass spectra of $Ir(hfa)_3$ and $Ir(acac)_3$. Losses of $CF_3\overline{CCHO}$ or $CH_3\overline{CCHO}$ from **I499**, yield ions **I389** (Scheme 3.63) or **I443** (Scheme 3.64), respectively.

Three major peaks are observed in the daughter ion spectrum of **I389**. The first corresponds to loss of a methyl group, and gives rise to the ion $LIrCO^+$, **I374**. The methyl group lost is assumed to have been bonded to the metal and not part of the intact ligand since loss of a trifluoromethyl group, which might have been expected if the latter case were true, was not observed. It is of interest to note that loss of $\cdot CF_3$ from **I443** (Scheme 3.64) is not observed. It has been recognized for some time that metal to perfluoroalkyl bonds are

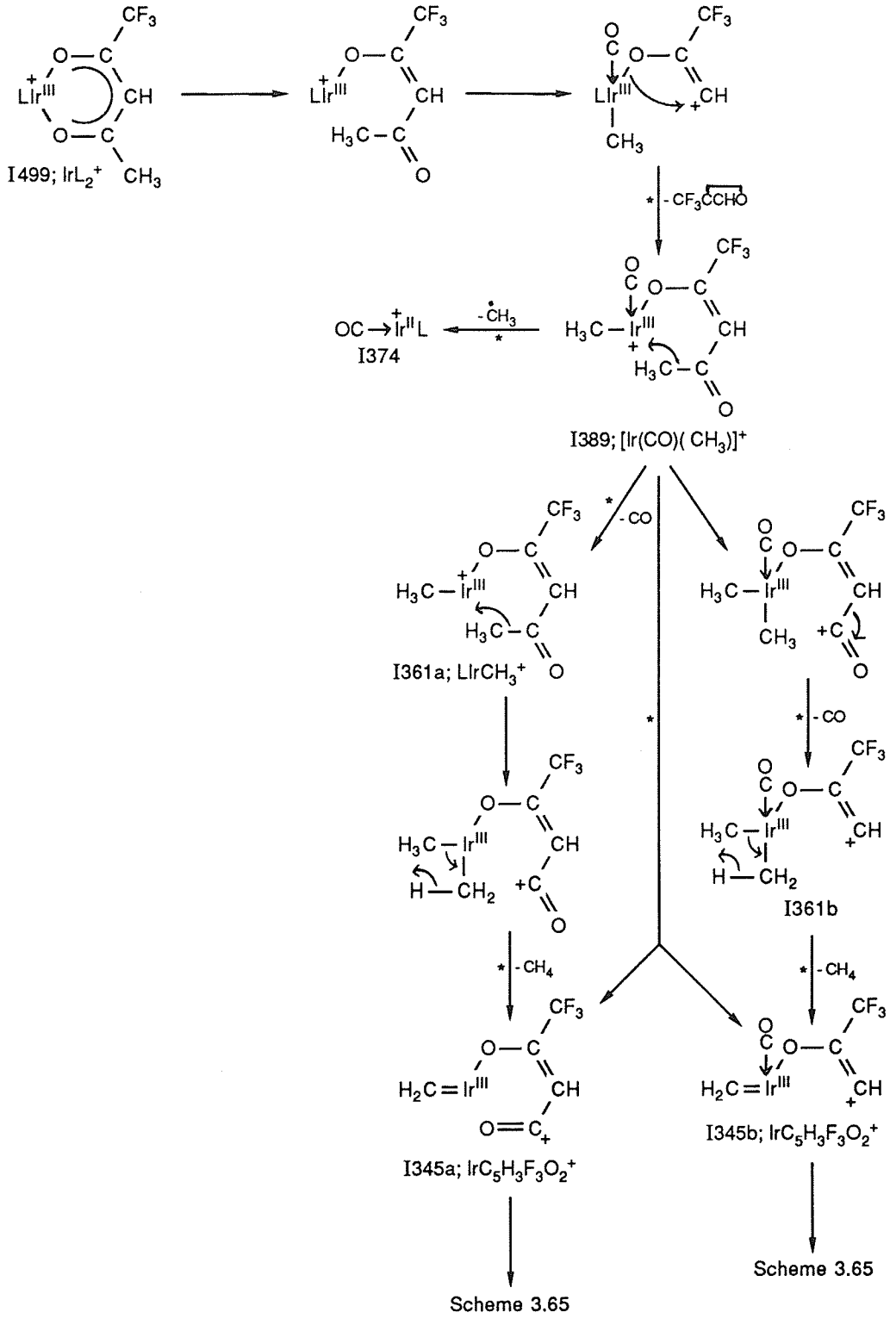
I499; IrL_2^+
I374
I389; $[Ir(CO)(CH_3)]^+$
I361a; $LIrCH_3^+$
I361b
I345a; $IrC_5H_3F_3O_2^+$
I345b; $IrC_5H_3F_3O_2^+$
Scheme 3.65
Scheme 3.65

Scheme 3.63

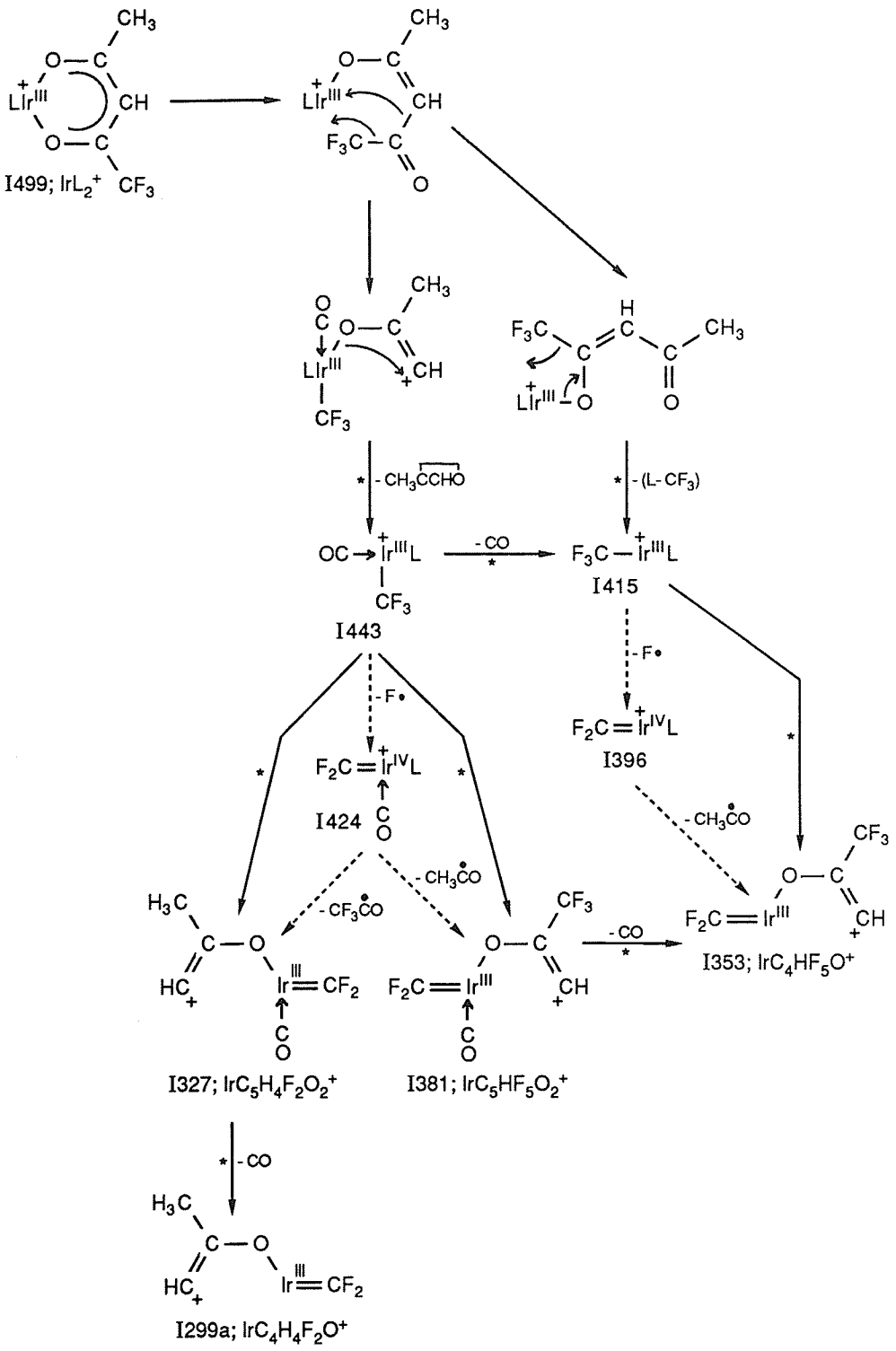
I499; IrL_2^+
I443
I415
I396
I424
I327; $IrC_5H_4F_2O_2^+$
I381; $IrC_5HF_5O_2^+$
I353; $IrC_4HF_5O^+$
I299a; $IrC_4H_4F_2O^+$
- CO
- F•
- $CH_3\dot{C}O$
- $CF_3\dot{C}O$

Scheme 3.64

more stable and thus presumably, thermochemically stronger than metal to alkyl bonds[73,108,109]. Blake *et al* [108,109] , by differential scanning calorimetry, measured the enthalpy change, $\Delta H°$, for the exothermic decarbonylation reaction

$$[Ir(COR)Cl_2(PPh_3)_2] \text{ -------> } [Ir(CO)(R)Cl_2(PPh_3)_2]$$

in the solid state. They found that $\Delta H°$ was sensitive to the nature of R, and became more exothermic as the number of fluorine atoms increased from R = CH_3 ($\Delta H°$ = -27±5 $kJmol^{-1}$) to R = CF_3 ($\Delta H°$ = -84±4 $kJmol^{-1}$). From these measurements they estimated that the Ir-CF_3 bond may be at least 57±9 $kJmol^{-1}$ stronger than the Ir-CH_3 bond. It has been suggested[112-116] that this stability is due at least in part to π back-bonding of filled d-orbitals on the metal atom into the C-F anti-bonding orbitals of the perfluoroalkyl group or, in valence bond terms, hyperconjugation of the type

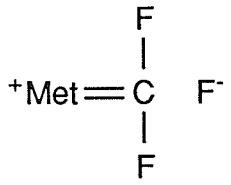

Contributions of such structures would be expected to strengthen the metal-carbon bond and also to weaken the carbon-fluorine bond. However, in a study of trifluoromethyl platinum complexes of the types *trans*-$Pt(CF_3)Q_2L^+$ and *trans*-$Pt(CF_3)ZQ_2$, where Q is $P(CH_3)_2(C_6H_5)$, L is a neutral ligand, and Z is an anionic ligand, Appleton *et al*[117] found that $^2J_{Pt\text{-}CF_3}$ for these complexes varied

linearly with $^2J_{Pt\text{-}CH_3}$ for the corresponding methyl-platinum complexes, except where L requires synergic σ-π bonding, i.e. L = CO. These results suggested that the Pt-CF_3 bond does not depend very much on π back-bonding for its stability. The former argument, however, would certainly explain the tendency of ions such as $LIrCF_3^+$ and $[LIr(CO)(CF_3)]^+$ to rapidly lose ·F in the mass spectra of this complex and of $Ir(hfa)_3$ (Scheme 3.46). Although the ions $[LIr(CO)(CF_2)]^+$, **I424** and $LIrCF_2^+$, **I396**, (Scheme 3.64) are not observed in the mass spectrum of this complex, their presence as intermediates in the formation of the ions $IrC_5HF_5O_2^+$, **I381**, $IrC_5H_4F_2O_2^+$, **I327**, and $IrC_4HF_5O^+$, **I353**, from **I443** and of **I353** from **I415** is inferred. (These overall pathways are supported by metastable ion decompositions). These losses are assigned to the rapid removal of ·F and either $CH_3\dot{C}O$ or $CF_3\dot{C}O$. In the mass spectrum of $Ir(hfa)_3$, the ions $[LIr(CF_2)(CO)]^+$, **G478**, and $LIrCF_2^+$, **G450**, are present and in both cases a metastable ion decomposition corresponding to the loss of $CF_3\dot{C}O$ is observed (Scheme 3.46).

Elimination of CO from **I389** (Scheme 3.63) gives rise to the low abundance ions $LIrCH_3^+$, **I361a**, and $IrC_6H_7O_2F_3^+$, **I361b** (depending on which carbonyl group is lost). As reasoned above, the CO group bonded to iridium should be preferentially lost (see discussion of the mass spectrum of $Ir(hfa)_3$, and loss of CO from **I443** to give **I415** (Scheme 3.64)). The most intense of the three peaks observed in the daughter ion spectrum of **I389** (Scheme 3.63) corresponds to loss of 44 u and is assigned to the rapid removal of CO and CH_4, yielding $IrC_5H_3F_3O_2^+$, **I345(a,b)**.

Scheme 3.65 shows the mechanisms proposed for decomposition of **I345(a,b)**. Losses of HF and two carbonyl groups in a variety of permutations, give rise to ions such as $IrC_4H_3F_3O^+$, **I317(a,b)**, $IrC_5H_2F_2O_2^+$, **I325**; $IrC_4H_2F_2O^+$, **I297(a,b)** and $IrC_3H_2F_2^+$, **I269**. Loss of $CF_3\overline{CCHO}$ from **I345b** to yield $[Ir(CO)(CF_2)]^+$, **I235**, is also observed.

The mechanisms proposed in Scheme 3.66 for the decomposition sequence: IrL_2^+ ----> $[IrL(L\text{-}CHO)]^+$ ----> $[IrL(L\text{-}CHO\text{-}CH_3)]^+$ ----> $LIrC_2F_3^+$ are exactly analogous to those proposed above for formation of the corresponding ions in the mass spectrum of $Ir(acac)_3$ (Scheme 3.35). A strong peak corresponding to the elimination of a methyl, but not a trifluoromethyl, group is observed in the daughter ion spectrum of **I470**. This supports the idea that the methyl group is lost from the metal atom and not from the remaining intact ligand.

Two of the more prominent metal-containing ions in the mass spectrum of this complex correspond to $LIr(CO)H^+$, **I375**, and $LIrH^+$, **I347** (%RA = 3.0 and 6.0, respectively). Unlike the corresponding ion, **H321**, in the mass spectrum of $Ir(acac)_3$ (see Scheme 3.53), **I375** is formed almost exclusively by the loss of the neutral fragment (L-H-CO) from IrL_2^+, **I499** (Scheme 3.67). **I347**, like its analogous ion in the mass spectrum of $Ir(acac)_3$, **H293**, (Scheme 3.53) is formed either by loss of CO from **I375** or by loss of (L-H) from **I499**.

Decomposition of **I347** (Scheme 3.68) involves migration of the CF_3 group to the metal, followed by consecutive losses of CO and HF to give $IrC_4H_5F_3O^+$, **I319**, and $IrC_4H_4F_2O^+$, **I299a**, respectively, or

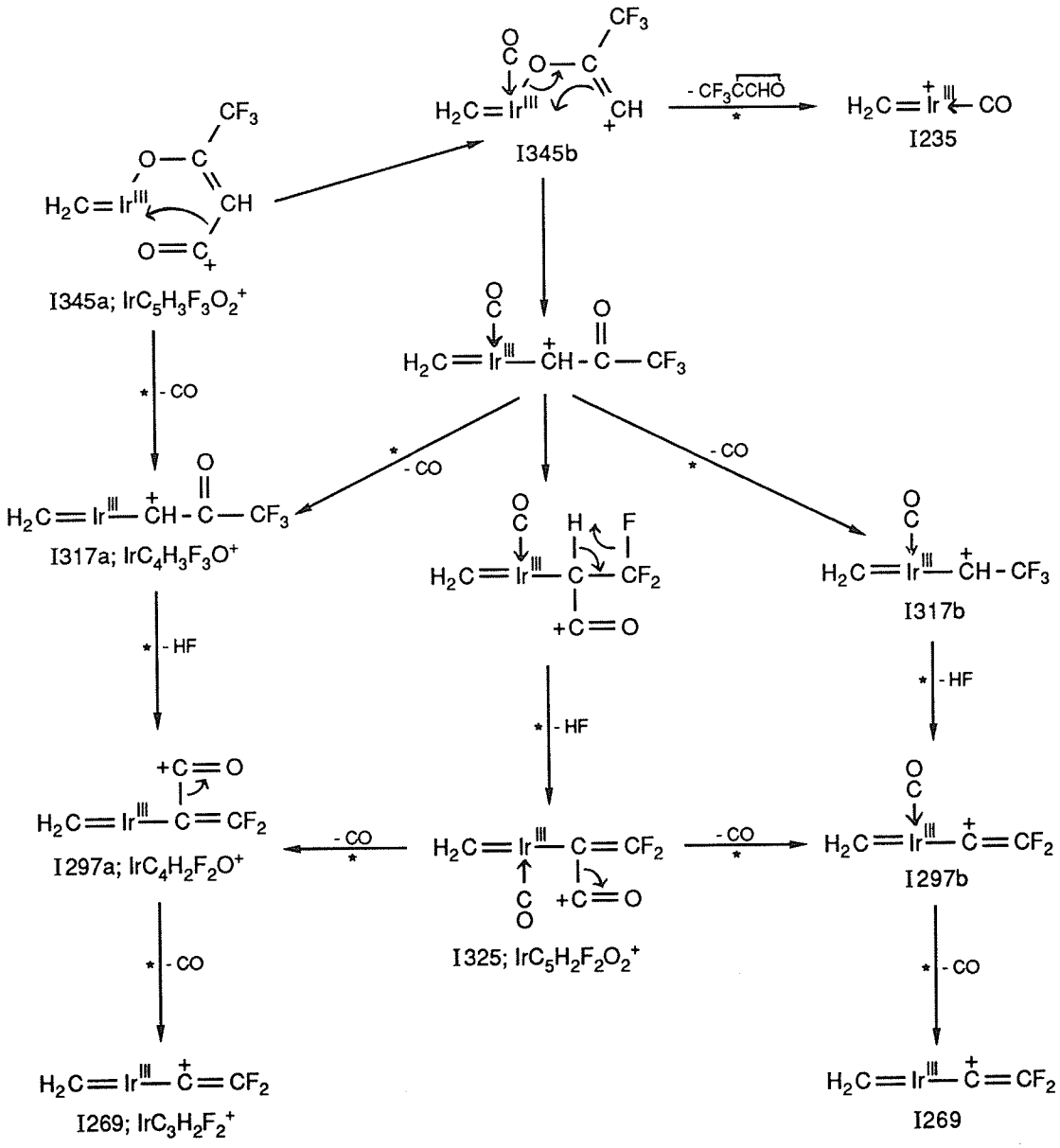
I345b
I235
I345a; IrC5H3F3O2+
I317a; IrC4H3F3O+
I317b
I297a; IrC4H2F2O+
I325; IrC5H2F2O2+
I297b
I269; IrC3H2F2+
I269
- CO
- HF

Scheme 3.65

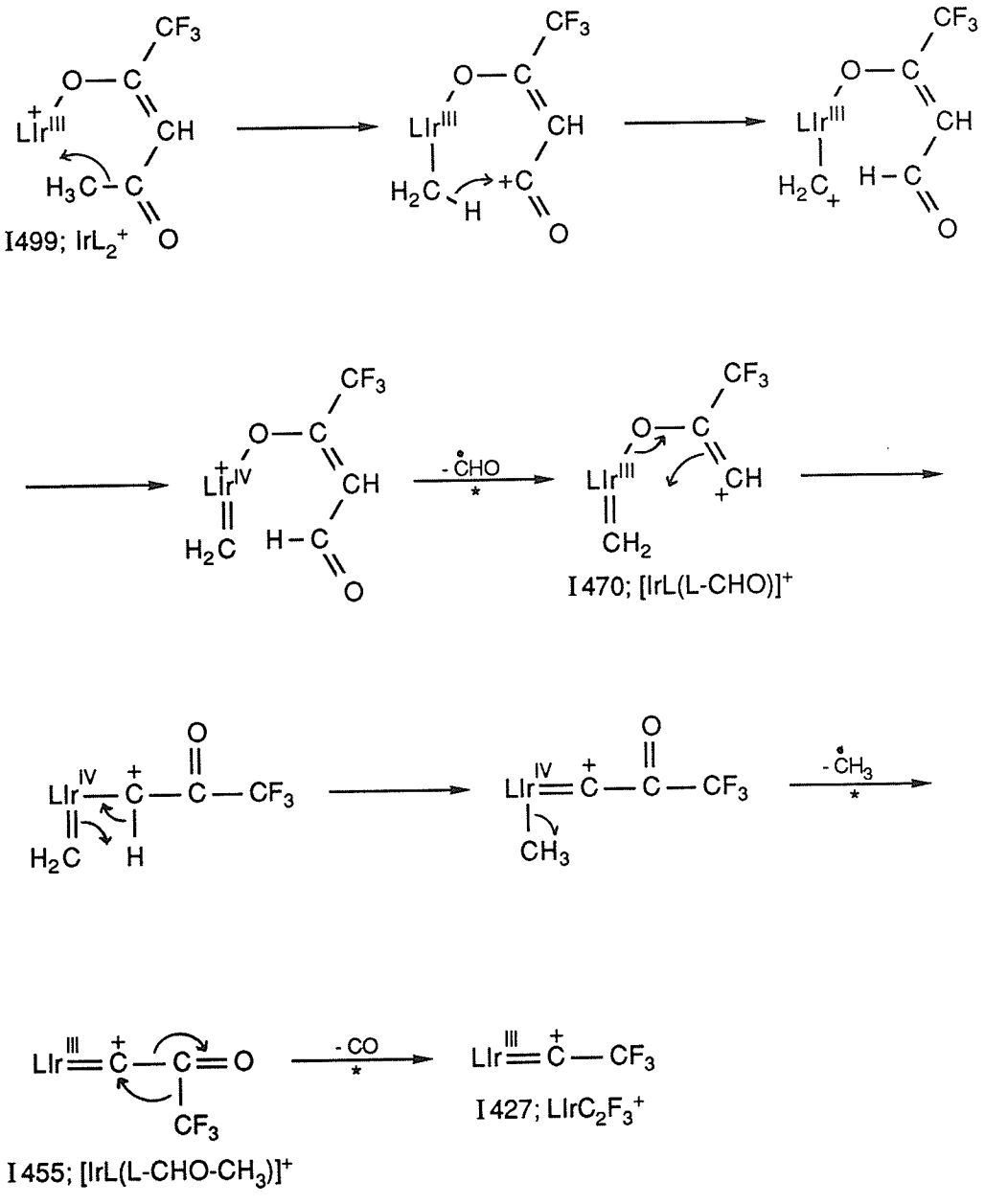
I499; IrL_2^+
I470; $[IrL(L\text{-}CHO)]^+$
I455; $[IrL(L\text{-}CHO\text{-}CH_3)]^+$
I427; $LIrC_2F_3^+$
- CHO
- CH_3
- CO

Scheme 3.66

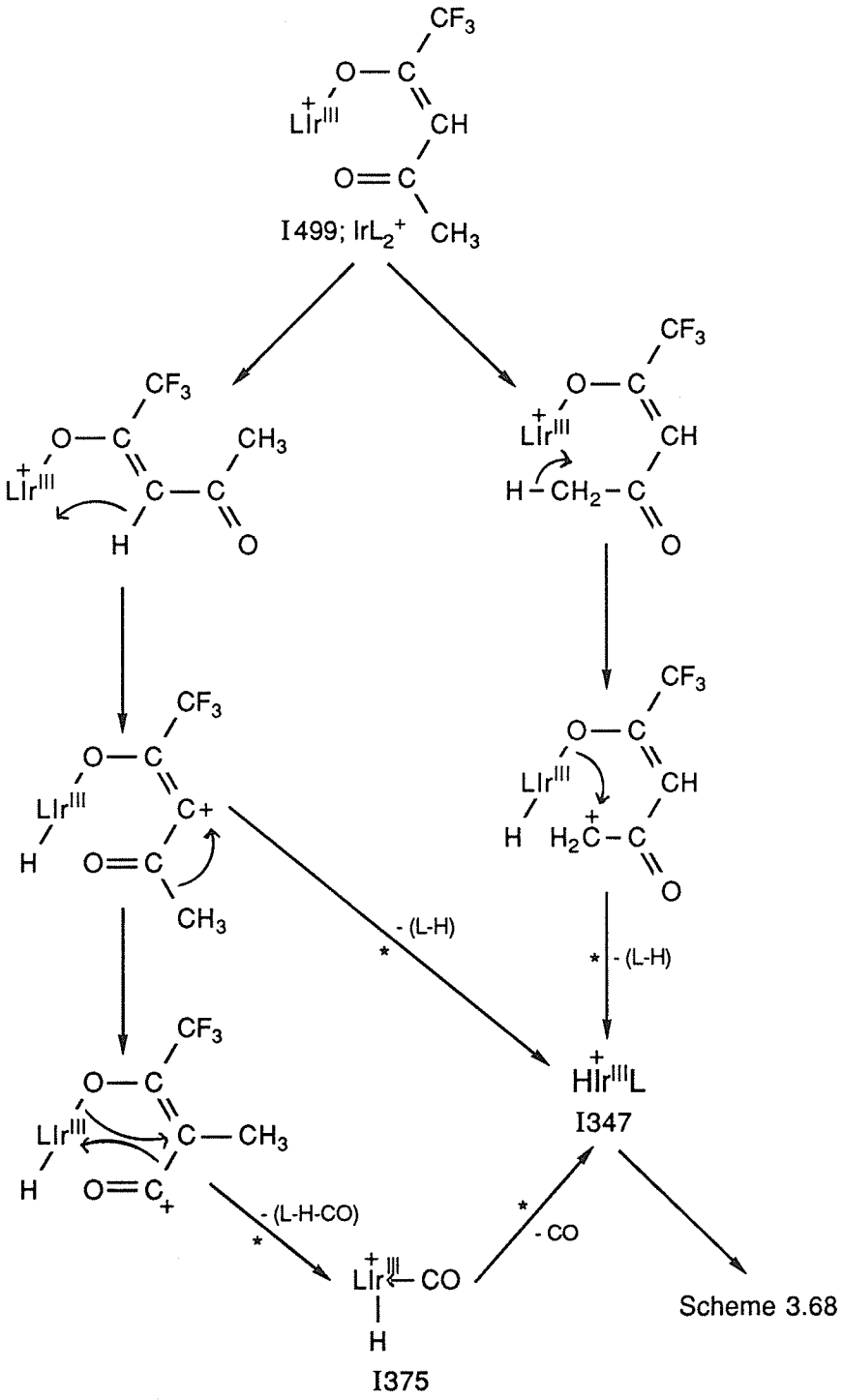

Scheme 3.68

Scheme 3.67

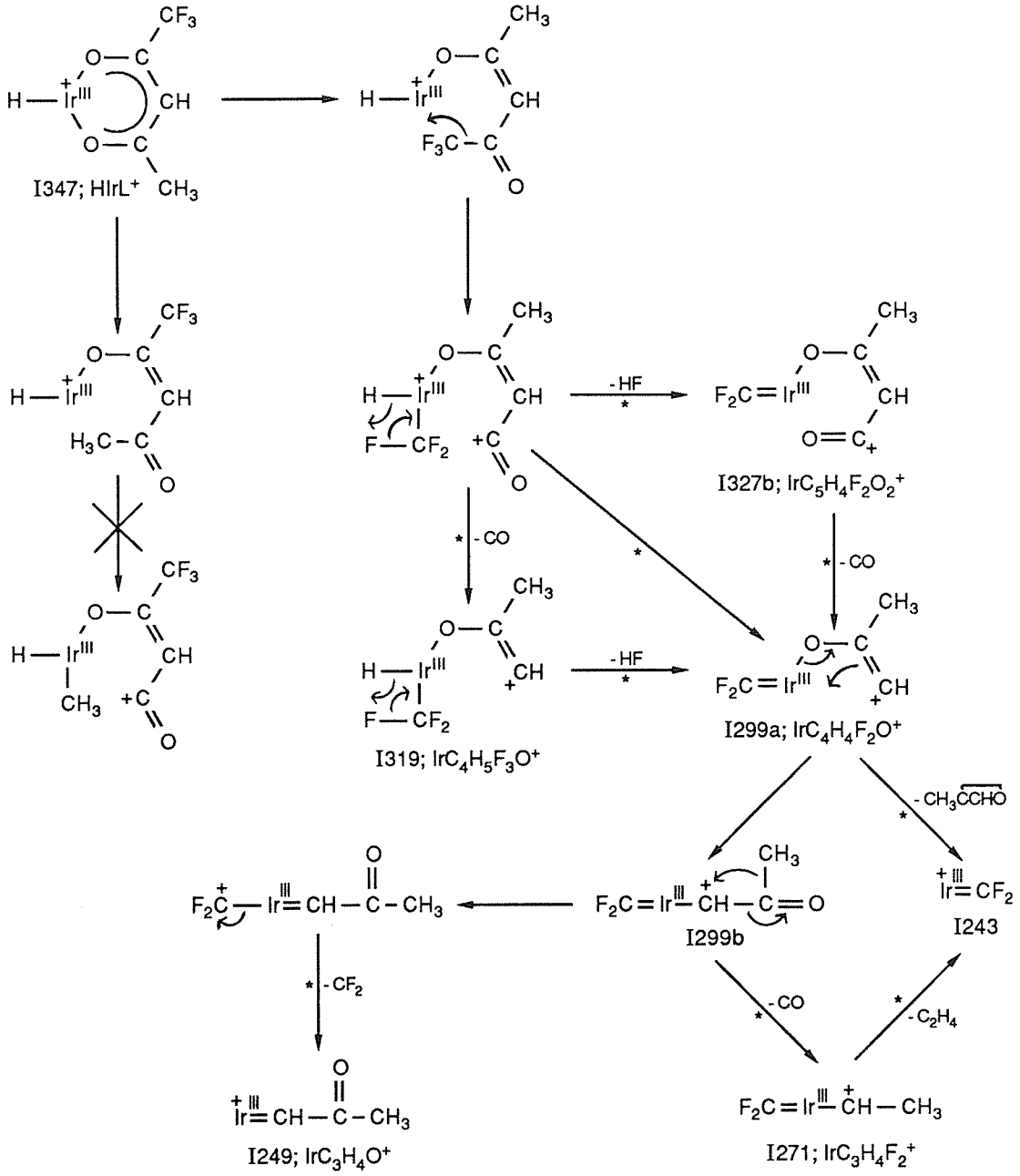
I347; HIrL+ CH3
I319; IrC4H5F3O+
I327b; IrC5H4F2O2+
I299a; IrC4H4F2O+
I299b
I243
I249; IrC3H4O+
I271; IrC3H4F2+
- HF
- CO
- CH3CCHO
- CF2
- C2H4

Scheme 3.68

by loss of HF first, yielding $IrC_5H_4F_2O_2^+$, **I327b**, and then CO to give, once again, **I299a**. This ion, in turn, can lose either $CH_3\overline{CCHO}$, CF_2, or CO to yield $IrCF_2^+$ (**I243**), $IrC_3H_4O^+$ (**I249**), or $IrC_3H_4F_2^+$, **I271**, respectively. Migration of a methyl group to iridium might also have been expected but the absence of fragmentation involving loss of CH_4 from **I347** and **I319**, observed for the analogous ions in the mass spectrum of $Ir(acac)_3$ (see Scheme 3.54), suggests that migration of the trifluoromethyl group is preferred.

As in the mass spectrum of $Ir(hfa)_3$, loss of CF_3CCH (94 u) from the bis complex ion, IrL_2^+, is observed, in this case yielding the moderately important ion $[LIr(CO_2)(CH_3)]^+$, **I405** (Scheme 3.69). For the ruthenium analogue, $Ru(tfa)_3$, a mass loss of 94 u from RuL_2^+, was also observed, verified by metastable ion decomposition evidence, but was assigned to the rapid removal of CO_2 and CF_2, accompanied by rearrangement of fluorine to ruthenium[68]. Accurate mass determinations show, at least in our case, that the observed 94 u mass loss is indeed due to elimination of CF_3CCH rather than (CO_2 + CF_2). Decomposition of **I405** is exactly analogous to that proposed above for the ion $[LIr(CO_2)(CH_3)]^+$, **H351**, in the mass spectrum of $Ir(acac)_3$ (Scheme 3.58). Loss of 60 Da is ascribed to the rapid removal of CO_2 and CH_4, to yield $IrC_5H_3F_3O_2^+$, **I345a**. Loss of CF_3CCH was not observed, possibly because of the predominance of other decomposition processes involving CF_3 migration to iridium. In this mass spectrum, unlike that of $Ir(hfa)_3$, no evidence of fluorine migration to the metal was observed.

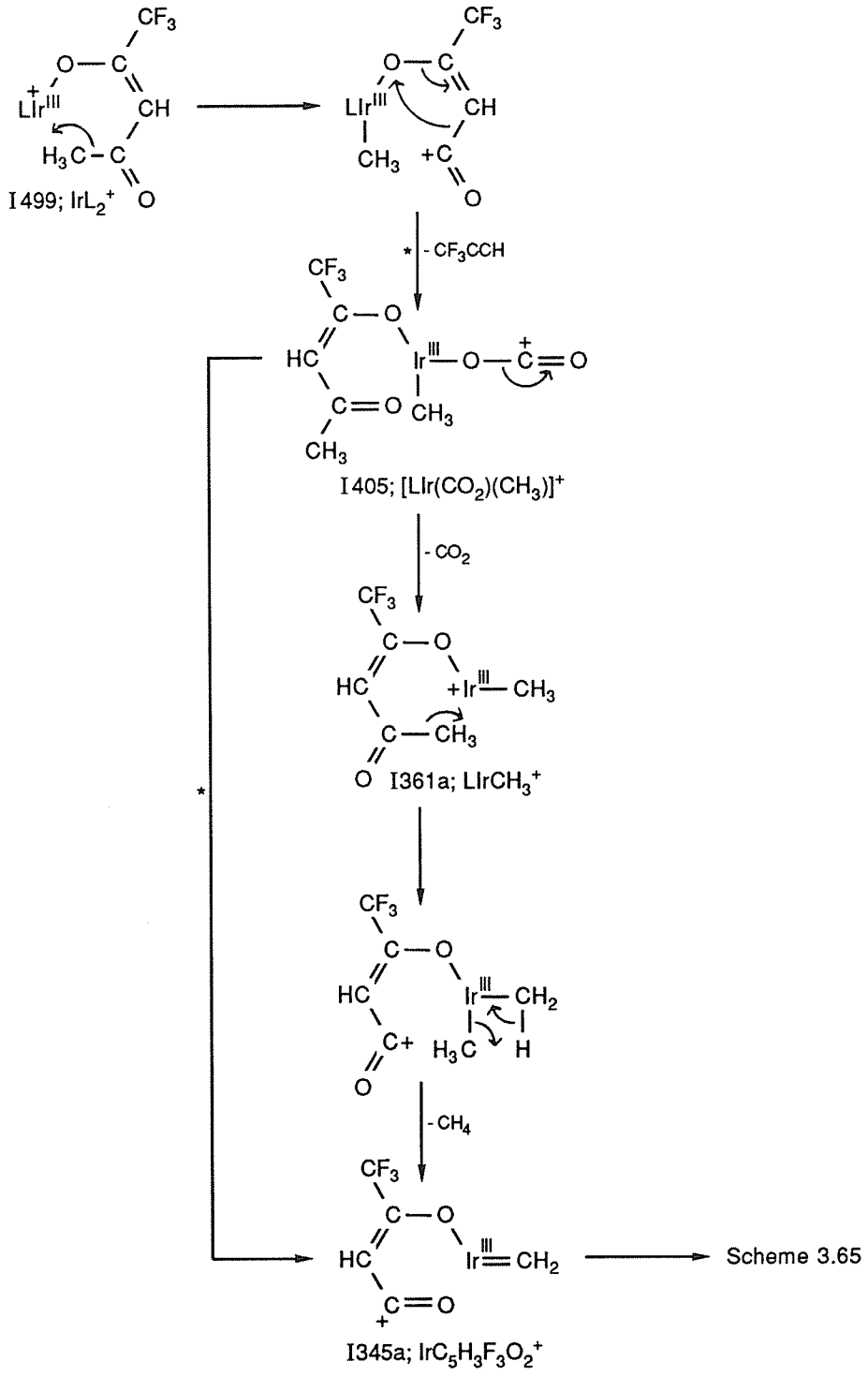
I499; IrL2+
- CF3CCH
I405; [LIr(CO2)(CH3)]+
- CO2
I361a; LIrCH3+
- CH4
I345a; IrC5H3F3O2+
Scheme 3.65

Scheme 3.69

3.3.2 ^{1}H and ^{19}F NMR studies

The ^{1}H and ^{19}F NMR chemical shifts (ppm) and corresponding intensity data for $Ir(hfa)_3$, $Ir(tfa)_3$ and $Ir(acac)_3$ are presented in Table 3.27. $Ir(tfa)_3$, which has unsymmetrical ligands, is formed as a nearly statistical mixture of *mer* and *fac* isomers. This is evident by the presence of four major peaks in the methyl and methine regions of the ^{1}H spectrum, recorded in $CDCl_3$ (Figures 3.42, 3.43) and in the CF_3 region of the ^{19}F spectra, recorded in acetone-d_6 and $CDCl_3$ (Figure 3.44). Three of the peaks in each of the corresponding regions, which are necessarily of equal intensity, may be assigned to the *mer* isomer and the fourth to the *fac* isomer. The intensity data shown in Table 3.27 suggest that the second peak in the fluorine spectra (in both solvents) and the third in both regions of the proton spectrum (counting from low field) can be assigned to the *fac* isomer.

The proton NMR spectrum of $Ir(acac)_3$ reveals two resonances in the intensity ratio 1:6, corresponding to the methine and methyl protons, respectively (Figure 3.45), while the ^{1}H and ^{19}F NMR spectra (not shown) of $Ir(hfa)_3$ each reveal only one signal, corresponding to the methine proton and the methyl fluorines, respectively. This is understandable since each complex has symmetrical ligands and therefore only one possible geometrical isomer.

Bonati and Ugo[118], in a study of the proton NMR spectra of the dicarbonyl derivatives of rhodium and iridium β-ketoenolates $(CO)_2Met(R^1COCHCOR^2)$ (where $R^1 = CH_3$ or CF_3; $R^2 = CF_3$ or Ph, Met = Rh or Ir), found that the signal due to the methine proton was very

Table 3.27 $\{^1H\}^{19}F$ and ^1H chemical shift (ppm) and intensity data for $Ir(hfa)_3$, $Ir(tfa)_3$ and $Ir(acac)_3$ complexes.

Complex	δ_{CF_3}	Intensity	δ_{CH_3}	Intensity	δ_{CH}	Intensity
$Ir(hfa)_3$	-72.751	-	-	-	6.521	-
fac-$Ir(tfa)_3$	-72.296	0.74	2.184	2.11	5.976	0.69
mer-$Ir(tfa)_3$	-72.251 -72.377 -72.423	1.00 1.05 1.03	2.213 2.196 2.168	3.02 2.93 3.08	6.016 5.984 5.951	0.92 0.86 1.00
•*fac*-$Ir(tfa)_3$	-74.374	0.69	-	-	-	-
•*mer*-$Ir(tfa)_3$	-74.336 -74.549 -74.572	1.00 1.03 1.00	-	-	-	-
$Ir(acac)_3$	-	-	2.004	6.24	5.48	1.00

^{19}F and ^1H spectra were recorded in acetone-d_6 and $CDCl_3$, respectively, unless otherwise noted.
Chemical shifts are believed to be accurate to ±0.001 ppm.
• Spectrum recorded in $CDCl_3$.

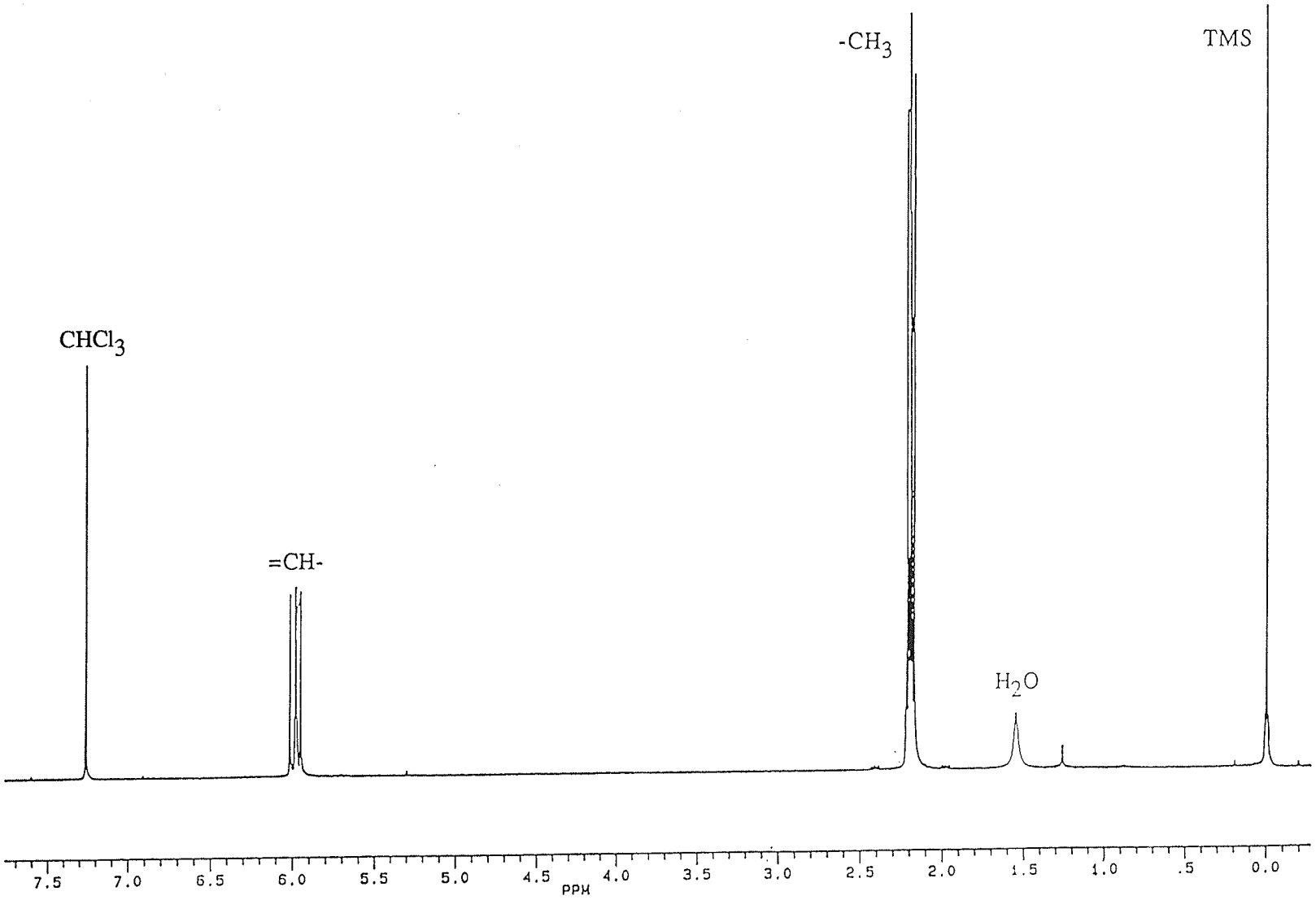

Figure 3.42 ^{1}H NMR spectrum of $Ir(tfa)_3$ recorded at 300.13 MHz in $CDCl_3$ at room temperature.

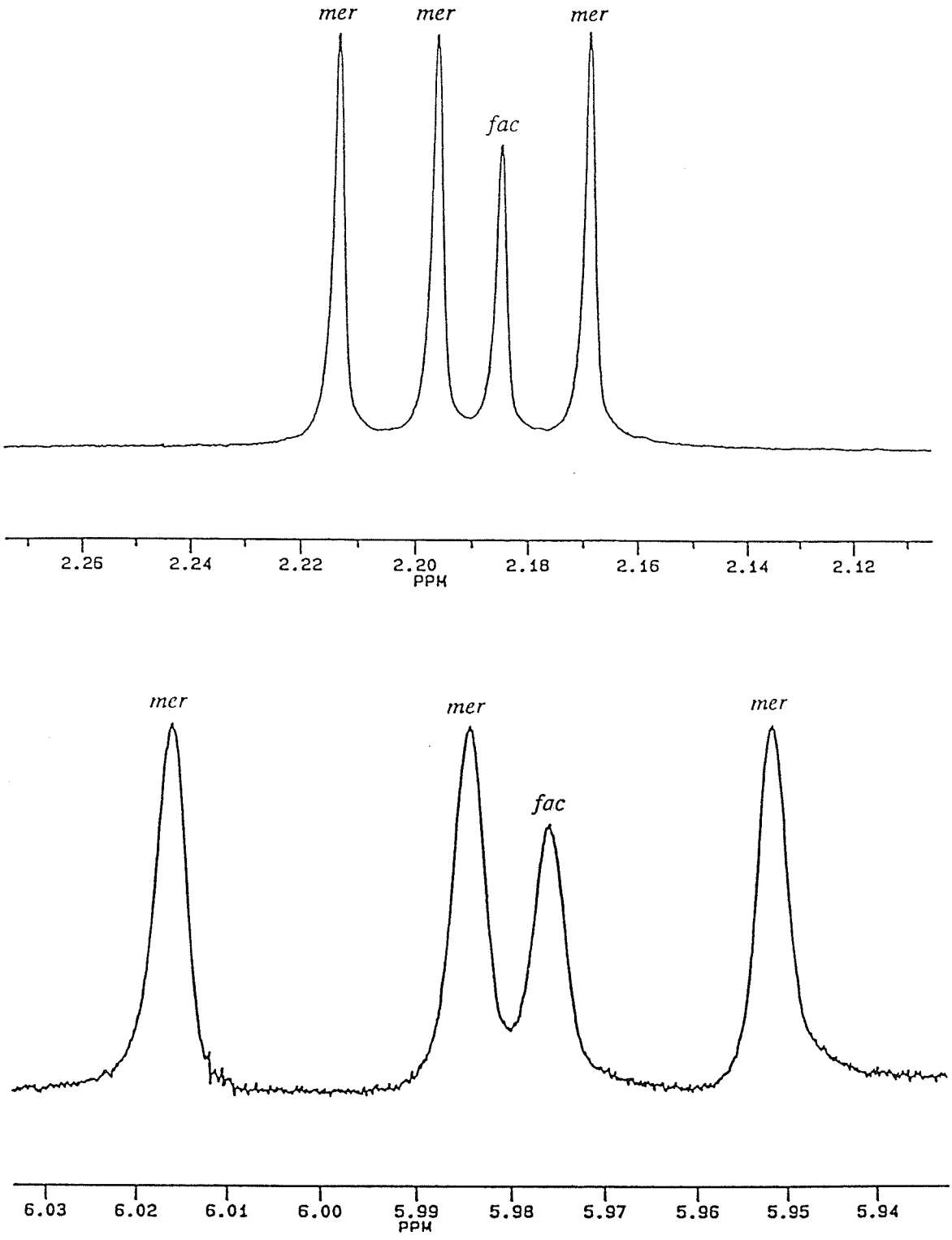

Figure 3.43 Methyl (top) and methine (bottom) regions in the ^{1}H NMR spectrum (with increased digital resolution) of $Ir(tfa)_3$ recorded at 300.13 MHz in $CDCl_3$ at room temperature.

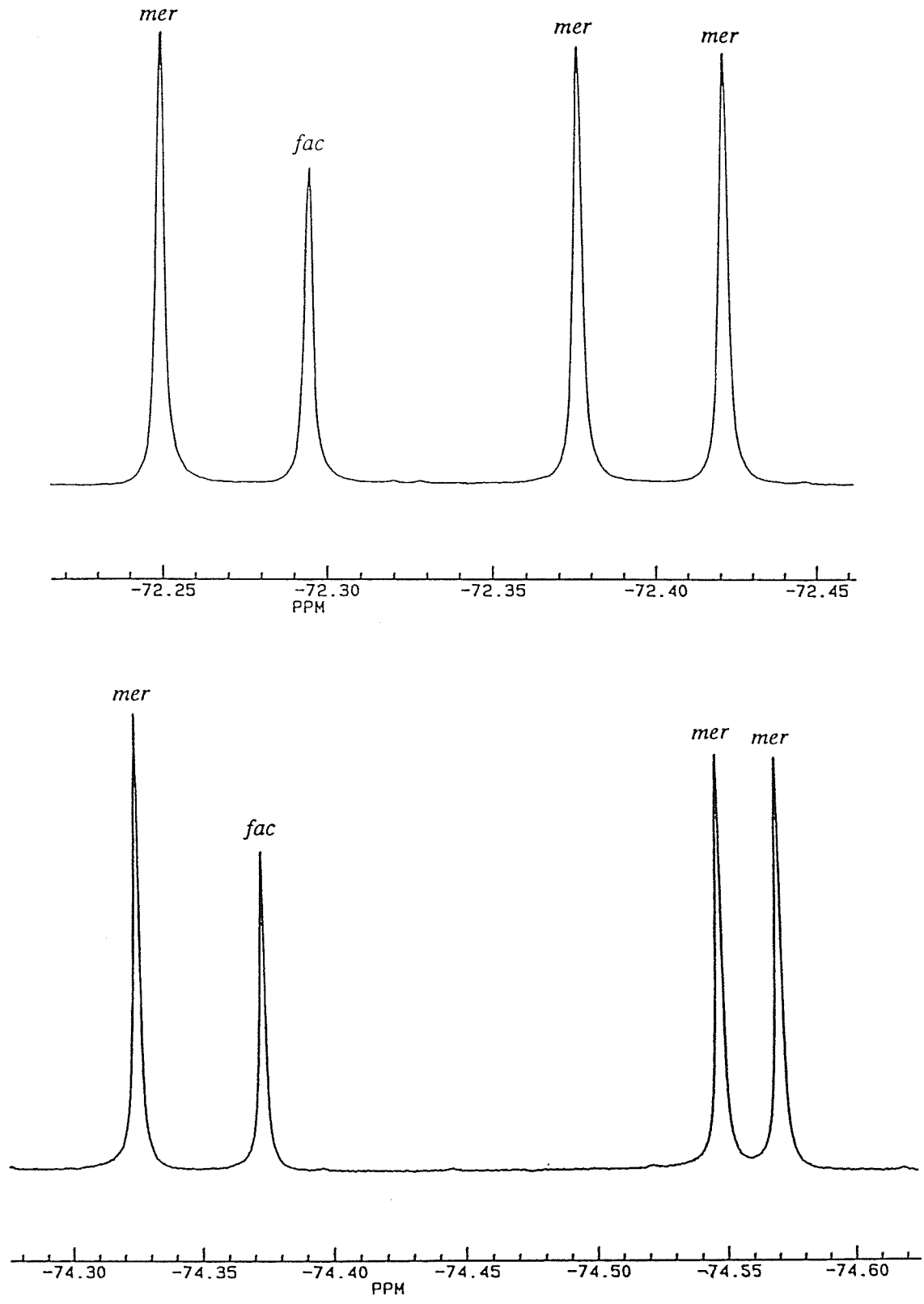

Figure 3.44 Trifluoromethyl resonances in the ^{19}F NMR spectrum (with increased digital resolution) of $Ir(tfa)_3$ recorded at 282.40 MHz in acetone-d_6 (top) and $CDCl_3$ (bottom) at room temperature.

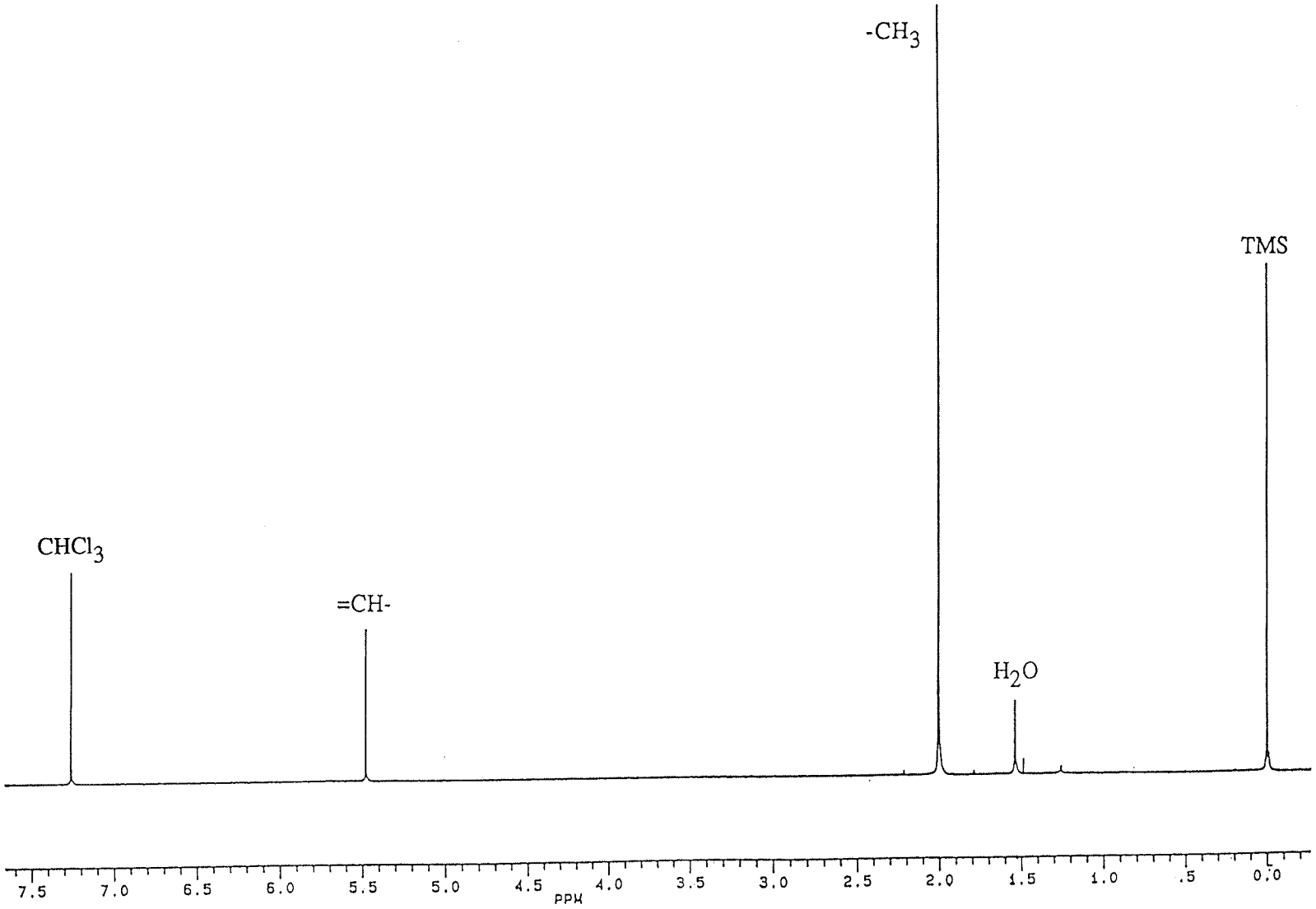

Figure 3.45 ^{1}H NMR spectrum of $Ir(acac)_3$ recorded at 300.13 MHz in $CDCl_3$ at room temperature.

sensitive to the nature of the other substituents. The position of the signal is shifted to lower field by electronegative substituents on the ring. This same trend is observed for the three iridium complexes in this study (see Table 3.27). Each addition of a CF_3 group moves the signal of the methine proton by ~ 0.52 ppm toward lower field.

Table 3.28 lists the various ^{19}F and ^{1}H chemical shifts (ppm) for $Co(tfa)_3$[119], $Rh(tfa)_3$[119] and $Ir(tfa)_3$. The values reported for the *mer* isomers are the mean chemical shifts of the three observed resonances. The variation in chemical shifts of the methine proton resonances as a function of the metal ion is not large, as has already been pointed out in the case of a number of metal acetylacetonates[119,120]. It is clear from Table 3.28, however, that both the methyl and trifluoromethyl resonances of the iridium complex occur at a higher field than the corresponding resonances of the cobalt and rhodium complexes. This is somewhat unexpected since the chemical properties of rhodium are usually more closely related to those of iridium than to those of cobalt[21]. A similar trend is observed for various dithio-β-ketoenolates of this triad, as well as for the Ni, Pd and Pt triad (see Table 3.29). In each case, as for the dioxo complexes, the methyl resonance of the third transition series metal complexes (Ir, Pt) occurs at a higher field than for their analogous first and second series transition metal complexes. This phenomenon seems to be independent of the geometry of the complex and of the heteroatoms coordinated to the metal.

Table 3.28 ^{1}H and ^{19}F chemical shifts (ppm) for Co, Rh and Ir trifluoroacetylacetonates.

Complex	δ_{CF_3}	δ_{CH_3}	δ_{CH}
fac-Co(tfa)$_3$	-72.83	2.40	6.05
fac-Rh(tfa)$_3$	-72.10	2.36	5.99
fac-Ir(tfa)$_3$	-74.37	2.18	5.98
mer-Co(tfa)$_3$	-72.82	2.41	6.04
mer-Rh(tfa)$_3$	-72.18	2.37	6.01
mer-Ir(tfa)$_3$	-74.48	2.19	5.98

Chemical shift data for Co and Rh complexes from Fay and Piper[119]. In the case of the *mer* isomers, the mean chemical shift is reported. All spectra recorded in $CDCl_3$.

Table 3.29 Methyl and methine chemical shifts (ppm) in the ^1H NMR spectra of various metal dithio-β-ketoenolates.

Complex	Ref.	δ_{CH_3}	δ_{CH}
$Co(SacSac)_3$	121	2.32	6.85
$Rh(SacSac)_3$	121	2.36	6.95
$Ir(SacSac)_3$	121	2.00	6.95
fac-$Co(OEtSacSac)_3$	122	2.09	6.48
fac-$Rh(OEtSacSac)_3$	122	2.08	6.52
fac-$Ir(OEtSacSac)_3$	122	1.91	6.56
mer-$Co(OEtSacSac)_3$	122	2.14	6.47
mer-$Rh(OEtSacSac)_3$	122	2.10	6.52
mer-$Ir(OEtSacSac)_3$	122	1.93	6.56
$Ni(SacSac)_2$	119	2.32	7.10
$Pd(SacSac)_2$	119	2.49	7.14
$Pt(SacSac)_2$	119	2.10	7.05
$Ni(OEtSacSac)_2$	123	2.31	6.59
$Pd(OEtSacSac)_2$	123	2.40	6.59
$Pt(OEtSacSac)_2$	123	2.18	6.58

All spectra recorded in $CDCl_3$.

In the case of the *mer* isomers, the mean chemical shift is reported.

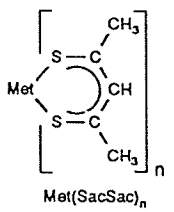

$Met(SacSac)_n$

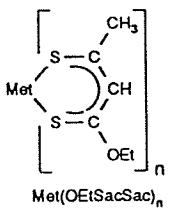

$Met(OEtSacSac)_n$

4 Summary

Factors having a major influence on the mass spectral fragmentation of the rhodium-containing complexes are: rhodium's preference for the +III oxidation state and its accessibility to the +IV, +II and +I oxidation states, its ability to coordinate strongly with sulfur and to form bonds with portions of the ligand, e.g. CO, CF_3, CH_3, C_6H_5, and H. In the mass spectra of $Rh(SbzC_2F_5)_3$ and $Rh(SbzC_3F_7)_3$, loss of sulfur from RhL_3^+ is noteworthy because the formation of abundant ionic species in which the rhodium-sulfur bond is retained implies strong rhodium-sulfur bonds. Sulfur is a soft base (class (b) ligand), which should preferably bond to soft acids (class (b) metal) such as rhodium (especially in a low oxidation state). However, the positive charge on RhL_3^+ formally raises the oxidation state of rhodium to +IV, while the three sulfur atoms compete for rhodium dπ-electrons. Both factors contribute to a decrease in the b-character of rhodium (i.e. increase in acid hardness). The $[RhL(L\text{-}S)]^+$ ion, also present in these spectra, is not formed by loss of sulfur from RhL_2^+ (in which Rh(III) is a softer

acid) but by loss of ·L from $[RhL_2(L\text{-}S)]^+$. $[RhL(L\text{-}S)]^+$ was also observed in the mass spectum of $Rh(Sacac)_3$ and to a lesser extent in that of $Rh(Stfa)_3$. However, although metastable ion decompositions of the molecular ion to $[RhL(L\text{-}S)]^+$ are observed, in neither case is the supposed precursor ion $[RhL_2(L\text{-}S)]^+$ observed in the normal mass spectrum. This implies, following the elimination of sulfur from the molecular ion, a rapid loss of ·L, and reflects rhodium's preference for the +III oxidation state. The observation of $[RhL_2(L\text{-}S)]^+$ in the mass spectra of the former two complexes was explained by an increase in stabilization of the molecular ion due to the presence of the aromatic substituents. A major feature in the mass spectra of $Rh(bzC_2F_5)_3$ and $Rh(bzC_3F_7)_3$ is the presence of ion species which contain a rhodium-phenyl bond. The proposed reaction mechanism involves a four-membered cyclic transition state in which the phenyl group migrates to the rhodium atom with simultaneous breaking of a rhodium-oxygen bond. Similar species are not observed in the analogous sulfur-containing complexes since their formation would require rhodium-sulfur bond scission which, due to strengthening of the rhodium-sulfur bond by $d\pi$-$d\pi$ bonding, would be less facile than rhodium-oxygen bond scission. Rhodium-containing ions are much more abundant in the mass spectra of the β-ketoenolate complexes than in those of their sulfur-containing analogues. This is ascribed to the lower tendency for the molecular ion of the former complexes to decompose to L^+.

In the mass spectra of the iridium complexes, the two most intense peaks in each mass spectrum correspond to the molecular ion, IrL_3^+, and the fragment ion IrL_2^+; the base peak corresponds to

IrL_3^+ for $Ir(acac)_3$ and $Ir(tfa)_3$, and to IrL_2^+ for $Ir(hfa)_3$. (In the mass spectra of the analogous rhodium complexes[65,104], RhL_2^+ corresponds to the base peak ion in all three cases.) The increased stability of the molecular ion in the iridium complexes reflects iridium's greater preference, compared to rhodium, for the +IV oxidation state. Ions of all three iridium complexes show an overwhelming tendency to decompose by losses of even-electron neutral species i.e. CO, CF_2, HF, CF_2CO for $Ir(hfa)_3$; CO, CH_4, C_2H_4 and CH_2CO for $Ir(acac)_3$, and a combination of these for $Ir(tfa)_3$. These consecutive losses can only be explained by initial scission of an Ir-O bond with simultaneous formation of an iridium-carbon bond. Migration of a CF_3 or CH_3 group to iridium, evident by formation of ions such as $LIrCF_3^+$, $[LIr(CO)(CF_3)]^+$, $LIrCH_3^+$ and $[LIr(CO)(CH_3)]^+$, would also facilitate loss of a carbonyl group. Numerous losses of neutral radicals are observed in the mass spectra of $Ir(hfa)_3$ and $Ir(tfa)_3$, occurring both prior to, and after, oxidation of Ir(II) to Ir(IV). The tendency of ions such as $LIrCF_3^+$ and $[LIr(CO)(CF_3)]^+$ to rapidly lose ·F in the mass spectrum of $Ir(hfa)_3$, and to a lesser extent in that of $Ir(tfa)_3$, is rationalized in terms of iridium's ability to form multiple bonds with carbon, and to the strengthening of the metal-carbon bond and subsequent weakening of the carbon-fluorine bond due to π back-bonding from filled d-orbitals of the metal atom into the C-F antibonding orbitals of the perfluoroalkyl group. Fluorine migration to the metal is observed only in the mass spectrum of $Ir(hfa)_3$.

The ^{19}F and ^1H NMR studies show that rhodium and iridium β-ketoenolates having unsymmetrial ligands, are formed as a nearly

statistical mixture of *mer* and *fac* isomers, while the thio analogues adopt a facial octahedral structure. (The latter result is corroborated by the X-ray structural studies of $Rh(Stfa)_3$.) The splitting patterns observed in the ^{19}F NMR spectra of the perfluoroalkyl complexes, $Rh(SbzC_3F_7)_3$, $Rh(bzC_2F_5)_3$ and $Rh(bzC_3F_7)_3$ are consistent with an ABX_3-type spin system. Geminal F-F coupling was not observed for $Rh(SbzC_2F_5)_3$, and for one isomer in the analogous dioxo complex (in toluene), indicating that both fluorines of their CF_2 groups are chemically equivalent. In the ^1H NMR spectrum of $Rh(Sacac)_3$ the observed splitting of the methyl signal on the sulfur side of the ligand is attributed to coupling of the protons with the rhodium atom. Coupling between the methyl and methine protons was ruled out since irradiation of the methine resonance did not have an effect on the observed methyl doublet.

Future work might involve the preparation and study of the iridium perfluoroalkyl complexes $Ir(SbzC_2F_5)_3$, $Ir(SbzC_3F_7)_3$, $Ir(bzC_2F_5)_3$ and $Ir(SbzC_3F_7)_3$, as well as the thio analogs of $Ir(hfa)_3$, $Ir(tfa)_3$ and $Ir(acac)_3$. While some progress was made in the preparation of the former complexes (not described in this thesis), they could not be completely purified by using column chromatography and fractional sublimation. HPLC may prove to be a viable alternative. Ir(III) is classified as a borderline acid and would be expected to form strong bonds with sulfur, as does rhodium in ions present in the mass spectrum of rhodium complexes. Its greater preference for the +IV oxidation state should serve to increase the stability of the molecular ion and, therefore, losses of neutral fragments such as S and CF_2 may be more prominent.

5 *References*

1. C.G. Macdonald and J.S. Shannon, Aust. J. Chem. **19**, 1545 (1966).

2. R.C. Mehrotra, R. Bohra and D.P. Gaur, **Metal β-Diketonates and Allied Derivatives**, Academic Press, London (1978).

3. K.C. Joshi and V.N. Pathak, Coord. Chem. Rev. **22**, 37 (1977).

4. J.B. Westmore, **Mass Spectrometry of Metal Compounds**, (J. Charalambous, Ed.), Butterworths, London, 147 (1975).

5. I.K. Gregor and M. Guilhaus, Mass Spectrom. Rev. **3**, 39 (1984).

6. J.S. Shannon and J.M. Swan, Chem. Commun. **33** (1965).

7. M.J. Lacey and J.S. Shannon, Org. Mass Spectrom. **6**, 931 (1972).

8. F.W. McLafferty, **Interpretation of Mass Spectra**, 3rd Ed., University Science Books, Mill Valley, Ca (1980).

9. M. Karni and A. Mandelbaum, Org. Mass Spectrom. **15**, 53 (1980).

10. J.E. Huheey, **Inorganic Chemistry. Principles of Structure and Reactivity**, 2nd Ed. Harper and Row, Publishers, New York (1972).

11. R.G. Pearson, J. Am. Chem. Soc. **85**, 3533 (1963).

12. C.K. Jorgensen, Inorg. Chem. **3**, 1201 (1964).

13. R.G. Pearson, Chem. Brit. **3**, 103 (1967).

14. R.G. Pearson, J. Chem. Ed. **45**, 581 (1968).

15. R.G. Pearson, J. Chem. Ed. **45**, 643 (1968).

16. R.G. Pearson, Chem. Commun. 65 (1968).

17. J.E. Huheey and R.S. Evans, Chem. Commun. 968 (1969).

18. J.E. Huheey and R.S. Evans, J. Inorg. Nucl. Chem. **32**, 373 (1970).

19. C.K. Jorgenson, **Structure and Bonding**, Vol. 1, Springer-Verlag, N.Y. (1968).

20. S. Ahrland, I. Grenthe, L. Johansson and B. Noren, Acta. Chem. Scand. **17**, 1567 (1963).

21. F.A. Cotton and G. Wilkinson, **Advanced Inorganic Chemistry**, 4th Ed., J. Wiley and Sons, N.Y. (1980).

22. J.L. Burmeister and F. Basolo, Inorg. Chem. **3**, 1587 (1963).

23. J.M. Miller, T.R.B. Jones and G.B. Deacon, Inorg. Chim. Acta. **32**, L75 (1979).

24. M.L. Morris and R.D. Koob, Inorg. Chem. **20**, 2737 (1981).

25. M.E. Rose and R.A.W. Johnstone, **Mass Spectrometry for Chemists and Biochemists**, Cambridge University Press, London (1982).

26. H.E. Duckworth, R.C. Barber and V.S. Venkatasubramanian, **Mass Spectrometry**, 2nd Ed., Cambridge University press, London (1985).

27. C.A. McDowell, **Mass Spectrometry**, McGraw-Hill Pub. Co., NY (1963).

28. R.G. Cooks, J.H. Beynon, R.M. Caprioli and G.R. Lester, **Metastable ions**, Elsevier Pub. Co. Ltd., Amsterdam (1973).

29. R.K. Boyd and J.H. Beynon, Org. Mass Spectrom. **12**, 163 (1977).

30. W.F. Haddon, Anal. Chem. **51**, 983 (1979).

31. D.S. Millington and J.A. Smith, Org. Mass Spectrom. **12**, 264 (1977).

32. L. Petrakis and C.H. Sederholm, J. Chem. Phys. **35**, 1243 (1961).

33. S. Ng and C.H. Sederholm, J. Chem. Phys. **40**, 2090 (1964).

34. R.J. Abraham and L. Cavalli, Molec. Phys. **9**, 67 (1965).

35. L. Cavalli and R.J. Abraham, Molec. Phys. **19**, 265 (1970).

36. L. Cavalli, J. Magn. Resonance **6**, 298 (1972).

37. K. Hirao, H. Nakatsuji, H. Kato and T. Yonezawa, J. Amer. Chem. Soc. **94**, 4078 (1972).

38. K. Hirao, H. Nakatsuji and H. Kato, J. Amer. Chem. Soc. **95**, 31 (1973).

39. D.F. Evans, Disc. Faraday Soc. **34**, 139 (1962).

40. N. Boden, J. Feeney and L.H. Sutcliffe, J. Chem. Soc. 3482 (1965).

41. K.L. Servis and J.D. Roberts, J. Amer. Chem. Soc. **87**, 1339 (1965).

42. K.L. Williamson and B.A. Braman, J. Amer. Chem. Soc. **89**, 6183 (1967).

43. M.L. Huggins, J. Amer. Chem. Soc., **75** 4123 (1952).

44. R.K. Harris and V.J. Robinson, J. Magn. Resonance **1**, 362 (1969).

45. N.F. Ramsey and E.M. Purcell, Phys. Rev. **85**, 143 (1952).

46. N.F. Ramsey, Phys. Rev. **91**, 303 (1953).

47. H.M. McConnell, J. Chem. Phys. **24**, 460 (1956).

48. M.J. Stephens, Proc. Roy. Soc. **A243**, 274 (1957).

49. M. Karplus, J. Chem. Phys. **30**, 11 (1959).

50. H.S. Gutowski, M. Karplus and D.M. Grant, J. Chem. Phys. **31**, 1278 (1959).

51. G.E. Maciel, J.W. McIver Jr., N.S. Ostlund and J.A. Pople, J. Amer. Chem. Soc. **92**, 4151 (1970).

52. S.P.S. Porto, J. Molec. Spectros. **3**, 248 (1959).

53. W.F. Edgell, P.A. Kinsey and J.W. Amy, J. Amer. Chem. Soc. **79**, 2691 (1957).

54. R.D. Chambers, L.H. Sutcliffe, and G.J.T. Tiddy, Trans. Faraday Soc. **66**, 1025 (1970).

55. J. Hilton, J. Magn. Resonance **14**, 241 (1974).

56. C. Schumann and F. Cavagna, J. Magn. Resonance **18**, 172 (1975).

57. C.W. Haigh, J. Hilton, L.H. Sutcliffe and G.J.T. Tiddy, J. Magn. Resonance **18**, 241 (1975).

58. S.L. Manatt and M.A. Cooper, J. Amer. Chem. Soc. **99**, 4561 (1977).

59. T. Schaefer, W. Niemczura, C.-M. Wong and K. Marat, Can. J. Chem. **57**, 807 (1979).

60. G.H. Stout and L.H. Jensen, **X-ray Structure Determination: A Practical Guide**, MacMillan Co., New York, (1968).

61. L.W. Tari, G.A. Stern, J.B. Westmore and A.S. Secco, Acta. Cryst. **C46**, 197 (1990).

62. F. Duus and J.W. Anthonsen, Acta. Chim. Scand. **40**, B31 (1977).

63. R.K.Y. Ho, S.E. Livingstone and T.N. Lockyer, Aust. J. Chem. **19**, 1179 (1977).

64. M. Das, Inorg. Chim. Acta. **48**, 33 (1981).

65. S. Kawanishi, A. Yokoyama and H. Tanaka, Chem. Pharm. Bull. **21**, 2653 (1973).

66. L. Davignon, J.M. Manoli and A. Dereigne, J. Less-Common Metals **21**, 341 (1970).

67. L. Davignon, A. Dereigne and J.M. Manoli, J. Less-Common Metals **21**, 345 (1970).

68. M.L. Morris and R.D. Koob, Inorg. Chem. **22**, 3502 (1983).

69. S.E. Livingstone and N. Saha, Aust. J. Chem. **28**, 1249 (1975).

70. S.E. Livingstone and D.S. Moore, Aust. J. Chem. **29**, 283 (1976).

71. M. Das and S.E. Livingstone, Aust. J. Chem. **27**, 1177 (1974).

72. J.A. McCleverty and G. Wilkinson, J. Chem. Soc. 4200 (1964).

73. M.R. Churchill, **Perspectives in Structural Chemistry**, Vol. 3, Wiley and Sons Inc., New York, 141 (1970).

74. R.B. King and A. Efraty, J. Organometal. Chem. **36**, 371 (1972).

75. M. Das and S.E. Livingstone, Aust. J. Chem. **27**, 53 (1974).

76. M.L. Reimer, Ph.D Thesis, **Mass Spectrometry of Fluorinated Metal-β-diketonates and Monothio-β-diketonates**, University of Manitoba (1988).

77. M.J. Lacey, Org. Mass Spec. **1**, 115 (1968).

78. M. Das and S.E. Livingstone, Aust. J. Chem. **27**, 749 (1974).

79. M. Das. Inorg. Chim. Acta. **76**, L111 (1983).

80. C. Reichert and J. B. Westmore, Can. J. Chem. **48**, 3213 (1970).

81. T.T. Gill, **Isotope Cluster Eaminer: A Software System for Microcomputer Analysis of Mass Spectral Data**, M.Sc. Thesis, University of Wisconsin (1983).

82. R.J. Abraham, **The Analysis of High Resolution NMR Spectra**, Elsevier Pub. Co. Ltd., New York (1971).

83. A locally modified computer program **Numarit**. J.S. Martin, A.R. Quirt and K.E. Worvill. The NMR program library. Daresbury Laboratory, Daresbury, U.K.

84. M. Das, S.E. Livingstone, J.H. Mayfield, D.S. Moore and N. Saha, Aust. J. Chem. **29**, 767 (1976).

85. D.T. Haworth, M. Das, J. Fluorine Chem. **20**, 487 (1982).

86. O. Siiman, D. Titus, J. Amer. Chem. Soc. **96**, 2353 (1974).

87. N.N. Greenwood and A. Earnshaw, **Chemistry of the Elements**, Pergamon Press, Toronto, 1290 (1984).

88. M. Tomoeda, M.Inuzuka and T. Furuta, Tetrahedron Letters, 1233, (1964).

89. A. Bondi, J. Phys. Chem. Soc. **94**, 441, (1964).

90. B.F. Hoskins and C.D. Pannan, Inorg. Nucl. Chem. Lett. **11**, 409 (1975).

91. C. Sreelatha, V.D. Gupta, C.K. Narula and H. Noth, J. Chem. Soc. Dalton Trans. 2623 (1985).

92. G. Bandoli, U. Mazzi, H. Spies, R. Munze, E. Ludwig, E. Ulhemann and D. Scheller, Inorg. Chim. Acta. **132**, 177 (1987).

93. J.Ollis, M. Das, V.J. James, S.E. Livingstone and K. Nimgirawath, Cryst. Struct. Commun. **5**, 679 (1976).

94. J.P.R. De Villiers and J.C.A. Boeyens, Acta Cryst. **28**, 2335 (1972).

95. P.K. Hon, C.E. Pfluger and R.L. Belford, Inorg. Chem. **5**, 516 (1966).

96. P.K. Hon, C.E. Pfluger and R.L. Belford, Inorg. Chem. **6**, 730 (1967).

97. J. Iball and C.H. Morgan, Acta Cryst. **23**, 239 (1967).

98. R.C. Mehrotra, R. Bohra and D.P. Gaur, **Metal Beta-Diketonates and Allied Derivatives**, Academic Press, London (1978).

99. B. Morosin and J.R. Brathovde, Acta Crysta. **17**, 705 (1964).

100. S. Okeya, S. Ooi, K. Matsumoto, Y. Nakamura and S. Kawaguchi, Bull. Chem. Soc. Jpn. **54**, 1085 (1981).

101. G.J. Palenik and K.R. Dymock, Acta Cryst. B**36**, 2059 (1980).

102. J.G. Rodriguez, F.H. Cano and S. Garcia-Blanco, Cryst. Struct. Commun. **8**, 53 (1979).

103. B. Wenclawiak, A.A. Pinkerton and N.J. Terrill, Inorg. Chim. Acta. **149**, 213 (1988).

104. G.A. Stern, M.Sc. Thesis, **A Mass Specrometric Study of Some β-diketonate and monothio-β-diketonate complexes of Ni(II), Zn(II), Pd(II), Co(III) and Rh(III)**, University of Manitoba (1985).

105. M.A. Gallop and W.R. Roper, Adv. Organometal. Chem. **25**, 121 (1986).

106. C. Reichert, G.M. Bancroft and J.B. Westmore, Can. J. Chem. **19**, 1545 (1966).

107. W.D. Courier, W. Forster, C.J. Lock and G. Turner, Can. J. Chem. **50**, 8 (1972).

108. D.M. Blake, J. de Faller, Y.L.Chung and A. Winkelman, J. Amer. Chem. Soc. **96**, 5568 (1974).

109. D.M. Blake, A. Winkelman and Y.L.Chung, Inorg. Chem. **14**, 1326 (1975).

110. R.E. Fraas, R.W. Kiser and G.L. Chaney, Org. Mass. Spectrom. **2**, 1171 (1969).

111. J. Charalambous, R.G. Gossett, M.H. Johri and M.J. Kensett, Inorg. Chim. Acta. **22**, 101 (1977).

112. R.B. King and M.B. Bisnette, J. Organometal. Chem. **2**, 15 (1964).

113. J. B. Wilford and F.G.A. Stone, Inorg. Chem. **4**, 389 (1965).

114. F.A. Cotton and J.A. McCleverty, J. Organometal. Chem. **4**, 490 (1965).

115. H.C. Clark and J.H. Tsai, J. Organometal. Chem. **7**, 515 (1967).

116. F.A. Cotton and R.M. Wing, J. Organometal. Chem. **9**, 511 (1967).

117. T.G. Appleton, M.H. Chisholm, H.C. Clark and L.E. Manzer, Inorg. Chem. **11**, 1786 (1972).

118. F. Bonati and R. Ugo, J. Organometal. Chem. **11**, 341 (1968).

119. R.C. Fay and T.S. Piper, J. Amer. Chem. Soc. **85**, 500 (1963).

120. R.H. Holm and F.A. Cotton, J. Amer. Chem. Soc. **80**, 5658 (1958).

121. G.A. Heath and R.L. Martin, Aust. J. Chem. **24**, 2061 (1971).

122. A.R. Hendrickson and R.L. Martin, Inorg. Chem. **14**, 979 (1975).

123. A.R. Hendrickson and R.L. Martin, Inorg. Chem. **12**, 2582 (1973).